Integrated Geophysical Investigations of a Methane Releasing Pingo in a Changing Permafrost Environment, Svalbard

Craig Paul Hammock

A thesis submitted to Swansea University in fulfilment of the requirements for the Degree of Doctor of Philosophy

Swansea University

2022

Abstract

Open-system pingos form a fluid-flow conduit through continuous permafrost that enables the release of methane; a potent greenhouse gas. However, the factors that impact the formation and structure of open-system pingos remains poorly understood, and the parallels that these terrestrial landforms have with methane emitting submarine forms is uncertain. In this thesis, a series of geophysical investigations are conducted on Lagoon Pingo, Svalbard: a coastal open-system pingo that emits locally significant quantities of methane. In investigations into pingo structure through electrical resistivity tomography, resistivities imply that Lagoon Pingo is dominated by segregation ice, thereby highlight the impact of frost-susceptible, fine-grained sediments on pingo formation. Seismic investigations outline the depth of these sediments locally (~68 m), and indicate an uncertainty surrounding the flow path of local groundwaters. Constraining the groundwater dynamics through self-potential investigations, elevated magnitudes in potential measurements on the northern side of the pingo are interpreted as groundwaters flowing beneath the pingo complex from an alluvial fan on the northern side of Lagoon Pingo. Transient electromagnetics, when combined with seismic velocities within a four-phase model, identify a heterogeneous layer containing alluvial fan deposits beneath the open-system pingo. The integrated geophysical observations highlight the role that alluvial fans can have in pingo growth, by providing a hydraulically conductive medium through poorly permeable sediments characteristic of Holocene marine environments. This can act as a confined aquifer, explaining the artesian conditions at Lagoon Pingo. This also provides sedimentological circumstances that were favourable for previous pockmark formation, and may explain how a spring has persisted through Holocene sedimentation. These integrated geophysical investigations therefore highlight the role that alluvial fans have in pingo formation, and indicate how open-system pingos may evolve from submarine seeps and pockmarks.

Declarations and Statements

This work has not previously been accepted in substance for any degree and is not being concurrently submitted in candidature for any degree.
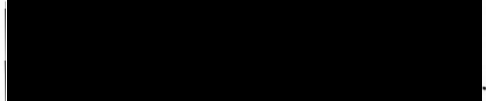
Date 29/09/22

This thesis is the result of my own investigations, except where otherwise stated. Other sources are acknowledged by footnotes giving explicit references. A bibliography is appended.

Date 29/09/22

I hereby give consent for my thesis, if accepted, to be available for photocopying and for inter-library loan, and for the title and summary to be made available to outside organisations.

Date 29/09/22

The University's ethical procedures have been followed and, where appropriate, that ethical approval has been granted.

Date 29/09/22.

Authorship Declaration for the Inclusion of Publications

The following people and institutions contributed to the publication of work undertaken as part of this thesis:

Author	Initials	Institution(s)
Craig P. Hammock (PhD Candidate)	CPH	Department of Geography, College of Science, Swansea University
		Centre for Arctic Gas Hydrate, Environment and Climate, Department of Geosciences, UiT The Arctic University of Norway
		Department of Arctic Geology, University Centre in Svalbard (UNIS)
Bernd Kulessa	BK	Department of Geography, College of Science, Swansea University
		School of Technology, Environments and Design, University of Tasmania
John F. Hiemstra	JFH	Department of Geography, College of Science, Swansea University, Singleton Park, Swansea, SA2 8PP, Wales, UK
Andrew J. Hodson	AJH	Department of Arctic Geology, University Centre in Svalbard (UNIS), 9171 Longyearbyen, Norway
		Department of Environmental Science, Western Norway University of Applied Sciences
Alun Hubbard	AH	Centre for Arctic Gas Hydrate, Environment and Climate, Department of Geosciences, UiT The Arctic University of Norway
		Geography, University of Oulu

Paper Details and Contributions:

Title: Seismic and electrical geophysical characterization of an incipient coastal open-system pingo: Lagoon Pingo, Svalbard.

Originally published in Earth and Space Science (doi: 10.1029/2021EA002093), located in Chapter 4.

Candidate (CPH) contributed to the conceptualization, methodology, collection of data, analysis, interpretation, writing, review and editing, and funding acquisition. (80%)

BK contributed to the conceptualization, methodology, collection of data, review and editing, funding acquisition and supervision. (8%)
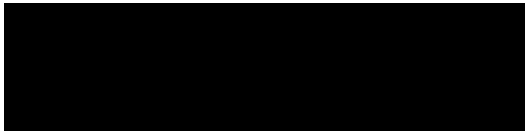
JFH contributed to the conceptualization, review and editing, funding acquisition and supervision. (7%)

AJH contributed to the conceptualization, review and editing, funding acquisition and supervision. (2.5%)
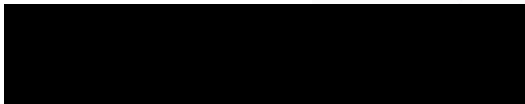
AH contributed to the conceptualization, review and editing, funding acquisition and supervision. (2.5%)

We the undersigned agree with the above "proportion of work undertaken" for the above published peer-reviewed manuscripts contributing to this thesis.

(Saltash, 20 Sept, 2022)

(Swansea, 22 Sept, 2022)

(Swansea, 22 Sept, 2022)

(Longyearbyen, 20 Sept, 2022)

(Tromsø, 23 Sept, 2022)

Table of Contents

List of Tables

List of Figures

Abbreviations

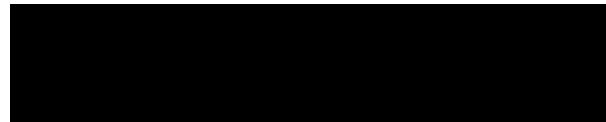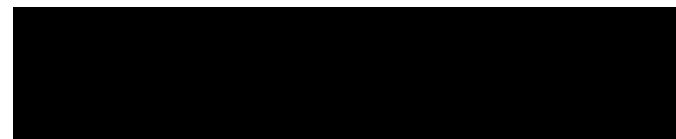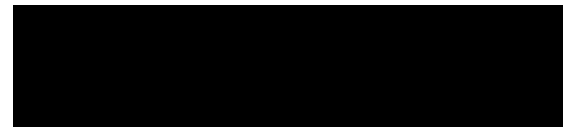|	
1-D	One Dimensional
2-D	Two Dimensional
4PM	Four Phase Model
a.s.l.	Above Sea Level
BP	Before Present
CH_4	Methane
CO_2	Carbon Dioxide
CSAMT	Controlled Source Audio-Magnetotellurics
DEM	Digital Elevation Model
ERT	Electrical Resistivity Tomography
FD	Finite Difference
FFT	Fast Fourier Transform
GHSZ	Gas Hydrate Stability Zone
GPR	Ground-Penetrating Radar
GPS	Global Positioning System
GUI	Graphical User Interface
MAAT	Mean Annual Air Temperature
MCMC	Markov Chain Monte Carlo
MuLTI-TEM	Multimodal Layered Transdimensional Inversion for Transient Electromagnetic Data
N_2O	Nitrous Oxide
NaCl	Sodium Chloride (or Salt)
NE	Northeast
NMO	Normal Moveout
NW	Northwest
PDF	Posterior Depth Function
PDSM	Pre-Stack Depth Moveout
ppb	Parts per Billion
RCP	Representative Concentration Pathway
RMS	Root-Mean-Square Error
SE	Southeast
SIRT	Simultaneous Inversion Reconstruction Algorithm

SNMR	Surface Nuclear Magnetic Resonance
SOC	Soil Organic Carbon
SP	Self-Potential
SW	Southwest
TEM	Transient Electromagnetics
VPDB	Vienna PeeDee Belemite

Acknowledgements

I would firstly like to thank my supervisors, Bernd Kulessa, Alun Hubbard, Andy Hodson, John Hiemstra, and Sarah Thompson, for all their enthusiasm, support, and guidance in completing this project. The support was greatly appreciated, and I thank you all for the many opportunities that were given to me throughout my PhD.

This thesis would not be possible without the many people who gave up their time and energy to help out in the field. Thanks to Emma, Veerle, James, Viktor, Will, Mikkel T. H., Naomi, Laura, Thit, Christina, Daniela, Marjolein, Mikkel B., Anton (a.k.a. Tony), Ian and Karlotta. At times, the going got tough, especially amid some challenging circumstances, but the perseverance paid off. Additionally, thank you to the UNIS logistics department, and to Sara Mollie Cohen in particular, for the loan of the electrical resistivity tomography instruments, and for the necessary training and support required for me to undertake fieldwork safely.

Thanks to Richard Hann and Armin Dachauer for collecting the Structure-from-Motion DEM whilst I was in the field (Hann and Dachauer, 2020).

Thanks to the NERC Geophysical Equipment Facility for letting me borrow their transient electromagnetics equipment (twice), and for their training and support in its use for the fieldwork. It ultimately proved to be an important piece of this work, and I am grateful for the opportunity to be able to use it. Additionally, thank you to Siobhan Killingbeck, for all the help and support provided in the use of MuLTI-TEM.

Thank you to the University Centre in Svalbard for hosting me for almost two years, amid a global pandemic. A further thanks goes to the Svalbard Treaty. It proved to be very useful. Additionally, my time on Svalbard would have not been so enjoyable, were it not for those who I am honoured to call my friends. Special shoutouts go to Vanessa, for the numerous dinner parties after a hard day's work, and to the "Legends of Longyearbyen" for some interesting adventures.

A wholehearted thanks to my parents, Jackie and Paul, for their love and care during my PhD.

Lastly, a wholehearted thanks to Karlotta, whose love, support and care throughout the PhD eventually got me over the finish line. I definitely would not have been able to get this far without it. You well and truly are the bestest egg.

This thesis was funded by postgraduate scholarship funded jointly by Swansea University and the Centre for Arctic Gas Hydrate, Environment and Climate (CAGE), University of Tromsø. Further fieldwork funding was provided by the Swansea University's College of Science Research Fund, by the Near-Surface

Chapter 1: Introduction and Aims

1.1. Research Context and Motivation

As the second most abundant greenhouse gas in the Earth's atmosphere (Nisbet et al., 2020), and the cause of one fifth of all anthropogenic radiative forcing (Nisbet et al., 2016), methane has a considerable role in the increase of global air temperatures (Forster et al., 2021). The rise in air temperatures is greatest in the Arctic, where warming is amplified by a series of positive feedbacks (Pithan and Mauritsen, 2014). Since the industrial revolution, the Arctic has warmed by more than 2˚C to 3˚C (Post et al., 2019). This rate of warming is approximately double that of the rest of the world (Serreze et al., 2009; Hinzman et al., 2013).

Our ability to model and understand future methane emissions relies heavily on our understanding of the nature of emission processes. In permafrost environments, where the ground that is at or below 0˚C for two or more consecutive years (van Everdingen, 2005), this is particularly important. Whilst permafrost is susceptible to substantial changes due to a climate impacted by greenhouse gas emissions (Jakobsson et al., 2014), these environments also contain large reservoirs of methane equal to twice the amount that is currently resident in the Earth's atmosphere (Schuur et al., 2008; 2009; Hugelius et al., 2014). The release of this methane forms a positive feedback loop, which may fuel an acceleration in temperature increases, which in turn increases the rate of permafrost degradation (Schuur et al., 2008; 2009). Yet whilst a number of emission processes from permafrost degradation are well understood (e.g. Koven et al., 2011; Lawrence et al., 2015; Turetsky et al., 2019; 2020; Walter Anthony et al., 2012), continuous permafrost have often been presumed to form a "cryospheric cap" that inhibits gas migration and emissions.

More recent investigations of open-system pingos on Svalbard within continuous permafrost contradicts this notion, through the discovery of substantial emissions of methane (Hodson et al., 2019; 2020). Open-system pingos are ice-cored mound-like landforms formed from the freezing of hydraulically pressurised groundwater. In their role as conduits which enable

methane release through continuous permafrost, recent studies have argued that they may be considered as terrestrially analogous to submarine seeps that emit methane on the seafloor (Hodson et al., 2019). However, unlike submarine seeps, methane emissions from open-system pingos circumvent oxidisation within the marine water column (Myhre et al., 2016), and therefore correspond with the more direct emission of methane to the atmosphere.

Yet despite a recent appreciation for their role as a conduit of methane through continuous permafrost, open-system pingos are poorly understood (e.g. Gurney, 1998; Demidov et al., 2019; Kunz and Kneisel, 2021). Firstly, uncertainty remains regarding their structural composition. Whilst a core composed of massive ice has been traditionally considered as a defining characteristic of open-system pingos (e.g. Harris et al., 1988), others have argued that segregation ice is an important geomorphological component of some pingos (Mackay, 1973; 1978; Ross et al., 2007). Secondly, the hydrological characteristics of open-system pingos are poorly constrained (Ballantyne, 2018). As permafrost is generally considered to be an aquitard, envisaging how unfrozen groundwaters penetrate through the permafrost, and other impermeable media (e.g. fine-grained sediments) is difficult. Lastly, whilst some authors have theorised that open-system pingos may have evolved from submarine pockmark and seeps (e.g. Hodson et al., 2019), limited investigation has been conducted on discerning how these landforms may be related.

1.2. Thesis Aims and Objectives

Focusing on a coastal open-system pingo with observations of methane release, this aim of this thesis is to identify and analyse the structures, processes and mechanisms that result in open-system pingos forming conduits through which sub-permafrost methane can be released. Through the use of a range of geophysical methods, this thesis intends to fulfil the following objectives:

1) Assess and determine the internal structure and composition of a nearshore open-system pingo.

2) Identify the spatial and temporal hydrological regime of the pingo, and understand the nature of intra- and sub-permafrost groundwater migration.

3) Evaluate the factors that have resulted in open-system pingo formation in this location, and evaluate theories that open-system pingos are genetically linked to submarine seep and pockmark forms.

1.3. Thesis Format

This chapter (Chapter 1) provides a brief overview of the thesis topic, outlining the context, motivation and aims of the thesis.

In Chapter 2, the wider context of this thesis is expanded upon, and the key concepts underpinning the thesis are explained. The chapter commences with an explanation of permafrost, outlining the vulnerability of permafrost to a changing climate, and the feedback loop between methane and permafrost. Sources of methane within Arctic environments are then explained, including those which occur in the submarine environment, before an overview of the relevant pingo literature is provided.

Chapter 3 provides an overview of Lagoon Pingo, which serves as the focus of these targeted geophysical investigations. Within this chapter, the local and regional context of Lagoon Pingo is explained, and previous geophysical investigations of the pingos within Adventdalen are discussed.

Each of the following three chapters are presented as independent studies of Lagoon Pingo, with distinct introductory, methodology, result, interpretation and discussion sections. Chapter 4 uses a combination of electrical resistivity tomography with active source seismic methods to delineate the internal structure and composition of the pingo near surface.

Chapter 5 details the use of a self-potential array to determine the spatiotemporal flow of groundwater around Lagoon Pingo. In addressing the hydrological characteristics of the pingo, this chapters identifies the dominant

flow pathway into the pingo, and determines external factors that may influence the nature of the central pingo spring.

Chapter 6 addresses some of the questions that arise from the electrical resistivity, active seismics and self-potential studies, through collection, interpretation and analysis of a transient electromagnetic dataset. This chapter tests the hypothesis that a unit of alluvial fan deposits beneath the pingo provides a permeable layer which enables the local flow of groundwaters necessary to form an open-system pingo in this location. To enhance interpretation of the obtained transient electromagnetics, measurements are integrated with the active seismic data collected in Chapter 4 within a model that estimates the rock, ice, water and air content of the subsurface. The factors that affect the formation of the pingo in this location are discussed.

Chapter 7 discusses the findings of these combined geophysical investigations, and outlines the implications of these studies on local and broader knowledge. Other sites are identified that may be analogous or similar to Lagoon Pingo, and warrant investigation.

Lastly, in Chapter 8, concluding remarks compare the studies with the intended objectives of the overall thesis. Finally, suggestions for further work both at Lagoon Pingo and elsewhere are outlined, building upon the core findings of this thesis.

Chapter 2: Background

In this chapter, I provide background to the overall thesis. Firstly, I provide an overview of permafrost, and explain its definition, distribution and structure. To contextualise the study, the vulnerability of permafrost to climate change is discussed, and how this forms a positive feedback loop considering the amount of methane stored within permafrost environments. Following this, the role of methane in climate change is discussed, and the series of sources in the high Arctic that contribute to emissions within methane budgets. This includes submarine methane sources, and their related landforms. Lastly, I provide a review of pingos, and explain the focus of open-system pingos in these investigations considering how recent studies have highlighted these landforms as hotspots of methane emissions in continuous permafrost environments (Hodson et al., 2019; 2020).

2.1. Permafrost Definition and Distribution

Whilst permafrost is often mistakenly referred to as "frozen ground", the correct definition is strictly based on temperature. The International Permafrost Association define permafrost as "*ground (soil or rock and included ice or organic material) that remains at or below 0˚C for at least two consecutive years*" (van Everdingen, 2005). Permafrost is defined irrespective of moisture or ice content, can be cryotic (frozen) or non-cryotic (unfrozen), and whilst the etymology of the term suggests permanence, permafrost should be considered a perennial feature as natural or man-made changes may cause ground temperatures to rise above 0˚C.

Permafrost is a widespread phenomenon; underlying 23.9% of the exposed land area in the Northern Hemisphere (Zhang et al., 1999). As permafrost represents a product of heat exchange between the ground and atmosphere, climate is the primary variable in dictating its distribution. Consequently, much of Earth's permafrost exists at high latitudes and altitudes, where mean annual air temperatures (MAATs) are below 0˚C. In the Northern Hemisphere, extensive permafrost occurs in Arctic regions including Northern Canada

(O'Neill et al., 2019), Alaska (Osterkamp, 2005; Jorgenson et al., 2008), Svalbard (Humlum et al., 2003) and Siberia (Romanovsky et al., 2007), and extends deep into sub-Arctic Canada (Brown et al., 2014) and Russia (Pavlov, 1994). Outside of high latitude regions, permafrost pervades much of the Earth's major mountainous regions, including the European Alps, Himalayas, Scandes and Altai mountains (French, 2017). In the Southern Hemisphere, permafrost can be found on the Antarctic continent, sub-Antarctic islands and the Andes (Schuur et al., 2008; Vieira et al., 2010).

Permafrost can be classified into four categories based upon its extent (Figure 2.1): continuous (90 - 100% coverage), discontinuous (50 - 90%), sporadic (10 – 50%) or isolated (< 10%; van Everdingen, 2005). In continuous regions, cryotic ground is generally assumed to be omnipresent, except in isolated zones beneath lakes and river channels. Discontinuous permafrost is ordinarily depicted as frozen bodies, distributed amongst otherwise zones of unfrozen ground. In sporadic or isolated instances, permafrost is restricted to islands, which occur as a consequence of localized differences in soils, vegetation or other variables that affect the thermal conductivity and diffusivity of the subsurface (Schuur et al., 2008).
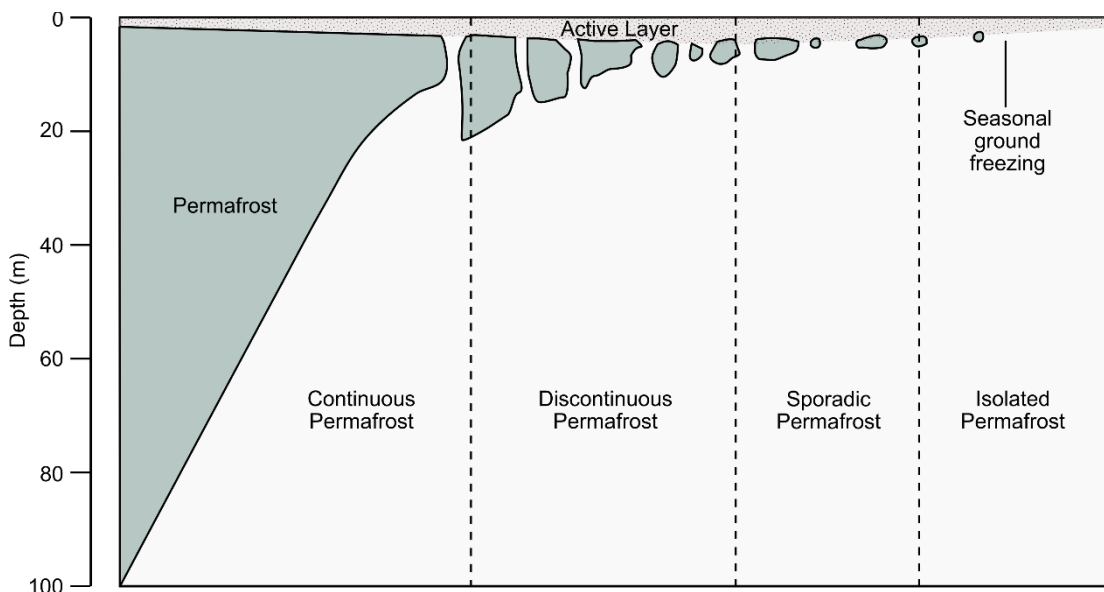
Figure 2.1. The approximate differences in permafrost extent and depth within continuous, discontinuous, sporadic and isolated permafrost environments (adapted from Ballantyne, 2018).

It is important to note that cryotic ground may persist even where mean annual air temperatures are above freezing. For example, permafrost thicknesses exceed 180 m in the Kuskokwim River valley in Alaska, despite annual mean temperatures above freezing (French, 2017). This is because present-day permafrost is a product of both past and present climates (Péwé, 1975). Where permafrost was formed in climate conditions that are colder than the present day, it is commonly referred to as relict permafrost (Ballantyne, 2018).

Whilst past and present climate provides the primary control on permafrost extent, a broad range of secondary variables influence the spatial extent of permafrost, particularly in discontinuous or sporadic regions. These complex factors which influence permafrost extent include local relief and aspect (Campbell et al., 2021), soil type (Jorgenson et al., 2010), vegetation (Li et al., 2021; Heijmans et al., 2022), snow cover (Lawrence and Slater, 2010; Park et al., 2015; Gisnås et al., 2016), fire (Holloway et al., 2020; Li et al., 2021) and water (Lawrence and Slater, 2005). In combination, these variables not only dictate the spatial extent of permafrost, but also the structure, mechanical state and thickness in localized zones.

2.2. Structure of Permafrost

Permafrost is typically overlain by a layer which seasonally freezes and thaws. This is commonly referred to as "the active layer" (shown in Figures 2.1 and 2.2), and can be between tens of centimetres in high latitude, continuous permafrost regions (e.g. Bockheim, 1995), to several meters in sub-Arctic discontinuous permafrost regions (Christiansen et al., 2010). In the continuous permafrost zone, the active layer normally reaches the permafrost table, whilst in discontinuous zones, the active layer may be separated from bodies of permafrost by unfrozen sections. The thickness of this layer varies yearly, depending on the complex interaction of variables that affect the thermal and hydrological properties of the near-surface, including air temperature (Hinkel and Nelson, 2003; Åkerman and Johansson, 2008), aspect and relief (Repelewska-Pękalowa and Pękala, 2004; Cao et al., 2017), vegetation (Beck et al., 2015), snow cover and regime (Hrbáček et al., 2016; Atchley et al.,

2016), soil and rock type (Farbrot et al., 2013; Hipp et al., 2014), and the overall water content (Clayton et al., 2021).
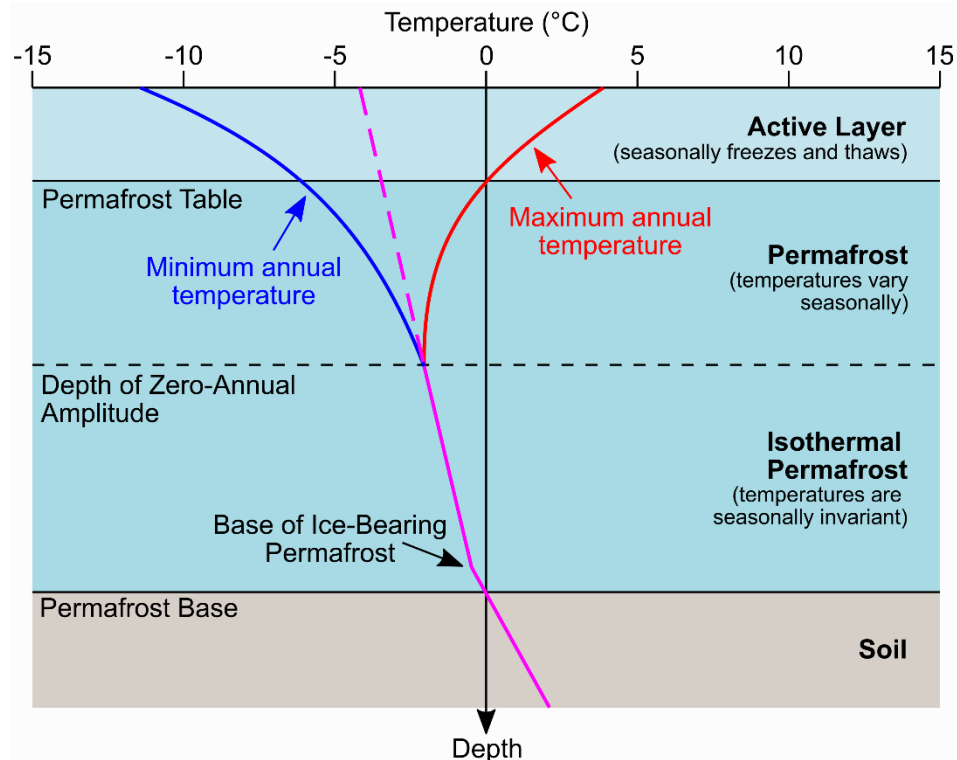
Figure 2.2. The typical vertical temperature profile in permafrost, with minimum, maximum and average annual temperatures plotted. The change in gradient towards the permafrost base is caused by differences in thermal conductivities in frozen and unfrozen ground (modified from Osterkamp and Burn, 2002).

In continuous permafrost regions where the active layer typically extends to the top of permafrost, some authors suggest an additional layer that retains characteristics of both the active layer and underlying permafrost (Shur, 1988; Shur et al., 2005). This layer is referred to as the transient layer (Shur et al., 2005), and represents a zone which undergoes freeze-thaw transitions on a sub-decadal to multi-centennial timescale. In undergoing these infrequent transitions, Shur et al. (2005) indicates that this zone can be ice-enriched, and results in the formation of cryogenic soil structures that increases latent heat required for the thaw of underlying permafrost.

The zone beneath this transient layer, permafrost, corresponds to where temperatures are below 0˚C all year round. This permafrost can be classified according to how it was formed. Epigenetic permafrost forms whereby the

sediment body has previously accumulated, and where the energy lost to the surface exceeds that of the geophysical heat flux (Ballantyne, 2018). Where sediments are actively being deposited, and permafrost aggrades upwards into these accumulations, syngenetic permafrost forms. In some cases, permafrost can form from a combination of upward and downward aggradation; these permafrost bodies are polygenetic (e.g. Shur et al., 2004).

As the freezing of sediments varies on a range of sediment and hydrological properties, unfrozen sections may occur within permafrost, even within zones where permafrost is considered continuous (e.g. Keating et al., 2018). A section of unfrozen ground within permafrost is known as a talik (van Everdingen, 2005). Taliks can have a pronounced effect on a wide range of construction, groundwater circulation, and on the carbon-permafrost feedback, amongst other effects (O'Neill et al., 2020). In areas where permafrost is formed in areas where groundwaters are saline, or otherwise consist of impurities that inhibit the ground freezing, a cryopeg may form. These areas of perennially cryotic ground that remain unfrozen arguably impact on groundwater circulation within permafrost (Keating et al., 2018), and may impact on the permafrost response to climatic forcings (e.g. Grosse et al., 2011; Shur et al., 2005). Most notably, cryopegs can form areas of enhanced activity for methanogenic microbes, which can contribute to local greenhouse gas emissions (Jansson and Taş, 2014).

The transition between permafrost, and the underlying strata above 0°C is marked by the permafrost base. In a scenario where the ground conditions are in equilibrium with the present-day climate, and in absence of other factors that may exhibit a control on freezing conditions (e.g. salinity), the permafrost base would likely mark the boundary between cryotic and non-cryotic sediments. Investigations of the permafrost base are normally limited to a quantification of its depth, in order to provide an understanding of the thickness of frozen ground (e.g. Jorgenson et al., 2008). Despite this, recent studies have indicated that the transition zone at the base of permafrost may represent an important zone for understanding the condition of permafrost. For example, Kasprzak et al. (2017) argue that low resistivities identified on Svalbard indicate the effect of seawater on the thermal state of coastal permafrost.

2.3. Permafrost Vulnerability to Climate Change

Global surface air temperatures have increased approximately 1.2˚C since the mid-1800s, with far-reaching impacts on natural systems on Earth (Chen et al., 2021). These changes in global climate are largely attributed to the anthropogenic emission of greenhouse gases in the atmosphere (Forster et al., 2021). Greenhouse gases such as carbon dioxide (CO_2), methane (CH_4) and nitrous oxide (N_2O) have a relatively high thermal absorption capacity, and persist in the atmosphere for a long period of time (Serrano-Silva et al., 2014). As a result, greenhouse gases regulate the Earth's climate, by affecting the proportion of absorbed longwave radiation within the Earth's energy budget. The atmospheric concentration of greenhouse gases has increased rapidly since the end of the industrial revolution; carbon dioxide concentrations have increased from 278 parts per million in 1750 to 410 parts per million in 2019, whilst methane concentrations have increased from 729 parts per billion in 1750 to 1866 parts per billion in 2019 (Forster et al., 2021). Further increases in greenhouse gas emissions are suggested to exacerbate changes in climate, resulting in further increases in temperature, amongst other impacts (Chen et al., 2021).

The impact of climate change is particularly pronounced in the Arctic (Hinzman et al., 2013), whereby temperatures have increased twice as fast than the global average (Serreze et al., 2009; Cohen et al., 2014). This is commonly referred to as Arctic amplification (Pithan and Mauritsen, 2014). Whilst the exact processes which result in this spatial heterogeneity in climate warming remains under debate (Cohen et al., 2014; Previdi et al., 2021), the variables which are suggested to impact this broadly fit within two categories: mid-latitude effects that are transported poleward in the troposphere, and feedback loops within the Arctic environment. In terms of mid-latitude effects, a re-analysis of climate data by Graversen et al. (2008) suggests that atmospheric heat transport may occur, transporting anthropogenic climate forcings from low-latitude atmosphere preferentially towards the poles. In contrast, local effects include feedbacks relating to diminishing sea ice extent (Winton, 2006; Serreze et al., 2009; Dai et al., 2019), changes in Arctic cloud cover and water vapour content (Graversen and Wang, 2009), increased emission of longwave

radiation with temperature increases in polar regions (Pithan and Mauritsen, 2014), and forcings from the local emission of greenhouse gases (McGuire et al., 2009; Schuur et al, 2015; Bowen et al., 2020).

As a subsurface phenomenon which is primarily controlled by climate, permafrost is particularly vulnerable to warming temperatures. An increase in temperature in Arctic environments will encourage the development and extension of thermokarst; ground subsidence caused by the melting of excess ground ice. The impact of thermokarst and thaw on permafrost environments are varied. In Arctic environments, these impacts may include the thaw of ice wedges to form a hummocky terrain marred by thermokarst gullying (Jorgenson et al., 2006; Osterkamp et al., 2009), the degradation of frost mounds such as pingos, lithalsas and palsas (Vallée and Payette, 2007; Beck et al., 2015), the formation and expansion of thermokarst lakes in areas of ice-rich permafrost (in't Zandt, 2020) and the drainage of lakes in discontinuous permafrost environments (Yoshikawa and Hinzman, 2003), the changing of hydrological regimes in Arctic rivers (Peterson et al., 2002; Pohl et al., 2007), and accelerated processes of coastal erosion (Nielsen et al., 2022). In mountainous permafrost environments, the thaw of permafrost may lead to rock slope instability (Gruber and Haeberli, 2007; Huggel et al., 2010), enhanced periods of debris flow activity (Lewkowicz and Way, 2019) and the melt-out of rock glaciers (Robson et al., 2022).

Permafrost thaw also impacts upon future climate through a series of feedback effects (Schuur et al., 2008; 2009; 2015; Turetsky et al., 2019). Approximately 60% of the world's soil carbon in thought to occur in about 15% of Earth's total land area, in permafrost (Hugelius et al., 2014; Schuur et al., 2015). Estimates of soil organic carbon (SOC) within the upper 3 m of global permafrost indicate that this is in the range of ~1100 Pg to ~1500 Pg, totaling approximately twice the amount that exists within Earth's atmosphere (Hugelius et al., 2014; Natali et al., 2021). This is due to a series of processes that occur within permafrost environments that result in the preferential formation of pools of SOC. For example, aeolian, alluvium, colluvium or otherwise proluvium processes result in the accretion of soils with high SOC contents within permafrost zones (Hugelius et al., 2014). The relative increase in surface height from soil

accretion prompts the formation of an ice-rich syngenetic permafrost under cold conditions, preserving soil organic carbon by inhibiting decomposition, due to cold temperatures and poor soil drainage (Davidson and Janssens, 2006). Additionally, the repeated freeze and thaw of sediments in the active layer result in the cryoturbation of soils, whereby humic-rich topsoil is subducted into deeper layers (Van Vilet-Lanoë, 1998; Kaiser et al., 2007; Bockheim, 2007).

The thaw of permafrost due to a warming climate exposes soils to decomposition by microbes that produce greenhouse gases (Walter Anthony et al., 2018). Recent projections indicate that under an intermediate scenario (denoted by the IPCC's representative concentration pathways (RCP) 4.5), cumulative emissions from thawing permafrost will equal 27 to 100 Pg of carbon by 2100, leading to global warming of between 0.05 to $0.15°C$ (Schaefer et al., 2014). In a more extreme scenario whereby greenhouse gas emissions remain unmitigated (RCP8.5), McGuire et al. (2018) suggest the loss of between 6 and 16 million km^2 of permafrost, with a mean loss of 341 Pg of soil carbon over the next two centuries. In either scenario, this represents an increase in the relative fraction of global emissions attributable to permafrost, with models for intermediate scenarios calculating an increase from 3% at present to 11% by 2100 (Schaefer et al., 2014). Permafrost thaw thereby only serves to increase greenhouse gas concentrations in the atmosphere further, which exacerbates warming further and encourages further permafrost degradation and thaw (Schuur et al., 2009; 2015; Tarnocai, 1999; Khvorostyanov et al., 2008; Turetsky et al., 2020). Of the greenhouse gases released from permafrost environments, whilst carbon dioxide (CO_2) and nitrous oxide (N_2O) have notably significant contributions to atmospheric budgets (Voigt et al., 2020), methane (CH_4) warrants particular attention, as both a greenhouse gas with a high global warming potential (Nisbet et al., 2016), and for its suggested, yet uncertain role in the forcing of glacial millennial-scale climate cycles (Walter et al., 2007).

2.4. Methane

Methane is a potent greenhouse gas, with a 100-year global warming potential approximately 32 times greater than that of CO_2 (Etminan et al., 2016). However, despite an absolute concentration of CO_2 in the order of ~220 times that of CH_4 (Ruppel and Kessler, 2017), one fifth of anthropogenic radiative forcing is attributable to methane (Nisbet et al., 2016). The importance of methane within the global atmospheric system is underlined by its reaction with hydroxyl radicals. When methane reacts with hydroxyl radicals, the oxidising capacity of the atmosphere is reduced and ozone is generated within the troposphere, itself a notable greenhouse gas. As methane is relatively short lived (8-9 years within the atmosphere; Forster et al., 2021), it is both a key target for further understanding and climate change mitigation. Nisbet et al. (2020) notes that reducing methane emissions is a "low-hanging fruit for climate action", as mitigation measures would have a rapid effectiveness.

The proportion of methane gas within the atmosphere has increased considerably since the pre-industrial era, with particularly rapid increases throughout the 20th Century. Using ice cores, the mole fraction of methane in 1850 was suggested to equal approximately 830 ppbv^{-1} (e.g. Kirschke et al., 2013), as opposed to the more recent global mean of 1953 ppbv^{-1} measured in 2016. Present day increases in the mole fraction of methane are suggested to be in the order of 8-9 ppbv^{-1} yr^{-1}, equating to a net emissions increase of approximately 25 Tg of methane per year (Worden et al., 2017). At a time where CO_2 emissions are perceived to be stabilising by some (Haustein et al., 2017), methane emissions continue to accelerate with a considerable influence over the rate of climatic change (Worden et al., 2017).

The global methane budget is determined through the balance of many terrestrial and aquatic methane sources against a series of sinks, which is dominated by the atmosphere. To understand the nature of methane emissions into the atmosphere, methane is classified into three broad categories based upon their genesis: biogenic, thermogenic and pyrogenic (Saunois et al., 2016a). Biogenic methane is produced microbially by methanogens, which are typically found in anaerobic environments (e.g.

natural wetlands or rice paddies), oxygen-poor freshwater systems, or through the decomposition of organic waste (Kirschke et al., 2013). Methane which is formed through geological processes occurring over millions of years is referred to as thermogenic, with natural sources including both terrestrial and submarine seeps, and mud volcanoes (Kirschke et al., 2013). Thermogenic methane is also emitted through the anthropogenic burning of fossil fuels (e.g. oil, coal and natural gas). Lastly, pyrogenic methane is generated through the incomplete combustion of biomass and soil carbon, either through natural wildfire or anthropogenic burning (Kirschke et al., 2013). Biogenic, thermogenic and pyrogenic methane signatures vary in δ13C signature, with isotopic analyses providing a means of genetically deriving the methane source in regions whereby this is otherwise ambiguous (Dlugokencky et al., 2011; Brownlow et al., 2017).

In an attempt to estimate the annual methane flux to the atmosphere, and assess the relative contribution of individual sources and sinks, a range of models have been applied. These are classified into two types: top-down inversions that use atmospheric observations and transport models to derive individual sources and sinks of methane, and bottom-up models that extrapolate methane estimates from representative studies of known sources and sinks (Nisbet et al., 2014). In top-down studies, the application of atmospheric constraints provides estimates which are arguably more reflective of global level quantities, at the expense of a less explicit constraint of the source of methane (Saunois et al., 2019). In a top-down inversion covering global methane sources and sinks during the period 2000-2009, Kirschke et al. (2013) estimates methane emissions amounted to 548 Tg CH4 yr^{-1} (526 – 569 Tg CH4 yr^{-1}), with sinks equalling 540 Tg CH4 yr-1 (514 – 560 Tg CH4 yr^{-1}). Conversely, bottom-up methane budget models can identify the relative contribution of individual methane sources, but often have high uncertainties, resulting from the extrapolation of methane measurements. Thus, some studies question the spatial representativeness of bottom-up models, as methane measurements are often extrapolated from a relatively small number of baseline study sites, often studied intensively on account of known emission activity or accessibility (Dlugokencky et al., 2009; Vaughn et al., 2018). In a

bottom-up model covering global sources during the period 2000-2009, Saunois et al. (2019) derived a lower best estimate of 595 Tg CH4 yr^{-1}, with an uncertainty range of 489 Tg CH4 yr^{-1} to 749 Tg CH4 yr^{-1}.

In both of the top-down and bottom-up decadal methane budgets produced by Kirschke et al. (2013) and Saunois et al. (2019), the sources of methane emissions are categorised into five groups: natural wetlands (including those in permafrost environments; Saunois et al., 2016b), other natural sources (including termites, geological sources, permafrost and gas hydrate related), agriculture and waste, fossil fuel and biomass/biofuel derived. As seen in Table 2.1, categories pertaining to anthropogenic sources contain low uncertainties, whilst natural sources are relatively poorly constrained. For example, Saunois et al. (2019) highlights that uncertainties in natural wetland, freshwater and geologically derived sources largely result from poor spatial constraints. Other natural sources are uncertain given sources can be spatio-temporally complex (e.g. ebullition; e.g. Walter Anthony et al., 2016), vary in emission rate within different ecosystems or environments (e.g. termites; van Asperen et al., 2021) or as a consequence of a very limited number of measurements (e.g. submarine seeps; Portnov et al., 2016). The substantial uncertainty surrounding natural methane sources, and in particular those that are termed "other" and are unrelated to natural wetland environments, highlight the difficulties in constraining the nature, quantity and prevalence of methane release from natural environments (Dlugokencky et al., 2009).

The accurate modelling of methane estimates is important considering the vast quantities of soil carbon present within permafrost. As Arctic environments undergo amplified effects from warming caused by greenhouse gas forcings, methane budgets form an important tool in predicting emission rates and future climatic implications (Forster et al., 2021). Similarly, as these environments contain a range of important methane sources, modelling requires accurate observations of the nature of methane emissions from these locations (Saunois et al., 2016a; 2016b).

Table 2.1. Bottom-up estimates of methane from emission sources for the period 2000-2009 (Kirschke et al., 2013). Note how natural sources are comparatively poorly constrained, when compared to anthropogenic sources.

Sources	Emissions (Tg CH$_4$ yr^{-1})	Range of Estimates (Tg CH$_4$ yr^{-1})
Natural Sources	347	238 – 434
Wetlands	*217*	*177 - 284*
Other Sources	*130*	*61 – 200*
Anthropogenic Sources	331	304 – 368
Agriculture and Waste	*200*	*187 – 224*
Biomass Burning (incl. Biofuels)	*35*	*32 – 39*
Fossil fuels	*96*	*85 - 105*

2.5. Terrestrial Arctic Methane Sources

Arctic environments host a range of terrestrial methane sources that are perceived as susceptible to future climatic forcings. These include high latitude wetlands, areas where there are large quantities of near-surface ground ice and biomass in the tundra. Thompson et al. (2017) suggest that high latitude wetlands (defined here as those occurring north of the 50 N parallel) could currently contribute to as much as 15% of emissions into the global methane budget, with climatic warming resulting in the thaw of permafrost that releases nutrients and exposes organic-rich soils anaerobic decomposition (Lara et al., 2019). Additionally, as Arctic climates turn warmer and wetter, changes in snow cover and the hydrological state of permafrost are perceived to influence methane emission rates (Bohn et al., 2007). Furthermore, changes in temperature may influence the metabolic rate of methanogens (Christensen et al., 2003), prompting increased rates of methane generation and emission. However, recent work by Oh et al. (2020) argues that methane emissions derived from high-latitude wetland environments as a consequence of permafrost thaw may be overstated, as the role of methane-oxidizing bacteria known as high-affinity methanotrophs has previously been overlooked.
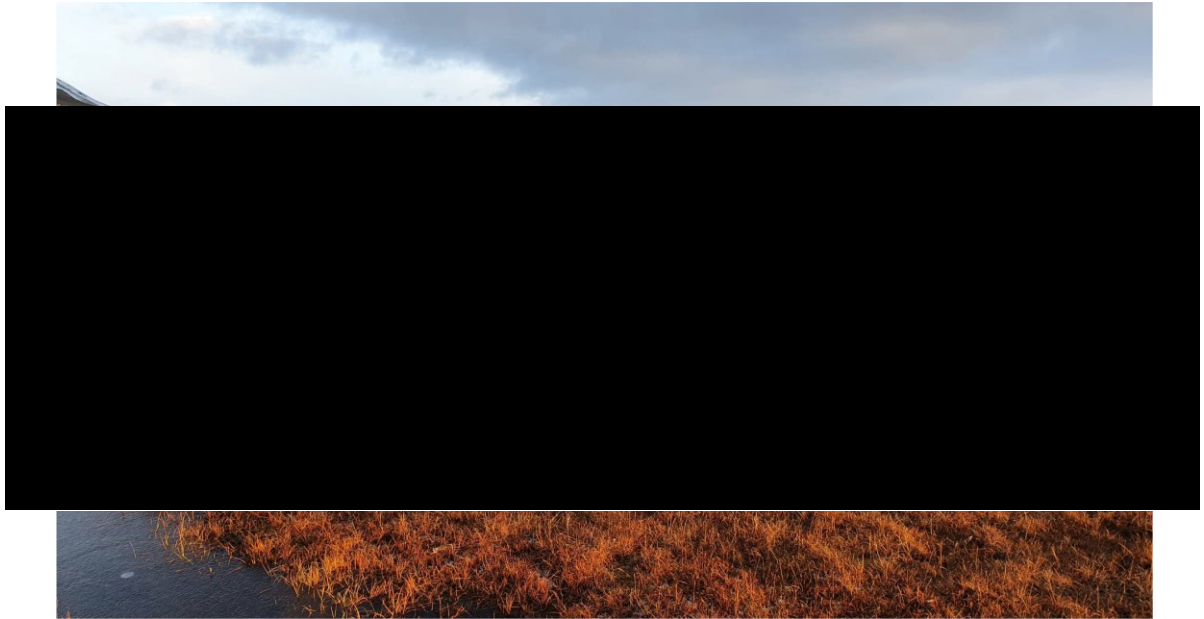
Figure 2.3. High latitude wetland environments, such as those in Adventdalen, Svalbard, contribute large emissions of methane to the global methane budget.

Increases in temperature as a result of a warming climate may also influence areas underlain with ground-ice, resulting in the abrupt thaw of carbon-rich soils (Turetsky et al., 2020). In areas that were formerly permafrost, carbon-rich material can becomes exposed to saturated conditions. Enhanced microbial activity results in an increased rate of CH_4 production, which can be directly emitted to the atmosphere. Turetsky et al. (2020) suggest that under a situation where emissions continue to rise (Representative Concentration Pathway (RCP) 8.5), a methane feedback from abrupt thaw may occur that results in the release of 1180 Tg CH4 per 1˚C global temperature increase. Of note is that regions particularly vulnerable to abrupt thaw events are also among the most carbon-rich; for example the Yedoma-type permafrost of Siberia and parts of Northern Canada contain up to 90% ground ice (Turetsky et al., 2019), but also contain large carbon and methane stores (Olefeldt et al., 2016).

Biomass and soil carbon are also susceptible, whereby the incomplete combustion of these components during wildfire contributes to the emission of pyrogenic methane to the atmosphere (Natali et al., 2021; Miner et al., 2022). Whilst the relative addition of methane from these sources is perceived to be small in present global budget estimates (Kirschke et al., 2013), warmer

temperatures are suggested to increase drought frequency, and will increase both the likelihood and intensity of wildfires (Hu et al., 2015).

2.6. Submarine Arctic Methane Sources

In addition to terrestrial sources of methane, submarine sources have been a point of contention over their potential contribution to the global methane budget (e.g. Myhre et al., 2016). Central to this debate is the role of gas hydrates; naturally-occurring ice-like solids that hold molecules of hydrocarbon gases, predominantly methane, within a rigid crystalline lattice of cages comprised of water molecules (Kvenvolden, 1993). The formation and prevalence of gas hydrates is controlled by the ionic impurities that comprise the clathrate, the composition of the gases, and the specific thermobaric conditions. This subsurface zone where the right combination of low temperatures and high pressures are thought to persist is commonly referred to as the "gas hydrate stability zone". As one of the few regions that fit each of the specific temperature, pressure and gas composition prerequisites needed for stability, gas hydrates are perceived to be prevalent on the continental margins surrounding the Arctic Ocean (Portnov et al., 2016), with further suggestions that quantities persist terrestrially (Betlem et al., 2019).

The volume of methane and heavier hydrocarbons stored within gas hydrate is uncertain, although it is often thought that quantities are large enough to invoke a substantial risk to global climate (Westbrook et al., 2009). Estimates of the amount of methane in gas hydrates are highly speculative (Ruppel, 2015). For example, through an assessment of global gas hydrate stability likelihood, the probability of reservoir lithology, and the likelihood of local gas generation, Johnson (2011) estimated that the amount of gas-in-place in methane hydrates equalled 1,600 Gt C. Conversely, estimates based upon measurements of methane release during past climatic shifts, such as that during the Paleocene-Eocene thermal maximum, suggest that the amount of gas-in-place may equal 12,400 Gt C (Dickens, 2011). Ultimately, there are too many unknowns, including the extent of gas hydrate bearing sediment, the total volume of these gas hydrates and the respective gas content within each

gas hydrate accumulation. As a result, some studies have suggested that more care should be taken in estimating gas hydrate, especially within Arctic environments where small scale studies have been extrapolated unnecessarily (e.g. Ruppel, 2015; Ruppel and Kessler, 2017).

Despite the uncertainty in the quantities of gas hydrate, especially within the Arctic, a wide range of submarine forms have been discussed as evidence for methane release from dissociating gas hydrates. These include pockmarks, submarine pingos, and submarine seeps.

2.6.1. Submarine Pockmarks

Pockmarks are concave depressions that occur on seabeds following the rapid expulsion of methane. They range from 10 – 700 m in diameter and can be up to 45 m deep (Hovland et al., 2002). Pockmarks vary in their shape, with circular, elongated and eye-shaped forms, ordinarily with a flatter bottom and steepening side walls. Pockmarks are also often found in clusters or in strings, often as a result of focused fluid flow along zones of fracture or through near-vertical faults.

Pockmarks form following the rapid expulsion of methane, and therefore represent unequivocal features of methane escape (Fig 2.4). To facilitate their formation, pockmarks require a particular range of sedimentary circumstances. Firstly, the underlying geology must permit fluid flow into the near surface (Hovland, 1987). The underlying strata is commonly porous, serving as a reservoir for gas storage. Secondly, the seabed must typically consist of fine-grained, low permeability sediments, that focus and inhibit rapid gas escape (Hovland et al., 2002). As such, pockmarks occur in a range of sedimentary environments, such as estuaries (Martens et al., 1998; Brothers et al., 2012) and coastal areas (Bayon et al., 2009; Riboulot et al., 2013; 2019), and are typically associated with petroleum-generating environments (Roy et al., 2014; Portnov et al., 2016).
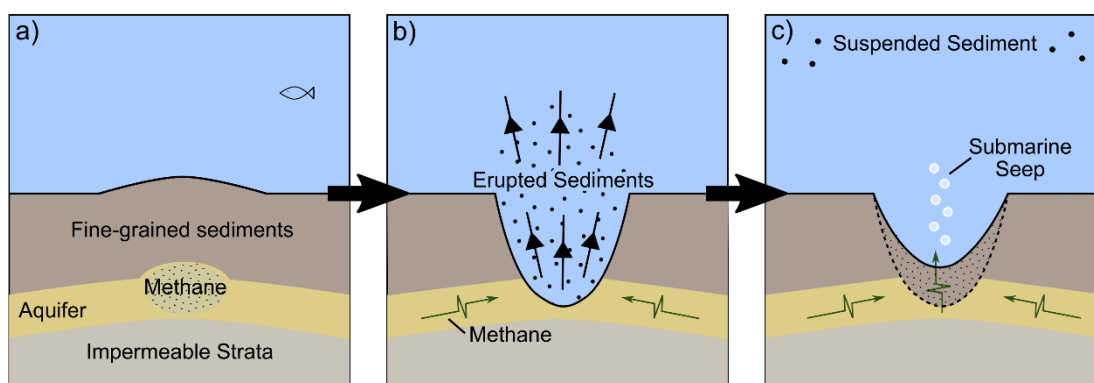
Figure 2.4. The theoretical process of pockmark formation (adapted from Hovland, 1987). (a) Methane accumulates in the shallow aquifer, building up pressure that may deform the overlying poorly permeable fine-grained sediments. (b) Overstressing of the overlying dome causes it to fail, prompting the start of the eruption phase. This is marked by rapid, violent gas escape, which mobilised the fine-grained sediments. (c) Following eruption, the weakness in the low permeability sediments can be exploited by methane, forming a submarine seep.

If the sedimentary and geological conditions allow, pockmark formation is often perceived to consist of three phases: a pressure building phase, an eruption phase, and a release phase. In the initial pressure building phase, interstitial gas accumulates in a shallow reservoir layer, directly beneath the more impermeable layer directly above it (Hovland, 1987). This gas build up may occur due to the dissociation of gas hydrate (e.g. Portnov et al., 2016), although this could also be free methane from underlying gas-generating provinces (e.g. Roy et al., 2014). Hovland (1987) theorises that continued pressure build up may result in the doming of the seabed. The continued accumulation of methane and other hydrocarbons within this reservoir exhibits an increasing stress on the fine-grained overburden. The eruption phase that follows is quick, caused by the stress-induced failure of the overburden. The sudden drop in pressure is suggested to result in the free flow of gases out of the pockmark, in potentially violent eruptions (Hovland, 1987). This also results in the mobilisation of sediments, forming the crater-liked depression. The final release phase commences once the violent eruption of the accumulated gas slows. The newly formed pockmark presents a gap within the uppermost, impermeable layer, providing a point of weakness that can be exploited for methane venting. This may form a submarine seep, and explains how

observations of pockmarks often coincide with evidence of methane seepage or escape (Chand et al., 2009). However, it should be noted that much of this mode of formation remains theoretical; as pockmarks are formed through rapid, one-time events, in locations which are difficult to access, the exact formation process has not been directly observed or documented (Hovland et al., 2002).

2.6.2. Submarine Pingos

Named after their terrestrial counterparts, submarine pingos (sometimes referred to as hydrate pingos or simply as "pingo-like features"; Serov et al., 2015) are dome-shaped mounds identified on the seabed. They are up to 40 m tall, and can be up to 2 km in diameter (Paull et al., 2007), and have been identified on the continental shelf off the coast of Norway (Hovland and Svensen, 2006), on the Beaufort Sea Shelf (Paull et al., 2007) and in the South Kara Sea (Serov et al., 2015).

Two separate hypotheses have been discussed regarding the formation submarine pockmarks. Early hypotheses discuss the idea that submarine pingos in the Beaufort Sea were formed terrestrially during low relative sea level during the late Pleistocene, before becoming submerged following marine transgression during the Holocene (Shearer et al., 1971). However, dating of organic sediments within these Beaufort Sea pingos indicate that some pingos post-date the local marine transgression (Paull et al., 2007). In explaining these pingos, Paull et al. (2007) discusses the idea that pingos may form in a shallow marine environment, following shelf flooding in Holocene (Bondarev et al., 2002; Paull et al., 2007). Under their scenario, shallow gas accumulations emitted from the dissociation of gas hydrate is suggested to drive the doming of the seafloor (Paull et al., 2007). This corresponds with the theorised initial phase of submarine pockmark formation (Figure 2.4a; e.g. Hovland, 1987), although no direct observations of the evolution of any current submarine pingo into a pockmark have been made. It is entirely possible that both formation hypotheses may be true, as evidenced in seismic and drilling studies of submarine pingos in the South Kara Sea (Serov et al., 2015).

2.6.3. Submarine Seeps

Whilst pockmarks and deep-sea pingos are morphologically very different, they are unified by the characteristic that these evolve due to the migration of methane into the near-surface, through hydraulically conductive strata. When this methane reaches the seabed and escapes into the overlying water column, it is referred to as a submarine seep or a gas flare.

Active submarine seeps have been observed in a range of Arctic environments, including the Kara Sea (Portnov et al., 2013), close to the coastline of Svalbard (Roy et al., 2014; Portnov et al., 2016; Myhre et al., 2016), and on the East Siberian Continental Shelf (Shakhova et al., 2010a; 2010b; 2014). These are commonly described in relation to the dissociation of gas hydrates following oceanic warming (Ferré et al., 2012), although this is not exclusively the case (Roy et al., 2014). The quantity of methane emitted from submarine seeps is purportedly significant, with fluxes of CH_4 from seeps on the East Siberian Continental Shelf equal to 17 Tg yr^{-1} (Shakhova et al., 2010a; 2014), or ~3% of the total global methane budget to the atmosphere (Myhre et al., 2016). Subsequent investigations have doubted this, as statistical modelling and observations from the region suggest an upper limit of 4.5 Tg yr^{-1} in methane emissions for the wider region (Berchet et al., 2016).

In recent years, the impact of methane release from submarine seeps has therefore been questioned. For example, Fisher et al. (2011) argued that the relative impact of this methane release on atmospheric composition is argued to be negligible, as methane is dissolved within the water column despite the low solubility of methane within seawater (Ruppel and Kessler, 2017). This was evidenced by the measurement of methane fluxes from above active gas seeps on the continental margin of Svalbard (Myhre et al., 2016).

In contrast, active terrestrial springs containing methane circumvent oxidisation within the water column, resulting in a direct atmospheric contribution. Until recently, terrestrial seeps within permafrost environments have often been overlooked on account of the notion of a "cryospheric cap" restricting the evasion of methane from deeply buried biogenic and thermogenic sources (Gautier et al., 2009; Walter Anthony et al., 2012).

However, recent work by Hodson et al. (2019; 2020) highlight the occurrence of active groundwater springs which directly emit methane to the atmosphere, and thereby subvert the methanotrophic water column present within submarine and lacustrine environments. In particular, pingos warrant further attention as sites of potential methane evasion, given these provide evidence of groundwaters penetrating through continuous permafrost. In Hodson et al. (2019), terrestrial pingos are considered to be analogous to submarine methane landforms and seeps, although the nature of this relationship has not yet been described.

2.7. Terrestrial Pingos

Pingos (occasionally referred to as "hydroaccoliths") refer to a series of landforms that are formed from the freezing of pressurised groundwater injected into the near-surface permafrost. The term "pingo" is derived from the Inuit word for conical hill (Porsild, 1938), and whilst they are typically dome-shaped, pingos can exhibit a wide range of forms. It is estimated that the number of active pingos exceeds 11000 (Grosse and Jones, 2011), with pingos found within a range of high-latitude (e.g. Canadian Arctic and Subarctic, Northern Alaska, Greenland, Svalbard and Russia) and high-altitude environments (e.g. Mongolia and the Qinghai-Tibetan plateau). As pingos require sub-zero temperatures for their formation, pingos are considered unequivocal indicators of permafrost, past or present (Holmes et al., 1968; Pissart, 1985).

The freezing of pressurised groundwater in the near-surface commonly results in the formation of a massive ice core, which has previously been considered as a defining characteristic of pingos (Harris et al., 1988). The formation and growth of an ice core causes the deformation of the overburden sediments, resulting in the doming of the surface. In spite of this, some studies have previously suggested that segregation ice is dominant within some pingo forms (e.g. Mackay, 1973; 1978; Ross et al., 2007). For example, detailed investigations of pingos within the Canadian Arctic argue that segregation ice is present in significant quantities, and should be considered a prominent

geomorphological component (e.g. Mackay, 1973; 1978). More recent geophysical investigations of pingos formed within fine-grained, frost-susceptible sediments in Svalbard have also suggested pingos may be composed of segregation ice, on account of low resistivities precluding the presence of massive ice (Ross et al., 2007).

Over periods ranging from hundreds to tens of thousands of years, pingos are perceived to undergo cycles of growth and decay (Figure 2.5; Ballantyne, 2018). Initially, the pingo progressively heaves upwards, producing a landform with steepening sides and a summit that is slowly increasing in height. The continued pingo uplift exerts increasing tensile stresses on the surface sediments, which result in the formation of dilation cracks (Mackay, 1988). Eventually, the pingo ice core may become exposed at is summit, as cracks expand to form trenches and gullies, or where solifluction or slumping of sediments occurs on the steep pingo sides (Babiñski, 1982; Mackay, 1988). This exposure represents a critical trigger (e.g. Mackay, 1987; 1988), as this leads to the melt of the ice core. The formation of a depression within the ice core from this melt often leads to a small lake or pond evolving on the surface. A pingo in an advanced state of decline is often represented by a circular ridge of ice-cored sediment, with a central, often water-filled depression (Mackay and Burn, 2011).

Pingos are polygenetic in nature, and are often categorized into one of two types (French, 2017). Closed-system (sometimes referred to as hydrostatic) pingos exist as a consequence of hydrostatic pressure build-up caused by the freezing of a closed sub-surface water body. In contrast, open-system (sometimes referred to as hydraulic) pingos form from the injection of hydraulically pressurised groundwater into the near-surface. Whilst pingos have previously been categorised based on how groundwaters are pressurised, some authors have noted that some pingos may evolve on account of a combination of hydrostatically and hydraulically pressurised groundwaters (Gurney, 1998). In investigations of pingos on Banks Island, Canada, Gurney and Worsley (1996) infer a combination of hydrostatic and hydraulic formation processes, as groundwater supplies are influenced by a series of dynamic, interlinked taliks. In recent investigations of open-system

pingos in Adventdalen, Svalbard, the downward aggradation of permafrost has been discussed as a mechanism that provides hydrostatic pressure that may drive groundwaters towards the surface (Hornum et al., 2021). In this thesis, the terminology of "open-system" and "closed-system" is used, as the groundwater pressure mechanism is not necessarily well defined.
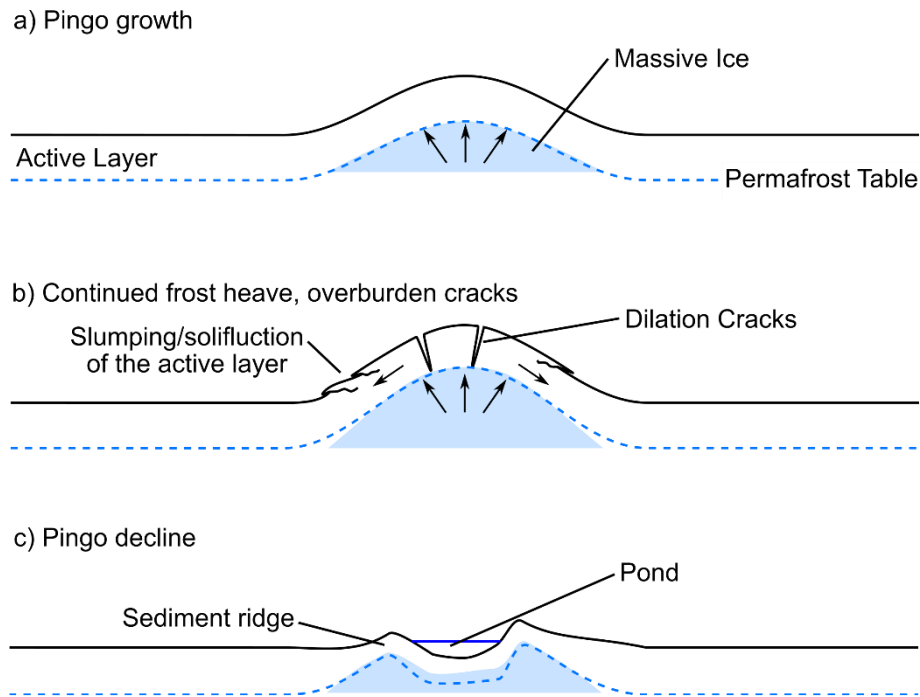
Figure 2.5. Demonstration of the life cycle of a pingo, from initial growth to maturity and decline. (a) The injection of pressurised water into the near-surface prompts the growth of injection ice that domes the overburden sediments. (b) Continued growth of this ice exerts tensile stresses on the overburden, resulting in the formation of dilation cracks. The slumping or solifluction of sediment can occur on the steep pingo sides. (c) Following exposure and melt of the ice core, the pingo degrades into a circular ridge of sediment, with a central depression often containing a pond.

2.7.1. Closed-system Pingos

Closed-system pingos occur as a result of hydrostatically pressurised groundwater, following the lateral freezing and aggradation of permafrost into taliks. Closed-system pingos are typically found within extensive lowland areas with little or no vertical relief (French, 2017). Large concentrations of closed-

system pingos are located within the Mackenzie Delta (Mackay, 1962; Mackay, 1978; 1979), north-eastern Siberia (Wetterich et al., 2018), on the Yukon coastal plain, on western Victoria Island and on Banks Island (French, 2017), with isolated pingos found elsewhere within the Canadian Arctic.

The processes of closed-system pingo formation are relatively well-constrained (Fig 2.6), following extensive studies conducted on these landforms by J. R. Mackay (e.g. Mackay, 1962; 1973; 1978; 1979; 1985; 1987). Typically, in continuous permafrost, spring snowmelt results in the pooling of surface water into lakes, altering the subsurface thermal regime by changing the offset between air and ground surface temperatures. Where lakes are sufficiently deep enough such that they do not freeze to their bed over winter, the sediments underlying the lake will remain unfrozen, forming a talik which is theoretically enclosed laterally and at depth. However, these lakes have been found to catastrophically drain as a result of coastal retreat, thermal erosion, or through the thermal incision of ice-rich sediments (Mackay, 1988). Lateral aggradation of the permafrost into the talik can then occur, expelling pore water into the remaining unfrozen space where the permafrost is thinner to produce an unfrozen water lens. Freezing of this water lens from the surface then results in the formation of a thickening, expanding massive ice core, causing the doming of overburden sediments (Mackay, 1994). Such closed-system pingos can persist for thousands of years, with continued up-doming of sediments eventually resulting in the exposure of the ice-core to the surface, thus enabling this to melt, leading to subsidence at the pingo summit.

2.7.2. Open-system Pingos

In comparison to closed-system pingos, open-system pingos are relatively poorly understood. Open-system pingos form from the upwelling of groundwaters under artesian conditions. Similar in size to closed-system pingos, open-system pingos can exist in isolation or within clusters, and can form within a wide range of sediments, including colluvial, alluvium and tills (Ballantyne, 2018). In northern Quebec, pingos have been found to feature fractured bedrock, demonstrating the pressures with which groundwater is

26

injected into the near-surface (Seppälä, 1988). This is emphasised further with the occurrence of a spring outflowing from the top or flanks of some open-system pingos, which can often be perennial in spite of sub-zero winter temperatures (e.g. Liestøl, 1977). In general, open-system pingos have been associated with thin, discontinuous permafrost environments, such as central Alaska (Holmes et al., 1968) and central Yakutia (French, 2017). However, a number of open-system pingos are found within continuous permafrost, including in Svalbard (Liestøl, 1977; Yoshikawa, 1993; Yoshikawa and Harada, 1995; Yoshikawa and Nakamura, 1996; Ross et al., 2005; 2007), Northern Alaska (Hamilton and Obi, 1982) and Greenland (Worsley and Gurney, 1996).
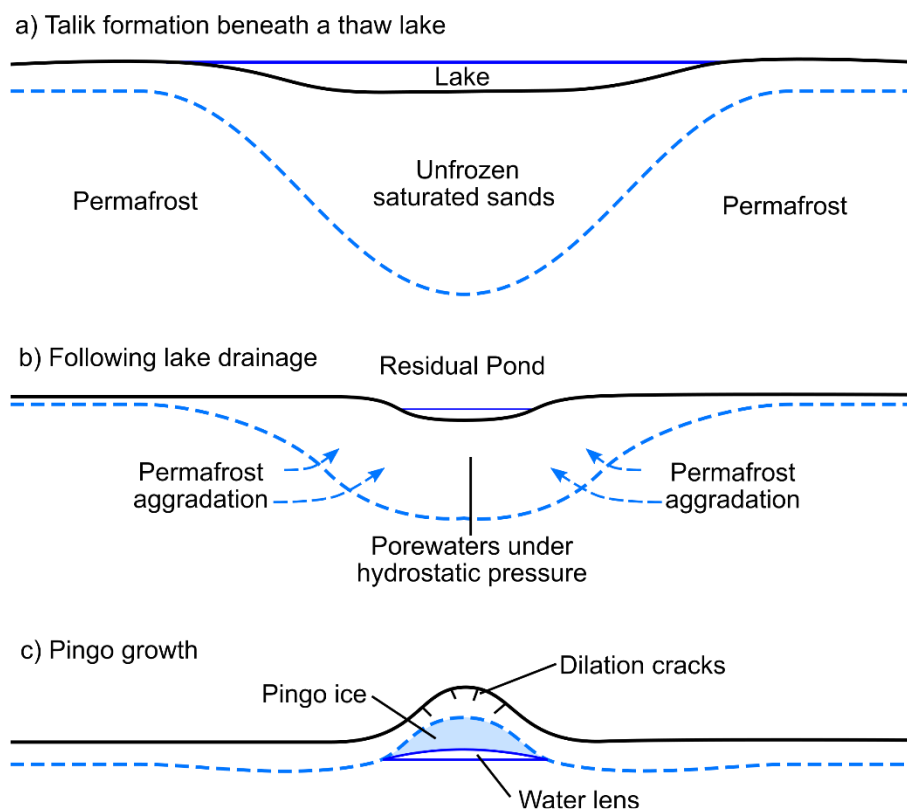
Figure 2.6. Schematic demonstrating the formation of an closed-system pingo (modified from Mackay, 1998). (a) Beneath a lake, a talik consisting of saturated sands form. (b) Drainage of the lake results in the aggradation of permafrost into the talik, resulting in the expulsion of porewaters and the build-up of hydrostatic pressure within the near surface. (c) Downward freezing into the talik results in the formation of an ice core, and the heave of the overburden sediments.

Early models of open-system pingo formation were conceptualised by Müller (1959) and Holmes et al. (1968), following observations of pingos on Greenland and Alaska respectively. Focusing on pingo hydrology, Müller (1959) argues that the pressures required for pingo formation in Greenland are high, and that these may only be explained by the restricted flow of artesian groundwaters within permeable substrates. Permafrost is considered as an aquiclude, restricting the flow of groundwaters to beneath, or in rare cases within, the permafrost. In describing how pingos preferentially form close to the base of valley slopes in Central Alaska, Holmes et al. (1968) suggests that abrupt increases within the permafrost thickness at the base of valleys restricts lateral flow of groundwaters, and therefore localise a site for pingo formation. In addition, both Müller (1959) and Holmes et al. (1968) describe how pingo formation requires a finely balanced combination of geological and thermal conditions. They argue that quantities of groundwater must be relatively small, as a large volume of groundwater would result in "too much heat in the system and prevent the freezing of the pingo" (Holmes et al., 1968, p. 31), and that temperatures must be sufficient close to freezing such that they could freeze in the near-surface. Where both of these conditions are met however, artesian groundwater would be expected to freeze in the near-surface, resulting in the doming of surface sediments.

For the pingos common on the valley floor on Svalbard, these early formation hypotheses proved problematic (Liestøl, 1977). As permafrost acts as an aquitard, how do the aquifers on Svalbard recharge given that permafrost is continuous? In the recharge of aquifers, Liestøl (1977) suggested that polythermal glaciers provide an opening in the continuous permafrost. Through the base of temperate parts of these polythermal glaciers, meteoric waters infiltrate into the subsurface, and flow downslope beneath the permafrost through permeable substrates or bedrock discontinuities. Subsequent investigations on Svalbard support this recharge mechanism to explain the warm springs found in Bockfjorden (Haldorsen et al., 2010).
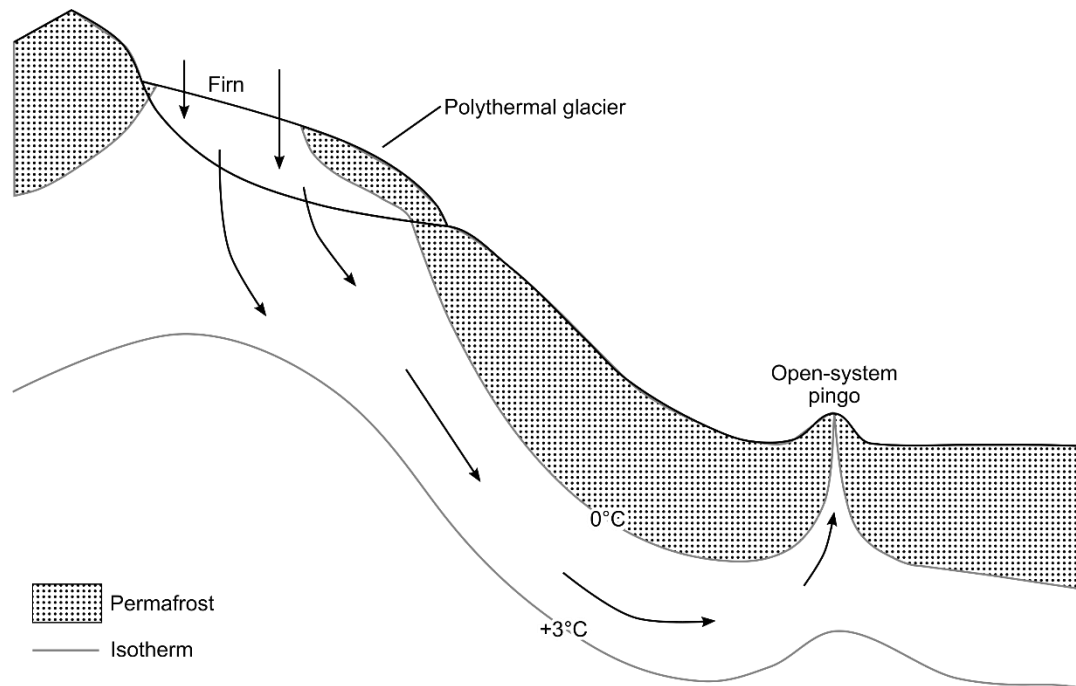
Figure 2.7. Vertical profile depicting the extent of permafrost and the groundwater migration pathway for an open-system pingo in continuous permafrost (adapted from Liestøl, 1996).

Similarly, the model of Holmes et al., (1968) is limited as it does not reflect the full distribution of open-system pingos. In Svalbard, pingos that are located in the centre of vast fjord-valleys have been identified (e.g. Liestøl, 1977; Demidov et al., 2022), which are counterintuitive to the idea that pingos result from the thickening of permafrost at the valley-slope transition. In their assessment of the open-system pingos located on the valley floor of Adventdalen, Svalbard, Yoshikawa and Harada (1995) address this problem by dividing open-system pingos into three groups. In the first group, Yoshikawa and Harada (1995) argue that pingos are preferentially located along geological faults, that which provide a structural weakness that enables groundwater flow through permafrost. Associations between pingo locations and the existence of local faults have been found in Alaska (Hamilton and Obi, 1982), Greenland (Worsley and Gurney, 1996; Scholz and Baumann, 1997) and Svalbard (Liestøl, 1977; Pekala and Repelewska-Pekalowa, 2004; Hornum et al., 2021), amongst other locations. Secondly, Yoshikawa and Harada (1995) prescribe the distribution of some pingos relating to the migration of sub-glacial groundwaters. This follows the mechanism of Liestøl

(1977), in that groundwaters percolate beneath the beds of polythermal glaciers, although the notion that this presents a distinct type *per se* is questionable. Lastly, Yoshikawa and Harada (1995) introduce the idea that some pingos are distributed in near-shore areas, due to the isostatic uplift of the ground following deglaciation. In these areas, they argue that permafrost is comparatively thin, and thus groundwaters are able to penetrate and freeze within the near-surface more easily. These environments are characterized by fine-grained, frost-susceptible sediments, and geophysical investigations have therefore attributed their surface expression to segregation ice (Ross et al, 2007).

Humlum et al. (2003) noted that pingos in Svalbard are often located at the base of Holocene alluvial fans. Analysis of pingo distribution on Svalbard appear to confirm this perception, identifying that collocation with alluvial fans is the most common geomorphological position (Demidov et al., 2022). In explaining the formation of open-system pingos close to alluvial fans, Humlum et al. (2003) suggests that groundwater may flow through coarse-grained deposits within alluvial fans, above more impermeable permafrost below. As alluvial fans thin towards their base, groundwater is forced upwards before freezing in the near-surface. However, this theory has not yet been tested, and a direct link between alluvial fans and open-system pingos is unclear.

Ultimately, the characteristics and formation of open-system pingos remain poorly understood. In continuous permafrost particularly, the penetration and recharge of groundwater through hundreds of meters of cryotic sediments is difficult to envisage (Ballantyne, 2018). The recent identification of open-system pingos in Adventdalen, Svalbard serving as conduits enabling the release of methane therefore warrants a reconsideration of pingo theory (Hodson et al., 2019; 2020). In particular, the parallels between submarine seeps and open-system pingos are of particular interest (Hodson et al., 2019).

Chapter 3: Field Site Description

3.1. Adventdalen

In explaining the pingo which forms the focus of these investigations, it is first important to understand the regional context for this study. Adventdalen (78˚12'N, 16˚00'E; Figure 3.1) is situated in the central part of Spitsbergen, on the high Arctic archipelago of Svalbard. Geomorphologically, Adventdalen is a glacially modified U-shaped valley, with steep bedrock walls and relatively flat base (see Figure 3.2). The valley forms a sub-tributary of the greater Isfjorden system, that drained ice from central Svalbard to the continental shelf edge during the Late Weichselian (MIS 2; c. 12.5 ka BP). Following the retreat of the Barents Sea Ice Sheet, a high-rate of glacio-isostatic rebound that surpasses eustasy has resulted in a rapid relative sea level fall during the Holocene (3.7 mm yr^{-1}; Auriac et al., 2016). Consequently, the present-day sea level is 62 – 70 m below that of the late Pleistocene (Lønne & Nemec, 2004). Present day Adventdalen is therefore a depositional environment, with a rapid rate of sedimentation producing a succession of aeolian, deltaic and glaciomarine sediments on the valley bottom (Gilbert et al., 2018). These fine-grained sediments are approximately 60-70 m thick (Braathen et al., 2012), and are characterised by a high porosity (35 – 55%) and low hydraulic conductivity (Tavakoli et al., 2021).

The geology of Adventdalen is well-constrained (see Figure 3.3). Beneath fine-grained marine and deltaic sediments deposited following the Late Weichselian (12.5 – 10 ka BP) are a succession of shales formed during the early Cretaceous period. This formations dip at low angles towards the southwest (Dallmann, 2019; Hornum et al., 2020). This succession of shales is purportedly fractured (Olaussen et al., 2020), likely due to glacial loading and unloading during the advance of the Barents Sea Ice Shelf during the Weichselian glacial period (Neuzil, 2012). For the southern part of Adventdalen, the top of this succession is the Carolinefjellet formation, which consists of intercalated mud and siltstones (Huq et al., 2017). Below this formation, the Lower Cretaceous Helvetiafjellet formation comprises of alternating sandstones and shale units, and provides a 40 – 150 m thin aquifer

across the region (Dallmann, 2019). This is underlain by the Lower Cretaceous Rurikfjellet formation, a layer which is up to ~400 m thick (Huq et al., 2017) and is comprised of an upper unit dominated by sand- and siltstones, and a lower shale rich unit (Dallmann, 2019).
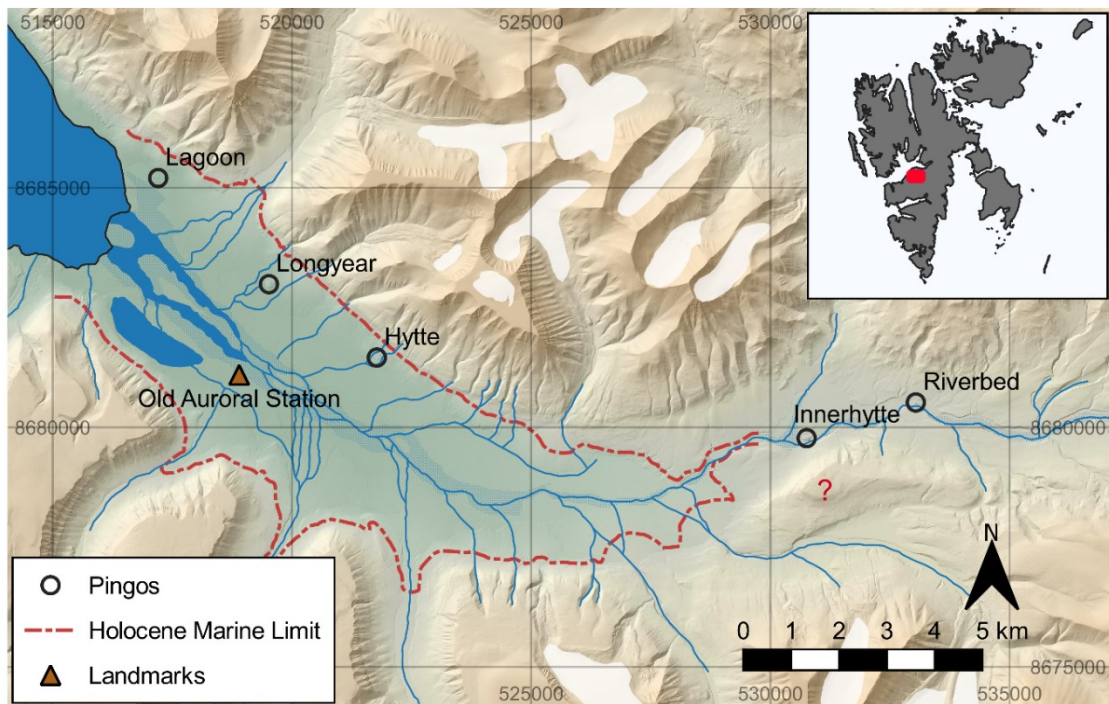
Figure 3.1. The location of the pingos and the site of the CO2 Lab Project within Adventdalen (Old Auroral Station), alongside the approximate extent of the Holocene marine transgression. The location of Adventdalen on Svalbard is shown on the inset map. Topography is depicted using a 5 m-resolution 2010 DEM (Norwegian Polar Institute, 2014). Coordinates are shown in UTM 33N.

Below the Rurikfjellet formation, the Agardhfjellet formation consists of dark laminated shales, with localised silty layers (Braathen et al., 2012; Huq et al., 2017). The Agardhfjellet formation beneath Adventdalen was formed between the middle Jurassic and early Cretaceous, and is approximately 250 m thick (Koevoets et al., 2018). This formation is particularly notable for some distinctive characteristics; firstly, it is rich in organic content, and is noted for discoveries of thermogenic gas (Koevoets et al., 2016; Dallmann, 2019). Generally, the Agardhfjellet formation is considered to belong to the same production event as the Hekkingen formation, which is the most important source rock for oil and gas exploration within the southwest Barents Sea

(Henriksen et al., 2011; Dallmann et al., 2019). Secondly, the Agardhfjellet formation is distinct for hosting phosphatic nodules (Krajewski, 1990), which requires consideration in the context of potential groundwater systems within Adventdalen. Beneath the Agardhfjellet formation, at depths of over 750 m, is the De Geerdalen Formation. The De Geerdalen formation is an aquifer, and consists primarily of sandstones.

Figure 3.2. An photograph of Adventdalen taken in winter from the summit of Lindholmhøgda, facing towards the southeast. Adventdalen is a U-shaped valley, characterized by high valley sides and a flat base.

As an environment of low hydraulic permeability, with both Rurikfjellet and Agardhfjellet formations acting as aquitards, Adventdalen has been suggested as a site of potential carbon capture and storage. This led in the Longyearbyen CO_2 Lab project, which aimed to explore the use of the De Geerdalen formation as a reservoir for carbon emissions from the local coal-fired power plant. As a result, a number of detailed borehole logs and geophysical studies have been obtained in the valley, providing a detailed overview of the local groundwater and fluid migration system. Well logs show that unconsolidated Holocene deposits within the valley provide a hydraulic cap to fluid flow escape (Gilbert et al., 2018). In terms of geophysical studies, imaging within Adventdalen was found to be problematic, with Holocene deposits in the upper layer of the study site complicating the interpretation of geophysical images (Olaussen et al., 2020). Seismic investigations suggest that few regional layers provide good reflectors, although the contrast between Holocene deposits and

the underlying early Cretaceous aquifers is among these (Olaussen et al., 2020). The most notable result from this series of investigations was the identification of wet gas from unconventional strata beneath Advendalen. Water injection testing of the Agardhfjellet formation led to the discovery of shale gas (at depths of 640 – 700 m) in quantities that potentially warranted production (Ohm et al., 2019; Olaussen et al., 2020).
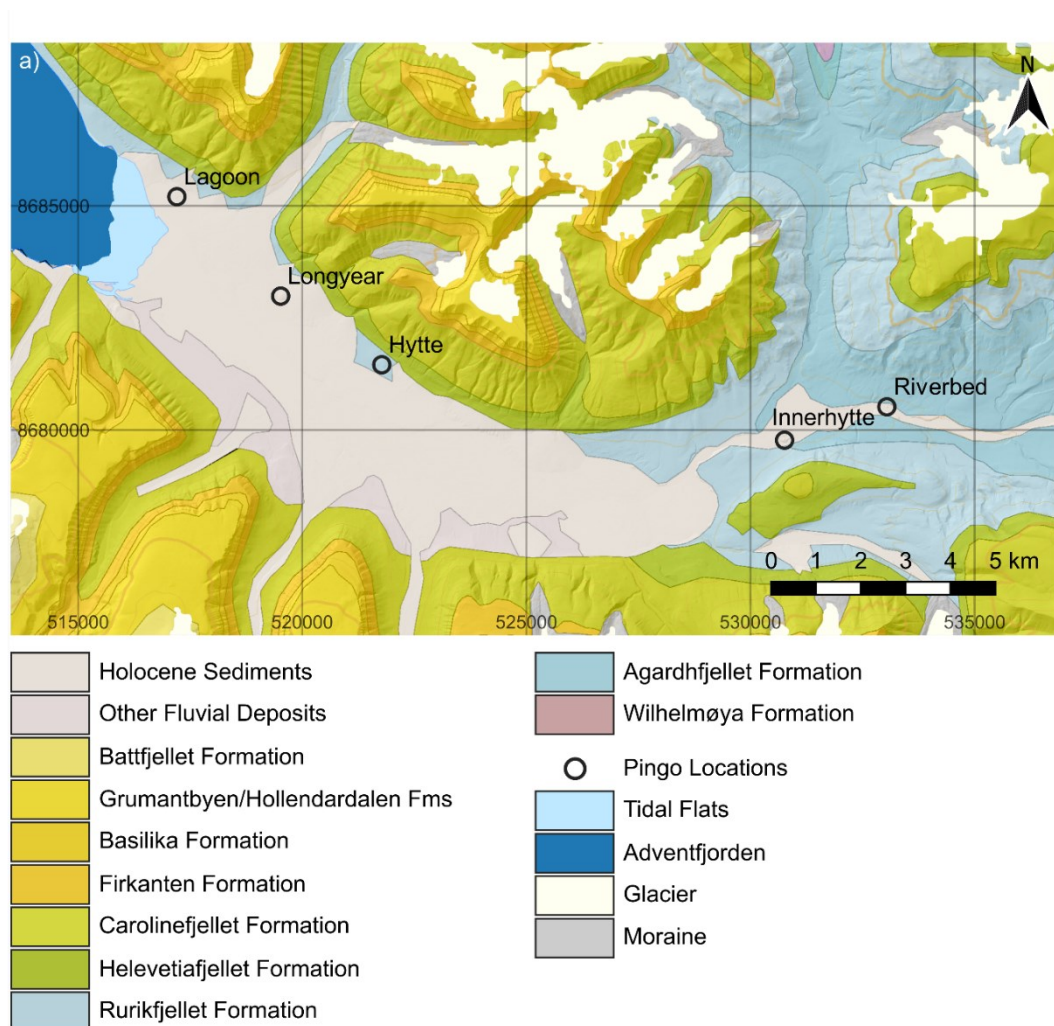
Figure 3.3. Surface geology in Adventdalen (adapted from Major et al., 2000; hillshade derived from Norwegian Polar Institute, 2014).

Evidence of gas escape has been identified with the presence of pockmarks in Adventfjorden. Pockmarks in Adventfjorden are up to 140 m wide, and up to 8 m deep (Forwick et al., 2009). These individual pockmarks vary in shape, with both circular and elliptical forms identified (Forwick et al., 2009). However, it is also noted that pockmarks are particularly clustered, with a series of pockmarks chained together forming a "pockmark trough" in the northwestern

part of the fjord (Forwick et al., 2009; Roy et al., 2014). These pockmarks are suggested to have formed postglacially (Forwick et al., 2009; Portnov et al., 2016), where sedimentation during the Holocene forms a low permeability cap above shales that allow gas migration, and produce conditions conducive to pockmark and seep formation. The gas is thought to be thermogenic, and has been suggested to occur from the Agardhfjellet Formation (Forwick et al., 2009; Roy et al., 2014).

Present day Adventdalen is characterised by a polar tundra climate (Kottek et al., 2006), with the mean annual air temperature (MAAT) at Old Auroral Station equal to -3.4°C between 2017 – 2018 (Christiansen et al., 2019). Annual precipitation is approximately 200 mm, with 60% of this falling as snow (Eckerstrofer and Christiansen, 2011). Despite this, a shift towards a wetter, warmer climate has been noted in recent years (Christiansen et al., 2013; Matsuoka et al., 2018), with 2020 forming the warmest summer on record (Nilsen, 2020).

In Adventdalen, the local climate controls the thermal state of the permafrost (Christiansen et al., 2013). Permafrost is prevalent and laterally continuous, with the permafrost thickness estimated to be 20 m near the coast, extending to ~100 m in the centre of the valley and up to 300 m – 400 m thick at higher altitudes (Humlum, 2005). Active layers are generally 0.8 m to 1.2 m thick (Christiansen et al., 2010), as demonstrated through boreholes and frost probing throughout the valley. Beneath the Holocene marine limit, permafrost is suspected to have aggraded since glacial retreat, and thus permafrost is of Holocene age (Gilbert et al., 2018). This additionally means that permafrost below the Holocene marine limit is saline. Through the collection of shallow cores throughout Adventdalen, Cable et al. (2018) identify porewater electrical conductivities of 17 ± 9 mS cm^{-1} associated with the fine-grained saline muds, and conductivities of 17 ± 12 mS cm^{-1} within alluvium in the valley. Additionally, they identify cryopegs (layers of unfrozen ground within otherwise cryotic sediments) beneath 6 m. This corroborates with the geophysical investigations of Keating et al. (2018), who used a combination of surface nuclear magnetic resonance and controlled source auto-magnetotellurics to identify an unfrozen water content of up to ~10% within the lower parts of the valley. In doing so,

they argue that the possible implications of permafrost condition on greenhouse gas emissions requires consideration.

The combination of generally thick continuous permafrost, a local cold climate and the knowledge of a wet gas accumulation from the CO_2 Lab project has prompted suggestions that gas hydrates may be stable onshore Svalbard. Thermobaric modelling of the gas hydrate stability zone indicates that the valley slopes are likely to contain gas hydrates (Betlem et al., 2019), with the thickness of this zone suggested to be up to 600 m thick in the mountains surrounding Adventdalen. Despite this, it is noted that no discovery of terrestrial gas hydrates has been documented on Svalbard, either through drilling or in geophysical explorations. Low signal-to-noise ratios and low vertical resolutions inhibit the identification of bottom-simulating reflectors within current seismic datasets in Adventdalen, despite relatively good data coverage (Bælum et al., 2012; Betlem et al., 2019). Furthermore, gas hydrates and the permafrost-bearing succession of Cretaceous shales are expected to have a limited contrast in acoustic properties, and thus further seismic investigations are unlikely to identify gas hydrates beneath Adventdalen (Betlem et al., 2019).

Recent research has focused on how Adventdalen's pingos may provide conduits that enable sub-permafrost methane to escape (Hodson et al., 2019; 2020). Adventdalen contains five pingos which occur along the northern side of the valley (Figure 3.1). Of these pingos, Lagoon Pingo occurs closest to the contemporary coastline, whilst Riverbed Pingo occurs ~24 km in-land. Of these pingos, the westernmost and lower three occur within the Holocene marine limit, whilst Innerhytte is suggested to occur close to the boundary of fine-grained Holocene marine muds and clays. Combined with radiocarbon dates, the formation of these pingos within marine sediments in the valley has led to the suggestion that these pingos form a chronology of pingo form, from inception (Lagoon Pingo), to maturity (Longyear Pingo), and subsequent rejuvenation following decline (Hytte Pingo). The pingos in Adventdalen have received varying degrees of attention; whilst Innerhytte is arguably the most well studied (Rossi et al., 2018), Lagoon Pingo has hitherto received far less attention. In particular, Lagoon Pingo is chosen as a focus for this series of

geophysical studies due to a poor understanding of its structural and groundwater dynamics, despite the identification of methane emanating from it, and the suggestions that Lagoon Pingo may have evolved from a submarine seep (Hodson et al., 2019).

3.2. Lagoon Pingo

The focus for geophysical investigations in this thesis is Lagoon Pingo: the westernmost of five open-system pingos (Figure 3.1) located in the valley of Adventdalen, Svalbard. As shown on Figure 3.4, the pingo is located close to the present-day coastline, on the edge of a lagoon (Moskuslaguna) which sits above the present-day tidal range. This lagoon is sheltered by a beach ridge that extends from a neighbouring alluvial fan, although driftwood and other non-native material indicates a susceptibility to storm tides. The topography of Lagoon Pingo is dissimilar to idealized dome-shaped conceptions of traditional open-system pingos, and consists of a series of small mounds reaching a maximum height of ~8 m, with the pingo spanning 500 m in length and 200 m in width in a parallel NW-SE orientation with the valley.

Two separate springs are present at Lagoon Pingo: an outflow in the centre of the complex surrounded by a series of mounds with the highest elevation, referred to as Pingo Spring, and a separate spring situated on the relatively flat north-western part of the site, referred to as Lake Spring. Each of these springs occur in small, shallow ponds on the surface. These springs feature year-round flow, but are covered in the winter months by icings, which form due to the freezing of these ponds. These icings are dynamic, and are known to heave and fracture throughout the winter months (Hodson et al., 2019). The electrical conductivity of Lagoon Pingo groundwater is 5 – 7 mS cm^{-1} (Hodson et al., 2019).

Figure 3.4. 3-D visualisation facing north depicting Lagoon Pingo and its surrounds. Summer orthophoto is provided by the Norwegian Polar Institute (2021), overlain on a 5 m DEM (Norwegian Polar Institute, 2014).
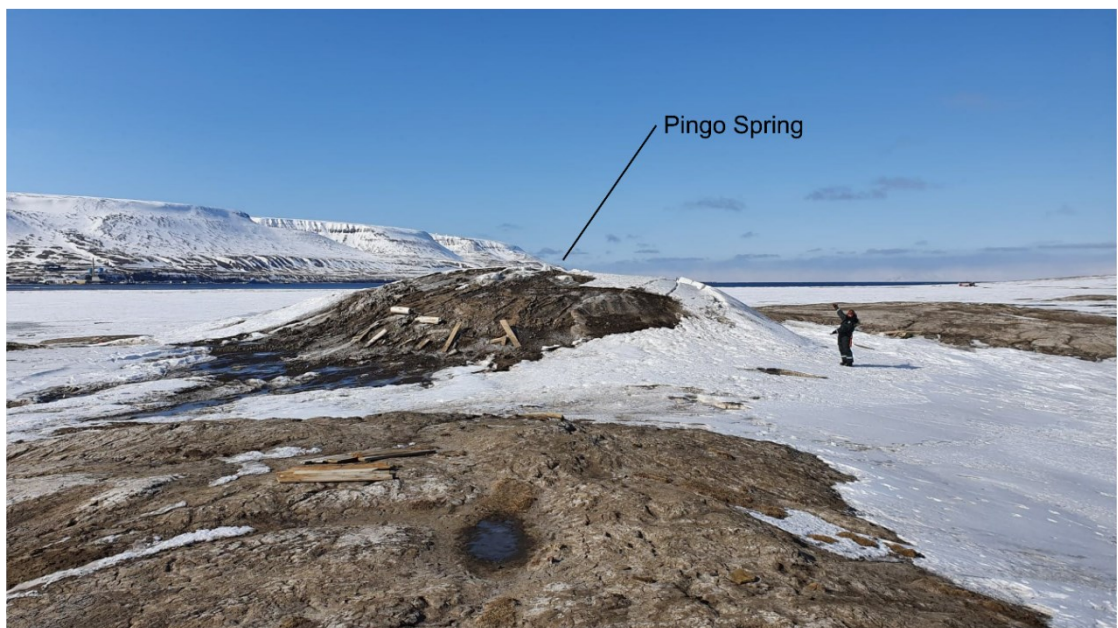
Figure 3.5. Photograph of the central Pingo Spring taken in May 2020 facing south-southwest towards Longyearbyen Airport.

Lagoon Pingo is suggested to have formed relatively recently, with radiocarbon dating of surface sediments indicate that Lagoon Pingo formed 140 ± 20 yr BP (Yoshikawa and Nakamura, 1996). This corresponds well with localised conceptual models of landscape formation. As part of a detailed study on the

Hiorthfjellet alluvial fan (shown on Figure 3.4), located down-valley from Lagoon Pingo, Lønne and Nemec (2004) describe the geomorphic evolution of the landscape (depicted on Figure 3.6) in relation to relative sea level rises and falls (shown on Figure 3.7). At the end of the Weichselian (c. 10 ka BP), the rapid retreat of the ice sheet resulted in the formation of the Hiorthfjellet alluvial fan, amid high sea levels due to glacioeustasy. The fan was fuelled by a temperate glacier that had been left behind following ice sheet retreat (see B on Figure 3.6), which supplied water and sediment in abundance. As sea level fell rapidly due to glacioisostatic rebound of Svalbard (see C on Figure 3.7), the Gilbert-type alluvial fan prograded quickly, at an estimated rate of 0.31 m yr-1 (Lønne and Nemec, 2004). This progradation was sustained by sediment and water derived from the continued glaciation of the catchment, which persisted until c. 6 ka BP.

As the rate of sea level fall reduced towards the mid-Holocene, the deglaciation of the catchment resulted in rapidly decreased sediment and water supply, thus resulting in a decreased rate of fan progradation. Wave action is considered to be the primary driver of progradation during this time, with sediment supplied derived from longshore drift (Lønne and Nemec, 2004). At approximately 5.4 ka BP, relative sea level began to rise slowly (see D on Figure 3.7), caused by imbalances in the rate of glacioisostatic uplift compared to glacioeustatic sea level rise (Landvik et al., 1998). It is hypothesised that a transgressive spit formed during this time, whilst a wave-cut escarpment formed down-valley of the fan.

This mid-Holocene marine transgression was ultimately relatively short-lived, with relative sea-level falling rapidly at 4.6 ka BP (see E on Figure 3.7). Whilst the surface of the fan aggraded slowly towards the late Holocene, marine processes dominated, with the initial formation of an escarpment and regressive beach at the shoreline. As sea level stabilised (see F on Figure 3.7), the erosion and longshore drift of sediments at the base of this alluvial fan gradually forms an accretionary spit (see F on Figure 3.6), resulting in the sheltering of this part of the fjord. This subsequently results in a low-energy environment, and thus likely resulted in the deposition of marine silts and clays to produce the present-day lagoon within which Lagoon Pingo is located.

a) End of the Pleistocene

sediment accumulation
along ice margin

glacier

glacioisostatic
uplift
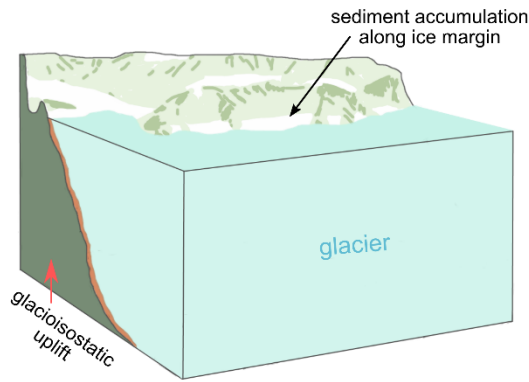
b) Beginning of the Holocene
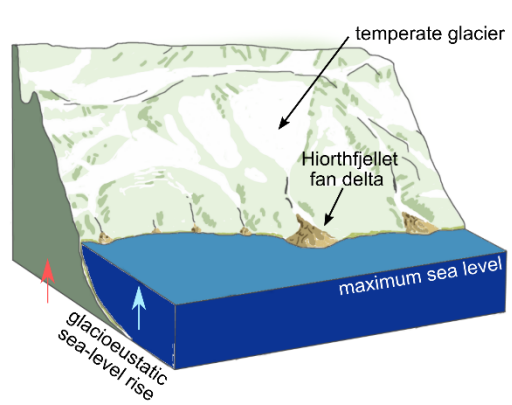
temperate glacier

Hiorthfjellet
fan delta

maximum sea level

glacioeustatic
sea-level rise

c) Early Holocene

glacier retreats

relative sea level falling

accretion of sediment
by waves and longshore drift

d) Middle Holocene

ice-cored moraine
turns into a rock glacier

wave-cut escarpment

transgressive spit

relative sea level rises

e) End of the Mid Holocene

rock glacier

regressive
beach forms

relative sea level falls

f) Late Holocene

sheltered
lagoon forms
behind spit

spit

relative sea level stabilises
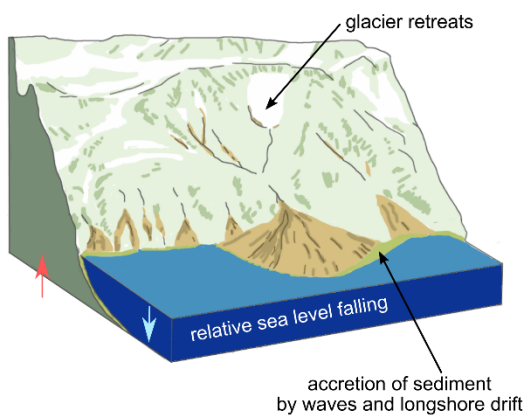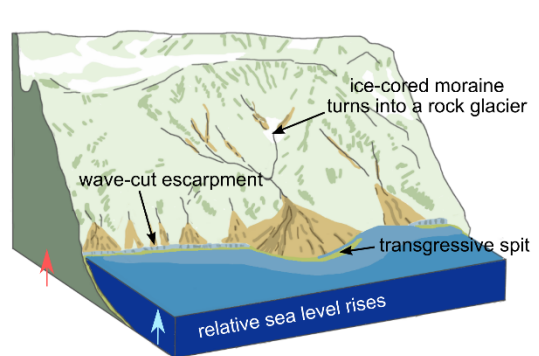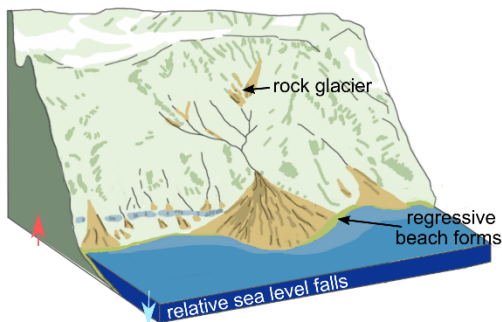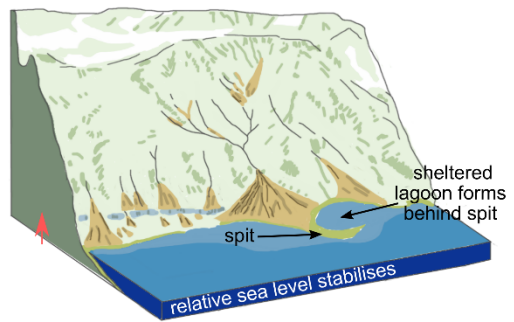
Figure 3.6. The recent geomorphic evolution of the area within which Lagoon Pingo is located (modified from Lønne and Nemec, 2004). (a) shows the glaciation of the area at the end of the Weichselian, whilst (b) depicts the temperate glacier above the developing Hiorthfjellet alluvial fan. (c) shows the aggradation of the alluvial fan with rapid sea level fall, whilst (d) and (e) depicts the consequences before and after the mid-Holocene marine transgression respectively. (f) reflects the landscape most recently, whereby the development of a spit from the Hiorthfjellet alluvial fan has produced a sheltered lagoon within which present-day Lagoon Pingo sits.

40
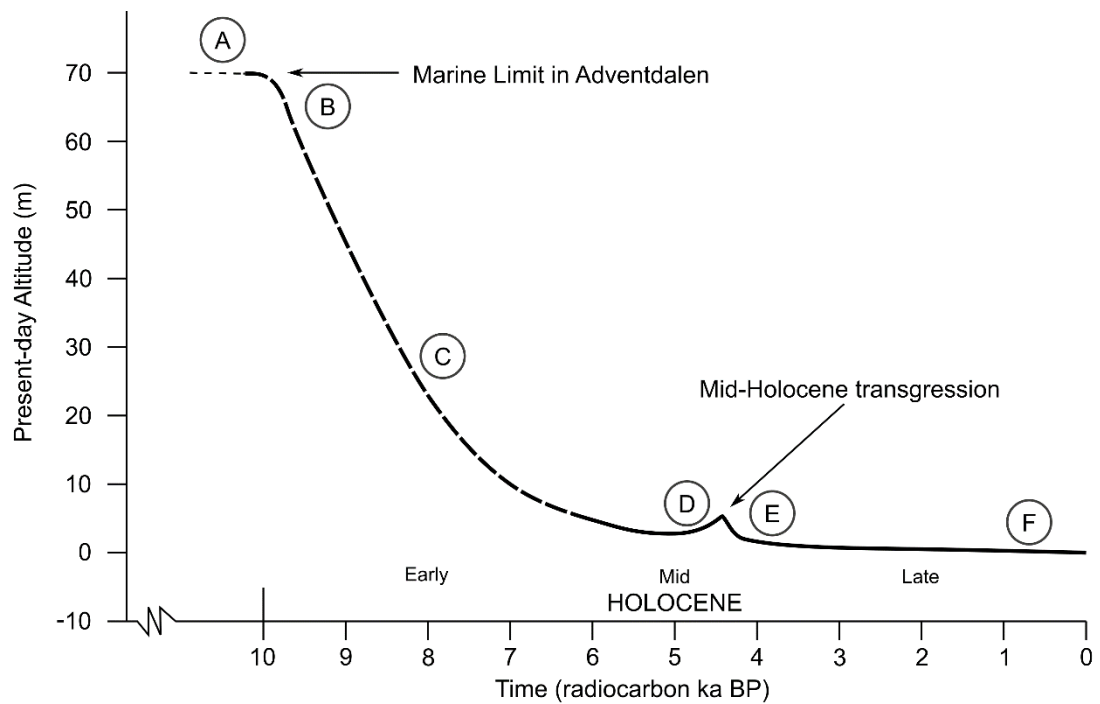
Figure 3.7. The relative sea level within Adventdalen compared to the present-day altitude, as derived from the sedimentary record of the Hiorthfjellet alluvial fan and other local data (modified from Lønne and Nemec, 2004). (A) to (F) correspond to the interpretative diagrams shown in Figure 3.6.

Geophysical studies of Lagoon Pingo have been limited to summer electrical resistivity surveys and borehole sampling (Yoshikawa and Harada, 1995; Harada and Yoshikawa, 1996). They describe a low resistivity (1.1 Ωm), shallow (0.8 m) surface layer, interpreted as the seasonally frozen active layer, above a deeper (~22.8 m), extensive permafrost layer with resistivities of at least an order of magnitude greater. The deepest layer is characterised by low resistivities similar to the active layer, with borehole validation confirming a transition from frozen to unfrozen sediments. It should be noted however that the exact location of this borehole is uncertain; with no evidence of a borehole at the site having been identified.

More recently, studies have identified active methane emissions from Lagoon Pingo. Estimates of methane release by Hodson et al. (2019) suggests a year-round methane release of ~64 kg CH_4 a^{-1} by diffusion alone, exceeding that of wetland emission estimates when normalized for surface area. These methane emissions vary seasonally due to the formation of an ice lid freezing across the springs during the winter months. Whilst methane emissions continue

during the winter months, the meltout of this ice lid in the early summer results in the dilution of the ponds where these groundwater springs occur. Low $\delta 13C$-CH_4 values of -71 ‰ VPBD are suggested to be consistent with the supply of a sub-permafrost groundwater containing primarily biogenic methane, although a thermogenic imprint on this is considered possible, especially during the winter months (Hodson et al., 2019). In Adventdalen, methane in fractured sandstones directly beneath the permafrost are biogenic in origin, with deeper reservoirs of thermogenic methane capped by Rurikfjellet mudstones (Huq et al., 2017). However, later investigations have questioned this source of thermogenic methane, as fluid migration from these shale-rich formations is limited (Hodson et al., 2020).

Others have suggested that dissociating gas hydrates may influence methane in the local groundwater system (Hornum et al., 2020), given models that indicate that the mountain slopes of Adventdalen almost certainly contain natural gas hydrates (Betlem et al., 2019). This corresponds with theories that Lagoon Pingo was formed from a pre-existing submarine methane seep, following glacio-isostatic uplift and sedimentation following deglaciation since the Last Glacial Maximum (Hodson et al., 2019).

3.3. Other Adventdalen Pingos

Whilst geophysical studies of Lagoon Pingo have been limited, the other pingos within Adventdalen have been investigated more thoroughly. A brief summary of relevant studies of these pingos is noted here, to provide context for the geophysical investigations that have been undertaken at Lagoon Pingo in this thesis.

3.3.1. Longyear Pingo

Approximately 3 km east of Lagoon Pingo, Longyear Pingo is located on the valley floor in Adventdalen, close to the tributary valley of Ugledalen. Longyear Pingo conforms to the typical circular dome shaped geomorphology of a pingo (Fig. 3.8), measuring approximately 350 m in diameter, and 15 m in height.

The pingo is located at ~12 m a.s.l., and is therefore located within the Holocene glaciomarine and deltaic sediments. Early radiocarbon dating of driftwood within Longyear Pingo provides an age of 2,650 ± 55 yr BP (Svensson, 1971). Notably, no pingo outflow has been observed at Longyear Pingo recently (e.g. Liestøl, 1977; Hodson et al., 2020; Demidov et al., 2022), with Ross et al. (2007) suggesting that a crater developed close to the summit and drainage gullies on the pingo sides provide evidence of decay.

As a site with no evidence of pingo outflow, studies of Longyear Pingo have been restricted to geophysical investigations. Two electrical resistivity profiles collected by Ross et al. (2007) depict exceptionally low resistivity values (10 – 400 Ωm) within the immediate near-surface, with limited pockets of higher resistivity values elsewhere (250 – 1,000 Ωm). Low resistivities are attributed to the salinity of the host sediment and permafrost. Meanwhile, higher resistivities are thought to suggest the dominance of segregation ice lenses within the pingo. Alongside observations made at Hytte Pingo, Ross et al. (2007) prescribe a mode of formation for Longyear Pingo similar to that of other ground-ice landforms, such as lithalsas (e.g. Pissart, 2002).

Figure 3.8. An photograph of Longyear Pingo taken during April 2021, facing north-northwest. Snowmobile on the right side of the pingo for scale.

3.3.2. Hytte Pingo

Hytte Pingo (sometimes referred to as Førstehytta) is located at the base of Bassenfjellet, approximately 6 km from Lagoon Pingo on the coast. This is the last pingo that exists entirely within Holocene marine muds and clays, and is located close to the Holocene marine limit. Hytte Pingo is also the largest among those in Adventdalen, measuring ~800 m long, 275 m wide, and 20 m tall. This pingo appears to go through periods of enhanced activity, with running springs occurring during the winter months (Liestøl, 1977; Ross et al., 2007), followed by lulls whereby no activity is observed (Yoshikawa and Harada, 1995). More recently, no spring outflow was identified here during 2019 (Hodson, pers. comm), although a spring was identified within a stream flowing through the pingo complex in 2020. Radiocarbon dating of shells found within pingo sediments provide an age of 6,980 ±70 yr BP (Yoshikawa and Nakamura, 1996).

Similar to Lagoon and Longyear Pingo, the presence of fine-grained Holocene glaciomarine sediments leads to resistivities that are extremely low for frozen ground. At Hytte Pingo, resistivities of < 2 kΩm are suggested to preclude the existence of massive ice, with Ross et al. (2007) instead inferring that Hytte Pingo may also be dominated by segregation ice. In contrast, more recent geophysical investigations have attempted to identify the local flowpath to the surface at Hytte Pingo. Electrical resistivity tomography conducted in the summer showed a clear distinction in resistivities across the site, with high resistivities of 1 – 5 kΩm between the pingo and the mountainside, and lower resistivities (20 – 100 Ωm) on the southern side of the site (Hornum et al., 2021). In interpreting these results, Hornum et al. (2021) suggest low resistivities represent saline Holocene muds and clays with a high unfrozen content, whilst elevated resistivities represent shales or mudstones (presumably the Rurikfjellet formation; Major et al., 2000). Consequently, Hornum et al. (2021) argues that groundwater presumably flows along this geological boundary, with fracturing of local sedimentary units ultimately enabling pingo formation in this location.

3.3.3. Innerhytte Pingo

Located 16 km up-valley from Lagoon Pingo, Innerhytte Pingo sits between the mouth of Helvetiadalen and small mountain of Janssonhaugen. Innerhytte Pingo is the tallest pingo in Adventdalen, with a height of 28 m above the river plain, a length of 400 m and a width of 200 m (Liestøl, 1977). The pingo has a complex morphology as a consequence of Adventelva flowing around the southern side, with fluvial incision producing a steeply sloping southern flank in comparison to other flanks which feature much more gentle gradients from the valley bottom. The crest of Innerhytte Pingo consists of a broad crater containing a flowing spring in the summer, and an extensive icing which covers the steeply incised southern flank during the winter months. Located above the Holocene marine limit, Innerhytte exists within a series of Cretaceous muds, sands and shales.

With evidence of continued groundwater activity, alongside sediments which are more favourable to a wider suite of geophysical methods, Innerhytte is among one of the most well-studied open-system pingos on Svalbard. Earlier work largely focused upon groundwater chemistry, with striking increases in chlorine and sodium contents between initial measurements in the 1920s (Orvin, 1944) and 1970s (Liestøl, 1977). Furthermore, a large reduction in sulphuric oxide contents from 2.35 gl^{-1} to negligible levels was observed between this time period, with no reasonable explanation for these changes.

More recent work has focused upon geophysical characterisation of the pingo, with the completion of ground-penetrating radar, electrical resistivity tomography and seismic studies. Ground-penetrating radar studies conducted by Ross et al. (2005) describe an internal structure that suggest against a massive ice core, with strong subsurface reflectors that were likely to indicate a series of alternating ice and shale layers, although variations in chemistry, ice crystal properties, or air content could not be discounted. In addition to this, an internal structure comprised of buried ice bodies away from groundwater injection indicates spring migration over time. This work was followed up by electrical resistivity tomography conducted by Ross et al. (2007), who identified a near surface zone of relatively intermediate resistivity up to a depth

of 3-4 m, followed by a well-developed, high resistivity zone extending 25 m into the subsurface. These results contradict the previous GPR surveys somewhat, and whilst high resistivities can pertain to frozen bedrock, they do not rule out the presence of a plano-convex massive ice core. More recently, focus has shifted towards an identification of groundwater upwelling within the subsurface, with seismic surveys intending to evaluate the groundwater circulation beneath the pingo (e.g. Rossi et al., 2018). These seismic surveys identify a low-velocity layer (2 km s-[1]) at a shallow depth (40 – 60 m), which is suggested to relate to the pingo groundwater inflow and circulation.

3.3.4. Riverbed Pingo

Located within the riverbed of Adventelva, Riverbed Pingo is the easternmost of the chain of pingos in Adventdalen. Measuring 90 m in length, 50 m across and 7.8 m high at its tallest point (Piper and Porritt, 1966), this pingo is of an irregular morphology, consisting of a series of several small domes undergoing fluvial erosion at the margins (Liestøl, 1977). Similar to Innerhytte Pingo, this pingo is wholly above the Holocene marine limit and is therefore formed within Jurassic shales of the Agardhfjellet formation (Major et al., 2000).

By drilling and conducting electrical resistivity tomography on Riverbed Pingo over the course of three years, Yoshikawa (1993) aimed to identify the local cryostratigraphy. They identified an extremely shallow permafrost base at about 15.5 m, on the basis of an electrical resistivity contrast, in stark contrast to borehole measurements made nearby (102 m at Janssonhaugen; Isaksen et al., 2001). In terms of pingo structure, Yoshikawa (1993) describe a shallow ice core with evidence of epigenetic growth.

Later investigations of Riverbed Pingo have used ground-penetrating radar to characterise the pingo structure and composition. In Ross et al. (2005), ground-penetrating radar depicts a series of steeply dipping reflections close to the surface, and are interpreted as alternating ice and shale units. They furthermore prescribe the location of Riverbed Pingo to the existence of structural geological controls, as Riverbed Pingo is known to exist above a known décollement fault (Major et al., 2000).

Chapter 4: Seismic and electrical geophysical characterization of an incipient coastal open-system pingo: Lagoon Pingo, Svalbard

This chapter was published in Earth and Space Science in December 2021. Here, it is included in the thesis in an adjusted form. The Abstract and Plain Language Summary have been included, whilst the published Field Site section has been omitted as its content is included within Chapter 3 of the thesis. Supplementary material for this chapter has been included in Appendix 1. An afterword has been added to contextualise these earlier published findings with later chapters within the thesis. References for this chapter have been included within the Reference List at the end of the thesis.

Co-authors: Bernd Kulessa, John F. Hiemstra, Andrew J. Hodson, Alun Hubbard

Abstract

Whilst there has been a recent appreciation for the role of open-system pingos in providing a fluid-flow conduit through continuous permafrost that enables methane release, the formation and internal structure of these ubiquitous permafrost-diagnostic landforms remains unclear. Here, we combine active-source seismic measurements with electrical resistivity tomography (ERT) to investigate the structural and subsurface characteristics of an incipient open-system pingo actively emitting methane within the glacio-isostatically uplifting fjord valley of Adventdalen, Svalbard. Wavefront inversion of seismic refractions delineate a spatially heterogenoeus active layer, whilst deeper reflections identify the lithological boundaries between marine clays and underlying shales at ~68 m depth (p-wave velocity of ~1790 ms-1). Low

geometric mean inverted resistivities of 40 – 150 Ωm highlight the dominance of saline permafrost, whilst elevated resistivities (~2 kΩm) occur close to the groundwater spring and in heaved areas around the pingo. Based on our results, we speculate that segregation ice dominates the pingo structure, given the absence of a notable resistivity contrast characteristic of injection ice that is typically expected within early open-system pingo formation, and provides the most plausible geomorphic agent within the local fine-grained sedimentology. Our results thereby indicate that sediment grain size and moisture availability can provide important controls on pingo formation. This study shows that open-system pingos in coastal, saline permafrost environments may form differently, with implications for localized permafrost structure, its permeability to underlying gas reservoirs and consequent methane release.

Plain Language Summary

Considerable amounts of methane, a potent greenhouse gas, can flow through ground which is permanently below freezing (permafrost) through dome-shaped landforms called open-system pingos. These landforms occur in the lowlands of mountainous cold regions, from water under pressure from deep underground. However, the formation and internal structure of these landforms are unclear. We use geophysical techniques involving seismic waves and electrical resistivity to characterize the internal structure of a young pingo in Svalbard. Our seismic investigation find a seasonally thawing (active) layer with a variable thickness, and a deeper reflection at ~68 m which we interpret as the boundary between fine-grained Holocene marine clays and bedrock. Meanwhile, relatively low electrical resistivities indicate that the ground is saline, and suggest an internal structure that is dominated by discrete layers of ice known as segregated ice, as opposed to a large body of ice which is ordinarily expected. Our results indicate that sediment grain size and moisture availability are important controls on pingo formation. This is important as there may be differences in how these pingos form, and this will impact the structure

of local frozen ground and in how they allow the escape of methane stored deep beneath the permafrost.

4.1. Introduction

The ongoing degradation of Arctic permafrost is potentially one of the most significant, yet poorly understood consequences of amplified climate warming. The possible release of vast inventories of sequestered carbon as potent greenhouse gases is considered one of the most serious threats in future acceleration of warming (Pithan and Mauritsen, 2014; Nisbet et al., 2016). Processes including the desiccation and decomposition of carbon-rich soils and peatlands (Koven et al., 2011; Lawrence et al., 2015), the abrupt thaw of ground ice (Turetsky et al., 2019; 2020) and ebullition through lakes (Walter Anthony et al., 2012) are ongoing contributors to atmospheric methane. Moreover, natural gas trapped across the subsurface in either free form or gas-hydrates can be released in potentially massive quantities as the overlying impermeable permafrost cap degrades.

Our ability to model and understand future greenhouse gas emissions from permafrost environments relies heavily on knowledge of emission processes, and particularly on being able to predict the way ground ice might disintegrate. It is well-known that changing thermokarst landscapes (Turetsky et al., 2020) and vegetation patterns (Loranty et al., 2018; Grünberg et al., 2020) modulate thermal conditions in the ground, leading to significant localised differences in both extent and thickness of the permafrost. Geological and geomorphological processes and features also provide controls on the continuity and configuration of ground ice. Varying sediment properties (e.g. Lawrence et al., 2008) and geologic structures (Mishra et al., 2021) could lead to differences in thermal and hydrological properties and consequently to heterogeneities in the permafrost layer.

Among the heterogeneities within continuous permafrost environments are open-system pingos; permafrost-diagnostic mound-like landforms that are typically up to 40m in height and 100 - 500 m across (Harris et al., 2017; Ballantyne, 2018). Open-system pingos are widely considered to form

following the artesian injection of hydraulically pressurized groundwaters (Müller, 1959), recharged through the temperate zones of glaciers (Liestøl, 1977) into the near-surface. It is typically believed that initial pingo formation occurs following the freezing of injected groundwaters into massive ice lenses (also referred to as "injection ice"; Mackay, 1973), resulting in a characteristic, dome-shaped landform. However, whilst it is proposed that initial pingo growth occurs solely from injection ice (French, 2007), this would require the balance of water pressures, overburden strength and freezing rates, which vary naturally. Consequently, ice segregation, whereby porewater migration towards the freezing plane produces discrete ice lenses within the soils, is suggested to occur following initial pingo growth (Mackay, 1973; French, 2007), although more recent studies have questioned whether this dominates their geomorphology (Ross et al., 2007; Kunz and Kneisel, 2021). In addressing the distribution of open-system pingos, Yoshikawa and Harada (1995) suggest three groupings: (i) those formed whereby groundwaters exploit existing geologic faults and structures; (ii) those which occur in areas of artesian flow as a consequence of subglacial meltwaters (cf. Liestøl, 1977) and, (iii) those occurring in nearshore or low-lying environments, undergoing glacio-isostatic uplift. Despite this categorization of their hydraulic properties, the mechanism and processes which govern pingo formation still remain poorly understood (Gurney, 1996; Demidov et al., 2019; Kunz and Kneisel, 2021), and studies assessing early pingo forms remain limited.

This need for detailed information on the internal structures and genesis of open-system pingos has been emphasized by recent studies highlighting significant methane emissions from these landforms (Hodson et al., 2019; Hodson et al., 2020), and the need for an understanding of ground-ice distributions given risk of permafrost thaw (Turetsky et al., 2019). As open-system pingo formation is inherently linked to groundwater flow through permafrost, their role in providing a flow conduit through which deeply-seated methane migrates has come under increased scrutiny (Hodson et al., 2019; 2020). The significance of open-system pingos enabling methane release has been shown in emissions estimates from Lagoon Pingo in Adventdalen, Svalbard, whereby Hodson et al. (2019) suggests year-round methane release

of ~64 kg CH_4 a^{-1}, by diffusion alone, exceeding that of wetland emission estimates when normalized for surface area (Pirk et al., 2017). Methane emissions have indeed been found at four of the five pingos in Adventdalen (Hodson et al., 2020). In essence, it has been suggested that these landforms are terrestrially analogous to submarine pockmarks and gas seep forms, which have been extensively studied on the Barents Sea Shelf (Portnov et al., 2013; Andreassen et al., 2017; Serov et al., 2017). Critically, unlike submarine forms where escaping methane is oxidized within the water-column, terrestrial open-system pingos release gas that directly contributes to the atmospheric carbon budget.

Here, we use a combination of active-source seismic and electrical resistivity tomography (ERT) techniques to characterize the internal structures of Lagoon Pingo, in Adventdalen, Svalbard. This coastal, incipient open-system pingo, represents the youngest in a chain of five formed from Holocene glacio-isostatic uplift, and was specifically selected because of its documented methane release (Hodson et al., 2019; 2020). We hypothesise that the geomorphology is dictated by lenses of massive, injected ice (Mackay, 1973), forming as a consequence of the near-surface freezing of groundwater upwelling, and that the present-day springs flow around these lenses to the surface. We test this notion by constraining the near-surface structure of Lagoon Pingo to understand the genesis of open-system pingo forms, and assess how these interact with groundwater springs and associated methane release.

4.2. Methods and Data Acquisition

4.2.1. Methods

4.2.1.1. Seismic Investigations

Active source seismic investigations are well established in geomorphological studies (Schrott & Sass, 2008). Seismic methods are based upon the principle that elastic waves travel through different subsurface media at different velocities, with this dependent upon composition and material density. By

measuring the elapsed time between the triggering of a quantified seismic signal, and its return following refraction or reflection from a subsurface change in acoustic impedance, a non-intrusive interpretation of subsurface properties can be obtained. Further detail can be established through an understanding of the polarity and amplitude of the obtained seismic returns, should data quality permit.

The use of seismic methods within permafrost environments is highly dependent upon sharp increases in P-wave velocity where media is frozen (Zimmermann & King, 1986). Consequently, seismic refraction and reflection methods are commonly used in the detection of permafrost extent (Schrott & Hoffmann, 2008). For example, seismic refraction methods are often used to determine active layer depth, given that the P-wave velocities of the active layer (400 – 1500 ms^{-1}) and frozen permafrost (2000 – 4000 ms^{-1}) show sufficient contrast (Hauck & Vonder Mühll, 2003; Hauck et al., 2007). Notably however, refraction methods are limited in requiring velocities to increase with depth. In permafrost environments, whereby frozen layers often exhibit increased P-wave velocity, this inhibits the detection of the permafrost base. Seismic reflection methods are often used to obtain interfaces deeper within the subsurface, and have been utilised within permafrost and periglacial environments to determine the depth of the permafrost base (Schwamborn et al., 2002).

4.2.1.2. Electrical Resistivity Tomography (ERT)

ERT utilises differences in the ability of materials to resist the flow of an electrical current to establish bulk electrical resistivity contrasts within the subsurface. These bulk resistivity characteristics are controlled by different mechanisms that enable the flow (e.g. conduction, the reciprocal of insulation) of electrical current through media: particle conduction, surface conduction and ionic (or electrolytic) conduction. Particle conduction relates to conductivity caused by a high number of free electrons, often within metallic materials. Surface conduction occurs through the electrical double layer at the interface between particle and fluid, which is controlled by porewater content and the

electrical properties of the media (e.g. cation exchange capacity, zeta-potential). Lastly, ionic (otherwise known as electrolytic) conduction refers to that caused by the transit of ions through media, normally resulting from liquid flow. As a consequence, ionic conduction is typically controlled by the porosity, saturation, pore connectivity, and fluid conductivity of a material (Mollaret et al., 2019). These three mechanisms determine the bulk conductivity, and thus the bulk resistivity, of a given medium.

ERT is commonly applied to establish soil properties (e.g. lithology, porosity, structural characteristics, and pore fluids), stratigraphy and heterogeneities within a given subsurface (Klein & Santamarina, 2003). In permafrost environments, the differences in conduction between electrically conductive liquid water and resistive ice render ERT an effective method for the identification and interpretation of frozen and unfrozen sediments, with typical applications including the identification of active layer depths (e.g. Kasprzak, 2015; Léger et al., 2017), the permafrost base (You et al., 2013; Sjöberg et al., 2015) and in the detection of ground ice (Hauck & Vonder Mühll, 2003). However, whilst frozen pore water content typically increases electrical resistivity by several orders of magnitude, exceptions can occur in fine-grained marine clays where pore waters are conductive and surface conduction mechanisms exist at the particle-ice-water interfaces within the pore spaces (e.g. Revil & Glover, 1998).

4.2.2. Data Acquisition

4.2.2.1. Seismic Investigations

Active source seismic data were acquired in August 2019 across two profiles which together cover the length of the pingo complex. The data were acquired using two Geometrics Geode 24 Channel seismographs, with profiles consisting of 48 100 Hz geophones deployed at 4 m spacings. Shots were made using a sledgehammer source on a metal baseplate at 4 m intervals midway between geophones and up to 10 m off-end, with additional shots taken every 10 m up to a distance of 50 m from the end of the profile. A set of

10 shots were taken per shotpoint in order to allow stacking, with each profile therefore containing 610 shots in total.

Processing of the seismic reflection data was completed in REFLEXW version 9.5 (Sandmeier, 2020). Whilst planimetric positions of shotpoints and geophones were obtained by tape measure, GPS positions of geophones were taken using a Garmin eTrex handheld GPS with horizontal accuracy of c. 5 meters, to obtain topography using a 2009 summer 5 m DEM (Norwegian Polar Institute, 2014). Traces that were visibly noisy or dead were manually removed from shotgathers prior to stacking. To analyse seismic reflections across the site, a common midpoint gather was produced using the 4 m-spaced shots by resorting and stacking traces according to their offset. The velocity of identified hyperbolae were then obtained through manual curve-fitting within REFLEXW. An initial estimation of the internal velocity was obtained through Dix's formula (Dix, 1955) to form a preliminary model, although it is noted that this does not satisfy the assumptions of standard NMO velocity analysis (Bradford, 2002). Consequently, we use this model following the recommendations of Bradford and Sawyer (2002), by applying this estimation on unstacked data through a pre-stack depth migration (PSDM). Unstacked data were processed by applying a manual gain adjustment (to enhance signal with depth) and bandpass filtering (to minimize surface waves), followed by resampling at 3 ms due to processing constraints, and finally a pre-stack depth migration using Kirchhoff weighted factors for the summation of raypaths.

To analyse seismic refractions, first onsets were manually picked for each shotpoint. Following traveltime analysis as per standard procedure in REFLEXW (Sandmeier, 2020), a two-layer wavefront inversion was subsequently conducted using the forward and reverse traveltimes, by utilising a finite difference approximation of the eikonal equation which is analogous to the FD-vidale method used in forward raytracing (Vidale, 1988; 1990; Sandmeier, 2020). Seismic refraction tomography was conducted to provide a secondary analysis of the data, whereby the Simultaneous Inversion Reconstruction Algorithm (SIRT; van der Sluis & van der Vorst, 1987) was used to automatically adapt synthetic data to observed travel times through calculation of the seismic P-wave ray paths. In accordance with initial

wavefront inversion data, an initial model with a surface P-wave velocity of 375 ms^{-1}, increasing by 200 ms^{-1} with each metre in depth was used. The parameterization of the tomographic inversion is shown in the Supplementary Information (Table A1.1). Goodness of fit was assessed using forward raytracing through a finite difference calculation (Vidale, 1988; 1990).

4.2.2.2. Electrical Resistivity Tomography

A series of electrical resistivity tomography (ERT) profiles were collected in early April 2019 using an ABEM SAS1000 Terrameter, whilst the site remained frozen. Two profiles (R1 and R2 in Fig. 4.1) were collected to encompass the NW-SE extent of the site, with each profile containing 53 stainless steel electrodes at a spacing of 5 m to cover full extent of 260 m. These profiles contained an overlap over central parts of the site to ensure suitable data coverage over the primary upwelling and for error analysis. These profiles were supplemented by shorter, quasi-perpendicular transects containing 21 electrodes to cover a lateral extent of 100 m (R3 - R5 in Fig. 4.1). Wenner array configurations were used for each profile to provide the best compromise between vertical and horizontal resolution in an uncertain environment, given that contact resistance was high (Hauck & Vonder Mühll, 2003). Where electrodes occurred in snow-covered areas, snow pits were dug, and all electrodes were hammered in using a rubber mallet until firmly emplaced within the ground. To counteract electrode contact issues resulting from the high resistivity of frozen surfaces in sub-zero conditions, a saline solution was poured onto each electrode prior to each measurement, and snow pits were dug where required. Given the variable surface conditions, the instrument was set to select current automatically for each measurement within all profiles. For each profile, normal and reciprocal measurements were obtained. However, despite our best efforts, poor contact for a minority of electrodes resulted in failure to measure a potential for some electrode configurations, with success rates shown in Table 1. Configurations whereby either or both of the normal or reciprocal measurements failed were consequently excluded from further data processing.
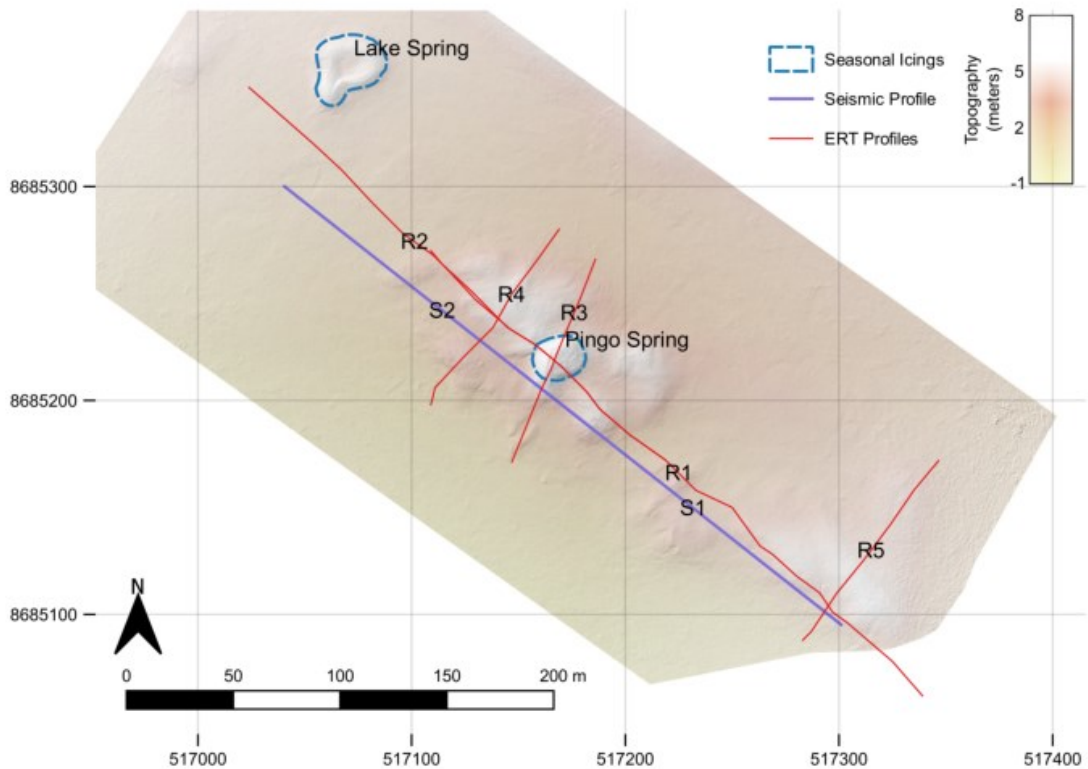
Figure 4.1. Locations of profiles over the Lagoon Pingo site, depicted on a sub-metre DEM derived using Structure-from-Motion in April 2020 (Hann & Dachauer, 2020). Co-ordinates shown are UTM 33N.

The data were further pre-processed and inverted in ResIPy (see Blanchy et al., 2020); an open-source graphical user interface (GUI) for the Occam's type R2 inversion algorithm (Binley & Kemna, 2005). Firstly, data were filtered through comparisons of results obtained by normal and reciprocal measurements, with those that exceeded a 10% difference in apparent resistivities excluded. For some profiles, this resulted in the exclusion of a high proportion of measurements (shown in Table 4.1), largely pertaining to measurements occurring from particular electrodes (see Figure A1.3). To account for errors within measurements and to discretise the initial model, an error model was subsequently fit. This follows Koestel et al. (2008), where the assumption is that true error relates to both an absolute (*a*) and a relative component (*b*), which are used to determine data weightings and parameterise

the final inversion model. To complete this, measurements were binned by their apparent resistivity into groups of ~20 and fit to an error model. For shorter profiles (R3 – R5), a linear error function was used owing to the smaller number of measurements, given by:

$$\varepsilon = a + b\rho$$

(4.1)

where ε is the standard deviation and ρ is the mean of each bin in Ohms. Constants a and b were then defined by the best linear fit. For longer profiles, a linear error model provided a poor fit for measurements which contained lower mean resistivities, and thus constants a and b were defined through the best fit of a power-law based error function where:

$$\varepsilon = b\rho^a$$

(4.2)

The inversions were discretised using a custom transfinite mesh, built around surface topography as defined by a decimeter-resolution DEM derived through Structure-from-Motion photogrammetry from a drone survey conducted in April 2020 (cf. Westoby et al., 2012; Hann & Dachauer, 2020). The horizontal resolution of the mesh foreground was defined by 2 cells per electrode, whilst the vertical cell size increased away from the surface where sensitivity to the input data was expected to be greatest. The foreground meshes were constrained by depth using a default 2/3 of the maximum dipole length, and the initial model resistivity was set to the geometric mean of apparent resistivity for each profile.

The inversion using the R2 algorithm involves a least-squares weighted function (Blanchy et al., 2020), which aims to find the smoothest model that conforms to and remains consistent with the data. For each model, the weights were updated as the inversion progressed using a routine based on Morelli and LaBrecque (1996).

The inverted models were appraised for their reliability through multiple methods. Inversions were initially checked using normalised model error, as

per Binley et al. (1995), to ensure that these fit within a ±3% threshold. Following this, the sensitivity of the inverted models to the initial data were checked using an accumulated sensitivity map (Park & Van, 1991; Kemna, 2000; Binley & Kemna, 2005), calculated through the evaluation of both the Jacobian and data weighting matrix. A threshold of 0.001 x S_{max} was used to determine parts of the inversions which were deemed sensitive to the initial data (Kemna, 2000). This sensitivity matrix is presented with each resistivity profile below, and areas which are below this sensitivity threshold are shown as semi-transparent. Lastly, the reliability of separate inversions were tested by analysis of the correlation between profiles where these intersect (see Supplementary Information).

Table 4.1. Number of successful and failed measurements for configurations within each profile, with rates of excluded measurements following further pre-processing.

Profile	Total number of configurations	Successful measurements (normal and recirprocal)	Measurements following filtering
R1	443	388	206
R2	443	214	100
R3	63	61	52
R4	63	61	53
R5	63	63	61

4.3. Results

4.3.1. Seismic Reflection

The result of our seismic reflection investigations are shown by the common midpoint gather in Figure 4.3, whereby a hyperbolae beginning at ~80ms at zero offset is the most apparent feature. This homogeneous reflector remains visible up to approximately 160 m from the shotpoint following geometric correction, and exhibits a P-wave velocity of ~1787.1 ms^{-1} once corrected for the overlying active layer. A multiple of this can be seen at wide offsets, with this particularly clear where offset is negative due to noise obtained in the

opposite direction. The only other reflection feature apparent is the air wave with a P-wave velocity of 330 ms^{-1}.
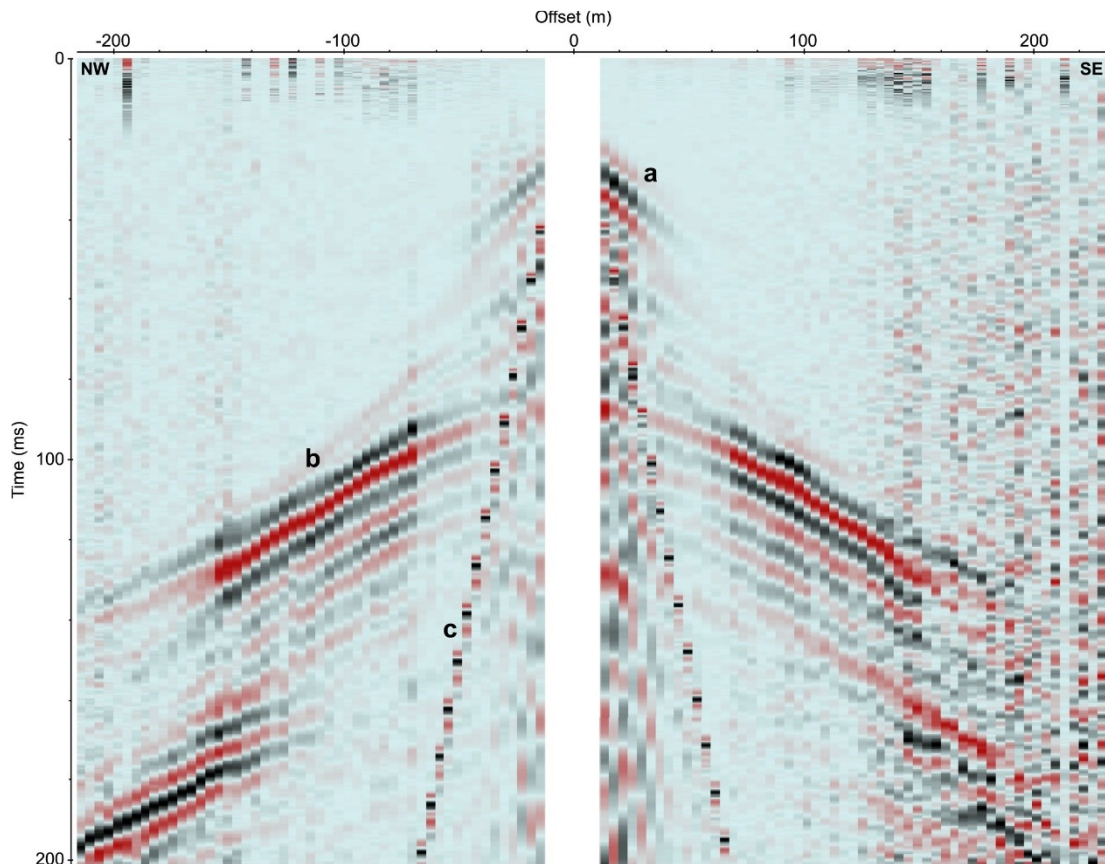
Figure 4.2. Common midpoint gather depicting homogeneous refractions and reflections from across Lagoon Pingo, shown without gain. Letters indicate (a) the near surface P-wave refraction from Holocene marine clays, (b) P-wave reflection from the boundary between overlying fine-grained marine sediments and underlying strata and (c) the direct air wave.

4.3.2. Seismic Refraction

In addition to deeper reflection features, a near-surface refraction is highlighted on the common midpoint gather (Figure 4.2) with a preliminary manual interpretation suggesting a shallow active layer with P-wave velocities of ~394 ms^{-1} above a deeper second layer with a V_p of 2110 ms^{-1} (see Figure A1.1).

Figure 4.3 shows the wavefront inversion (red line), assuming that a two-layer model persists in the near-surface of the Lagoon Pingo site (as derived from the preliminary analysis of the common midpoint gather), and 2-D refraction

tomography obtained from the first arrival picks of seismic data. The wavefront inversion identifies a lower velocity layer overlying a higher velocity layer within the immediate subsurface at the site, with depths consistent with analogous coastal sites elsewhere on Svalbard (e.g. Christiansen et al., 2020). The greatest depths occur in the northwestern part of the profile in a low-lying, flat section close to the lake spring, where values in excess of ~3 m are obtained. Whilst the wavefront inversion largely echoes the shape of the surface topography, the minimum layer depth of 1.1 m occurs within heaved sediments where the topography is most variable. Estimates of upper layer P-wave velocity from the wavefront inversion equal 385 ± 20.7 ms^{-1}, highlighting a homogeneous layer with a low P-wave velocity across the length of the profile.

In contrast, the seismic tomography model shows an increase in velocity with depth, but depictions of two distinct layers is ambiguous (Figure 4.4a). Velocities of ~400 ms^{-1} at the surface increase to 600 - 700 ms^{-1} at a depth of 2-3 m due to the initial model used, and increase rapidly thereafter. Notably, the tomography depicts lateral variations in P-wave velocity below a depth of 5 m, with lower P-wave velocities at greater depths over flat, low-lying parts of the profile when compared to heaved areas where surface topography changes are greater. For example, at approximately 400 m along the profile, P-wave velocity equals ~1500 ms^{-1} at a depth of ~10 m from the surface, whereas velocities exceeding 3000 ms^{-1} are found at the same depth at approximately 200 m. A depiction of layering within the subsurface would be most apparent within the calculation of first derivative, and is evidenced by central parts of the profile displaying a rapid change in velocity gradient within the upper 2 m of the subsurface. However, this occurs at a shallower depth than the calculated wavefront inversion, and is not apparent between 120 – 180 m and from a distance of 380 m onwards, through the topographically flat northwestern end of the profile. Following forward raytracing using a finite difference algorithm, traveltimes derived from the tomographic model provided an RMS error of 1.35 ms in comparison to observed data, corresponding with 2 ms guidelines suggested for RMS where refractions are less than 30 m in depth (Sandmeier, 2020).
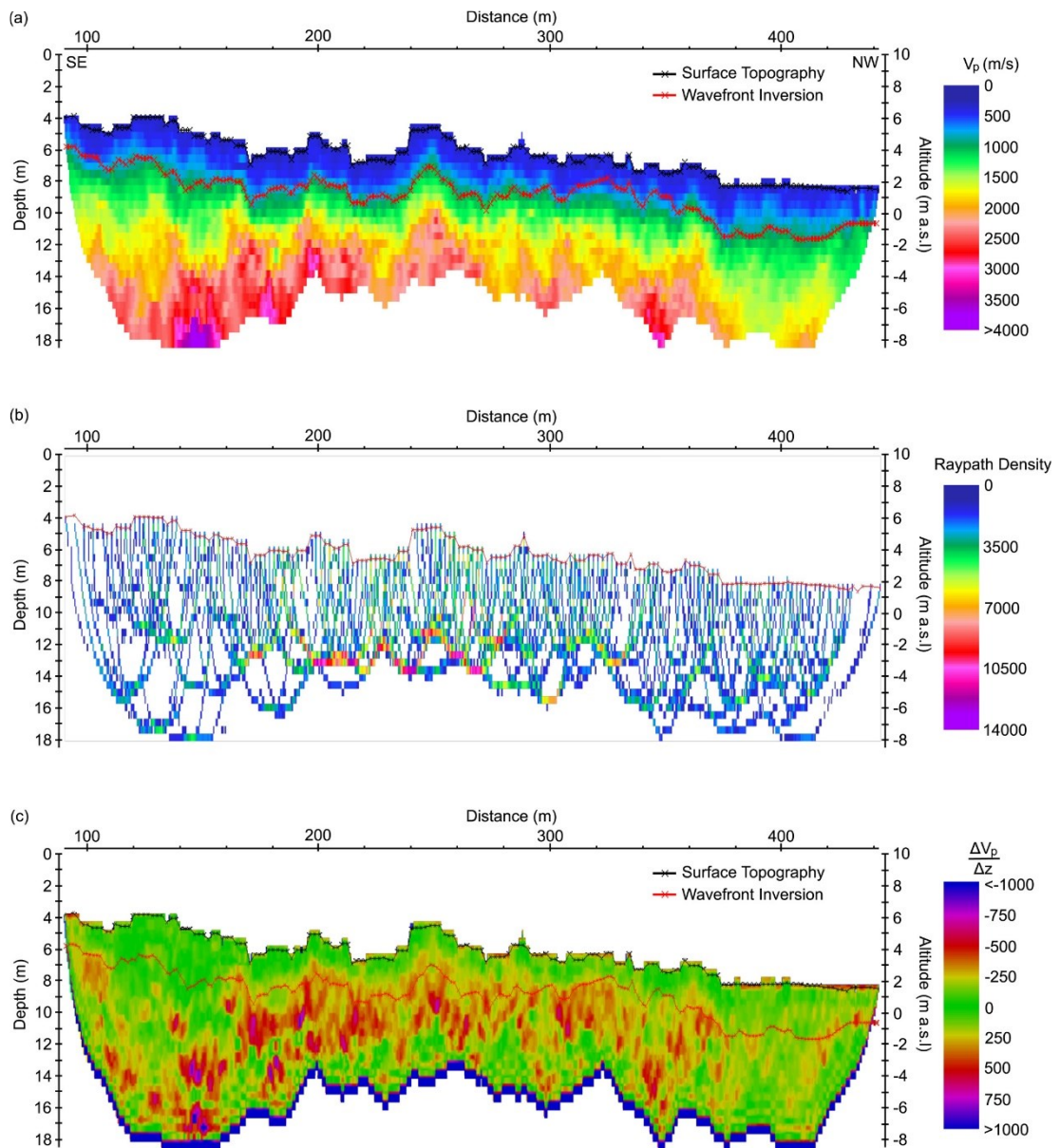
Figure 4.3. (a) Seismic wavefront inversion, as shown by the black line, and refraction tomography across the long line (from SE to NW) at the Lagoon Pingo site. (b) Map highlighting the density of raypaths from which the tomography was calculated. (c) The calculated and smoothed first derivative of the tomography, with the wavefront inversion overlain.

4.3.3. Electrical Resistivity Tomography

Tomograms obtained from the inversion of electrical resistivity measurements on the long profiles (Fig. 4.4) depict a high range of inverted resistivities, with

large zones of comparatively low inverted resistivities (10 – 100 Ωm) intercepted by near-surface areas of elevated inverted resistivity values. On Line R1, these elevated zones of increased resistivities are most apparent between 50 – 70 m, and between 170 – 220 m on the eastern side of the pingo icing (235 m). This zone is additionally shown on R2, whereby flat sections otherwise depict inverted resistivities of the order of 10 – 100 Ωm. Whilst the pingo icing is not within the sensitivity threshold for Line R1, Line R2 indicates inverted resistivity values the order of 100 MΩm. Where sensitive, the average R2 value for the crossover between these two profiles equalled 0.82 (see the Supplementary Information), with weaker R2 values around the margins of inversion sensitivity.

The accumulated sensitivity matrix shown in Figure 4.4 indicates a complex pattern of resistivity across the pingo, as a consequence of poor contact resistance upon initial gathering of these measurements, and given the high data exclusion rate following filtering. In particular, sensitivity around the pingo icing is problematic, with dark zones of low sensitivity present at ~2 – 3 m depth within this structure evident for both profiles.
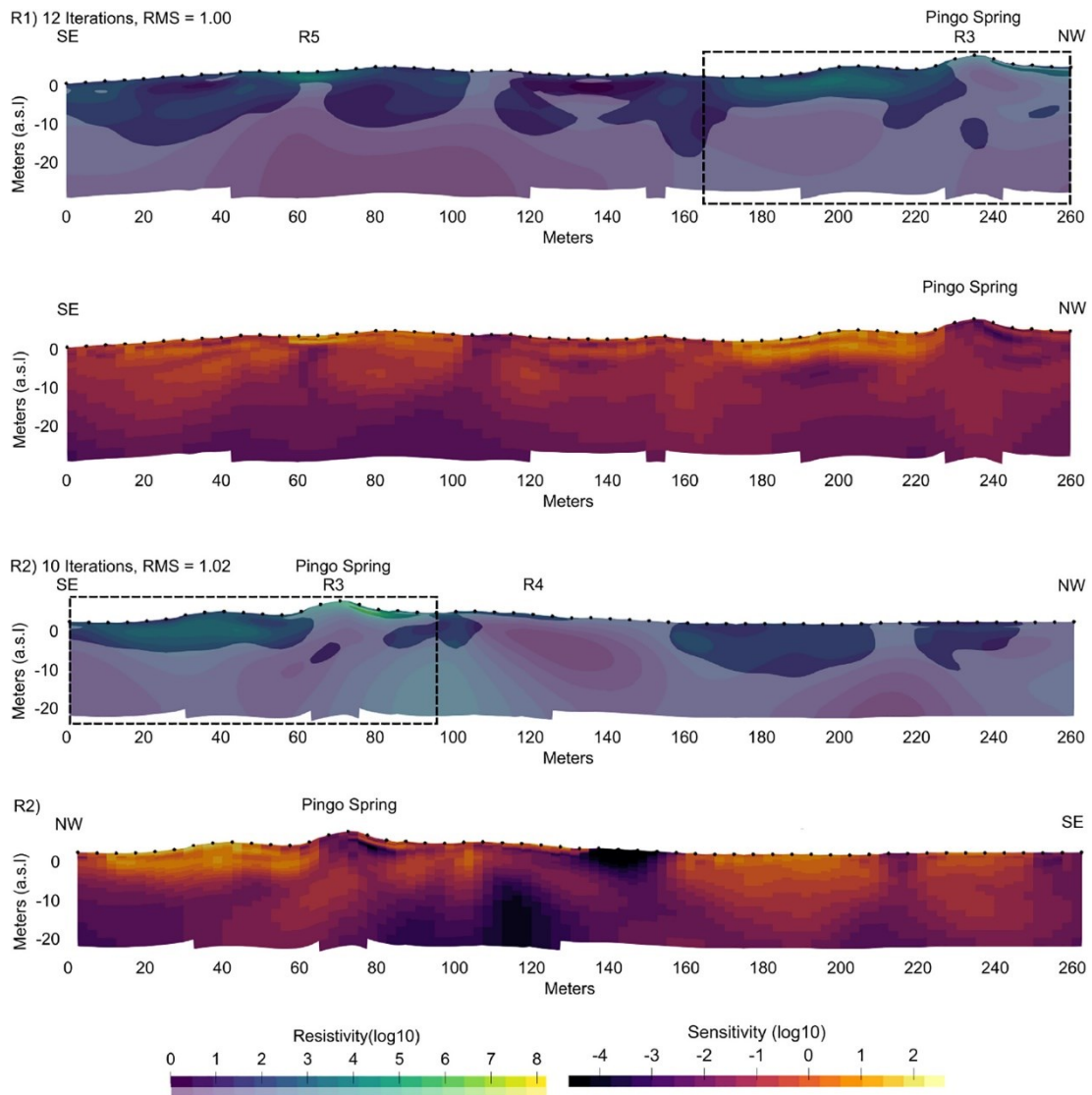
Figure 4.4. The final inversion results for long profiles R1 and R2, with resistivity results outside of the sensitivity threshold shown translucently, accumulated sensitivity maps shown below respective resistivity profiles, and dotted boxes showing the crossover between profiles.

Shorter tomograms and associated sensitivity profiles (Fig 4.5) depict similar patterns in inverted resistivity and sensitivity, with low overall inverted resistivities intercepted by isolated zones of elevated inverted resistivity values which correspond well to local topographic highs. Line R3 depicts a transect across the pingo icing, whereby the topographic high provides the highest inverted resistivities (10 MΩ.m). This is flanked by zones of lower inverted resistivities within the sensitivity threshold, between 10-100 Ωm on the northern side and up to 1000 Ωm on the southern side. Unlike longer profiles, the inversion here remains sensitive over the pingo icing, although this

63

sensitivity is limited to the upper 5 m of the centre of this profile. Line R4 shows higher inverted resistivity values (22 kΩ.m) at a depth of 5 m in the centre of this profile (50 m), which occurs approximately 10 m south of the local topographic high. Line R5 also depicts a pattern of elevated inverted resistivity values corresponding to higher elevations, with an area at approximately 70 m along the profile and at 5 – 15 m depth which shows an inverted resistivity of 150 – 300 Ωm. This contrasts with a geometric mean apparent resistivity across the profile of 44.3 Ωm. For both lines R4 and R5, high sensitivities encourage confidence in these inversions. Whilst the crossover of longer profiles and lines R3 and R4 was rendered redundant due to low sensitivities at their intersection, the crossover between R1 and R5 provided R^2 values of 0.9432 (see Supplementary Information), which highlights that these profiles follow the same vertical trend of resistivity change.
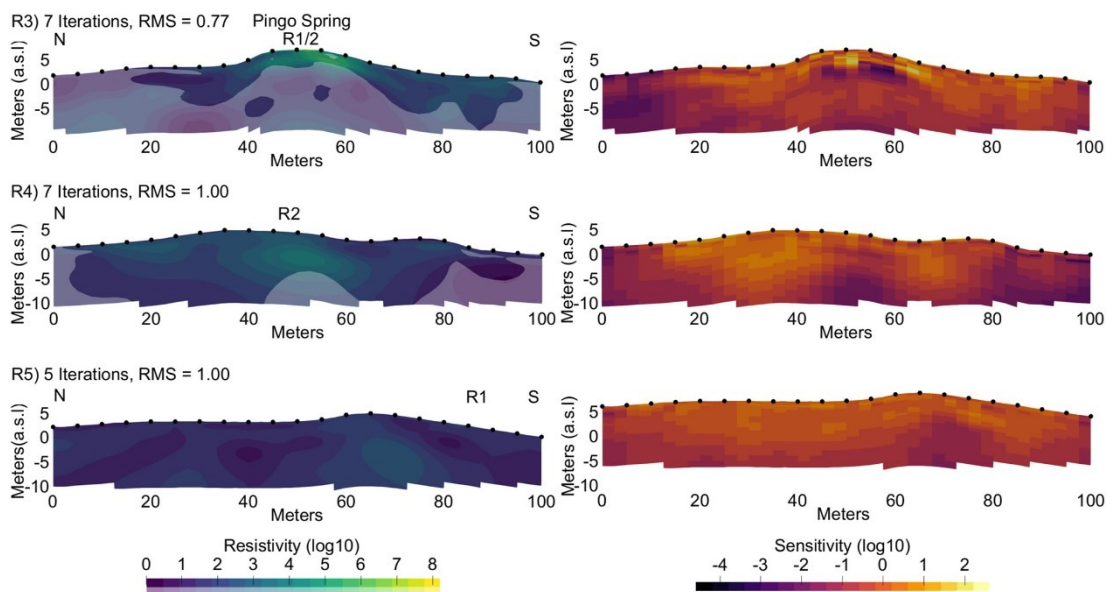
Figure 4.5. The final inversion and their associated accumulated sensitivity map for each of the shorter profiles.

4.4. Interpretation

In conducting multi-method geophysical investigations of Lagoon Pingo, we aimed to establish its composition and internal structures and to improve understanding of the mechanisms that characterise the early stages of pingo

development. In particular, we test the idea that Lagoon Pingo has developed from the emergence of a submarine pockmark through active glacio-isostatic uplift of the area (Hodson et al., 2020). Our results yield insights into incipient pingo structure that does not conform with typical pingo development, and which has implications for the understanding of methane release from such landforms.

The upper layer identified from our seismic refraction data is interpreted as the active layer that covers the length and breadth of the field site. Average P-wave velocities of ~ 380 - 400 ms^{-1} correspond well with other seismic velocity measurements made in unfrozen Arctic Quaternary sediments (Hunter, 1973; Yoshikawa et al., 2006). However, this active layer is variable throughout the site, as is evidenced by wavefront inversion calculations depicting a range from 1.1 m to values exceeding 3 m. At the top end of this range, measurements are substantially thicker than active layers recorded elsewhere within Adventdalen, including 1.54 m measured at Janssonhaugen (Isaksen et al., 2001). Both geographical and measuremental factors should therefore be considered to explain this relatively thick local active layer. In terms of geographical factors, Lagoon Pingo is located at sea-level near the present coastline, and thus warmer microclimatic conditions could drive more extensive summer thaw compared to further up-valley. For example, the annual mean air temperature at the coast between 2014 and 2018 was -1.6 ºC (Svalbard Lufthavn; Norwegian Meteorological Institute, 2021), compared to -3.8 ºC and -3.0 ºC for Janssonhaugen in 2017 and 2018 respectively (Christiansen et al., 2020). Additionally, saline porewater may play a role in depressing the freezing point of the local Holocene marine muds compared to sites such as Janssonhaugen, which lies outside of the limit of marine transgression. Furthermore, given that the topographically elevated areas of the pingo have an open exposure to wind, thermally insulating snow is often scoured from these areas, thus leading to earlier exposure to solar insolation at the start of spring thaw compared to other sites. However, whilst these geographical factors may impact local active layer depths, limitations in the number of data points and in the wavelength of seismic waves (~3.9 m) may impact the wavefront inversion. Whilst the first derivative of the seismic

tomography does appear to depict changes in P-wave velocity gradient within central parts of the profile, this layering is unclear within topographically flat parts of the line where calculations of active layer based on the wavefront inversion provided the greatest thicknesses. Consequently, whilst active layer thicknesses identified elsewhere within Adventdalen (e.g. Isaksen et al., 2001; Christiansen et al., 2020) are within the error bounds of our own measurements, it is possible that these might be somewhat greater or more spatially variable at Lagoon Pingo.

In the seismic reflection data, there is an unexpected absence of clear reflections in the upper 50 m, which is inconsistent with earlier findings of Yoshikawa and Harada (1995), whose resistivity data reveal permafrost thicknesses of ~23 m. As the presence of the pingo is diagnostic of permafrost, a permafrost base should be evident. Yet, whilst frozen media ordinarily results in a substantial increase in P-wave velocity (Hauck et al., 2007), the lack of a reflection could point to a number of possible scenarios. For example, the acoustic impedance of saline permafrost and unfrozen marine clays may be too similar to differentiate. Additionally, there could be substantial heterogeneity in permafrost thickness across Lagoon Pingo, which causes a lack of a clear reflection when combining traces by their offset between source and receiver, irrespective of their location at the site. Furthermore, a high unfrozen pore-water content within the permafrost would also serve to lower the acoustic impedance between permafrost and non-permafrost layers, which would be consistent with the valley-scale studies of Keating et al. (2018) who suggest substantial unfrozen water contents of up to ~10% in the lower parts of the valley. Indeed, previous ERT work elsewhere in Svalbard by Kasprzak et al. (2017) indicates that a bottom active layer may be present in coastal permafrost, which may provide a gradient of acoustic impedance at the permafrost base, as opposed to a clear boundary. Ultimately, the absence of a clear interface highlighting a contrast between frozen and unfrozen sediments provides uncertainty over the extent and condition of this permafrost.

At greater depths, the primary reflection visible on the common midpoint gather at 68 m is interpreted as the boundary between Holocene marine muds and

clays, and underlying shales, through both corroboration with previous research within the valley (e.g. Bælum et al., 2012) and through velocity calculations after accounting for the active layer. This is problematic for the proposed origin of Lagoon Pingo as an uplifted submarine pockmark, as it requires the fluid and gas upwelling to have persisted while high volumes of a non-hydraulically conductive substrate, i.e. marine clays, were being deposited on top of it. This would require exceptional hydraulic pressures to maintain, or, alternatively, faulting or another heterogeneity to provide a viable fluid flow pathway. Whilst geological structures have been proposed as fluid flow pathways for Hytte Pingo (Hornum et al., 2021), such features are not known to occur at Lagoon Pingo and have not been identified through these geophysical investigations. While we were unable to identify such deposits from our seismic or ERT profiles at greater depths, there is a possibility that coarse materials from a neighbouring alluvial fan extend beneath the pingo from the north, which might provide at least part of the explanation.

In contrast to the seismic investigations, ERT profiles were collected during the spring when the active layer was still frozen. Although a difference in the physical properties may occur given the annual refreezing of the active layer and associated transitional zone, inverted bulk resistivities in the upper 2 m of ERT profiles (Figs. 4.4 and 4.5) do not provide any indication of differences in physical properties (e.g. ice content). Instead, our survey results correspond well to visual observations made in the field at the time of the measurements. Areas of high resistivities (> 10 kΩm) match areas of surface icing, including the highest resistivities occurring where the perennial central pingo spring is situated. Lower resistivities (<100 Ωm) coincide with exposed frozen marine muds and clays.

Elsewhere within the ERT profiles (Figs. 4.4 and 4.5), and particularly at depths greater than 8 m, persistent low resistivity values (10^1 - 10^3 Ωm) can be interpreted as permafrost. Whilst the resistivity of permafrost is commonly between 1 kΩm - 1 MΩm (Kneisel & Hauck, 2008), previous studies conducted further up-valley (Harada and Yoshikawa, 1996; Ross et al., 2007) and in other coastal environments (Yoshikawa et al., 2006; Rangel et al., 2021) have demonstrated that permafrost resistivities can be substantially reduced in

cases where sediments contain unfrozen porewater due to high dissolved salt content. Indeed, porewater salinities of 30 - 40 ppt have been recorded in Adventdalen (Gilbert et al., 2019). Experiments by Harada and Yoshikawa (1996) using Adventdalen sediments identify porewater salinity as a fundamental factor in the persistence of low resistivities (< 100 Ωm), despite low temperatures (-8˚c) and volumetric water contents (12%). Seismic velocities support this interpretation of saline permafrost, fitting well to both previous seismic investigations in analogous environments (King et al., 1988) and effective-medium models derived from laboratory investigations (Dou et al., 2016; 2017). In the modelling of P-wave velocities provided by a fine-grained saline permafrost core, Dou et al. (2017) found velocities between 2000 - 2500 ms^{-1} persisted where temperatures are -2˚C to -5˚C, which is consistent with our average value of ~ 2110 ms^{-1} as revealed by the initial seismic refraction analysis, and with local climatic conditions (Christiansen et al., 2020).

Lateral variations in inverted resistivities correspond well with surface topography, with increased resistivities at depths in close proximity to, but not directly beneath local topographical highs. This trend is particularly apparent in the shorter transects obtained over the pingo, with lines R4 and R5 highlighting zones with inverted resistivities of 0.2 – 2.2 kΩm beneath topographically elevated parts of the profiles. Given the position of Lagoon Pingo within a glacially scoured, relatively flat valley, and with no apparent geological differences to explain an inhomogeneity, the differences in observed physical properties are expected to provide a geomorphological explanation for current pingo form and genesis. Classic pingo formation theory (e.g. Müller, 1959) dictates that a massive ground ice core is responsible for pingo uplift, formed from the near-surface freezing of pressurised groundwater. However, observed inverted resistivities of ~2 kΩm in topographically raised areas are low compared to those commonly recorded for bodies of massive ice (generally >20 kΩm; cf. Kulessa, 2007; Vieira et al., 2008), and in comparison to icings on the surface, which despite exposure, might otherwise feature similar resistivities. One alternative explanation for the internal structure and surface geomorphology of the open-system pingo is segregation

ice, whereby groundwater migrates and freezes into discrete layers within fine-grained soils, leading to pingo heave. Indeed, early notes on Adventdalen pingo morphology by Yoshikawa (1993) report on segregation ice within the immediate near-surface of the pingo, above a plano-convex massive ice core. Similar observations were reported in previous geophysical studies at Longyear and Hytte pingos (Ross et al., 2007), whereby resistivities of <2 kΩm in topographical highs were interpreted as segregation ice, although no massive ice core was identified. Furthermore, geophysical investigations of an open-system pingo in Yukon, Canada also failed to observe a massive ice core, proposing segregation ice as the primary frozen component (Kunz and Kniesel, 2021). Notably, their ERT profiles also depicted higher inverted resistivities in close proximity, yet not directly beneath, local topographic highs, which was interpreted as the most significant ground ice occurring towards the flanks of the pingos. Our observations echo these studies, which gives confidence in our interpretation that the observed low resistivities and a relatively low topographic imprint is segregation ice serving as the primary geomorphic component.

Replicable negative resistivities obtained in the long profiles are also consistent with the presence of segregation ice lenses. These occurred in areas of higher elevation (e.g. R1 170 – 220 m; see Fig. 4.4) that are not presently influenced by the upwelling groundwater spring. Whilst negative resistivities have often been regarded as erroneous (Jung et al., 2009), we argue that the occurrence of negative apparent resistivity on both normal and reciprocal profiles (see Supplementary Material) meets our stringent data filtering criteria and do not constitute data quality issues. As recent numerical and modelling studies have shown, negative resistivities may arise in specific field scenarios. For example, through a series of dipole-dipole array numerical simulations, Jung et al. (2009) demonstrated the occurrence of negative resistivity values as a consequence of U- or crescent-shaped geological structures. In addition, Lee and Cho (2020) indicate that an extreme range of resistivities may also result in negative apparent resistivities. Elements of both of these factors may hold true at Lagoon Pingo. For example, the dome-shaped winter and spring icing occurs in a depression that is occupied in the

summer by a small pond. This shape resembles the crescent-shaped geological structure described in the former scenario. In respect to the latter scenario, an extreme range of resistivities (10^8 Ωm) at the Lagoon Pingo site is caused by the close proximity of extensive yet highly resistive surface icings, segregation ice within the near surface and otherwise electrically conductive clays. This extreme range (10^8 Ωm) may additionally provide an explanation for negative apparent resistivities despite using a Wenner configuration, which is more robust and less susceptible to noise when compared to the aforementioned studies whereby dipole-dipole configurations were used. Yet whilst results here correspond well to previous modelling studies, further ground truthing is required to confirm the validity of the interpretation of these negative resistivities, and their occurrence in permafrost environments.

4.5. Discussion

4.5.1. Pingo Genesis

Previous studies have suggested that Lagoon Pingo provides an example of a glacio-isostatically uplifted pockmark, formed following the emergence of a pre-existing methane seep. This presumes that the flow pathway existed prior to terrestrial exposure. Yet whilst the recent development (140 ± 20 years BP) of the terrestrial pingo is evidenced through radiocarbon dates of mollusc shells (Yoshikawa and Nakamura, 1996), the presence of a seismic interface at ~68 m depth, interpreted as the boundary between Holocene marine muds and clays, and underlying shale bedrock is problematic for this formation process. Given that these fine-grained marine muds and clays have low hydraulic conductivity (Olaussen et al., 2020), it is difficult to perceive how the groundwater upwelling was under sufficient hydraulic pressure to persist through the accumulation of these sediments above it.

Despite detailed and targeted surveys, it remains unknown whether a heterogeneity exists that would enable the preferential flow of groundwater through the non-hydraulically conductive sediments at Lagoon Pingo, and whether such heterogeneities influence other coastal methane seeps and

pockmarks. For example, whilst recent geophysical investigations have determined that Hytte Pingo is formed above an important geological boundary (Hornum et al., 2021), no known geological interfaces or faults (cf. Ciric, 2019) underlie Lagoon Pingo, nor have such features been identified within this geophysical study. Despite this, the presence of a groundwater spring necessitates a fluid flow pathway (Yoshikawa and Harada, 1995). One potential explanation for enhanced groundwater flow in the subsurface is that coarse-grained sediments, such as sand and gravel from the alluvial fan located to the north of the pingo, may extend beneath the pingo, providing a hydraulically conductive heterogeneity which enables groundwater flow. This has previously been discussed by Humlum et al. (2003), who suggest that unfrozen groundwater may flow within the lowermost layers of coarse-grained deposits above impermeable permafrost, before pressurisation where these deposits thin at the alluvial fan base. Whilst this scenario does not explain the observed emission of methane per se (Hodson et al., 2019; 2020), or would necessarily be compatible with the local thickness of permafrost derived by Yoshikawa and Harada (1995), the alluvial fan could provide sufficient coarse-grained sediment to enable a glacio-isostatically uplifted pockmark system to persist terrestrially.

4.5.2. Structural Controls and Pingo Formational Processes

In contrast to uncertainties regarding the deeper geological structures at Lagoon Pingo, the geophysical data presented here provide insight into the near-surface structure of incipient pingos and the nature of their formation within fine-grained marine muds and clays. In this study, segregation ice provides the most plausible explanation for the topography of the pingo, provided the overall context of the field site, and the characteristics identified within the geophysical data. Whilst previous studies have identified segregation ice within open-system pingo forms (Yoshikawa, 1993; Ross et al., 2007), it has largely been associated with late stages of pingo growth and development (Mackay, 1973; 1985). Our interpretation of segregation ice within the incipient Lagoon Pingo, and the conspicuous absence of a massive

ice core calls for a reconsideration of early open-system pingo formational processes.

In explaining the present-day geomorphology and architecture of Lagoon Pingo, we suggest two primary controls on incipient pingo development: sedimentology and groundwater availability. In regard to sedimentology, fine-grained soils facilitate the formation of segregation ice (Smith, 1985), whereby thin lenses of ice form as water is drawn (via cryosuction) to the freezing plane. As fine-grained sediments feature smaller pores, capillary action tends to be greater, and thus a greater negative pressure is exerted upon liquid water. Coarser-grained, more permeable sediments in contrast are better suited for ground ice formation (Pissart, 2002), perhaps explaining the absence of injection ice emblematic of traditional pingo structures (Ballantyne, 2018).

In terms of groundwater availability, the in-flow of upwelling groundwater provides a localised region of elevated moisture contents that is conducive to enhanced segregation ice formation. At Lagoon Pingo, this may be further aided by differences in the groundwater chemistry between the pingo spring and porewater within the sediment. Existing electrical conductivity measurements on the groundwater spring provide relatively low values of 5 – 8 mS cm^{-1} (Hodson et al., 2019; Hornum et al., 2020), when compared with typical values of ~17 mS cm^{-1} (Cable et al., 2018) for porewaters elsewhere in Adventdalen. Whilst the exact nature of the intrusion of upwelling groundwater through fine-grained marine clays and permafrost is unknown, groundwaters with lower solute content would be more susceptible to freezing, and would offer part of the explanation for why segregation ice formation could be more prominent here compared to elsewhere within the valley. The low hydraulic conductivity of the marine muds and clays within Lagoon Pingo would also contribute by limiting the lateral migration of these upwelling groundwaters, resulting in a locally high moisture contents and lower groundwater resistivity that enhances freezing activity.

Parallels can be drawn between the current geomorphology of Lagoon Pingo and lithalsas in fine-grained alluvial or lacustrine environments (Wolfe et al., 2014). In both cases, segregation ice plays a prominent role as a result of

elevated moisture availability and sediments with poor permeability, thus promoting cryosuction processes. Whilst many contemporary lithalsas occur in close association with surface water bodies that provide the moisture required for cryosuction and frost heave (Wolfe et al., 2014), the existing groundwater upwelling at Lagoon Pingo provides this moisture, enabling increased segregation ice formation relative to the surrounding area in which saline porewater dominates. Additionally, the fine-grained nature of marine clays within Adventdalen bear similarities to sediments within structurally similar lithalsas, including on Holocene plateaus in Northern Quebec (Allard et al., 1996). We therefore propose that Lagoon Pingo, in its present form, represents a hybrid form, with a lithalsa-esque internal structure punctuated by the hydraulically-pressurised spring typical of traditional open-system pingos.

If there is a genetic relationship between incipient Lagoon Pingo and other pingo forms further up-valley (Longyear and Hytte Pingo), it remains unclear how our interpretation of segregation ice in early stage pingo development may evolve into more established open-system pingo forms. Whilst Ross et al. (2007) provide a similar interpretation of low resistivities (< 2 kΩm) as suggesting segregation ice within Longyear and Hytte pingos, it is difficult to conceive how segregation ice could be responsible for ~20 m of elevation heave. Recent drilling elsewhere on Svalbard also casts doubt on segregation ice providing the dominant structure within established open-system pingos. In the coring of marine-based pingos in Grøndalen, Demidov et al. (2019) demonstrate massive ice exceeding 20 m in thickness beneath a pingo of 9 m height. Whilst numerical simulations of palsas and lithalsas analogous to our proposed structure of Lagoon Pingo have demonstrated that segregation ice can produce ~6 m of heave over a period of 150 years (An & Allard, 1995), further coring is necessary to validate the precise architecture of frozen ground within these pingos.

4.5.3. Implications on Spring Emergence and Methane Emission Mechanism

Our interpretation of a segregation ice dominated incipient pingo form may have wider significance on the emission mechanisms of deeply-seated methane within continuous permafrost environments. Whereas injection ice would ordinarily preclude cryopegs or conduits through which fluid flow can occur, segregation ice can persist as discrete ice lenses between unfrozen sediment pockets. Additionally, elevated ice contents and segregated ice lenses within the sediment are likely to influence local pore pressures, and may interact with or otherwise maintain the groundwater spring. However, without discerning the nature of the groundwater upwelling (e.g. whether water in-flow occurs under a diffusive or advective conduit-like regime), it is difficult to establish the exact nature of the influence of such structures. Further research, particularly coring, would be required to provide the necessary insight into the exact nature of pressurised groundwater flow within permafrost.

4.6. Conclusions

Using a combination of active seismic and ERT data, this study interprets the internal structure and characteristics of an incipient open-system pingo. The pingo releases a substantial methane flux to the atmosphere, and its terrestrial genesis was previously attributed to the uplift of a submarine pockmark (Hodson et al., 2019; 2020). Our findings call for an alternative hypothesis given the thick layer of Holocene marine muds and clays (~68 m) which would have been deposited on the active submarine spring, though this cannot be entirely discounted due to the possible role of local coarse alluvial fan sediments in changing hydraulic conductivities of sub-pingo materials.

Our speculation that segregation ice is dominant within an incipient pingo form is at odds with established theories of open-system pingo formation, which presume that initial growth normally occurs through the formation of injection ice following the near-surface freezing of pressurized groundwater. This study highlights sediment grain size as a fundamental control on early pingo formation, with fine-grained sediments such as those in Holocene marine

environments providing high porewater pressures conducive to segregation ice formation. Moisture content provides an additional control, and is sourced by the groundwater spring which further facilitates localized pingo formation. We therefore speculate that the result is a landform with an internal structure analogous to a lithalsa, yet with the mechanism of a typical open-system pingo. However, in absence of definitive evidence of segregation ice beneath Lagoon Pingo, future work, which may include coring and time-lapse resistivity imaging, is required to fully elucidate the subsurface nature of this incipient landform.

Our study highlights the continued uncertainty over pingo genesis and development. Whilst segregation ice has previously been proposed as playing an important role in pingo growth, its presence within an incipient form is ambiguous and indicates further plurality in the genesis of pingo landforms. This structure likely influences local porosities and pressure regimes, and may therefore impact upon groundwater upwelling and subsequent methane release. Despite this, as our geophysical data did not discern the the actual flowpath of groundwater through the sub-zero sediments, there remains a need for further study of subpermafrost and intrapermafrost groundwater migration.

Afterword

Whilst the ERT and seismic data presented within this chapter presents no evidence towards the hypothesis that a pockmark is responsible for the location, formation, and evolution of Lagoon Pingo, self-potential and transient electromagnetic data collected and processed following the publication of this chapter in Earth and Space Science prompted a reconsideration of this theory. Chapters 5, 6 and 7 therefore reconsider the idea of pockmark evolution in the development of Lagoon Pingo, given that the new data is consistent and reasonably explained by this hypothesis.

Chapter 5: Self-Potential Investigations on the Groundwater Dynamics at Lagoon Pingo, Svalbard

5.1. Introduction

The hydrology of permafrost environments is complex, as frozen ground impacts on the movement, storage and exchange of water between the surface and deeper, sub-permafrost aquifers (Walvoord and Kurylyk, 2016). Permafrost has commonly been considered as an impermeable barrier, confining water flow to the seasonally-thawing active layer, beneath the permafrost and in isolated, unfrozen layers or areas known as taliks (Woo, 2012; Lamontagne-Hallé et al., 2018). However, evidence of intrapermafrost flow can be found throughout permafrost environments, through pingos (Ballantyne, 2018), and perennial springs (Andersen et al., 2002). Yet due to the complexity, remoteness, and variability of these environments, an understanding of permafrost hydrology remains limited (Lamontagne-Hallé et al., 2018). The need for this improved understanding of permafrost hydrology has been renewed following the identification of methane emissions emanating from pingo springs on Svalbard (Hodson et al., 2019).

Identifying how the groundwater travels through the localised subsurface will therefore aid a greater understanding of the potential origins of methane that is released to the wider atmosphere, in addition to the local hydrological dynamics. Using self-potential methods, this study therefore investigates the fluid flow network around the central pingo spring at Lagoon Pingo, Svalbard. In doing so, this study intends to fulfil the following objectives: (a) identify the direction from which groundwater enters and approaches the pingo complex, and (b) determine how factors such as weather, tides and icing fracture impact upon the pingo subsurface groundwater dynamics. By doing so, this study will enable an evaluation of the local hydrological system, and the implications that this has on the pingo dynamics and methane release.

5.2. Methods

5.2.1. The Self-Potential Method

Self-potential is a passive geophysical method that measures the natural electrical potential between two points. The measurement of self-potential signals within the near-surface is conducted between two non-polarising electrodes connected to a voltmeter with a high impedance (normally > 100 MΩ) and high sensitivity (at least 0.1 mV; Revil and Jardani, 2013). Natural electrical potentials are associated with the occurrence of electrical currents in the ground, which predominantly occur from two main sources: electrokinetic potential generated by the flow of pore water, and through the gradient of chemical potential within the subsurface porewaters (Revil et al., 2012; Revil and Jardani, 2013).

To understand this, it is important to note how water molecules interact whilst flowing through mineral or soil grains. The interaction of ions present within the flowing porewater around a mineral or soil grain produces an electrical double layer (shown in Figure 5.1). The inner, or Stern layer, consists of counterions electrically absorbed onto the charged mineral or soil grain. The second layer, commonly referred to as the diffuse layer, consists of free ions that are then attracted to the first layer through the processes of electric attraction and thermal motion. There are two consequences of this double layer: firstly, that the porewater is never neutral, and therefore influences the occurrence of electrical currents concerned with the generation of natural potential. Secondly, that the double layer influences the surface conductivity and chargeability within porous materials.

The interaction of flowing water with the excess counterions in the diffuse layer generates electrokinetic (otherwise known as streaming) potentials. In porous media, the relationship between streaming potentials measured between two electrodes (∇V_p) and a hydraulic gradient ($\nabla \Phi$, where Φ is equal to the combined potential from water pressure and elevation) is described by the Helmholtz-Smoluchowski equation (Helmholtz, 1879; von Smoluchowski, 1903; Kulessa et al., 2003a; Zhang et al., 2022). Using the notation of Kulessa

et al. (2003a), by assuming that electrical conductivity is constant across the flow distance at a given point of time:

$$\nabla V_p = -\frac{L}{\sigma}\nabla\Phi$$

(5.1)

where:

$$L = -\frac{c_0 n\varepsilon\zeta}{\mu}$$

(5.2)

The streaming potential coupling coefficient, which is the change in voltage generated per change in fluid pressure driving the flow, is provided by L, whilst c_0 is an empirical correction for flow path tortuosity, n is the porosity of the sediment, ε is the dielectric permittivity, and μ is the dynamic viscosity (Kulessa et al., 2003a). ζ is the zeta-potential (in V), which describes the electrical potential at the shear plane between the surface of the sediment grain, and the water flowing around it (see Figure 5.1). The differences in self-potential measurements caused by electrokinetic potentials are commonly small in magnitude; often no more than tens of millivolts (Bogoslovsky and Ogilvy, 1973; Revil et al., 2002; Darnet et al., 2003; Rizzo et al., 2004).

Electrochemical potentials are generated as a result of differences in the concentrations of electrolytes within the groundwater (Reynolds, 2011). For example, where there is a salinity (NaCl) gradient with equal number of cations and anions, anions (Cl⁻) are more mobile than cations (Na⁺), thus producing a current driven by this difference in mobility (Revil et al., 2012). In many cases however, gradients of electrolytic concentrations are normally balanced over time through diffusion (Reynolds, 2011). Where redox potentials do exist, these are often of a much greater magnitude than those of streaming potentials, and are commonly negative in polarity (Corwin, 1989; Naudet et al., 2003; Naudet et al., 2004; Rizzo et al., 2004; Revil et al., 2010; Doherty et al., 2010; 2015).
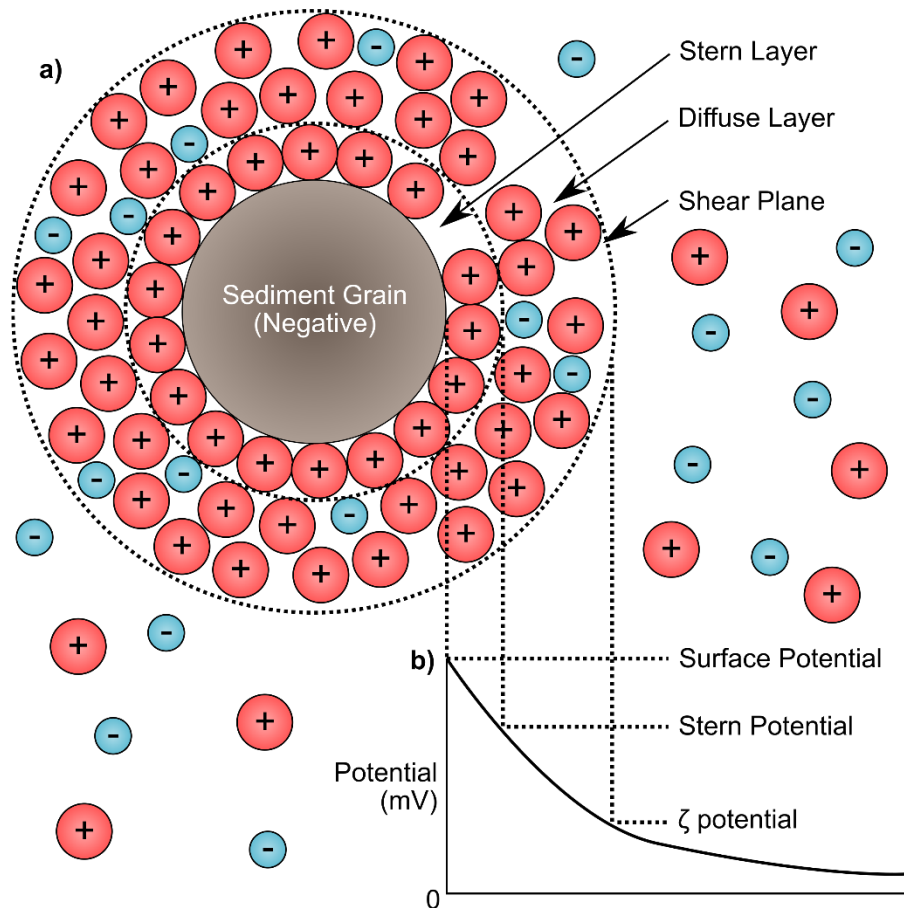
Figure 5.1. (a) Depiction of the electrical double layer around a negatively charged sediment grain with water flow within the porespace, and (b) how this corresponds to potential as a function of distance (adapted from Revil et al., 2012; Jones, 2012).

The interpretation of self-potential measurements made between two electrodes on the surface requires an appreciation of other factors that affect the magnitude and polarity of these measurements. Notably, the amplitude of self-potential measurements decay with source depth (Fournier et al., 1989; Revil et al., 2003; Thompson et al., 2012). As such, the flow of groundwaters at a greater depth from the surface within a confined aquifer would correspond with a lower magnitude self-potential signature, and vice versa. Additionally, changes in surface temperature affect subsurface potentials (e.g. Ernstson and Schrerer, 1980; Perrier and Morat, 2000), as thermal gradients in the subsurface can generate a source current density within porous sediments (Revil et al., 2013).

Within permafrost environments, the application of self-potential methods has been limited. Studies utilising self-potential techniques within permafrost environments are largely focused on discerning groundwater flow. In self-potential measurements on rock glaciers and talus slopes within Alpine permafrost in the southern Swiss Alps, Scapozza et al. (2008) show how self-potential measurements are effective in assessing changes in water content, and delineate groundwater flow pathways. Meanwhile, Thompson et al. (2012) used self-potential to map the flow of lake waters within a glacial lake moraine dam. Lastly, Weigand et al. (2020) demonstrated how a system of spatiotemporal self-potential measurements may contribute to the understanding of hydrological flow processes in Alpine permafrost slopes at risk of failure. As features underpinned by groundwater flow, open-system pingos are therefore logical targets for self-potential methods.
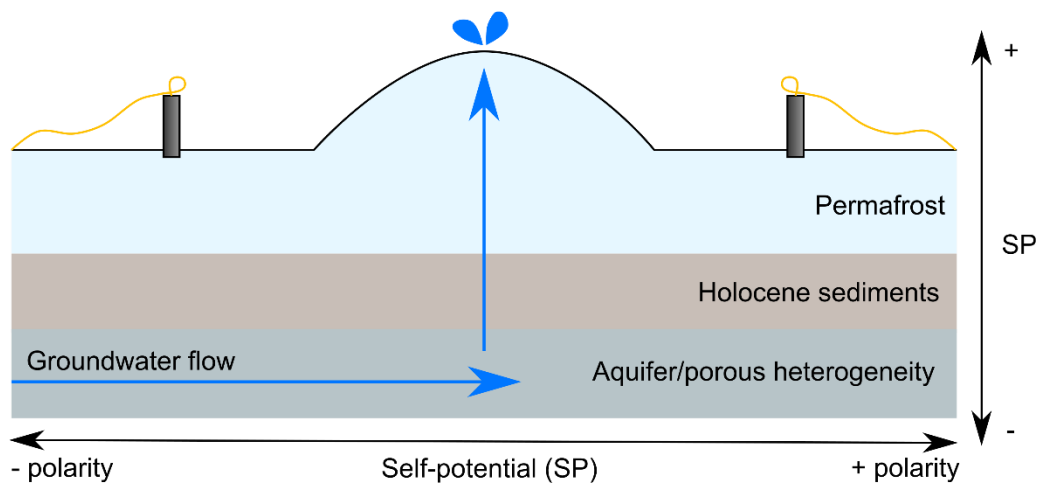
Figure 5.2. A conceptual model of the self-potential expected with the flow of groundwater at depth beneath the open-system pingo, and from the upwelling of groundwater.

In interpreting the self-potential signatures hypothesised for open-system pingos, comparisons can be made with self-potential investigations conducted alongside pumping tests designed to estimate the hydraulic properties of aquifers. In general, positive self-potential anomalies are commonly identified in the direction of preferential flow (Revil et al., 2005; Revil and Jardani, 2013; Kukemilks and Wagner, 2021), wherein the drag of pore water amongst soil and mineral particles results in a polarization of charge, caused by excessive electrical charges within the pore water. Thus, in pumping tests, the

abstraction of water is commonly associated with positive self-potential anomalies on the surface (Semenov, 1980). Assuming an unconfined aquifer, the pumping of water increases the depth to the water table, forming a cone of depression, thus increasing the hydraulic gradient. The increasing flow of groundwater into the borehole therefore forms a positive anomaly (Reynolds, 2011). In contrast, the injection of water at depth corresponds to negative self-potentials, as demonstrated by previous synthetic and laboratory experiments (Minsley, 2007; Vasconcelos et al., 2014). The combination of these factors alongside the knowledge of the impact of amplitude decay with distance from the source provides an overview of self-potential signals expected from an open-system pingo (Figure 5.2).

5.2.2. Data Acquisition and Processing

Self-potential surveys were collected between the 23rd of March and 23rd of April 2021, using six commercially available lead/lead-chloride Petiau electrodes (Petiau, 2000). To monitor the groundwater inflow towards the pingo complex, four Petiau electrodes were placed at a distance of 20 m around the central pingo spring (electrodes 1 – 4; locations shown in Figure 5.3). These were connected to a reference Petiau electrode, which was placed on a pingo-related topographical high in the east of the site. It was determined that this was the most suitable location for this electrode, given the potential for non-pingo related streaming potentials occurring on the alluvial fan slopes to the north of the site, as well as the potential for snowmelt and subsequent run off to cause an undue influence in this electrode should this be placed off the edge of the pingo complex. To monitor and detect noise and other influences on electrical potential measurements, a final Petiau electrode was placed on the opposite side of the reference electrode, with 5 m between them. Locations of these electrodes were obtained by handheld GPS, with time averaging used to ensure planimetric precisions of ±2 m. These Petiau electrodes were connected to a Campbell Logger CR1000X using 18 AWG tinned copper electrical wire, with a high tensile strength and thick outer insulation to limit potential breakages.

Potentials were measured every five seconds in the field continuously, except for small interruptions caused by battery replacements or array maintenance. In some cases, maintenance was conducted on the array whilst measurements were being taken; these were removed following post-processing of the dataset. Additionally, further measurements were removed upon evaluation of the data where extreme changes in magnitude and polarity were identified between consecutive 5 second measurements. For further analysis of overall patterns and trends within the SP data, an hourly moving average was calculated, with each calculation therefore comprised of 720 points.
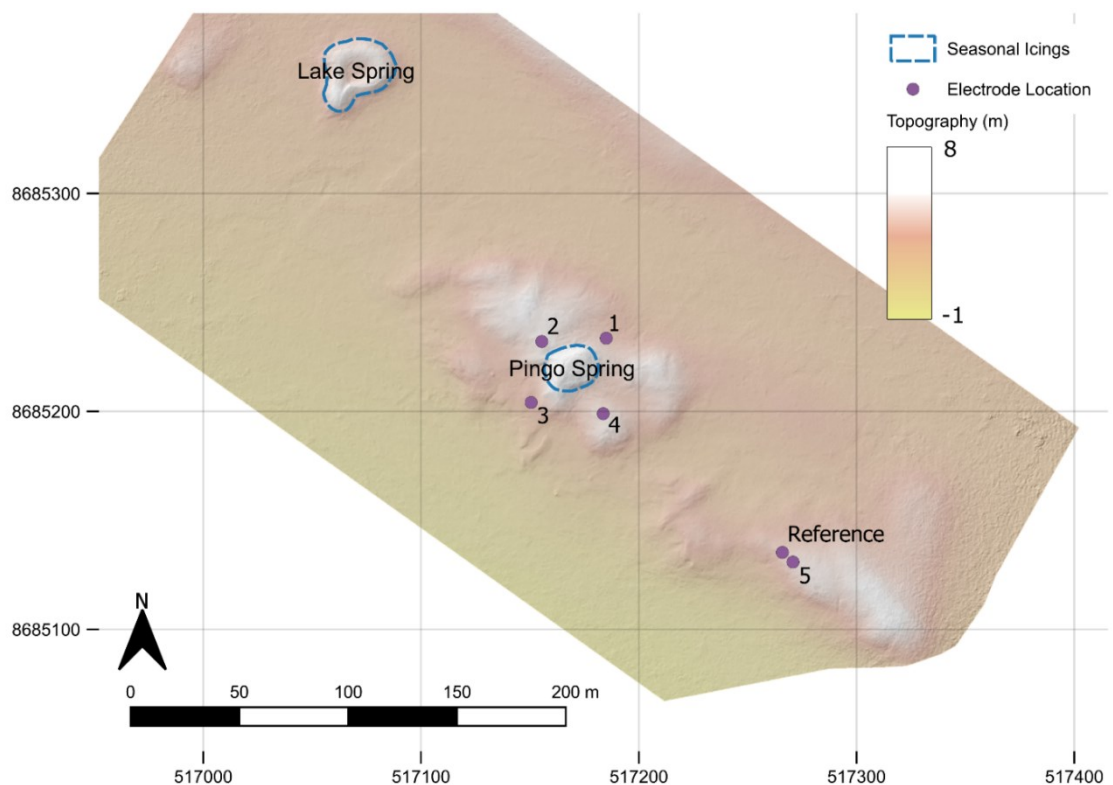
Figure 5.3. Map depicting SP electrode locations in relation to pingo groundwater upwellings. The topography is derived from a DEM produced by Structure-from-Motion (Hann and Dachauer ,2020). Co-ordinates in UTM 33N.

To assess the relative influence of possible sources of electromagnetic noise, publicly available datasets have been used to further analyse the signature received, including weather data obtained from the University Centre in Svalbard (2022), and F-component (the total intensity of the magnetic field

vector) data collected by the Kjell Henriksen Observatory, located approximately 12 km inland from the Lagoon Pingo site (Johnsen, 2021).

Lastly, to discern whether tidal or solar forcings accounted for the change in magnitude within the temporal SP data, a Fast Fourier Transform (FFT) was applied to the record for each electrode. Fourier transforms have previously been applied in other observations of subsurface water flow, such as in glacier drainage (Kulessa et al., 2003b). In the event of a local tidal influence on pingo inflow, Fourier analysis should identify a quasi semi-diurnal change in FFT power spectra. Fourier transforms were applied on the data following processing, using MATLAB version 2020b.

5.3. Results

5.3.1. Data Quality

As shown by Figure 5.4, most electrodes recorded data consistently and continuously between March 24th and April 8th at 18:30, and again between April 10th at 13:00 until the study end date on April 22nd. This primary gap within recordings was due to battery maintenance within this period.

Overall, a small number of measurements were removed, as shown by Table 5.1. For most electrodes, the number of measurements removed was negligible across the study period (< 0.1%), with most of these removals due to maintenance on the array (e.g. during checks on connections to the Petiau electrodes). The exception to this was Electrode 4, whereby a large number of measurements (5.9%) were removed. This corresponds with field observations, whereby checks on the array found that Electrode 4 was disconnected on the 5th of April, following a period of high winds.
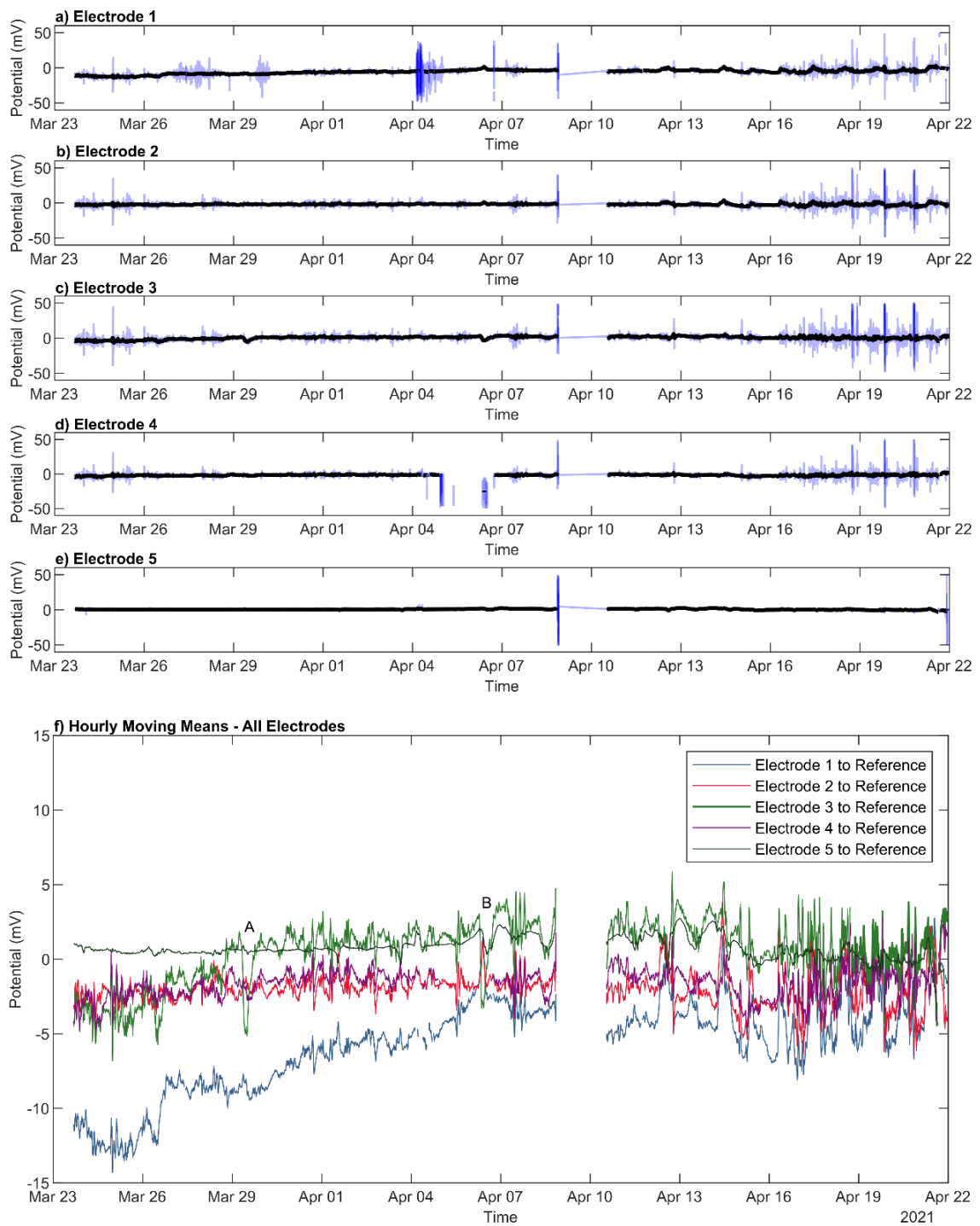
Figure 5.4. Self-potential data following processing. Subplots (a) to (e) show the hourly moving mean compared to the processed measurements which were obtained every 5 seconds. Plot (f) shows these hourly moving means compared to one another. On this plot, A and B mark high magnitude events that are interpreted as related to the hydrofracture of the lid above the central pingo spring.

Table 5.1. Measurements kept and removed following processing.

Electrode	Good Measurements	Measurements Removed	Percentage Measurements Removed
1	477216	395	<0.1%
2	477254	357	<0.1%
3	477170	441	<0.1%
4	449508	28103	5.9%
5	476718	893	<0.1%

5.3.2. Spatiotemporal Pattern

The potential measurements (Figure 5.4) show differences in amplitude within each of the electrodes, although the absolute values are relatively small, ranging between -15 and 10 mV. General statistics following removal of noisy measurements are shown in Table 5.2. The highest magnitudes are consistently received at electrode 1, with average readings of -5.65 ± 3.65 mV, followed by electrode 3, which features a positive average potential. Despite their locations on opposite sides of the pingo spring, electrode 2 and 4 are relatively similar in signal magnitude (-1.93 ± 2.44 mV and -1.91 ± 2.81 mV respectively). Each of the electrodes which were placed around the pingo spring feature relatively high standard deviations when compared with electrode 5 (0.73 ± 1.10 mV).

Temporally, electrode 1 shows a reduction in SP magnitudes during the first half of the study period (Fig 5.4). This is underpinned by a rapid decrease in magnitude on the 26th of March, over the course of six hours during the daytime. Thereafter, SP magnitudes remain largely stable over the next 4 days, before the start of a gradual decline in hourly averages from -9 mV to -2 mV. This change in SP accelerates towards the end of this decline, whereby potentials switch polarity for a short period on April 6th. Following this, the SP signature remains largely between -5 and -2 mV, with occasional but rapid changes on April 12th and April 14th to positive self-potentials. However, after April 16th, substantial variability can be seen in measurements, with some erratic changes in self-potentials received up until the end of the study period.

Table 5.2. Averages and standard deviations for self-potential measurements following processing.

Electrode Number	Average (mV)	Standard Deviation (mV)
1	-5.65	3.65
2	-1.93	2.44
3	0.53	3.34
4	-1.71	2.81
5	0.73	1.10

Electrode 2 and 4 trend similarly to each other, with very low magnitude readings throughout the study period. These electrodes obtain negative polarity measurements throughout the majority of the study period. The exception to this is on April 6th, where, in tandem with electrode 1, hourly averages for electrode 2 increase from -2 mV to about 0.3 mV over the course of 6 hours, before returning to previous levels quickly. This occurred during the period where electrode 4 was disconnected, and thus it is not known if electrode 4 would have reflected a similar pattern. Similar to electrode 1, the period between April 16th and the end of the study period was earmarked by rapid fluctuations in measurements.

Compared to the other electrodes distributed around the central pingo spring, SP measurements obtained at electrode 3 are often reciprocal to the changes shown in the electrode on the opposite side of the pingo spring (electrode 1). Between March 23rd and March 26th, measurements are similar to electrode 2 and 4, with hourly averages largely between -3 and -6 mV. On March 26th, similar changes in SP measurements to electrode 1 are observed, with a relatively rapid drop in magnitude from -2 mV to -6 mV over the course of 6 hours. Thereafter, SP readings slowly increase, reaching 1.8 mV on March 29th, before a second, more substantial rapid drop results in a change from 1.8 mV to -5 mV over the course of 6 hours. The SP reading recovers to previous levels over the next 12 hours, before a sustained period where magnitudes are low (0 to 3 mV) but largely positive. A third rapid drop occurs on April 6th, reciprocating the rapid increase identified at the same time in electrode 1. Within the second half of the study period, further rapid fluctuations in measurements were identified on the 12th and 14th of April, wherein

measurements rapidly increase in magnitude for a very short period. Similar to the other electrodes, after April 16th, measurements obtained from electrode 3 were highly variable compared to the rest of the study period.

In contrast to the four electrodes located around the pingo spring, measurements from electrode 5 are largely consistent and extremely low (0 to 1 mV) for most of the first half of the study period. Fluctuations in measurements occur in tandem with the other electrodes, but they are small (± 1.5 mV) in magnitude in comparison. Within the second half of the study period, measurements remain low but are subject to gradual increases and decreases in magnitude. Similar to the other electrodes, measurements between April 16th and the end of the study period show greater variability, with short term fluctuations in readings.

5.4. Interpretation and Analysis

5.4.1. Magnitude of Measurements

In general, the magnitude of self-potential measurements obtained at Lagoon Pingo are very low, compared to other studies in various permafrost environments (e.g. Thompson et al., 2012; Weigand et al., 2020). This is not unexpected however, as these low magnitudes can be attributed to exceptionally low resistivities within the surface sediments at the site (40 – 150 Ωm; Chapter 4), and the relatively saline groundwater (5 – 7 mS cm^{-1}; Hodson et al., 2020). This inference is demonstrated within the relationship described by the Helmholtz-Smoluchowski equation (equation 5.1), where higher conductivities (the reciprocal of resistivity) results in lower streaming potentials.

The placement of electrode 5, located within 5 m of the main reference electrode, sought to provide confirmation that other self-potential readings corresponds with sub-surface electrokinetic potentials. As shown in Figure 5.4, electrode 5 was characterised by low magnitudes and stability throughout the measurement period. As a result, this demonstrates that the observed measurements represent a tangible signal related to the groundwater

dynamics within the vicinity of the pingo spring, and that measurements are generally of high quality.

5.4.2. Impact of Geomagnetic Activity and Weather

Some variance was identified within measurements, including within the quasi-reference electrode (electrode 5), and thus sources of environmental noise within self-potentials require consideration (e.g. Eppelbaum, 2021). This variance was most prominent within the last 7 days of measurements, where hourly mean averages depict more erratic changes in self-potential amplitude. Prior to a spatiotemporal analysis of the data, two sources of noise are considered here: geomagnetic activity and meteorological forcings.

Figure 5.5 shows how self-potential measurements obtained at Lagoon Pingo compare against data for local geomagnetic intensity. Over the majority of study period, the intensity of geomagnetic intensity within the Earth's magnetosphere is largely low (< 200 nT), with exceptions on the March 26th where a short, temporary increase in intensity (~ 330 nT) was observed. This explains the small drop in amplitude observed within all the electrodes, including Electrode 5 (the quasi-reference electrode). Despite this, other small changes observed within Electrode 5 do not correspond with the other smaller spikes in geomagnetic intensity.

In the last quarter of the study period, fluctuations in geomagnetic intensity correspond with very high variance in self-potential measurements observed within all electrodes. During this period, the intensity of geomagnetic activity routinely exceeds 100 nT, with a number of spikes where the F-component exceeds 350 nT. This corresponds well with the period where hourly mean averages show a high amount of variance and changeability. In comparison to the raw self-potential data taken every 5 seconds against the geomagnetic intensity, spikes in the F-component are collocated with the greatest amplitude potential measurements, highlighting the apparent influence of geomagnetic activity on self-potential measurements more generally.
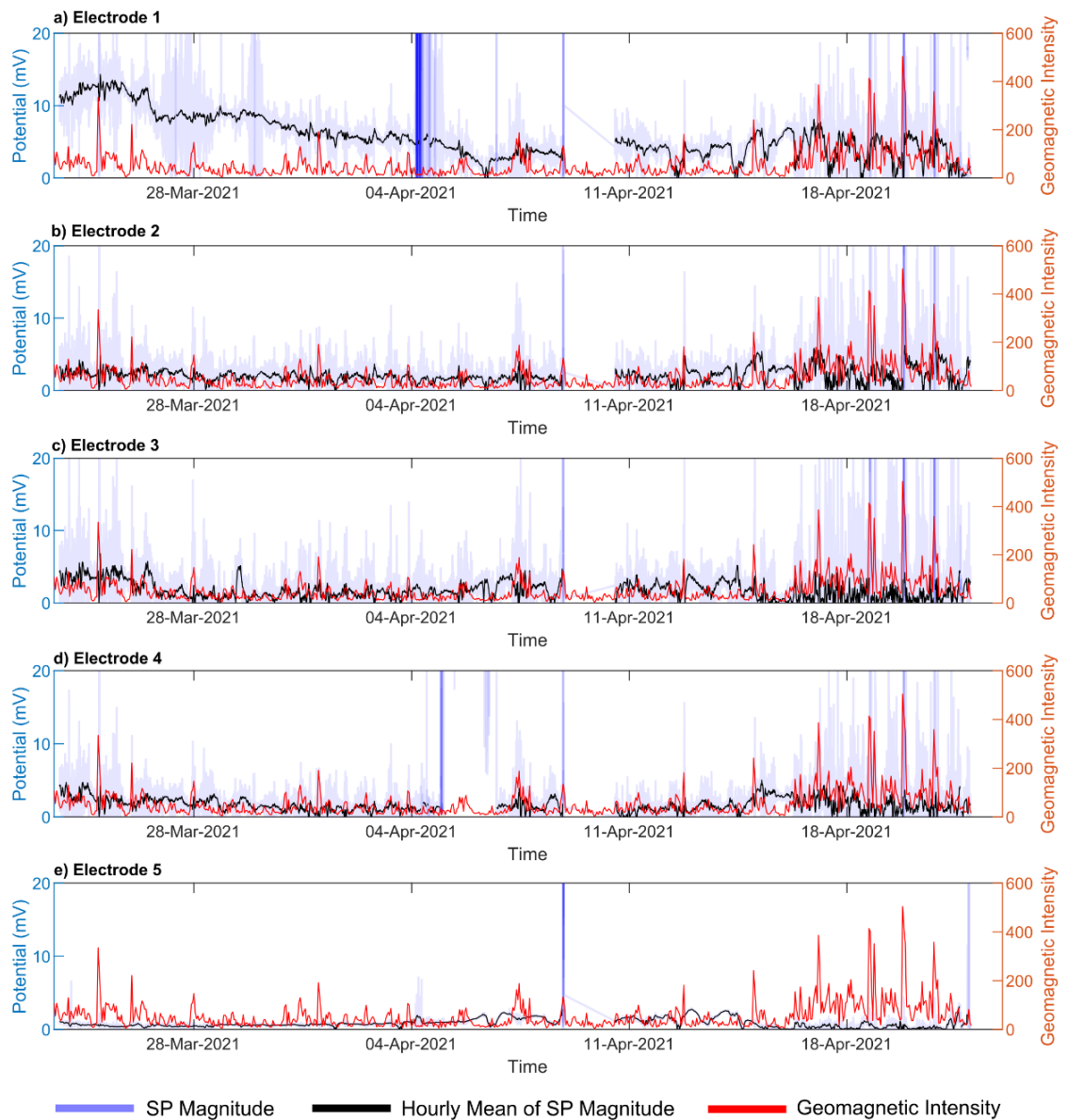
Figure 5.5. Comparison of the magnitude of self-potential measurements against geomagnetic intensity, as measured locally at the Kjell Henriksen Observatory (Johnsen, 2021).

In terms of the effect of local weather conditions, there is evidence of wind impacting on the self-potential measurements (see Figure 5.6). Most notably, the disconnection of electrode 4 on the 5th of April aligns with a period of high wind speeds, with gusts exceeding 28 ms^{-1}. This same period also corresponds well to a period wherein high variability of the processed measurements was observed in electrode 1, with rapid changes in magnitude and polarity identified. The other electrodes situated around the pingo spring

appear less affected by this same event, and this may be due to the positioning; wherein electrode 1 was exposed on the northern flank of the pingo complex, electrode 2 and 3 were likely to have been more protected from strong winds as they were located amongst pingo mounds within the overall elongated complex. These high winds were also established in the potential of electrode 5, resulting in a small increase in magnitude of ~0.8 mV during this period. Similar to this event, an earlier high wind event on the 27th of March also shows a greater impact on electrode 1 compared to other electrodes.

Temperatures fluctuated across the study period, ranging from lows of -18°C to highs above freezing. In particular, there are three periods where temperatures increase above freezing (0 °C), albeit often for a very short period: on the 28th of March for 6 hours, on the 9th of April where temperatures are about freezing for 6 hours, and across the 18th and 19th of April, whereby temperatures reach maximums of 3.7 °C. However, whilst these periods may expect enhanced electrical potential activity due to the melt-out of surface snow and the run-off of meltwaters, the impact within self-potential measurements is limited. In the first of these periods, raw self-potential measurements show slightly more variance than normal, although no impact is established upon the overall hourly mean average. The second period occurred whereby battery maintenance occurred, and thus this was not picked up by the self-potential data. The last, and arguably most significant of these periods occurred close to the end of the study, whereby measurements are marred by an extremely high variance attributed to intense geomagnetic activity at the time. As a result, no clear influence of increase temperatures can be seen here, although it is possible that this contributed in part to the high variance observed here.

Elsewhere, there is some evidence that colder periods impacted upon the quasi-reference electrode (electrode 5), and thus implies that this extreme may impact upon overall measurements within the array. For example, periods of low temperatures between the 13th and 15th of April appear collocated with drops in potential (up to 2 mV) within electrode 5, which could occur in part due to the change in voltage within the electrodes with temperature. As Revil and Jardani (2013) note, the operating range of the SDEC Petiau electrodes

(used within this study) is 0.21 mV ˚C. Whilst change in air temperature does not translate into an instantaneous impact upon ground temperatures, the heat flux between the two may impact enough to affect the voltage of these electrodes, especially considering the small overall magnitude of the measurements obtained. Future self-potential studies should consider this response, by collocating electrodes with temperature sensors (e.g. Weigand et al., 2020).

5.4.3. Spatiotemporal Analysis

Given the presumed lack of any significant lateral electrochemical gradient present around the Lagoon Pingo complex, the relative difference in self-potential measurements between the electrodes are likely associated with streaming currents. Therefore, higher magnitudes are likely to be indicative of groundwater flow activity. With electrode 1 featuring the self-potential measurements of the highest magnitude throughout the study period, the most likely interpretation is that this electrode features the highest groundwater activity of those in this study. With electrodes placed in a circle around the central pingo spring, to identify where groundwaters flow towards this upwelling, it can be argued that the measurements at electrode 1 correspond to the primary groundwater inflow towards and beneath the pingo. This assertion corresponds well with early pingo theory, wherein groundwaters are sourced from up-slope and are expelled under hydraulic pressure at lower altitudes (Holmes et al., 1968; Liestøl, 1977).
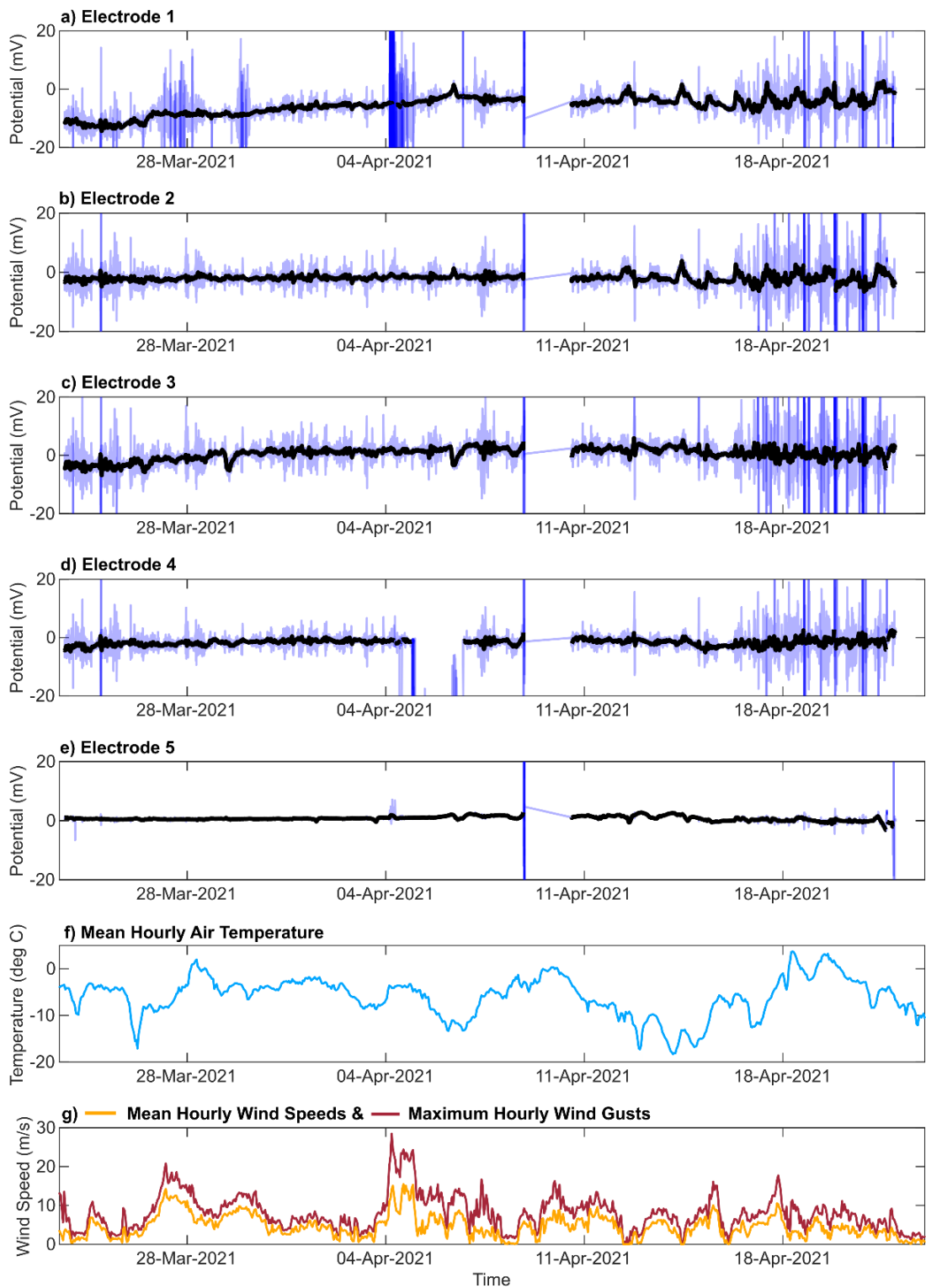
Figure 5.6. Comparison of self-potential measurements with wind speeds and temperatures, as measured locally at the University Centre in Svalbard (2022).

Following the diagram for Figure 5.2, where the expected polarity of measurements is highlighted in respect to the groundwater flow beneath the pingo, electrode 3 should therefore elucidate whether a preferential flow pathway can be asserted here, according to the responses observed within previous laboratory and field studies (e.g. Revil et al., 2005; Revil and Jardani, 2013; Kukemilks and Wagner, 2021). However, whilst largely positive potentials are observed at electrode 3, the average and temporal self-potential measurements are generally similar to electrode 5 (the quasi-reference). There are two possible explanations for the similarities between these electrodes. The first interpretation is that groundwater movement at electrode 3 is minimal, as activity at electrode 5 is also minimal due to its proximity to the reference electrode. This interpretation would assume that all of this groundwater inflow beneath the pingo would be diverted upwards through the spring, which is perhaps unrealistic given that spring discharges are generally low (Orvin, 1944; Hodson et al., 2020). Alternatively, the more likely explanation is that groundwater flow may be deeper beneath electrode 3, and thus sensitivity to the potential source is lost.

Short, temporary changes in the magnitude of measurements recorded at electrodes 1 and 3 provide evidence towards the latter of these interpretations, and indicate a link in groundwater dynamics between these electrodes. As depicted on Figure 5.4 by A and B, infrequent events which results in the rapid drop in potentials in Electrode 3 in tandem with increases in Electrode 1, despite often limited changes in the measurement of Electrode 2 and 4, implying that there is a groundwater pathway between these electrodes, and that this is impacted by low-frequency yet relatively high-magnitude events.

The timing of these rapid, short-term events correspond well with visual observations made at Lagoon Pingo during maintenance of the array, where freshly frozen ice was observed around the central pingo spring. These observations are demonstrated in Figure 5.7, wherein surface flow of water which quickly froze can be seen. Thus, one explanation of these events is that they relate to hydrofracture of the seasonal ice lid present across the spring at Lagoon Pingo (e.g. Hodson et al., 2019), as this heaves following continued groundwater outflow. As the schematic in Figure 5.8 demonstrates, lid fracture

results in the overspill of water from the pond within which the central pingo spring emerges. In turn, this unfrozen water may flow away from the ice lid, and within the vicinity of other electrodes, before quickly freezing. For example, this may explain the sudden changes in measurements observed at Electrode 3, and explains why these span a limited time period.

Thus, the question remains over the decline in magnitude of self-potentials in Electrode 1, and why following these rapid events, the potentials here never fully recover in amplitude. Whilst the rate of groundwater flow through this section could possibly encourage higher potential magnitudes, evidence for periods of enhanced fluid flow out of the central pingo spring is limited in current observations (Hodson et al., 2019). Conversely, as the magnitude of self-potential measurements decay with depth (Thompson et al., 2012), one interpretation is that these ice lid fracture and subsequent overspill events invoke a deeper groundwater inflow into the pingo.
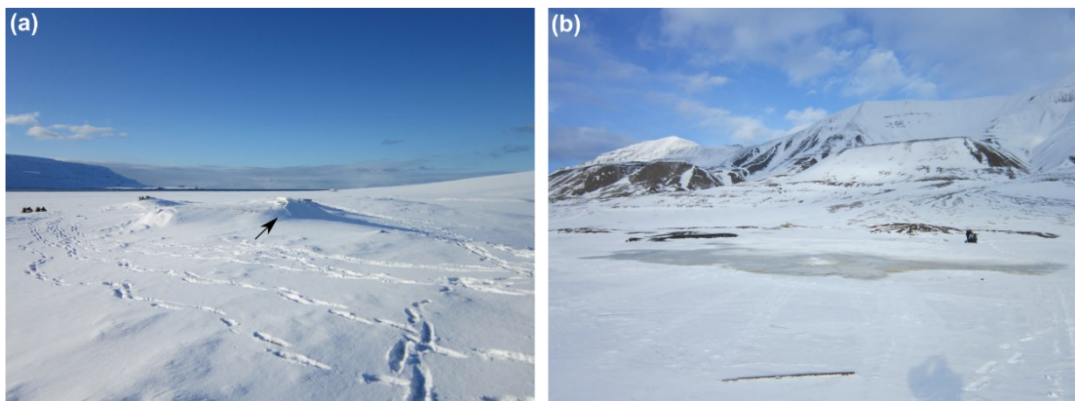
Figure 5.7. Photos showing evidence of ice fracture and overspill of groundwaters from the pingo spring. Image (a) shows evidence of a fresh fracture forming on the surface of the pingo icing (as marked by the arrow), taken on the evening of March 28th, directly preceding a perceived fracture event shown on self-potential measurements. Image (b) shows evidence of fresh fluid flow on the surface on the evening of March 26th, following a fracture event as identified on self-potential measurements.

However, this theory of deepening groundwater flow beneath electrode 1, as well as the existence of a clear groundwater flow pathway is complicated by pre-existing knowledge of poorly permeable sediments beneath Lagoon Pingo. As Chapter 4 demonstrated through seismic reflection aimed at determining homogenous media beneath the pingo, Lagoon Pingo is underlain by ~68 m

of Holocene marine muds and clays, characterised by poor permeability. Notably however, it remains uncertain whether there are any local heterogeneities that may enable groundwater flow beneath the site. Thus, following the groundwater inflow into the Lagoon Pingo complex seemingly emanating from the north-east wherein a large alluvial fan is present, one potential explanation could be that groundwater flow is largely focused within a coarser-grained sedimentary unit composed of alluvial fan deposits beneath the pingo. The presence of coarser blocks and clasts, similar to those observed within neighbouring alluvial fans (Lønne and Nemec, 2004), would provide hydraulic conductivity that would promote localised groundwater flow. This also fits with the ideas presented in Humlum et al. (2003), where it is noted that pingos are commonly located close to the base of alluvial fans. With the potential to be encompassed by poorly permeable sediments, in addition to permafrost on top, a layer containing alluvial fan deposits may be considered as a confined aquifer.

When assuming a layer containing coarser-grained deposits exists, the theory of deeper groundwater flow following ice lid fracture and overspill becomes more probable. Where the ice lid remains intact, or otherwise leakproof, and the pond where the pingo spring reaches the surface is full, the saturation level of the layer of coarser-grained alluvial fan sediments increases. In turn, this increases the pressure beneath the pingo, increasing the poteniometric head, and resulting in greater electrokinetic potential generated closer to the surface as it is continually recharged by groundwaters flowing from upslope. This charging of the coarser-grained unit would continue until the pressure within the confined aquifer is greater than the strength of the pingo icing. This causes the hydrofracture of this ice lid, leading to an outburst of pressurised water and the overspill of the pond. As pressures subside, groundwaters within the fracture freeze once again, forming a new ice lid, and repeating this process.
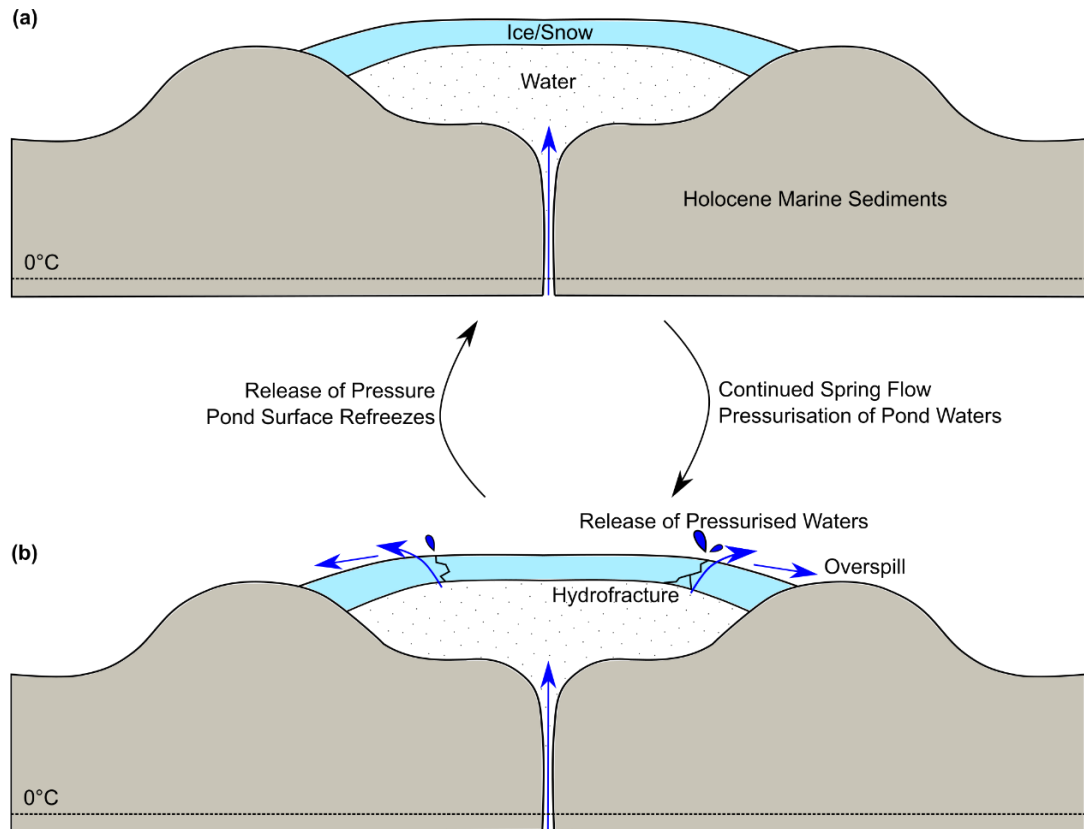
Figure 5.8. Schematic demonstrating the winter configuration of Lagoon Pingo (adapted from Hodson et al., 2019). (a) demonstrates the standard winter configuration, where continued spring flow builds beneath a solid ice lid. (b) Once the force exerted by pressurised waters exceed that of the strength of the ice lid, the icing fractures, and pressurised waters are released and spill out across the pingo complex (labelled event A and B on Figure 5.4f).

Against the observed response from electrode 1 and under this theorised model, the start of the study period suggests highly pressurised groundwater beneath the site, with groundwater flow at the top of this aquifer corresponding to higher magnitude potential readings. Once this pressure was released following the supposed fracture event of March 26th, electrokinetic potential at the top of this confined aquifer dropped, and remained stable under continued recharge. A weakened or freshly ice lid is likely to be at more risk of further fracture, and thus continued fracture events on March 29th and April 6th promptly reduce the pressurisation of this confined aquifer system. However, the assumption of a hydraulically conductive medium, presumed to be from the alluvial fan based on the evidence of self-potential here, should be considered. As there is no further evidence for a layer of alluvial fan sediments,

identifying the exact nature and characteristics of these deposits provides a suitable hypothesis and target for further geophysical investigation.

Within electrode 2 and 4, the largely similar and consistently low self-potentials observed likely reflect a comparatively low amount of groundwater flow. With these electrodes aligned with the long axis of the general pingo topography, these values may indicate groundwater flow within the poorly permeable Holocene marine muds and clays at the base of the relatively shallow permafrost. This would align with Chapter 4, wherein some movement of groundwaters is to be expected considering the cryosuction processes that are required in the formation of segregation ice, which is attributed as the primary cause of topographical elevation of the pingo. However, it should be noted that any groundwater migration within poorly permeable sediments is expected to be limited.

5.4.4. Fourier Transform

Fourier transforms of the obtained self-potential data intend to identify the role of cyclical events on the groundwater dynamics at Lagoon Pingo. These events include those from local tides, which may provide a forcing on the substrate underlying the pingo. This follows investigations that have previously determined a tidal influence on subsurface groundwater dynamics on glaciers (e.g. Kulessa et al., 2003b).

Analysis of the power spectra (Fig. 5.9) following a fast Fourier transform on the raw self-potential data indicates that measurements are dominated by a high-frequency component, and otherwise do not evidence of any other repetitive events. Indeed, no spikes in power spectra are identified in any of the electrodes. Whilst it was hypothesised that the coastal location of the pingo may have prompted a tidal forcing of the self-potential signature, the absence of a semi-diurnal increase in power spectra provides no evidence towards this, or indeed any other cyclical forcings.
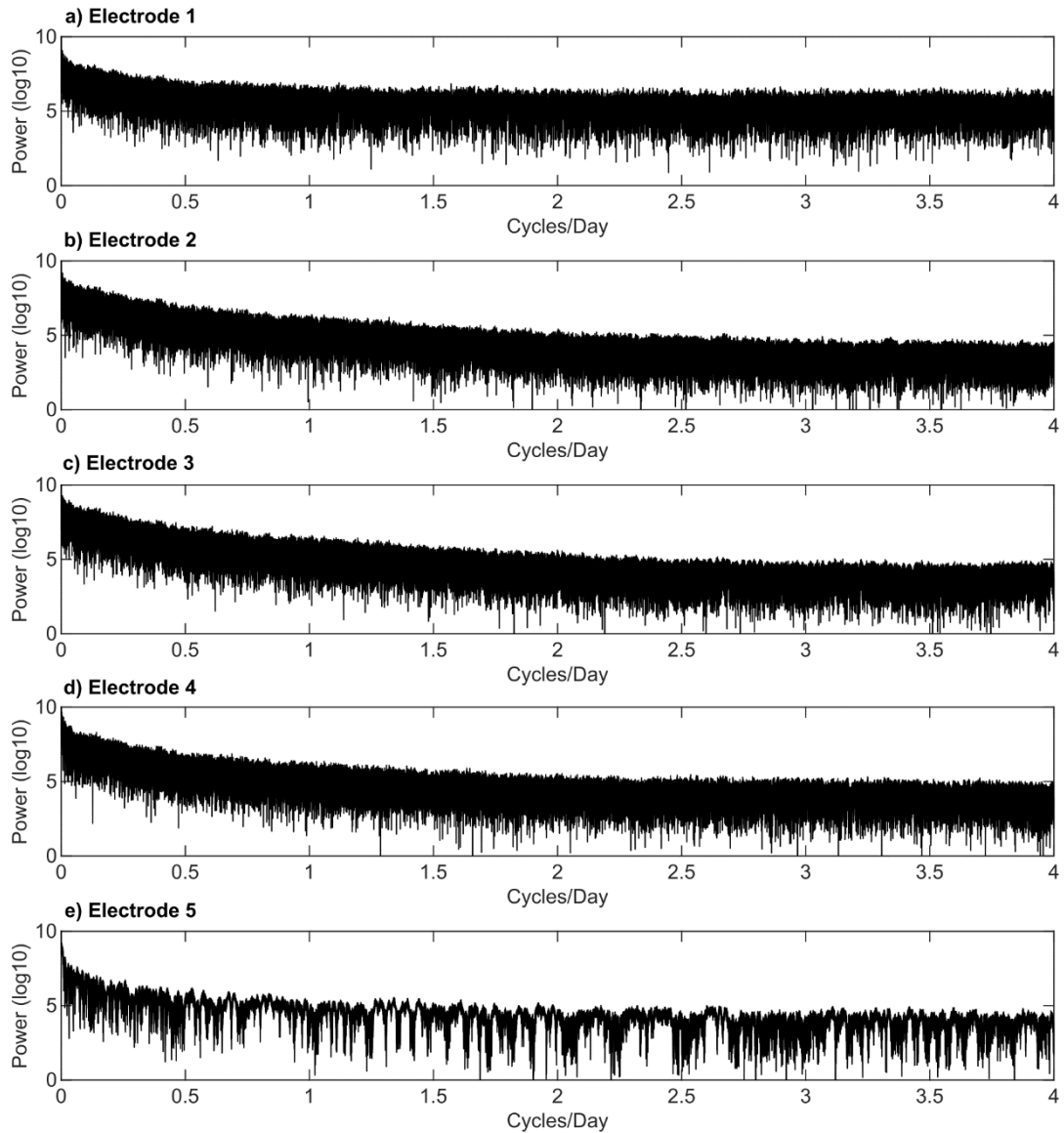
Figure 5.9. Fourier power spectra for self-potential measurements over the study period.

5.5. Discussion

In this chapter, an array of self-potential electrodes is used to establish the spatiotemporal pattern of groundwater flow around Lagoon Pingo, to identify the groundwater inflow around the pingo, assess the nature of local groundwater migration and determine factors that may influence spring flow and the associated methane release. Through differences within the magnitude, polarity and temporal variability of the self-potential signatures in relation to previous analogous studies, I interpret a primary groundwater flow

pathway that corresponds to a local alluvial fan, and points towards different possible methane sources.

The interpretation of dominant groundwater flow pathways derived from the north, which corresponds with the existence of an alluvial fan in this direction, suggests that alluvial fans may provide a fundamental role in enabling the groundwater flow associated with pingo flow. At Lagoon Pingo, it is postulated that this alluvial fan provides an layer of coarser-grained sediments beneath the pingo, that subsequently provides a hydraulically conductive media within the otherwise poorly permeable Holocene marine muds and clays. This suggests that the pingo represents a confined aquifer system. Indeed, recent assessments of pingo distribution on Svalbard indicate that a large number of pingos (47 out of 136) are located on the distal parts of alluvial or proluvial fans (Demidov et al., 2022), suggesting a geomorphological link between these landforms on Svalbard. This link was discussed by Humlum et al. (2003), wherein it was presumed that alluvial fans provided a preferential groundwater flow pathway, and that groundwaters were forced towards the surface where these alluvial fans thinned. In spite of this, evidence depicting the alluvial fan at depth both here and elsewhere within Svalbard pingos is limited. Future studies should therefore consider the extent to which alluvial fans enable spring flow and pingo formation within similar environments, and should evaluate the extent to which alluvial fans and pingos interact with one another.

At Lagoon Pingo, the identification of this flow pathway contradicts previous theories regarding the source of this groundwater, with implications for the migration of local methane. In Hornum et al. (2020), the unexpected freshening of pingo spring waters closer to the coast compared to those further inland is attributed to a palaeo-subglacial meltwater wedge that predates the Holocene and thins inland. Within this theory, groundwaters are presumably derived from those beneath the valley, and that lower salt content observed at Lagoon Pingo compared to those up-valley correspond with the mixing of local and palaeo-subglacial meltwaters. These are then forced towards the surface, driven by a mechanism underpinned by millennial-scale basal permafrost aggradation (Hornum et al., 2020). Whilst elements of pressurisation stemming from localised permafrost aggradation may hold true, the interpretation of this

dominant flow pathway through alluvial fan deposits instead points towards Lagoon Pingo as a separate system, with a different groundwater source derived from upland areas directly to the north. This idea is backed up with recent unpublished geochemical data, whereby Lagoon Pingo is shown to feature a high amount of phosphates relative to the other pingos within Adventdalen (Hodson, pers. communication). This enhanced phosphate content may be explained by the presence of phosphatic nodules within the Agardhfjellet formation, which is located with the mountains to the north of Lagoon Pingo. On the migration of methane, an upland source of methane cannot be discounted. As upland areas around Adventdalen are almost certain to contain gas hydrates given current comprehensive modelling of local gas hydrate stability conditions (Betlem et al., 2019), the contribution of gas hydrate dissociation to methane emissions from the pingo therefore requires consideration.

5.6. Conclusion

This chapter utilises self-potential measurements to ascertain spatiotemporal groundwater flow patterns at Lagoon Pingo, providing new insights into the local hydrological system. This is significant considering the contribution to local methane emissions through this open-system pingo, and how these greenhouse gas emissions are closely tied with the flow, recharge, and surface emergence of local groundwaters. Spatially, self-potential measurements indicate that groundwater inflow into the pingo system comes from the northeast, corresponding with a local alluvial fan and providing evidence alongside previous theories of pingo formation where hillslope alluvial deposits reach the valley floor (Humlum et al., 2003). Temporally, relatively high magnitude changes in self-potentials correspond with visual observations of fractures within the surface icing that covers pingo spring during the winter, therefore distinguishing the importance of these fracture events within the winter hydrological regime of the pingo. The identification of this groundwater flow pathway, alongside the impact that hydrofracture events have on the pingo lid may have implications on the local methane release dynamics. The

identification of groundwater inflow from upland slopes in the north implies that methane sourced from these mountain slopes should not be discounted, including those caused by the dissociation of gas hydrates acknowledge to persist deep within the mountain slopes within Adventdalen (Betlem et al., 2019). In terms of the hydrofracture of the ice lid, this has implications on the ventilation of anoxic groundwaters, and could correspond with direct methane release events (Hodson et al., 2019). Future studies may therefore wish to consider longer term self-potential monitoring of the pingo with higher spatial resolution, towards obtaining a full appreciation of the interplay between subsurface hydrological changes and surface icing fracture, in determining how these factors enable and promote the release of emissions. With alluvial fan sediments speculated to provide a hydraulically conductive medium beneath the pingo, identification of whether there is indeed a heterogeneity through these poorly permeable muds (clays and silts) should also form a research priority, especially when considering how Svalbard pingos are commonly collocated with alluvial fans (e.g. Demidov et al., 2022).

Chapter 6: Transient Electromagnetic Investigations of Alluvial Fan – Pingo Interactions Beneath Lagoon Pingo

6.1. Introduction

Whilst a recent appreciation for their potential role as a conduit enabling methane release through continuous permafrost (Hodson et al., 2019; 2020) has been obtained, our understanding of the mechanisms, processes and factors that affect open-system pingo formation and distribution is poor. Ballantyne (2018) outlines two core unanswered questions surrounding open-system pingo distribution: (i) how do the groundwaters required for open-system pingo formation recharge through continuous permafrost, and (ii) how does groundwater penetrate through the permafrost to form surface springs without freezing?

In attempting to address these problems, Yoshikawa and Harada (1995) categorised the distribution of open-system pingos into three groupings. Firstly, they argue that some pingos occur where groundwaters exploit pre-existing geological faults and fractures. There are many examples of pingos located on geological boundaries and faults (e.g. Yoshikawa et al., 1996; Worsley and Gurney, 1996; Hornum et al., 2021), but not all areas containing hydraulic pingos host faults or fractures (Ballantyne, 2018). Secondly, Yoshikawa and Harada (1995) argue that some open-system pingos occur in areas of artesian flow where groundwaters percolate beneath temperate glaciers. This idea was first established by Liestøl (1977) in explaining groundwater recharge in pingos on Svalbard, and has since been supported by further research and modelling (e.g. Haldorsen et al., 2010; Scheidegger et al., 2012). Lastly, Yoshikawa and Harada (1995) outline that some open-system pingos occur in nearshore or low-lying environments which undergo glacio-isostatic uplift. It is argued that permafrost within these environments is thin, and that groundwaters are therefore able to penetrate into the near-surface to form a pingo more easily. It is within this category that Lagoon Pingo fits best, as an open-system pingo close to the contemporary shoreline in an environment defined by glacio-isostatic uplift. Yet, these environments are

often comprised of fine-grained sediments that are at odds with the hydrological factors that are required within open-system pingos. These sediments are commonly poorly permeable, and it is therefore difficult to envisage how they permit the rapid injection of groundwaters, and subsequent discharge on the surface observed at some pingos. Other structures and mechanisms are thus required to facilitate the surface emergence of pingo springs.

In Chapter 5, the identification of elevated self-potential magnitudes close to the alluvial fan, within a low-lying environment underlying glacio-isostatic uplift prompts a reassessment of the idea that groundwaters flow within alluvial fan deposits beneath pingos (e.g. Humlum et al., 2003). At Lagoon Pingo, seismic investigations (Chapter 4) determined a ~68 m layer beneath the pingo, which was interpreted as Holocene marine muds and clays. As such, it is difficult to conceive how a perennial spring persists at Lagoon Pingo, without some form of local heterogeneity to enable fluid flow. Amid the possibility of coarser-grained alluvial fan deposits beneath the open-system pingo, the idea of pingo evolution from submarine pockmarks would also need to be reconsidered (Hodson et al., 2019). Whilst this theory was initially dismissed on account of the thick Holocene marine mud and clay assemblage (Chapter 4), it is noted that a layer of permeable alluvial fan deposits capped by poorly-permeable Holocene marine muds and clays would provide favourable circumstances for pockmark formation, with the alluvial fan forming a previous potential store of natural gas. Submarine pockmarks are known to occur within Adventfjorden, and are commonly located in areas where thin Holocene muds overlie gas-bearing aquifers (Forwick et al., 2009).

In this chapter, I test the hypothesis that a coarse-grained sedimentary unit beneath an active open-system pingo that has enabled the formation of Lagoon Pingo. This is achieved non-intrusively, through the collection and analysis of transient electromagnetic data on Lagoon Pingo. Using the MuLTI-TEM Bayesian inversion algorithm to provide greater uncertainty analyses compared to conventional methods, the acquired TEM data is combined with pre-existing seismic data (Chapter 4) into a system of established geophysical relationships to estimate the comparative rock, ice, air and water fraction of

the subsurface. These findings are used to explain the location and development of Lagoon Pingo, evaluate the interplay between open-system pingos and alluvial fans, and outline how the present day subsurface structure presents evidence towards the survival and terrestrial emergence of a submarine pockmark through Holocene marine sedimentation.

6.2. Methods

6.2.1. Transient Electromagnetics

Transient electromagnetics (TEM) is a method that enables the measurement of electrical resistivity with depth, through manipulation of an electromagnetic field on or above the Earth's surface. In a TEM survey, a static electromagnetic field is first generated by sending a current through a transmitter coil. This current is then abruptly switched off, inducing eddy currents in subsurface conductors that propagate from the vicinity of the transmitter coil into the subsurface. These eddy currents generate a secondary electromagnetic field, that induce a current within a receiver coil. The decaying amplitude of the secondary field is measured with time in gates through the response of the receiver coil. These responses are a function of time, with later gates therefore providing amplitudes from greater depths. As a more conductive subsurface generates larger eddy currents, a greater secondary electromagnetic field will be measured within the receiver coil and thus a slower transient decay can be implied. This process is then repeated with alternating polarity, with a modified square wave current sent through the transmission coil (as demonstrated in Figure 6.1). Repeated measurements enable the stacking of individual response curves, to provide a single response curve that enables electrical resistivity to be constrained with depth. Electrical resistivity measurements can then be used to interpret differences within the lithology, salinity and hydrogeology, amongst other characteristics.

Here, TEM measurements were acquired using a Geonics PROTEM system, which consists of the PROTEM 58 three-channel digital time-domain receiver, a PROTEM 47 battery powered transmitter and a 3-D multi-turn receiver coil.

In this study, a 100 m x 100 m transmitter coil was used to provide maximum depth penetration, with the receiver coil placed within the center of this loop. To establish the optimal gain settings and identify the level of background noise, initial measurements were made with no current through the transmitter coil. Subsequent parameters used during the collection of 1-D measurements are highlighted within Table 6.1.

Table 6.1. Parameters used in the acquisition of TEM data.

Parameter	Value
Number of Gates	30
Integration	30
Receiver Delay Time	0
On Time Measurement	0
Calibration Time Constant	0.1 sec
Transmitter Current	2.0A
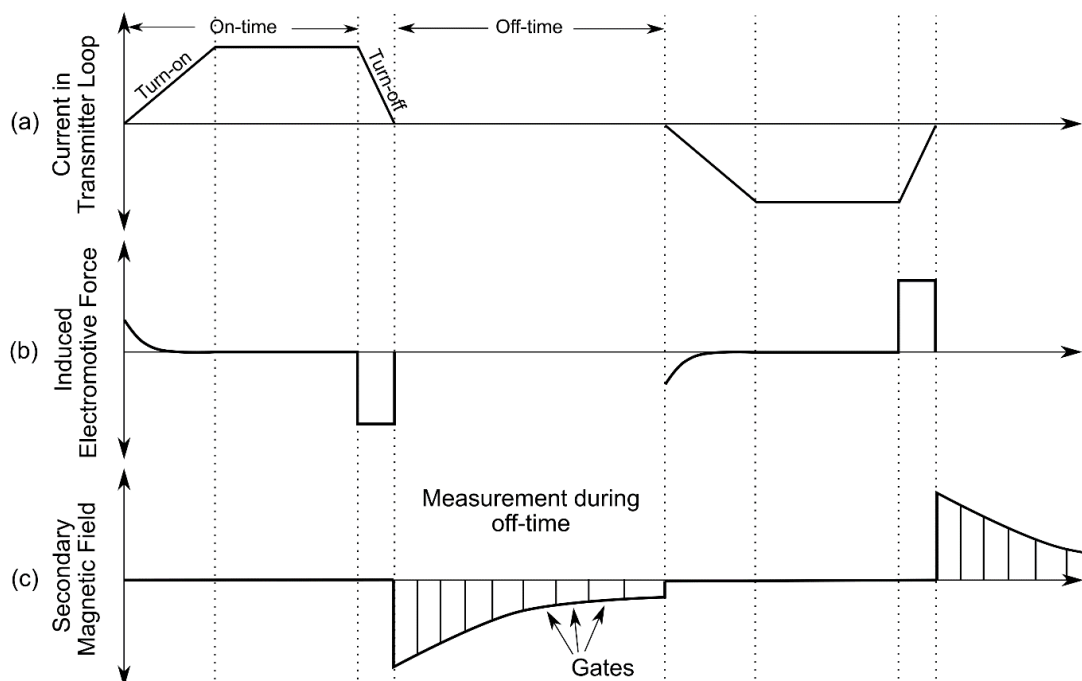
Figure 6.1. Principles of the TEM method (adapted from Sørensen et al., 2006). Assuming that the receiver coil is centered within the transmitter coil, (a) shows the modified square wave current that runs through the transmitter loop, (b) depicts the induced electromotive force within the subsurface and (c)

shows the relative secondary magnetic field that is subsequently measured within the receiver coil.

A series of 1-D measurements were obtained between April and May 2020, whilst the ground was still frozen. Measurements were made along two profiles as shown in Figure 6.2; a long profile, collocated with ERT measurements that were collected a year prior (see Chapter 4), and a second transect perpendicular to the first that provides measurements across the pingo from the alluvial fan towards the present-day coastline. In each profile, measurements over the pingo were taken every 50 m, extending to 100 m between measurements off the south-eastern end of the pingo. A total of 13 measurements were consequently made on the long profile, and 6 on the shorter transect, with both lines using the same measurement at the intersecting point, which is located directly above the central pingo spring. To provide the topography in plotting the finalized results, coordinates of receiver locations were obtained using the average coordinate over a 5-minute period using a Garmin eTrex handheld GPS, providing a planimetric position of ~2 m. These coordinates were then plotted using the combination of two DEMs; for receiver positions on the pingo which may change seasonally, receiver positions were obtained from a DEM derived from Structure-from-Motion photogrammetry during the acquisition of TEM data (Hann & Dachauer, 2020). This DEM was orthorectified using a regional DEM providing the topography of the area around the pingo at a horizontal resolution of ~5 m (Norwegian Polar Institute, 2014), which was used where the Structure-from-Motion DEM did not provide coverage.
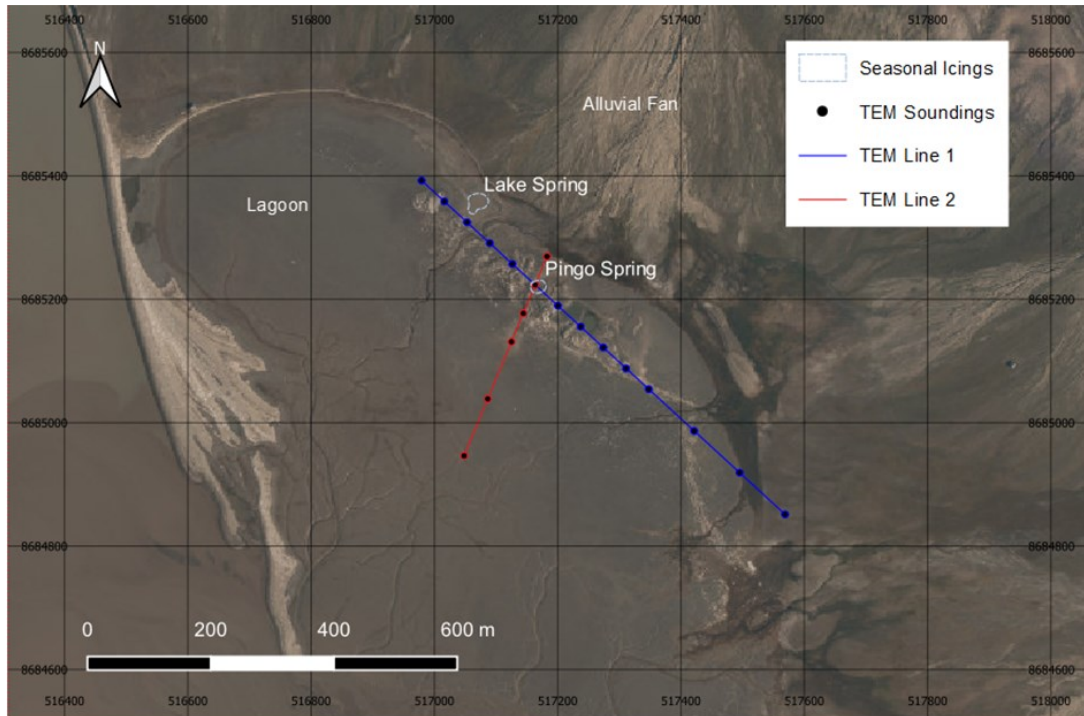
Figure 6.2. TEM sounding locations across Lagoon Pingo (Orthophoto: Norwegian Polar Institute, 2021). Co-ordinates are in UTM 33N.

6.2.2. Data Inversion

The inversion of the TEM data was conducted by using the MuLTI-TEM MATLAB inversion code (Killingbeck et al., 2020); a Bayesian inversion that determines the posterior distribution of resistivity as a function of depth. In summary, MuLTI-TEM uses the data input, along with a priori knowledge such as data constraints where applicable, to numerically approximate the posterior distribution by creating an ensemble of models. This ensemble is sampled using the Markov Chain Monte Carlo (MCMC) method, whereby each model within the chain is based on the previous, but with a random perturbation through a user-defined magnitude, and where models that have a greater posterior likelihood sampled more often than those that do not. The 1-D variation of resistivity with depth is determined using Voronoi nuclei, where the resistivity is determined by the nearest nuclei in the model. With a growing number of samples within the model ensemble, the numerically obtained posterior distribution becomes more likely to converge to the true posterior.

107

The data inputs into MuLTI-TEM consist of the voltage, which here is determined as a mean average recording of a stack window within each separate time-gate, and uncertainty defined as the variance of between each of the recordings used to comprise a stack window at each time gate. In some instances, it was noted that uncertainties for measurements in the early time-gates were low or zero, even though the overall mean response curve did not fit the expected exponential curve typical of raw transient electromagnetic readings. Thus, to compensate for potential noise within these measurements, a 7.5% minimum uncertainty of the overall mean voltage was stipulated for each time-gate (c.f. Killingbeck et al., 2020).

The other parameters used within the inversion of TEM data are shown in Table 6.2. The parameterization of the quantities of Voronoi nuclei, along with the selected magnitude of the model perturbations follow previous investigations using MuLTI-TEM in the inversion of TEM data in glacial environments (e.g. Killingbeck et al., 2020). Meanwhile, the depth of investigation is limited to 80 m as the uppermost unit in seismic investigations (~68 m; Chapter 4) represents the target of this study.

6.2.3. Four-Phase Modelling

To extend the interpretation of subsurface features present at Lagoon Pingo, electrical resistivity measurements obtained through the TEM were combined with seismic data (Chapter 4) gathered across the site within a series of multi-phase models. The four-phase model (4PM) approach was developed by Hauck et al. (2011) to improve interpretations for ground ice within and around rock glaciers in the European Alps. Since then, several iterations of this model have been applied within a range of permafrost environments (e.g. Pellet et al., 2016; Mollaret et al., 2020). In this investigation, the focus of the phase modelling is to delineate the hydrogeological properties of media beneath the pingo which enable groundwater to flow.

Table 6.2. Inversion parameters used in MuLTI-TEM inversion.

Inversion Parameter	Value
Weighting (data variance)	Difference between stacked measurements (minimum 7.5%)
Minimum number of floating Voronoi nuclei	0
Maximum number of floating Voronoi nuclei	80
Maximum depth	80 m
Burn-in number (number of iterations discounted at the start of the MCMC chain to counteract dependency to the initial conditions)	10 000
Total number of iterations of the inversion (incl. burn-in)	500 000
Number of MCMC Chains	1
Sigma Resistivity Change (log R; defines the magnitude of resistivity change perturbations)	2
Sigma move (meters; determines the possible magnitude of nucleus movement)	20
Sigma birth (log R; determines the birth or removal of new nuclei)	2

Fundamentally, the 4PM approach involves the assumption that the combined sum of the rock, ice, air and water fraction of any given subsurface section should equal 1:

$$f_r + f_w + f_i + f_a = 1 \text{ where } 0 \leq f_r, f_w, f_i, f_a \leq 1$$

(6.1)

where f_r, f_w, f_i and f_a are the fractions of rock, water, ice and air.

This can be combined with two further established geophysical relationships to provide a system of overall equations that relate these fractional contents to the resistivity and seismic velocity of the subsurface. Relating subsurface

resistivity (ρ) to the porosity (ϕ), saturation (S_w) and the resistivity of porewaters (ρ_w), Archie's empirical second law (Archie, 1951) stipulates that:

$$\rho = \rho_w (\phi)^{-m} \left(\frac{S_w}{\phi} \right)^{-n}$$

(6.2)

where m and n are parameters denoting the cementation exponent and saturation component respectively. Porosity and saturation are assumed to be directly related to the fractional rock content and can therefore be expressed as follows:

$$\phi = 1 - f_r = f_w + f_i + f_a$$

(6.3)

$$S_w = \frac{f_w}{\phi} = \frac{f_w}{1 - f_r}$$

(6.4)

Seismic constraints are introduced through an extended version of Timur's time-averaged slowness equation (Timur, 1968):

$$\frac{1}{v} = \frac{f_w}{v_w} + \frac{f_r}{v_r} + \frac{f_i}{v_i} + \frac{f_a}{v_a}$$

(6.5)

where v_w, v_r, v_i and v_a correspond to the P-wave velocity of the water, rock, ice and air components.

Combined therefore, the 4PM produces three equations that account for 4 unknowns, resulting in an underdetermined system of polynomial equations. Two solutions are put forward by Hauck et al. (2011) for this; a prescribed porosity model which requires porosities to be input from empirical or field data, or a more general model, whereby negative results for water or ice content are omitted, thus providing a range of possible solutions. However, more recent

studies have introduced iterative usage of 4PMs to circumvent problems caused by the need for prescribed porosity or non-unique solutions. Following Pellet et al. (2016), where previous or supplementary investigations have determined the boundary between frozen permafrost and unfrozen sediment within the same sub-surface medium, three-phase models that presume a negligible ice content beneath this boundary may be applied. This derives a generalized value for rock content (and thus porosity), which may then be used as an input in a porosity-dependent 4PM.

Additionally, in its original form (e.g. Hauck et al., 2011), the 4PM is not applicable to clayey environments, as Archie's empirical second law does not account for possible methods of electrical conduction other than those which occur ionically. Indeed, recent investigations by Revil et al. (2017) indicate that surface conduction may be more prevalent than initially thought, and thus should be factored into petrophysical calculations. To solve this problem, expansions can be made to this system of equations, using Archie's empirical second law with modifications made for possible surface conduction (ε; e.g. Kulessa et al., 2006). For example, an expanded form of the 4PM equation has been utilized by Mollaret et al. (2020), whereby:

$$\rho = \frac{\rho_w}{1 + \varepsilon\,\rho_w}(1 - f_r)^{-m}\left(\frac{f_w}{1 - f_r}\right)^{-n}$$

(6.6)

In this investigation, I apply both generalized and constrained versions of the 4PM, using the expanded form which contains modifications for electrical conductivity (e.g. Mollaret et al., 2020). As the generalized system of equations is strongly underdetermined, and thus there are a range of possible rock, ice, air and water content combinations that provide valid solutions to the four-phase model, initial models are produced to map the possible values for rock, ice, air and water content at Lagoon Pingo with a given resistivity-seismic velocity pair. This approach is identical to that of Hauck et al. (2011), whereby the relation between the four phases of the general model is provided for different velocity/resistivity pairs. Using the bulk velocity constraint for Holocene marine silts and clays identified within the seismic common offset

gather presented in Chapter 4 (1800 ms^{-1}), the solution space was mapped for three possible resistivities. These resistivities were selected following their identification in the electrical resistivity tomography of Chapter 4, and represent possible values that might be identified within the TEM imagery. Additionally, as the electrical conductivity of groundwaters emanating from the pingo spring at the surface (5 – 7 mS cm^{-1}; Hodson et al., 2019) are at the lower end of the range identified in valley-wide studies (17 ± 12 mS cm^{-1}; Cable et al., 2018), I consider the effect that these different salinities have on the four-phase modelling approach.

Following inversion of the acquired TEM data, constrained four-phase modelling was conducted following the approach of Pellet et al. (2016). Shown in Figure 6.3, I assume that the ice content beneath the permafrost boundary is equal to zero. These models are used to identify the average rock fraction in each 1-D profile for the underlying layer (unfrozen fine-grained Holocene marine silts and clays). As no known geological boundary intercepts the pingo at shallow depths (<30 m), this average rock fraction for each individual 1-D profile is then applied as a constraint within the permafrost layer to provide a complete solution to the four-phase model.

Four-phase models were completed using MATLAB (version 2020b). Parameterisation of these models are shown in Table 6.3, alongside a justification of each of the values used. Inputs to the models included the depth constraints for the rock and ice fraction as previously highlighted, in addition to mean and standard deviation of the ensemble models produced during the inversion of the TEM, and P-wave velocities from seismic refraction data as collected previously (see Chapter 4). Normal distributions were produced from these values, from which the phase models obtain a series of 1000 samples to reflect the range of uncertainties within phase modelling estimates. This value was selected as a compromise between ensuring enough samples to reflect the possible variability in the subsurface, against computational performance constraints.
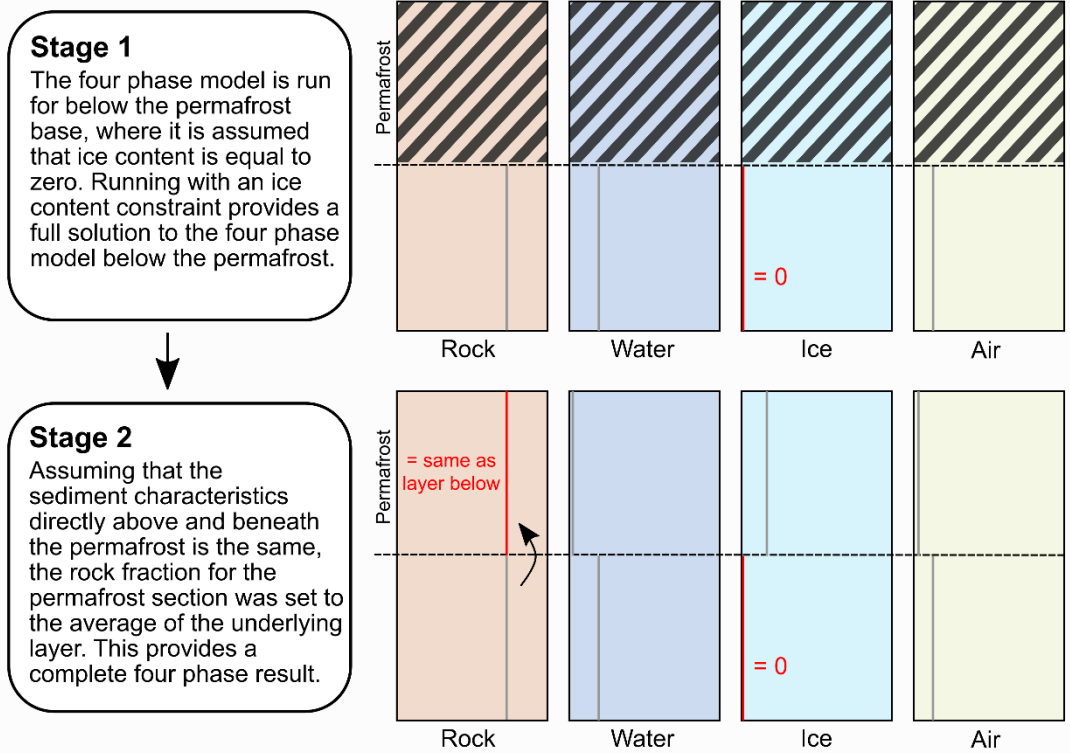
Figure 6.3. Schematic illustrating the workflow applied in obtaining complete four-phase models. In stage 1, the model is run below the permafrost under the assumption that the ice fraction equals zero. In stage 2, the mean average rock content for the layer beneath the permafrost is used as constraint to provide a full four-phase model for the permafrost layer.

6.3. Results

6.3.1. Four-Phase Solution Space Modelling

As the generalized four-phase system of equations is strongly underdetermined, with many separate combinations providing a viable solution, mapping the solution space to identify the relationship between the rock, ice, air and water contents allows for the analysis of how differences in resistivity and seismic velocity may reflect changes in subsurface composition. Here, the primary aim of this solution space modelling is to assess how changes in resistivity at depth identified using TEM data may correspond to changes in rock, ice, air, and water contents, to allow interpretation of potential alluvial fan heterogeneities present.

113

Table 6.3. Parameters used within the finalized four-phase model, along with a justification for the values used.

Parameter	Value	Justification
Porewater Resistivity (Ωm)	1.67	Value derived from the electrical conductivity of Lagoon Pingo groundwaters (Hodson et al., 2020).
Surface Conductivity (Sm^{-1})	0.2	Derived from Waxman and Smits (1968), using the porewater resistivity value as above.
P-wave velocity: rock (ms^{-1})	2470	Derived from Johansen et al. (2003), whom seismically mapped and model P-wave velocities of the sediments within Adventdalen.
P-wave velocity: water (ms^{-1})	1500	Typical value (e.g. Reynolds, 2011).
P-wave velocity: air (ms^{-1})	330	Standard air wave velocity.
P-wave velocity: ice in permafrost (ms^{-1})	3837.9	Value identified through modelling by Vogt et al. (2008).
Max. depth (m)	75	The P-wave parameterization for rock is not valid for layers beneath the Holocene marine muds and clays, and thus greater depth would be redundant.

Using the bulk velocity found for the top layer identified within seismic investigations in Chapter 4 (~1800 ms^{-1}), Figure 6.4 shows how the inferred composition of the subsurface varies when paired with a range of possible resistivities using site-specific parameters. As previously identified by Hauck et al. (2011), the generalized 4PM provides well constrained water and air content estimates, as evidenced by the comparatively small possible number of solutions for combinations of these values (Fig. 6.4e). At Lagoon Pingo, low resistivities pertain to a high level of saturation with water content estimated to contribute to ~35% of the volume of the underlying medium, whilst tenfold increases in resistivity result in a substantial reduction in water content. The relationship is exponential; decreases in resistivity contribute to an exponential increase in the amount of water content expected to occur within the pore space. As air content estimations are tied to changes in seismic velocity given

that air content is not directly parameterized within the empirical Archie's second law equation, the air content for different resistivity/seismic velocity pairs does not differ significantly (<10%). This assumes that velocity estimates are reliable; as only bulk velocities are considered here, these values may only represent air content across the whole of this uppermost layer identified within the seismic investigations (Chapter 4).

In contrast, ice and rock contents are less easily determined, with the 4PM able to discern the sum of ice and rock content, but unable to isolate one from the other. This is due to the similar P-wave velocity of ice and rock at this site, in addition to ice and rock both being resistive media (Hauck et al., 2011). However, if one of these factors can be constrained, either by attributing a porosity for a given medium or by assuming that ice content would equal zero beyond the bounds of the permafrost base, estimations of rock and/or ice content become much less ambiguous (Hauck et al., 2011). For pairings of possible resistivities at Lagoon Pingo against the known bulk seismic velocity, higher resistivity readings are attributed to a higher rock content and lower porosity, with decreases in resistivity corresponding to an exponential decrease in rock fraction.

Solution space modelling also enables an evaluation of the influence of salinity on the site, given the range in porewater electrical conductivities that have been reported for Lagoon Pingo spring water (5 – 7 mS cm^{-1}; Hodson et al., 2019) and those for saline sediments within the valley (17 ± 12 mS cm^{-1}; Cable et al., 2018). As shown by Figure 6.5, an increase in porewater electrical conductivity corresponds to a small increase in the possible rock content and decrease in potential water and ice fraction, although differences between the two salinities is minor.
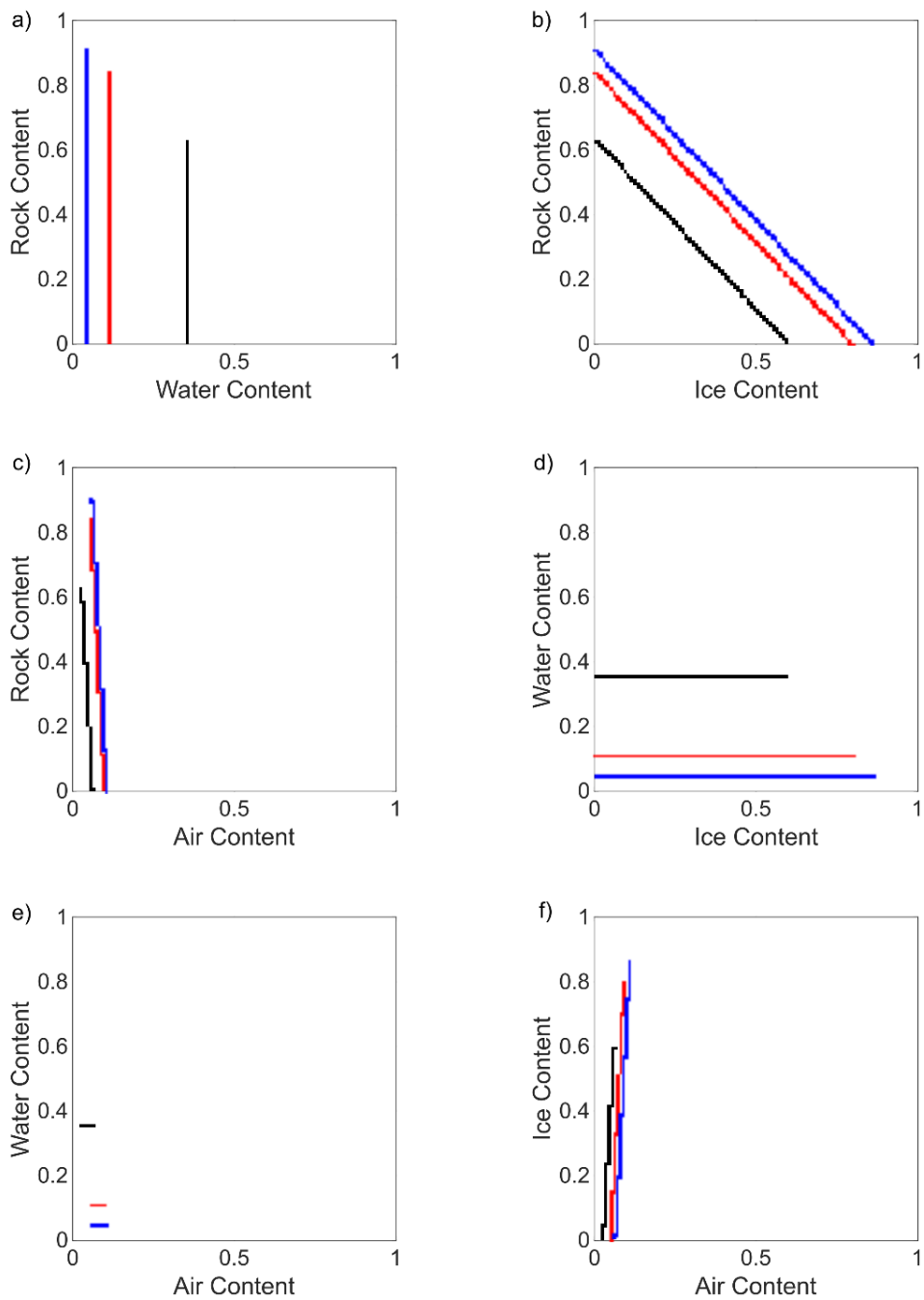
Figure 6.4. Generalized four phase models (4PM) depicting the map of solutions for possible resistivity-seismic velocity pairs at the Lagoon Pingo site. At Lagoon Pingo, for which these models are parameterized, large increases in resistivity are caused by either an increase in the fractional rock or ice content.
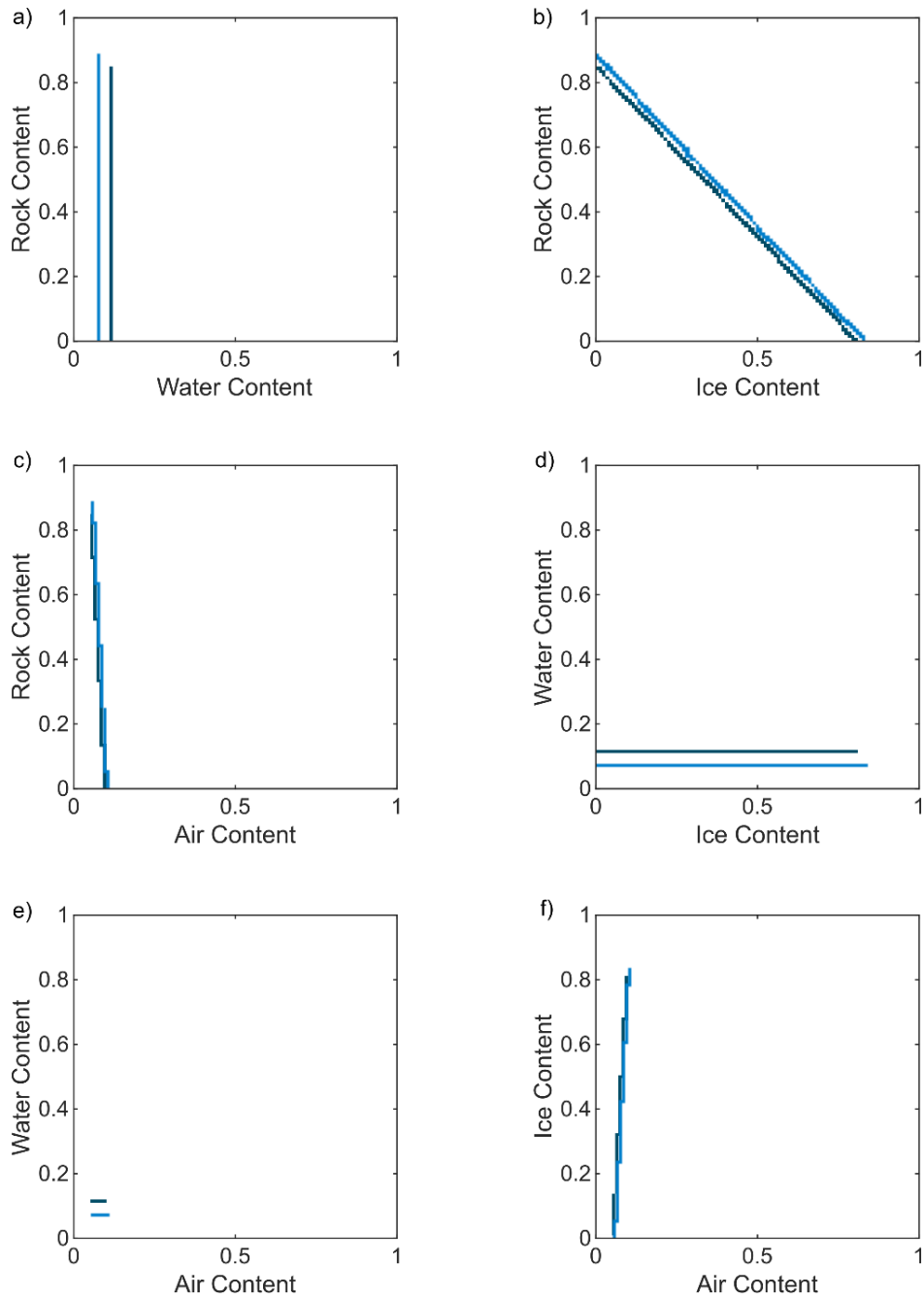
Figure 6.5. Generalised four phase models (4PM) depicting the map of solutions for identical resistivity (100 Ωm) and seismic velocity (1800 ms^{-1}) pairs within different possible salinities at the site.

6.3.2. 1-D Resistivity Profiles

Inversions of TEM measurements in the long profile (Fig. 6.6) depict a comparatively resistive uppermost layer (layer A), which varies in depth across the profile. This appears to shallow in 1-D inversions up-valley, with a depth of 15 m across the pingo progressively thinning to a depth of ~8 m in measurements made off the southeastern end of the pingo. Notably, the wide range of the posterior depth function (PDF) within measurements of this uppermost layer indicate that resistivities have a high degree of uncertainty.
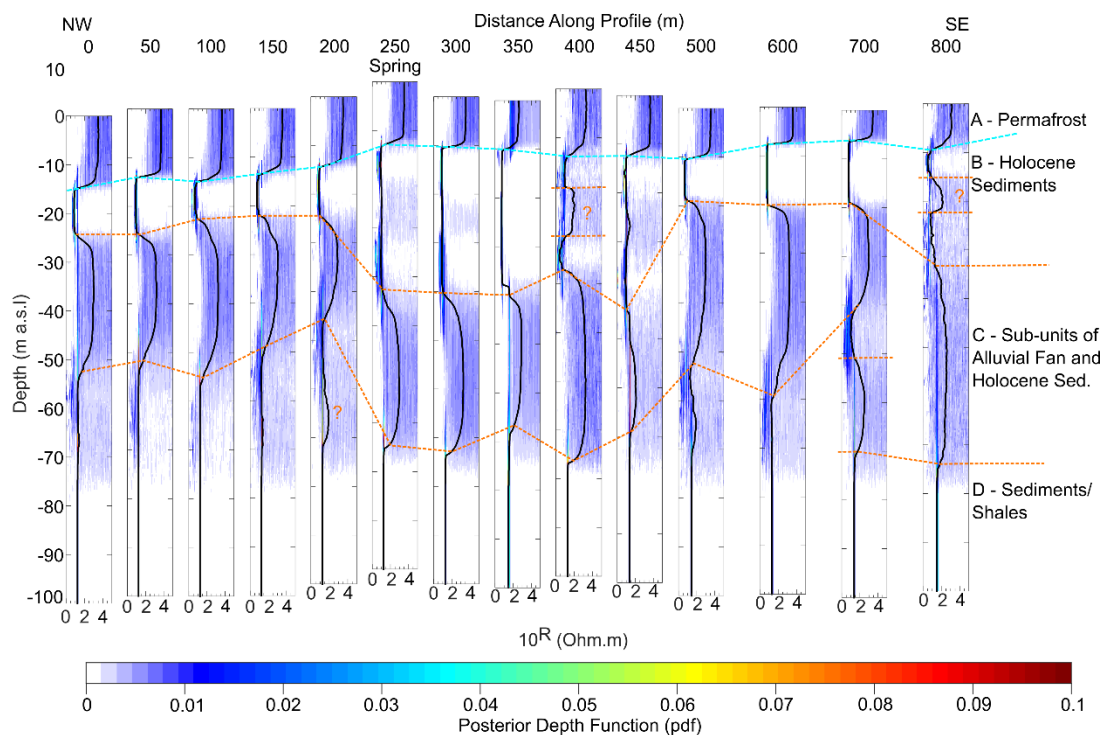
Figure 6.6. Block resistivity diagrams obtained following inversion of the acquired TEM data in 1-D profiles over the long profile. The black line represents the median of the inversion models, whilst the background reflects the posterior distribution of these models according to their frequency. Profiles have been adjusted according to the height of the receiver above sea level, and dashed lines show the interpretation of these 1-D inversions.

Below this first layer, TEM measurements depict low resistivities that persist in each of the 1-D profiles, with a comparatively narrow PDF and low uncertainty. The thickness of this layer (B on Figure 6.6) is variable; it is thinnest towards the ends of the pingo complex, where this layer is approximately 5 – 10 m thick (0 – 200 m and 500 – 700 m along the profile). In comparison, the 1-D profiles

across the center of the pingo complex (250 – 450 m along the profile), including the measurement made above the pingo spring, indicate that this layer is 30 – 35 m thick. At 400 m and 800 m along the profile, this layer is discontinuous, as the median model of this 1-D profile depicts a ~10 m thick, more resistive (10^3) section intercepting this. Similarly, at 250 m, 300 m and 450 m along the profile, the PDF shows some models with higher resistivities within Layer B, indicating some uncertainty within the inversion here.

The third layer (C on Figure 6.6) consists of elevated resistivities (~10^3 Ωm), although a wide PDF indicates that this layer contains high uncertainty. This layer is identified within all of the 1-D profiles, although the median of the models indicate that it is quite poorly resolved at 450 m and 800 m along the profile. Within 1-D profiles at both of these points, the median model shows a smaller increase in resistivity (~10^2 Ωm) compared to the rest of layer C, with uncertainty present as evidenced by some variability in the PDF. Notably, the thickness of this layer varies considerably along the profile. Between 0 – 100 m, this layer is approximately 30 m thick, thinning to 10 – 15 m thick at 150 – 200 m. Between 250 – 400 m, this layer is again approximately 30 m thick, despite commencing at a lower depth given the greater thickness of the above layer. This layer is thickest at 600 m, where the median resistivity model depicts a layer exceeding 40 m.

In the transverse profile, a pattern similar in resistivity magnitude and structure to the long profile can be identified. The uppermost layer (A on Figure 6.7) features higher resistivities that extend to a depth of ~ 9m from the coastal side (SW; Fig. 6.2) to ~14 m towards the alluvial fan (NE). Notably, there is substantial variability in the resistivity and PDF of this layer, with an apparent reduction in resistivity on the coastal side of the pingo (SW; Fig 6.2). In profiles at 0 and 50 m, median resistivity models of this upper layer depict a layer of approximately 10^3 Ωm, whilst profiles between 100 – 250 m have resistivities of ~10^2 Ωm, combined with a narrower range in PDF and thus, lower uncertainty. As such, the 1-D measurement made at 350 m does not follow this pattern, with resistivities of 10^3 – 10^4 Ωm more similar to those that were acquired in measurements taken on the pingo.
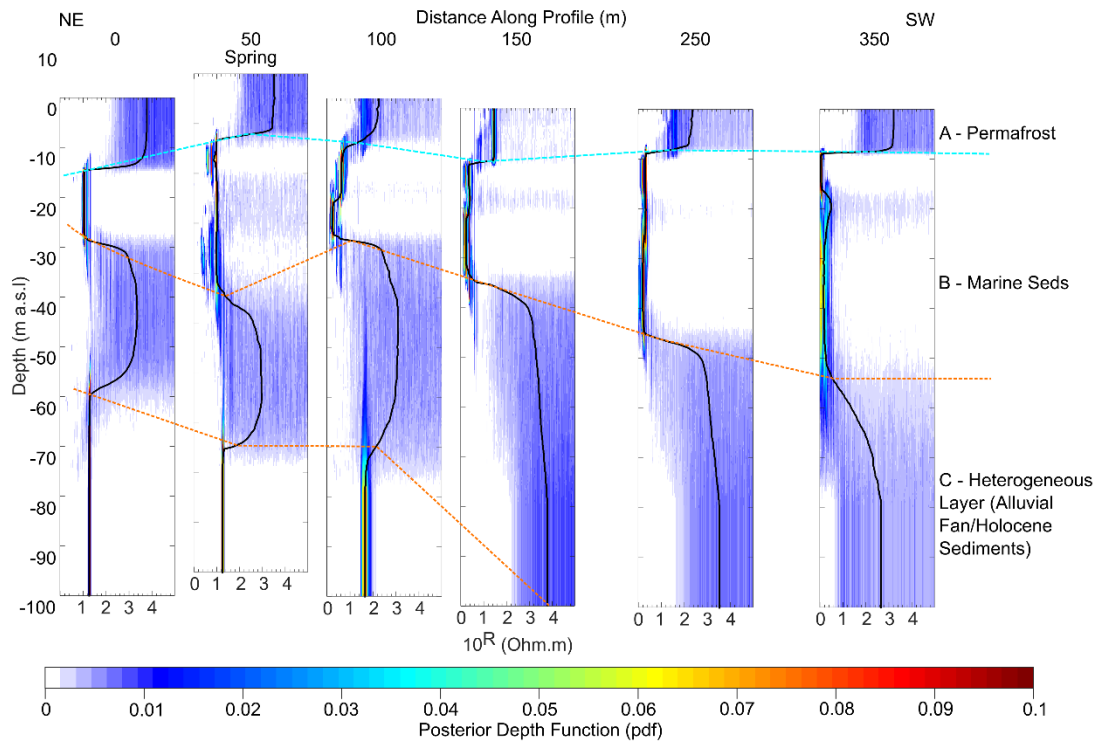
Figure 6.7. Block resistivity diagrams obtained following inversion of the acquired TEM data in 1-D profiles over the transverse profile. The black line represents the median of the inversion models, whilst the background reflects the posterior distribution of these models according to their frequency (red = most common, blue = least common). Profiles have been adjusted according to the height of the receiver above sea level, and dashed lines show the interpretation of these 1-D inversions.

Similar to 1-D measurements made in the long profile, a layer (B) with lower resistivities occurs beneath the uppermost section. However, the depth to which this layer extends to varies markedly across the profile. In general, the depth of this layer increases towards the present-day fjord coastline (SW; Fig 6.2), with this layer extending to a depth of 30 m at the northern end to 60 m in the most southerly measurement. The measurement made directly on top of the pingo spring (50 m along the profile in Figure 6.7) provides an exception to this pattern however, whereby this layer extends to a depth of 45 m below the surface. Despite this, it is notable that the resistivity of this layer decreases in measurements that are closer to the fjord. Measurements made close to the pingo complex highlight that this layer has resistivities exceeding 10^1 Ωm, whereas measurements made on the tidal plain indicate lower resistivities (~5 Ωm).

In each 1-D measurement in this profile, this lower resistivity unit is underlain by a region of higher resistivities, similar to those in the 1-D profile. In profiles close to the pingo, this layer extends to depths between 60 – 70 m, whereas profiles located on the fjord side of the pingo indicate this layer extends beyond the depth of the inversion (100 m). Resistivities vary across the profile, with lower median resistivities (~10^3 Ωm) generally found closer to the pingo complex compared to those on the fjord side (~10^4 Ωm). This higher-resistivity layer features a very wide range of PDF and thus high uncertainties overall.

6.3.3. Phase Modelling

Four-phase modelling aims to facilitate the interpretation of the transient electromagnetic measurements, through the use of established geophysical relationships (e.g. Archie, 1951; Timur, 1968), in combination with bulk seismic velocities (Chapter 4). Following the schematic in Figure 6.3, the first stage of modelling intends to identify a value for rock content fraction, and thus porosity, for the permafrost section. By assuming that the ice content beneath the permafrost base equals zero, a value for the rock fraction of the unfrozen layer can be obtained. The permafrost at Lagoon Pingo has been interpreted here as the uppermost layer, and the base of this as shown by the resistivity contrast between this layer (> 10^3 Ωm; layer A on Fig 6.6 and 6.7), and the underlying layer (~10^1 Ωm; layer B).

Table 6.4 shows the values obtained for the porosity of layer B across the long profile, according to the layer interpretation depicted in Figure 6.6. Averages for the rock fraction of the section vary from 48.9% to 64.1%, therefore representing a range in porosity from 35.9% to 51.1%. Notably, rock fraction is lower off the end of the pingo complex, with the four-phase model highlighting lower rock fractions at 500m and 800m along the profile. High standard deviations for some 1-D profiles (e.g. 100m and 400m) occur due to the high range in the posterior depth distribution within layer B. The average rock fraction across each of the 1-D models equals 55.6% (porosity = 44.4%). This porosity value compares well to previous sedimentological analyses

conducted within buried Holocene sediments in Adventdalen (35% to 55%; Tavakoli et al., 2021).

Table 6.4. Values for mean average rock fraction and porosity across the long profile.

Depth (m)	Mean Average Rock Fraction (%)	Mean Average Porosity (%)
0	57.9 ± 5.7	42.1
50	59.9 ± 5.0	40.1
100	52.0 ± 9.0	48.0
150	53.7 ± 7.5	46.3
200	57.6 ± 5.0	42.4
250	60.3 ± 7.3	39.7
300	58.1 ± 4.9	41.9
350	51.9 ± 3.9	48.1
400	63.4 ± 16.7	36.6
450	60.3 ± 8.5	39.7
500	48.9 ± 5.0	51.1
600	53.7 ± 3.8	46.3
700	54.3 ± 4.5	45.7
800	53.6 ± 4.9	46.4

In the second stage of the four-phase modelling, the rock fraction within the permafrost section of the model is set to this average rock fraction value. This overcomes the underdetermination of the four-phase model in an approach similar to Pellet et al. (2016), by assuming the sedimentological properties of the permafrost layer are identical to that of the sub-permafrost layer. The combination of the rock fraction constraint within the permafrost with the ice fraction constraint below the permafrost base therefore provides a complete four-phase model.

With representative models shown in Figure 6.8, four-phase modelling depicts clear differences in the fractional content of rock, water, ice and air within the layers observed at Lagoon Pingo. The pore space of the uppermost layer (A) is dominated by ice (generally 30 – 40%), with a low unfrozen water content (< 10%) and air content (~ 5% in most cases). For each of the 1-D profiles, the transition between this layer and the underlying layer is marked by a change

in ice and water contents, with a rapid drop in ice content corresponding to an increase in water content.
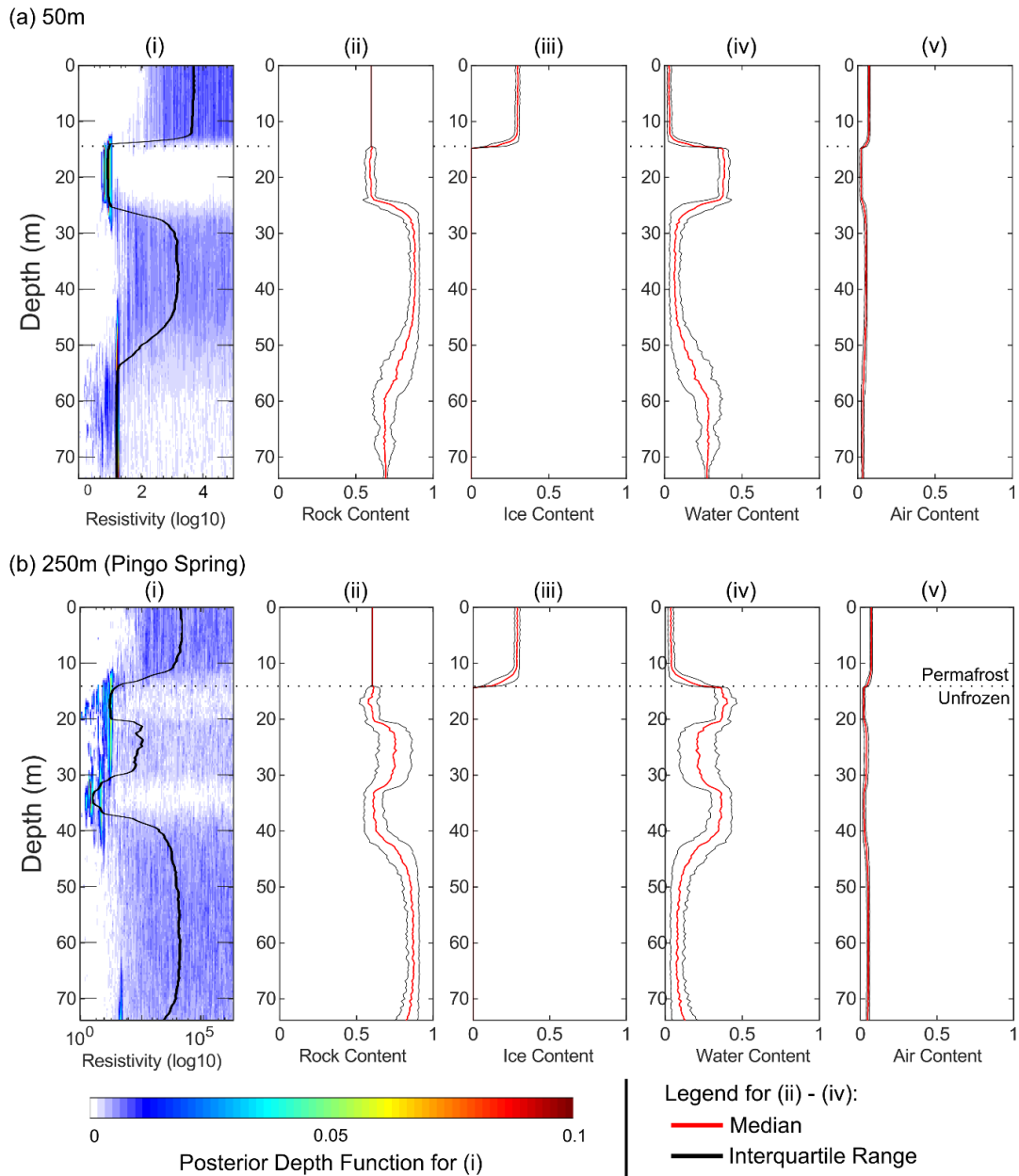
Figure 6.8. Four phase models for (a) 50m and (b) 250m along the long profile. (i) shows the posterior depth distribution and median result of the MuLTI-TEM inversion. The median and interquartile range of the (ii) rock, (iii) ice, (iv) water, and (v) air content is also shown. Uncertainty within the posterior depth distribution (b)(i) is reflected in the range of identified rock (b)(ii) and water (b)(iv) contents.

In Layer B, where the ice content is assumed to equal zero, water content dominates the pore space. The air fraction is lowest (2.5% of the total composition of the layer) in this layer, and thus this layer is heavily saturated. Below this layer, an increase in resistivity corresponds to a greater rock fraction. For example, in profiles taken on the northwestern part of the pingo, resistivities exceeding 10^3 Ωm correspond to a rock fraction exceeding 90%, indicating porosities of less than 10% in layer C. The majority of this pore space contains water, forming 5 – 10% of the overall composition of this layer. The air content of this layer is greater than the layer directly above it, although this remains low overall (< 5%).

6.4. Interpretation

As frozen sediments commonly exhibit high resistivities, along with the knowledge that open-system pingos in Svalbard are consistent with continuous permafrost, the uppermost layer may be interpreted as permafrost. This assertion is established through phase modelling, whereby the relatively elevated resistivities in this uppermost layer can only reasonably be explained by an increase in ice contents (30 – 40%; Figure 6.4) when following the assumption of a near-identical porosity between these two layers. Similarly, previous studies at both this site (Yoshikawa and Harada, 1995; Chapter 4) and those located elsewhere in Adventdalen (Ross et al., 2007), similar resistivity contrasts are equally interpreted as denoting permafrost boundaries. However, whilst Yoshikawa and Harada (1995) interpreted their ten-fold decrease in resistivity as the boundary between overlying permafrost and underlying, unfrozen marine clays, they identify the depth of this transition as 22.8 m, which is far below the average depth of 11 m as indicated by the TEM data here.

Below this uppermost permafrost layer, the presence of a relatively low resistivity media (~10^1 Ωm) across the field site is interpreted as unfrozen saline muds and clays. This corresponds well with previous studies conducted elsewhere on Svalbard (e.g. Kasprzak et al., 2017) and those that persist elsewhere in analogous environments (e.g. Overduin et al., 2012). In ERT

investigations completed elsewhere on Svalbard, values below 100 Ωm are suggested to preclude the existence of permafrost (Kasprzak et al., 2017), and are instead attributed to a 'bottom active layer' that occurs due to the salinity of the environment. On a coastal lagoon in Barrow, Alaska, Overduin et al. (2012) identified phase boundaries on the basis of changes in resistivity on the order of one magnitude, with values of < 10 Ωm indicative of unfrozen sediments.

Resistivity increases at depths between the permafrost boundary and that of the previously constrained interface interpreted through seismic reflection (~68 m; Chapter 4) imply a heterogenous section with this zone (Figure 6.6/6.7, layer C). However, permafrost can be precluded in explaining these resistivities, following previous site knowledge that Lagoon Pingo has emerged relatively recently (140 ± 20 yr BP; Yoshikawa and Nakamura, 1996). It is therefore unlikely that this enhanced resistivity section corresponds to frozen sediment, as this would presume an unrealistically rapid rate of permafrost aggradation. Changes in lithology can also be excluded in the explanation of this enhanced resistivity section, on account that the local geological context is well known (Major et al., 2000). Four-phase modelling can also be used to exclude salinity variations from a primary role (see Fig. 6.5), as an increase in salinity shows only a minor influence on the sedimentary characteristics.

Following phase modelling using site parameters (Fig. 6.4), where negligible ice contents are constrained following the identification of the permafrost base at an average depth of 11 m, resistivities of 100 Ωm combined with previously established seismic velocities of ~1800 ms^{-1} can only occur if the rock fraction increases relative to water or air content. This matches the expected profile of the alluvial fan, where larger clasts with a marine mud and clay infill between the intra-clast spacings would contribute to an overall reduction in porosity relative to the fine-grained Holocene marine muds and clays alone.

The geometry of this elevated resistivity layer also matches the hypothesis that alluvial fan deposits exist beneath the pingo. As depicted in the 1-D measurements made in line with the alluvial fan (shown in Figure 6.7), the upper bound of this elevated resistivity zone deepens as it extends further up-

valley, reflecting the surface expression of the slope of this alluvial fan. Whilst no detailed study on the chronology of this alluvial fan has been conducted to the author's knowledge, the relatively recent formation of the tidal lagoon (Lønne and Nemec, 2004) along with the well-established Holocene sedimentation that occurs within Adventdalen (Gilbert et al., 2018) provides a clear mechanism with which this alluvial fan may become buried beneath overlying marine mud and clay deposits.

Interestingly, the geometry of this elevated resistivity layer on both the long and transverse profile appears to indicate that this begins at a greater depth towards the central pingo spring. The combination of these two profiles resemble a concave depression in the presumed alluvial fan strata, with a depth of 10 m, width of 100 m and length of ~200 m. Whilst this is larger than other pockmarks in Adventfjorden, it is similar in size to those within the wider Isfjorden region (e.g. Forwick et al., 2009), and warrants a reconsideration of hypotheses surrounding the evolution of Lagoon Pingo from a submarine pockmark (Hodson et al., 2019).

At the bottom of layer C in each profile (Fig 6.6/6.7), the interface beneath the sections with high resistivities corresponds well to the depth of the inferred Cretaceous shale interface as identified in previous seismic investigations of the pingo (~68 m; Chapter 4). These resistivities (~20 Ωm) correspond well to the lower-end estimate for consolidated shales (see Reynolds, 2011), and corroborate well with previous investigations in Adventdalen that have identified a marine mud sediment of ~60 m at sites further up-valley (Cable et al., 2018).

6.5. Summary

In this chapter, transient electromagnetics is used to assess the extension of the alluvial fan buried within Holocene marine muds and clays beneath Lagoon Pingo. This follows the hypothesis of Chapter 5, where preferential fluid flow was inferred to be associated with the alluvial fan situated to the north-west of Lagoon Pingo, amid other more generalised theories of interactions between alluvial fans and pingos (e.g. Humlum et al., 2003). Transient electromagnetic

data identify a shallow permafrost layer (~ 11 m) which contradicts previous geophysical investigations of the pingo (c.f. Yoshikawa and Harada, 1995). Beneath this layer and a separate unfrozen Holocene marine mud and clay section, a layer with high resistivity (10^3 - 10^4 Ωm) and high uncertainty is interpreted as the interfingering of coarser-grained, alluvial fan deposits with fine-grained Holocene marine sediments. This interpretation is further supported by four-phase modelling, the well-constrained local geological (Major et al., 2000) and geomorphological (Lønne and Nemec, 2004) context, and the geometry of enhanced resistivities within the TEM transect. Within this layer, a concave depression with a geometry similar to other regional pockmarks occurs directly beneath the pingo spring, where fine-grained, poorly permeable Holocene marine muds and clays are otherwise at their greatest extent. The wider importance and implications of this finding are discussed within Chapter 7.

Chapter 7: Discussion

7.1. Restatement of Thesis Aim and Objectives

The research within this thesis was motivated by the need for detailed geomorphological and hydrological investigations on open-system pingos, given the recent appreciation of these landforms as a conduit enabling methane release through continuous permafrost (Hodson et al., 2019; 2020). Notably, there were apparent similarities between terrestrial open-system pingos, and submarine pockmarks and seeps that had not been extensively explored (Hodson et al., 2019). The aim of this thesis was to therefore identify and analyse the structures, processes and mechanisms that result in open-system pingos forming conduits through which sub-permafrost methane can be released. Focusing on Lagoon Pingo, this comprised of three primary objectives:

1) Assess and determine the internal structure and composition of a nearshore open-system pingo.

2) Identify the spatial and temporal hydrological regime of the pingo, and understand the nature of intra- and sub-permafrost groundwater migration.

3) Evaluate the factors that have resulted in open-system pingo formation in this location, and evaluate theories that open-system pingos are genetically linked to submarine seep and pockmark forms.

In order to complete these objectives, a series of geophysical investigations were undertaken, including electrical resistivity tomography and active source seismics (Chapter 4), self-potential (Chapter 5), and transient electromagnetics (Chapter 6); the location of each is shown in Figure 7.1. In this section, the core findings of the geophysical investigations in this thesis are discussed more broadly, and potential avenues for future research are highlighted.
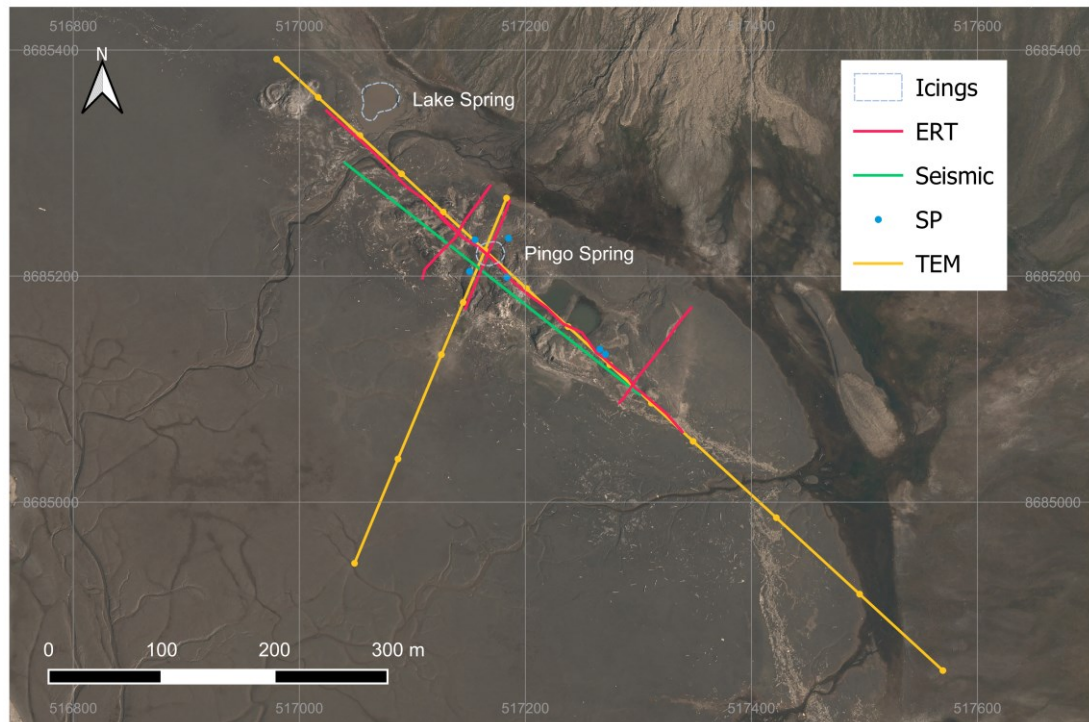
Figure 7.1. Locations of each of the geophysical investigations shown together (Orthophoto: Norwegian Polar Institute, 2021). Co-ordinates are in UTM 33N.

7.2. Implications of Findings on the Understanding of Open-System Pingos

7.2.1. Alluvial Fan and Open-System Pingo Interactions

Previous attempts at explaining the distribution of open-system pingos within continuous permafrost have focused on how groundwater flows beneath and through the permafrost. Yoshikawa and Harada (1995) provided a classification that assigns open-system pingos to one of three types: (i) those that occur above faults and fractures that permit the flow of sub- and intra-permafrost groundwaters, (ii) those that are derived from groundwaters which infiltrate beneath temperate or polythermal glaciers (e.g. Liestøl, 1977), and (iii) those that occur in areas undergoing glacio-isostatic uplift, wherein unfrozen groundwater flows to the surface through small-scale discontinuities within the comparatively thin, new permafrost. As Ballantyne (2018) notes, these categories hold true in particular circumstances, but do not cover the full breadth of circumstances in which open-system pingos occur. For example,

pingos within the last group are often formed in Holocene glaciomarine sediments that are poorly permeable and not conducive to groundwater flow. Aspects of group (ii) and group (iii) arguably hold true for different aspects of Lagoon Pingo (Hodson et al., 2019), but the presence within low-lying fine-grained sediments of Holocene age does not explain the location of Lagoon Pingo per se.

In more recent studies of the distribution of open-system pingos on Svalbard, Demidov et al. (2022) indicates that the majority of Svalbard pingos, including Lagoon Pingo, were located on the margins of alluvial fans. However, whilst an interaction between alluvial fans and open-system pingos has been theorised (e.g. Humlum et al., 2003), geophysical observations of this interaction was hitherto limited.

The use of self-potential (Chapter 5) and transient electromagnetics (Chapter 6) therefore provided evidence that ties the formation of open-system pingos to alluvial fans. In Chapter 5, the elevated magnitudes of self-potential readings on the northern side of the pingo are interpreted as indicating that flow into the pingo complex primarily comes from that orientation, and is linked to the alluvial fan as a result. Fluctuations in this signature are therefore interpreted as a change in depth of fluid flow, and suggest that the alluvial fan may extend beneath Lagoon Pingo. In Chapter 6, this hypothesis was tested. Transient electromagnetics across the pingo complex show a high resistivity ($10^3 - 10^4$ Ωm) layer beneath the pingo, with a geometry that depicts the deepening of this layer with distance from the alluvial fan slope. By combining with bulk seismic velocities (~1800 ms^{-1}; Chapter 4) in four-phase modelling, it is determined that increases in resistivity correspond well with a decrease in porosity. As an increase rock fraction corresponds to a decreasing pore space, high resistivities are attributed to coarser-grained alluvial fan deposits beneath the pingo.

Previous interpretational models of the geomorphological evolution of the wider region (see Figure 3.6) provides further insights into the nature of these alluvial fan sediments. Lønne and Nemec (2004) outline how the present-day spit formed up-valley of the Hiorthfjellet alluvial fan, as a result of wave action

eroding sediment that was transported inland by longshore drift. This resulted in a low-energy environment, shielded from marine processes besides occasional storm tides, and thus facilitating the deposition of fine-grained Holocene muds and clays. Amid this, the alluvial fan is likely to have continued aggrading, similar to the Hiortfjellet alluvial fan (Lønne and Nemec, 2004). Over time, changes in the dominance of the continued aggradation of Holocene marine silts and clays, and progradation of the alluvial fan is likely to produce an interfingering of these strata beneath the present-day pingo (see Figure 7.2), which corresponds to the uncertainty of this layer identified within the acquired TEM data. As Yoshikawa and Harada (1995) identified through radiocarbon dating, the pingo itself formed relatively recently (140 ± 20 yr BP); with the surface expression of Lagoon Pingo suggested to be defined by segregation ice formed as local permafrost continues to aggrade (Chapter 4).

Despite this apparent interplay between alluvial fans and open-system pingos, the geometry and positioning of the alluvial fan strata at Lagoon Pingo contradicts previous theories outlining why pingos appear to preferentially occur in close proximity to alluvial fan sediments. For example, Humlum et al. (2003) postulates that groundwaters are forced towards the surface as alluvial deposits thin towards their base, whilst they flow on top of more impermeable permafrost below. This theory is problematic at Lagoon Pingo for a number of reasons. Firstly, the thinning of alluvial sediments does not lead to the forcing of groundwaters to the surface per se; instead the pressurization of groundwaters corresponds to the range of hydrogeological factors that result in hydraulic gradients (Hornum et al., 2020). At Lagoon Pingo, TEM measurements made across the transect between the alluvial fan and towards the fjord (Fig. 6.7) suggest that the alluvial fan deposits extend beyond the location of the pingo, thus indicating that the pingo is not collocated with the alluvial fan base. Secondly, the permafrost at Lagoon Pingo is sufficiently shallow such that the idea that the alluvial fan is underlain by an impermeable permafrost layer can be excluded.
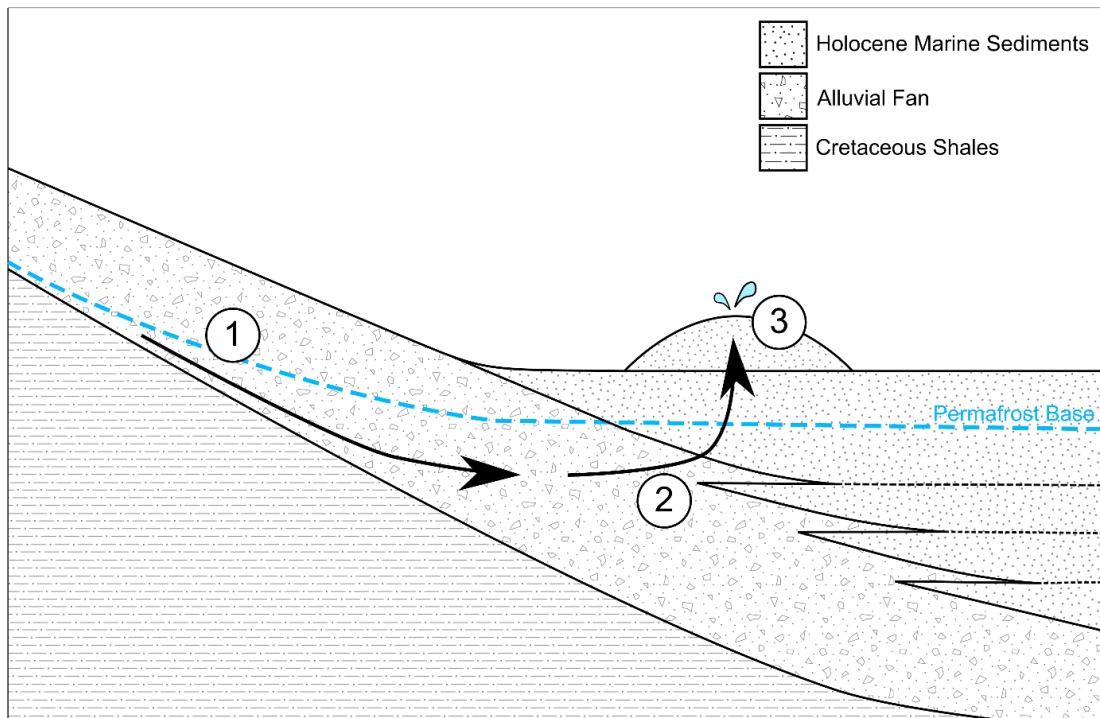
Figure 7.2. An interpretational cross-section of an open-system pingo collocated with the alluvial fan, based on the findings at Lagoon Pingo. Here, water derived from percolation beneath the base of glaciers in upland areas (1) flow downslope, constrained by continuous permafrost above and shales below. (2) This groundwater saturates the lower alluvial fan, constrained by poorly permeable layers above and below. This results in a high potentiometric head. (3) Following the flow path previously derived from a marine pockmark at this location, and maintained under continuous spring flow (Liestøl, 1977) groundwaters reach the surface.

Among possible hydrogeological mechanisms that might explain the formation of Lagoon Pingo in this location is the idea that the coarser-grained layer provides a confined aquifer, sandwiched between poorly permeable Holocene muds and clays below, and a combination of these sediments with continuous permafrost above. Similar to the theory first presented by Liestøl (1977), and later confirmed by Haldorsen et al. (2010), it is envisaged that sub-permafrost groundwaters are fed by the infiltration of water through local temperate glacier beds. For Lagoon Pingo, Tellbreen provides an example where infiltration can occur, with ground penetrating radar investigations by Bælum and Benn (2011) identifying parts of the glacier bed as wet-based. This then flows through hydraulically conductive formations (shown on Figure 7.3) into the alluvial fan, wherein this flows downslope beneath the base of permafrost (denoted by 1

on Figure 7.2). Saturation of the coarser-grained alluvial fan unit bound by poorly permeable Holocene marine muds and clays beneath the pingo (denoted by 2 on Figure 7.2) results in a potentiometric head above the height of the pingo spring, ensuring the continuous upwelling of hydraulically pressurized groundwaters. Continuous recharge of the aquifer and sustained maintenance of the hydraulic head would therefore result in continued spring flow.
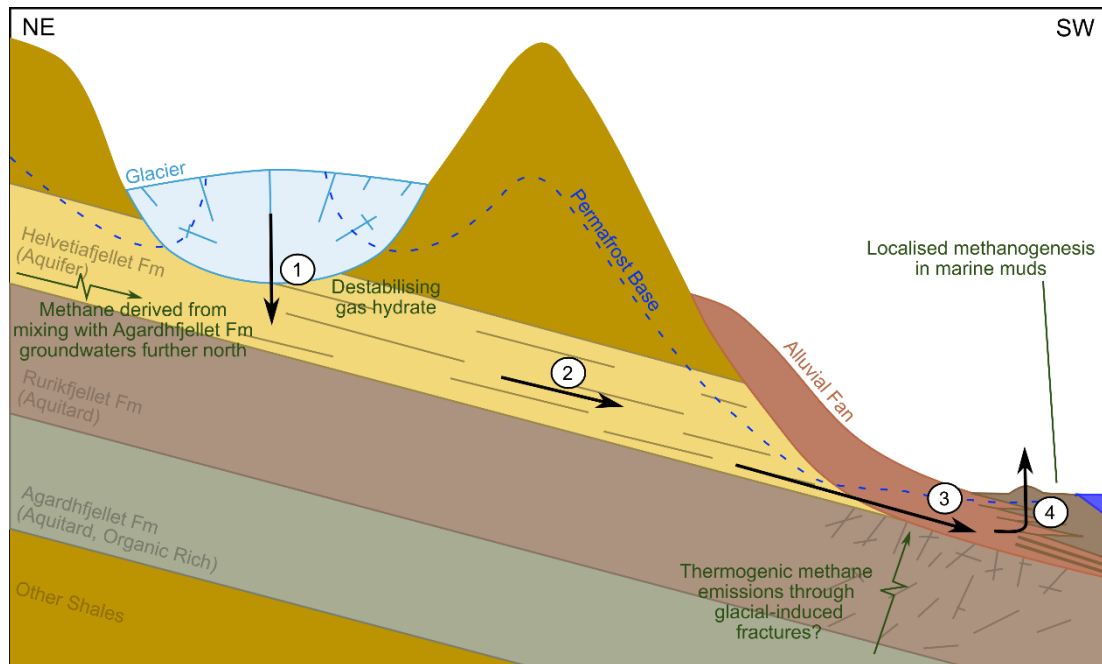
Figure 7.3. Conceptual schematic demonstrating groundwater flowpaths and possible methane sources for Lagoon Pingo (derived from Liestøl, 1997; Major et al., 2000). (1) Groundwaters are derived through the infiltration of groundwaters beneath the warm bases of local wet-based glaciers (e.g. Tellbreen; Bælum and Benn, 2011) as per Haldorsen et al. (2010) and (2) flow downslope through confined aquifers (e.g. Helvetiafjellet Fm.; Huq et al., 2017). (3) These enter the alluvial fan, and saturate the lower portion of the fan where this interfingers with poorly permeable Holocene marine muds and clays. (4) The high potentiometric head facilitates the exploitation of flow paths that have been maintained since hypothetical pockmark formation, enabling continuous groundwater flow through the pingo on the surface.

However, this does not explain the present-day location of Lagoon Pingo in itself. Notably, the pingo spring occurs where the overburden Holocene marine mud and clay assemblage is at its thickest, and where alluvial fan sediments appear to form a depression. It is therefore difficult to envisage how

groundwaters in this location would reach the surface, without the presence of a pre-existing groundwater flow pathway (e.g. Orvin, 1944). As such, the geometry of this alluvial fan section and need for a flowpath network warrants a reconsideration of the theory that Lagoon Pingo may have evolved from a submarine pockmark (e.g. Hodson et al., 2019).

7.2.3. Terrestrial Pockmark Emergence

Hodson et al. (2019) postulates that Lagoon Pingo may have evolved from a submarine pockmark or seep, following evidence of year-round methane release. In a seismic characterisation of homogeneities within the Lagoon Pingo site, Chapter 4 suggested that sustained groundwater flow would need to persist throughout deposition of ~68 m of poorly permeable Holocene marine muds and clays, which would require exceptional pressures to maintain. However, the identification of a unit of coarser-grained sediments at relatively shallow depths beneath Lagoon Pingo (Chapter 6) would mean that groundwaters only need to navigate a much shallower layer of these sediments than initially thought (c. 20 – 30 m). This would still require an explanation of how groundwater flows through relatively impermeable Holocene muds and clays, and permafrost, and as such, a reconsideration of a terrestrial emergence of pockmarks was warranted.

At Lagoon Pingo, characteristics that point towards a pockmark related genesis are the geometry of the alluvial fan unit beneath the pingo, and the observations of pockmarks within the region. In regard to the alluvial fan, it was noted in Chapter 6 how the central pingo spring occurred where the coarser-grained sediments were depressed. It was therefore postulated whether the concave shape of this depression resembled that of a pockmark. A pockmark and subsequent methane seep would provide an explanation to why the spring occurred where the overburden Holocene marine muds and clays were deepest locally, as consistent groundwater upwelling under artesian hydraulic pressure following pockmark formation would help to preserve a fluid flow migration network to the surface through Holocene sedimentation (e.g. Orvin, 1944).

However, this concave depression at the interface between coarser-grained alluvial fan deposits and fine-grained Holocene marine sediments meet is perhaps unusual, as the pockmark shape is normally formed within marine muds (Hovland et al., 2002). The eruption phase of pockmark formation would need to be sufficiently large to expel coarser alluvium (Hovland, 1987); whilst pockmark formation in coarser sediments is known to occur (e.g. Bostock et al. 2018; Miscallef et al., 2020), it represents an atypical formation circumstance that would require further modelling to affirm (Chand et al., 2012).

Despite this uncertainty, the location of Lagoon Pingo does provide a combination of factors that were favourable for pockmark formation. Bathymetry data of Adventfjorden depicts a considerable number of circular and elliptical pockmarks (Forwick et al., 2009). These were formed postglacially (Forwick et al., 2009; Portnov et al., 2016), whereby glacial retreat at the end of the Pleistocene led to the instability of gas hydrates within the fjord. In prescribing the factors that affect the formation of pockmarks off the coast of Svalbard, Forwick et al. (2009) outlines that Adventfjorden pockmarks are preferentially located where Holocene marine muds and clays are thinnest. This is true at Lagoon Pingo, whereby fine-grained Holocene marine sediment cover is thinner compared to elsewhere locally due to the alluvial fan deposits beneath the pingo.

Pockmarks and other methane seep features have often been found in close proximity to mass movement features such as submarine slide deposits (Hovland et al., 2002), leading to their association with events such as hillslope failures (e.g. Riboulot et al., 2013). However, whilst the eruption of fluids in the formation of pockmarks has commonly been inferred as causing hillslope failure and submarine slides (Riboulot et al., 2019), recent studies have instead indicated that conditions for pockmark development may be more favourable due to the sediments deposited in mass movement features (Riera et al., 2022). Integral to this is the idea that these failures results in stratigraphical discontinuities that modify and enable the pathways through which fluid migrates (Riboulot et al., 2013). Among mass movement features that are most similar to alluvial fans, and have been attributed to the formation

of pockmark features, are submarine fans (Bayon et al., 2009). For example, in investigations of a submarine fan within the Mediterranean, Bayon et al. (2009) identifies how submarine fans create preferential pathways for focused fluid flow. At Lagoon Pingo, it is envisaged that the alluvial fan may have provided a similar role, enabling fluid migration and perhaps the gas storage to produce favourable conditions for pockmark formation.

For a pockmark to evolve terrestrially to occur, a fall in relative sea level is required. Two possible mechanisms may contribute to this: isostatic uplift, and eustatic sea level fall. Whilst terrestrial pockmark emergence due to glacio-isostatic uplift is more probable given the present climate scenario where global sea levels are rising, eustatic sea level fall may have contributed to the exposure of pockmarks during the Pleistocene. At Lagoon Pingo, the terrestrial emergence occurred as glacio-isostatic uplift coincided with high Holocene sedimentation rates, and protection from marine processes by the local geomorphology. Following the retreat of the Barents Sea Ice Sheet, Adventdalen has experienced glacio-isostatic uplift of 3.7 mmyr^{-1} (Auriac et al., 2016), resulting in a rapid fall in relative sea level. Fjords that form through glacial scouring and remain following the retreat of the ice sheet may then be infilled; in the case of Adventdalen, high rates of sedimentation occurred due to the rate of glacio-isostatic rebound, although progradation of the delta within the fjord slowed following the wave of paraglacial sediment yield (Church and Ryder, 1972; Gilbert et al., 2018). Local circumstances also likely played a role in the emergence of Lagoon Pingo. The progradation of the Hiorthfjellet alluvial fan led to the formation of a spit (Lønne and Nemec, 2004), which enabled the formation of the lagoon within which Lagoon Pingo is located.

Presuming that Lagoon Pingo represents a landform derived from the terrestrial emergence and evolution of a submarine pockmark is true, it should be considered whether this is an isolated occurrence, or whether there are other sites that may also reflect the terrestrial evolution of submarine seep features. On Svalbard, there are a few sites that bear similarities with Lagoon Pingo. For example, Lagoon Pingo may share some characteristics with the pingos in Woodfjorddalen (Figure 7.4). In particular, the third pingo in Woodfjorddalen, which is otherwise referred to in the research literature as

"Woordfjorddalen 3" (e.g. Demidov et al., 2022) is of particular interest. This pingo is located within the lower delta of Woodfjorddalen, approximately 5 km away from the contemporary coastline. To the southwest of this pingo sits a large alluvial fan, flowing downslope from the Grevefjellet mountain. With an active pingo spring (Demidov et al., 2022), an elongated shape with multiple summits and a chaotic topography, and a location close to the base of an alluvial fan (Liestøl, 1977), many of the characteristics of this pingo are notably similar to Lagoon Pingo. Here, it can be argued that the alluvial fan provides hydrogeological characteristics similar to Lagoon Pingo, enabling fluid flow beneath the marine muds and clays in this location. These circumstances are similarly conducive towards pockmark formation following initial deglaciation, as an aquifer becomes confined by a thin layer of poorly permeable sediments (Forwick et al., 2009). The region is similarly undergoing active glacio-isostatic uplift, and may have prompted the terrestrial emergence of the pockmark to the present-day location close to the contemporary coastline, and facilitated the growth of an open-system pingo. It is however noted that it is not known whether this location is actively emitting methane, given that no known groundwater chemistry studies have been undertaken on this spring, due to the inaccessibility of this location.

In addition, it is possible that other open-system pingos within the Holocene marine limit on Svalbard may have initially been methane seep or pockmark features. Demidov et al. (2022) identify that 92 pingos exist below the Holocene marine limit, with 13 of these containing an active spring on the surface. Among pingos that should be considered for a genesis associated with submarine pockmarks and seeps include those in Bockfjorddalen and Dunderdalen (Fig. 7.4). In Bockfjorddalen, an open-system pingo occurs close to the contemporary coastline similar to Lagoon Pingo, although this occurs close to the break in slope. Conceptually, it is conceivable that this slope, which contains coarser-grained sediment and debris, provides a hydraulically conductive interface through which fluid flow was enabled, with burial beneath fine-grained marine muds and clays providing circumstances conducive to pockmark (and subsequent pingo) formation. In Dunderdalen, two pingos with active springs occur in close proximity to alluvial fans, and in thick Holocene

marine muds and clays. Amid uncertainty over their formation within poorly permeable Holocene marine muds and clays, evolution from a submarine pockmark or methane seep should be considered in the possible formation and maintenance of a fluid flow pathway to the surface.
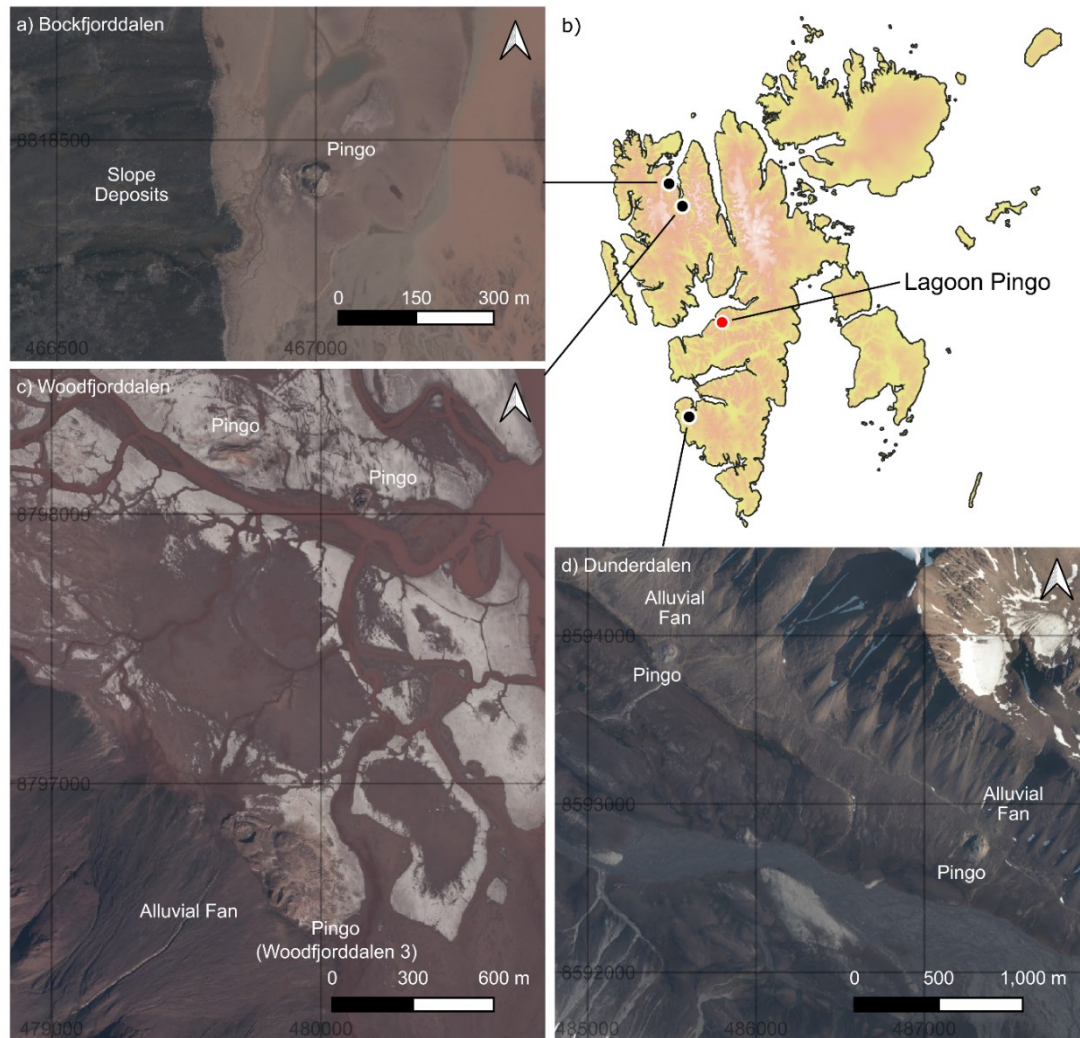
Figure 7.4. Sites that are considered to feature similar characteristics to Lagoon Pingo (orthophoto provided by Norwegian Polar Institute, 2021). Subplots depict (a) the location of the pingo in Bockfjorddalen close to the contemporary coastline, collocated with evidence of the slope, (b) the location of these pingos on Svalbard, (c) the pingos in the northern part of Woodfjorddalen, including those that occur in the delta and one that occurs at the base of an alluvial fan and (d) two pingos in Dunderdalen that both occur at the base of small alluvial fans.

7.2.4. Impact on Local Methane Dynamics

Lagoon Pingo was selected as a focus for these studies on account of year-round methane emissions. In previous investigations, estimates of the quantity of methane emissions at Lagoon Pingo are well-constrained by in situ measurements (e.g. Hodson et al., 2020), although some uncertainty over the source of this methane remains (Hodson et al., 2019). In suggesting that the groundwater inflow into the pingo complex is derived from the northeast, and in the direction where the alluvial fan is located, the self-potential measurements presented in Chapter 5 can be used to provide some insight into local methane dynamics.

Previous studies of methane beneath Adventdalen have identified two dominant sources. Directly beneath the base of the permafrost further in the valley (c. 120 m), a biogenic gas is present (Senger et al., 2017). At greater depths (>200 m), the Agardhfjellet formation hosts a thermogenic methane, as recently identified through drilling as part of the Longyearbyen CO_2 Lab project (Ohm et al., 2019). In explaining the apparent dominance of biogenic methane within Lagoon Pingo emissions (Hodson et al., 2019), Hodson et al. (2020) presume that gas migration exploits Holocene marine clays and fractured sandstone within the underlying Helvetiafjellet formation. Within this, thermogenic gas migration is suggested to be supressed within Rurikfjellet mudstones, despite the apparent presence of thermogenic imprint on the winter emissions from Lagoon Pingo.

The identification of the coarser-grained deposits through transient electromagnetics in Chapter 6, alongside the interpretation of self-potentials that indicate fluid-flow along the alluvial fan, suggests that other methane sources should also be considered. Thermobaric modelling of the gas hydrate stability zone in Svalbard indicates that upland areas are very likely to host natural methane hydrate (Betlem et al., 2019). It is assumed that these gas hydrates are likely derived from thermogenic gas, as local thermogenic gas discoveries have been found to contain a relatively high amount of heavy hydrocarbons, which in turn encourage greater gas hydrate stability (Huq et al., 2017; Betlem et al., 2019). Continued stability of these gas hydrates rely

on the maintenance of low temperatures and high pressures (Kvenvolden, 1993), and is closely tied to permafrost thickness and lateral extent (Makogon et al., 2007; Xiao et al., 2019). Under the amplified warming currently experienced on Svalbard, the degradation of permafrost may destabilise the upper sections of the gas hydrate stability zone (Betlem et al., 2019), with the alluvial fan here providing a preferential fluid flow pathway for free gas. This may provide a partial explanation therefore to observations of gas release from Lagoon Pingo, and may explain the apparent thermogenic imprint on these observations (Hodson et al., 2019), although the possibility of biogenic gas in these gas hydrates cannot be dismissed.

The importance that open-system pingos may represent in the context of methane release has previously been well-established by Hodson et al. (2019) and in Chapter 2. In contrast to submarine pockmarks and seeps, where methane emissions into the atmosphere are minor due to oxidation and methanotrophy within the water column (Myhre et al., 2016), methane emanating from open-system pingos is directly released into the atmosphere. The possibility that open-system pingos may be formed from the terrestrial uplift of submarine pockmarks is therefore significant, considering that these may act as conduits enabling substantiative methane release directly to the atmosphere.

7.2.5. Significance of Methane Release with Terrestrial Pockmark Emergence

Submarine methane seeps and pockmarks have long been considered for their role in enabling methane release during past climatic shifts (Hill et al., 2012), as well as in how they may result in runaway emissions of methane from dissociating gas hydrates under future warming scenarios (Milkov and Sassen, 2003; Reagan and Moridis, 2008; Stranne et al., 2016; Stranne et al., 2022). However, recent studies have questioned the methane flux to the atmosphere from submarine seeps and pockmarks, as methane undergoes oxidisation within sediments (Reeburgh, 2007; Knittel and Boetius, 2009) and the water column (Myhre et al., 2016). As open-system pingos circumnavigate

this ocean water column, oxidisation of methane is limited to local sediments and surficial ponds. The terrestrial emergence of pockmarks, that go on to develop open-system pingos, may therefore result in increased emissions to the atmosphere.

The idea that pockmarks and methane seeps may evolve into terrestrial forms requires consideration in the context of their potential role in past changes in climate. The role of gas hydrate dissociation, and subsequent methane release from submarine seeps and pockmarks in causing warming events has long been debated (e.g. Ruppel and Kessler, 2017). Examples of climatic events where a submarine gas hydrate dissociation hypothesis has been used to explain a hyperthermal or warming event include the Neoproterozoic (1000 Ma to 541 Ma; Kennedy et al., 2001; Jiang et al., 2003), Early Jurassic (~183 Ma; Kemp et al., 2005), the Paleocene-Eocene Thermal Maximum (~55.5 Ma; Minshull et al., 2016; Ruppel and Kessler, 2017), and during the Quaternary, whereby the "Clathrate Gun" hypothesis was used to explain the occurrence of Dansgaard-Oeschger events (Kennett et al., 2000; 2003). However, these hypotheses are commonly problematic; for example, the water column within the ocean would delay methane release to the atmosphere such that it does not corresponds to the timing of warming events (Minshull et al., 2016), or the carbon isotope signature does not indicate the dominance of a marine source (Bowen et al., 2001). In suggesting a means in which dissociating gas hydrates could be released directly to the atmosphere, terrestrial emergence of pockmarks in the form of open-system pingos provide a potential explanation towards these counterarguments.

Future studies modelling the apparent synergy between dissociating gas hydrates and climatic shifts may therefore wish to evaluate the role of terrestrially emerging methane seeps. Primarily, future work should consider the rate at which pockmarks may emerge under isostatic uplift or by eustatic sea-level fall scenarios, how these scenarios would impact upon gas hydrate stability, and whether methane release from terrestrial uplifted methane seeps would be enough for an impact upon global climate.

7.2.6. Pingos and Segregation Ice

In Chapter 4, the combination of relatively low, chaotic topography in frost-susceptible fine-grained sediments with low resistivities that preclude the existence of massive ice are used to infer that Lagoon Pingo is dominated by segregation ice. Further investigations using the electrical resistivity distribution of the subsurface through transient electromagnetics also fails to highlight a contrast resembling massive ice, and indicates that should massive ice persist, it would do so in relatively shallow permafrost (~13 m) within the near-surface. This contradicts general models of open-system pingo formation, wherein pingo formation is suggested to result from the formation of a massive or injection ice core (Harris et al., 1988). Whilst segregation ice has previously been identified and inferred within the other open-system pingos in Adventdalen (Yoshikawa, 1993; Ross et al., 2007), and in other pingos in Siberia (Soloviev, 1973), this has commonly been interpreted as a feature underpinning the later stages of pingo growth and development (Mackay, 1973; 1985). However, as Lagoon Pingo represents an incipient form, with a comparatively young age (140 ± 20 yr^{-1}), a reconsideration of this is necessary.

The study of Lagoon Pingo highlights the significance and need for an understanding of the sedimentary context for pingo formation processes. At Lagoon Pingo, the sedimentary context explains why segregation ice dominates within an incipient pingo form. The fine-grained Holocene muds and clays are frost-susceptible, and arguably more conducive to the formation of segregation ice (Smith, 1985). This dependence of sedimentary context is perhaps best highlighted in cores of pingos below the Holocene marine limit in Grøndalen, Svalbard (Demidov et al., 2019). Within these, massive ice is confined exclusively within assemblages of non-marine gravelly sands and loams. Where assemblages of fine-grained marine sediments begin, the boundary of massive ice is sharp; with layers of marine clays containing segregation ice. Ultimately, Lagoon Pingo highlights how the composition of open-system pingos might vary, and thus how different processes may produce landforms that are classified the same.

7.2.7. The Pingo-Lithalsa Continuum

The problems that definitions of open-system pingos currently have are well outlined by Ballantyne (2018). Earlier studies defined open-system pingos on account of their geomorphology and composition. The word "pingo" is derived from the Inuit for conical shaped hill (Porsild, 1938), for which Lagoon Pingo does not fit. In their glossary of permafrost terms, Harris et al. (1988) make the distinction that pingos consist of a core containing massive ice, formed by the injection of groundwaters. However, this explanation does not account for all open-system pingos, as this does not explain the inferred segregation ice domination at Lagoon Pingo (Chapter 4) or indeed at the other Adventdalen pingos (Ross et al., 2007).

More recent works have therefore attempted to constrain the definition of an open-system pingo, given the broad range in characteristics for which this terminology has been applied. Arguably the most unifying aspect that encompasses the full range of open-system pingo morphologies and composition is the process through which they have formed; whereby the groundwater hydraulic pressure exceeds the strength of the overburden to cause the upward heaving of the surface (Ross, 2013; Ballantyne, 2018). Even then, many pingos have been found to show evidence of formation under a combination of both hydraulic and hydrostatic pressures (Christiansen, 1995; Gurney and Worsley, 1996). These arguments have been levied against Adventdalen pingos, including Lagoon Pingo, whereby the aggradation of permafrost downwards following glacio-isostatic uplift amounts to a hydrostatic pressure that may encourage the upwelling of groundwater, and subsequent pingo formation (Hornum et al., 2021). Even though an explanation for the artesian conditions at Lagoon Pingo has been provided through the notion that the coarser-grained unit acts as a confined aquifer with a high potentiometric head, the distinction between closed- and open-system pingos upon their pressurisation mechanism is not necessarily clear cut.

The interpretation of segregation ice within Chapter 4 prompts discussions over the similarities between Lagoon Pingo and other permafrost mounds. It has been noted that the composition of some nearshore pingos are most

similar to lithalsas (Ross et al., 2007; Ross, 2013); frost mounds formed primarily from segregation ice that lack peat cover (e.g. Pissart, 2002; van Everdingen, 2005). This is true of Lagoon Pingo, whereby the geomorphology and structure of the pingo are more reflective of a lithalsa than that of a pingo, and thus Lagoon Pingo can be interpreted as a hybrid form. However, in contrast to lithalsas, Lagoon Pingo hosts year-round perennial springs.

Compared to the current, strict, but often insufficient categorisation of pingos and lithalsas (or indeed other frost mounds), Lagoon Pingo highlights that this terminology is best envisaged within a continuum or spectrum of frost mound forms. The inference that segregation ice dominates within Lagoon Pingo, on account of both its age and location within frost-susceptible soils, reflects a hybridity in its structure. Ultimately, a "one definition fits all" type approach does not reflect the true diversity of pingos that can occur.

7.3. Integrated Geophysics in Holocene Marine Environments

7.3.1. Electrical Resistivity Tomography

In Chapter 4, electrical resistivity tomography (ERT) was used to non-intrusively identify resistivity distributions around the pingo, which were interpreted in terms of pingo structures and form. However, whilst ERT was largely effective in determining the immediate near-surface of Lagoon Pingo, it is noted that some parts of the profile featured a high number of measurements that did not meet the pre-processing filtering requirements. Elsewhere, parts of the longer profiles contained low sensitivities. These issues are attributed to the collection of ERT data during the winter months.

Many of the failed measurements can be attributed to poor electrode contact resistances (e.g. Juliussen et al., 2012). This can be attributed to the difficulty in obtaining good contact with the subsurface into the frozen, and thus resistive surface, through the compacted snow. Yet whilst measures were taken to counteract possible issues with electrode contact, including the use of saline water around the electrodes, problems remained in some parts of the profiles. In environments such as Svalbard, the seasons where electrode contact

issues are more likely to occur coincide with the period where remote field sites are most accessible, as frozen ground enables travel by snowmobile. As opposed to galvanic systems, the use of capacitively-coupled systems may therefore be preferable in permafrost environments where the surface is highly resistive (Kneisel et al., 2008).

Further issues were apparent with the range of resistivity at Lagoon Pingo. The colocation of saline permafrost (~10 Ωm) with surface icings (> 10^4 Ωm) resulted in lower sensitivity beneath the icings in inversion models, and limited the depth of investigation in these areas. This limited the interpretation of subsurface structure, particularly around the pingo spring. Similar issues have been experienced in relation to ERT studies of other periglacial landforms within Adventdalen, where steep resistivity gradients resulted in poor inversion reliability (Juliussen et al., 2012). As these extreme ranges in resistivity are characteristic of saline permafrost environments such as Adventdalen, the possibility of poor sensitivity following inversion needs to be considered during survey design when conducting ERT investigations in other similar environments.

Despite issues with electrode contact and the range of resistivity within the environment, it was notable that electrical resistivity tomography features negative apparent resistivities in both normal and reciprocal measurements. Whilst these are usually considered erroneous (Jung et al., 2009), they are suggested to have occurred due to the concave shape of the pond through which the pingo spring emerges, and the extreme range in resistivity produced by the close proximity of high resistivity ice (>10^4 Ωm), and low resistivity marine muds and clays (~100 Ωm). The possibility that negative apparent resistivities can result from subsurface geological structures should therefore be explored further within the context of permafrost environments. Negative apparent resistivities may occur preferentially within environments characterized by glacio-isostatic uplift, as extreme resistivity contrasts between highly resistive ice and conductive saline permafrost are more common. These environments may also host geological and geomorphological structures similar to those discussed by Jung et al. (2009), in that conductive marine clays may be intertwined with resistive ice.

7.3.2. Seismic Investigations

In Chapter 4, seismic investigations were undertaken with the objective of identifying the structure underlying Lagoon Pingo. Active source seismic methods are well-established in geomorphological investigations (Schrott and Sass, 2008), and have previously been undertaken to identify the subsurface structure beneath Innerhytte Pingo (Rossi et al., 2018). At Lagoon Pingo, the wavefront inversion of seismic refraction data depicted a spatially heterogeneous active layer. Meanwhile, whereas seismic reflection data was expected to have identified the local permafrost thickness at a depth similar to that of Yoshikawa and Harada (1995), no clear interface was identified. Instead, common-offset processing of the seismic reflection data revealed a clear reflection at ~68 m, which was interpreted as the boundary between Holocene marine muds and clays, and underlying Cretaceous shales. This was subsequently introduced as an input parameter to the four-phase modelling, enabling an enhanced interpretation of the transient electromagnetic data. Ultimately, seismic investigations were successful in identifying the homogenous structure at Lagoon Pingo.

The absence of ground truthing through coring, boreholes or well logs limit the interpretation of the seismic data. Obtaining ground truth data at Lagoon Pingo could therefore be advantageous for a number of reasons. Firstly, it would provide verification of the interpretations, with seismic data allowing for the extrapolation of borehole or core data across a wider area. Secondly, it would enable the more enhanced parameterisation of a number of rock physics relationships, that could then be used to enhance interpretation of subsurface characteristics. For example, sediment analyses on Lagoon Pingo could be used to parameterise a Kozeny-Carman-Bear type relationship for fluid flow, which would further enhance the analysis of hydraulic conductivity and porosity on site.

The combination of more detailed seismic data alongside ground truth data would enable an enhanced analysis of subsurface characteristics. For example, this would enable a more thorough usage of the MuLTI (Multimodal

Layered Transdimensional Inversion; Killingbeck et al., 2019) set of inversion algorithms, which were otherwise used within the TEM inversion in Chapter 6. For example, in combination with borehole data, more detailed seismic data would enable an analysis and shear waves (V_s) as a function of depth. This would provide a much improved analysis of the local permafrost by providing detail regarding the depth and condition of this layer, providing more realistic constraints for later four-phase modelling.

7.3.3. Self-Potential Investigations

In Chapter 5, self-potential measurements have been proven to be useful in the spatial identification of groundwater flow patterns around an open-system pingo. Whilst self-potential measurements have previously been used in similar or analogous environments (e.g. Scapozza et al., 2008; Thompson et al., 2012; Weigand et al., 2020), they have hitherto not been conducted on the monitoring of open-system pingos with active groundwater springs to the author's knowledge. The identification of the spatial pattern of self-potential around Lagoon Pingo correspond with previous studies identifying the self-potential response of groundwater flow (e.g. Revil et al., 2005; Minsley, 2007), and indicates the potential future effectiveness of self-potential in establishing subsurface migration of groundwaters in similar environments.

Temporally, the changes in streaming potentials are more complex, yet provide insight into how self-potential techniques may be utilised effectively in the longer-term monitoring of pingo dynamics. Particularly, self-potential measurements at Lagoon Pingo correspond well with hydrofracture events related to the icing on the surface that caps the spring during the winter months. The understanding of the frequency of these hydrofracture events may be pivotal in identifying the nature of methane release during the winter months, given that methane emission through fractures within the ice lid is possible, and enable anoxic waters to ventilate (Hodson et al., 2019).

Despite this, the limitations in Chapter 5 are evident, and thus demonstrate a scope for future self-potential studies both at Lagoon Pingo, and elsewhere within methane-emitting open-system pingos. Firstly, there is scope for further

spatial resolution within self-potential measurements, to more precisely determine the network of groundwater flow around Lagoon Pingo. For example, this may be conducted by using more electrodes within the current spatiotemporal array. This would provide more datapoints around the pingo, thus providing a great constraint on the groundwater flowpaths. In a spatiotemporal self-potential array on the mountain slope of Schilthorn, Switzerland, Weigand et al. (2020) evaluated groundwater flow using 20 electrodes across 16 locations, enabling relatively high spatial resolution monitoring of the evolution of local permafrost evolution. Furthermore, Weigand et al. (2020) combine electrodes with additional temperature sensors, which would enable a more precise evaluation of temperature changes on self-potential signal.

Alternatively, the completion of a grid of self-potential measurements would have identified the 2-D spatial pattern of potentials around Lagoon Pingo, and would have enabled further evaluation on the local groundwater flow paths. Conducting this at Lagoon Pingo is challenging; localised driftwood debris washed up on the pingo following storm tides is problematic in the movement of a roving electrode connected to a reference. Whilst the opportunity to collect a 2-D grid of measurements was limited here due to a range of external factors (e.g. field assistant availability, instrument availability and logistical resource limitations), future investigations should intend to collect this for a more precise constraint on the local spatial groundwater dynamics.

Secondly, a longer-term measurement array would enable an analysis of the alluvial fan aquifer recharge, and pressure release through this hydrofracture mechanism over a longer time period. This would allow a determination of the frequency of these fracture events, and establish the factors that contribute to the fracturing of the icing lid on the perennial pingo spring. Obtaining an understanding and appreciation of the icing lid is pivotal towards accurately constraining rates of winter methane evasion rates, which are expected to contribute significantly towards annual emissions (Hodson et al., 2019). If combined with localised monitoring of methane, longer-term self-potential monitoring may contribute towards highlighting the dynamics of methane release associated with icing fracturing, given that this methane is trapped

whilst the ice lid remains intact (Hodson et al., 2019). In addition to this, continuation of the self-potential measurement array within the summer months would allow an assessment of how this corresponds to spring discharge from the pingo. This would then enable an interpretation of discharge during the winter months, without cracking or breaking the ice lid manually as is required at present. Understanding the discharge of Pingo Spring would allow for more precise estimates of methane emissions from the site, and enhance understanding of the factors that may result in the variability of groundwater discharge over time.

Lastly, Lagoon Pingo may provide an optimal location for more experimental self-potential arrays, providing a field laboratory for utilising the latest setups within an Arctic permafrost environment. Among possible setups that may be considered are those including so-called internet of things (IoT) devices, which are low-cost, adaptable to a range of scenarios, and easier to deploy and maintain. As Weigand et al. (2020) summarise, the latest microcomputer-based environments, such as Arduino or ESP32, provide open-source and adaptable platforms with which self-potential measurements could be made, without the requirement for consistent maintenance given these formats require low power. This is particularly pertinent in Arctic environments, where solar panels cannot be used effectively during low light conditions in the winter through the polar night. Additionally, these platforms may prompt the gradual move to a more decentralised and distributed system of self-potential monitoring, allowing the measurement of potentials based on a small group of electrodes as opposed to all electrodes connected to a centralised logger (Weigand et al., 2020). This would remove the single point of failure present within self-potential studies in general, improving the resilience over current arrays whilst lowering the need for constant maintenance.

7.3.4. Transient Electromagnetics

Chapter 6 demonstrates how transient electromagnetics (TEM) provides a non-intrusive, yet effective geophysical imaging method for obtaining the electrical resistivity properties of subsurface media within permafrost and High

Arctic environments. In the case of Svalbard, TEM is particularly effective when compared with galvanic electrical resistivity tomography (ERT) systems as it circumvents electrode contact issues apparent during the frozen months where these environments are commonly most accessible, as frozen rivers and surfaces allow traversal by snowmobile to remote areas. For example, previous studies conducted on Svalbard have highlighted particular problems related to electrode contact in the coldest months despite the use of mitigation practices such as the salting of electrodes (Juliussen et al., 2012; Chapter 4), in contrast to TEM which only relies upon relatively flat ground that allows for the placement of the receiver. Furthermore, in remote areas such as Svalbard, electrical interference and noise can be expected to be minimal, and low background noise was demonstrated in the preliminary readings taken without a transmitter current. In saline permafrost environments, TEM is particularly effective when compared to ERT, as these environments are susceptible to high resistivity contrasts between conductive sediments and resistive ice, and which may provide complex electrical responses with traditional ERT surveying methods, such as negative apparent resistivities (Jung et al., 2009). Consequently, the data enable a much greater depth of investigation when compared to ERT taken previously at the Lagoon Pingo site (Chapter 4) and those taken from elsewhere within the valley (Hornum et al., 2021), therefore enabling a geoelectrical evaluation of deeper subsurface structures and interfaces than would otherwise be possible.

Yet whilst the use of TEM here permits the non-intrusive investigation of deeper pingo structure, the true nature the alluvial fan is not necessarily clear, and thus the exact dimensions and sedimentology of this section requires further investigation. For example, whilst it is assumed that coarser, alluvially-derived sediments are interspersed with the fine-grained Holocene marine clays following our current understanding of the depositional history of the Lagoon Pingo surroundings (e.g. Lønne and Nemec, 2004; Gilbert et al., 2018), further work should consider to ascertain the true sedimentological characteristics of this coarser-grained layer beneath the pingo. Secondly, limitations in the sensitivity of the transient electromagnetic method to conductance (the product of conductivity and thickness) renders accurate

determination of the bounds of the interfingering of alluvial fan deposits and Holocene marine muds and clays difficult, as inversion of the acquired data is a non-unique problem (Killingbeck et al., 2020). The use of a probabilistic inversion approach that enables the use of constraints intends to minimize this issue, but whilst this clearly denotes the presence of elevated resistivities attributable to the alluvial fan between the permafrost base and top of the Cretaceous shales, further ground truthing through drilling or detailed well logs is required to accurate constrain the exact bounds of this section.

7.3.5. Four-Phase Modelling

Using the combination of seismic bulk velocities with MuLTI-TEM inversions of the transient electromagnetic data, four-phase modelling enabled enhanced interpretations of the subsurface resistivity distribution at Lagoon Pingo. The approach adopted followed that of Pellet et al. (2016), where it is assumed that the permafrost and sub-permafrost layer are similar in sedimentology, and thus a constrained rock fraction is used to set the porosity of the permafrost layer. Previous use of the four-phase model has been limited to the identification of subsurface ice contents (e.g. Hauck et al., 2011) and soil moistures (Pellet et al., 2016), with utilisation of this system of equations having almost exclusively occurred in studies of mountain permafrost (Hauck et al., 2011; Pellet et al., 2016; Mollaret et al., 2020). In Chapter 6, this approach is adapted to provide an explanation behind heterogeneities within the subsurface in a Holocene marine permafrost environment.

The approach adopted for Lagoon Pingo is advantageous, as it minimises the primary issues with the system of equations. In general, the four-phase model takes advantage of resistivity and velocity contrasts to prescribe an estimate to the rock, water, ice and air content of the subsurface (Hauck et al., 2011). As water and air are markedly different in velocity and resistivity values, these variables are commonly well-constrained. In comparison, as rock and ice can exhibit similar resistivities and seismic velocities, difficulties can arise when discerning the individual contribution of rock and ice fractions (Hauck et al., 2011). Under the assumption that there is no major sedimentological

difference between frozen and unfrozen layers, the application of a permafrost base constraint removes the need to identify the individual constraint of a rock and ice fraction. This also overcomes the inherent underdetermination within the general system of equations, as the three equations would otherwise dictate the value of four variables, thereby resulting in no unique solution.

At Lagoon Pingo, improvements could be made on the parameterisation of the four-phase modelling according to ground truth data. Whilst the four-phase model is currently parameterised as well as possible according to existing data and models, the collection of samples from wells or boreholes may provide further parameterisation that can be incorporated. Wells and boreholes would additionally be able to permit the more accurate definition of permafrost and porosity constraints, therefore improving the accuracy of the four-phase models. Lastly, data from cores or well samples would provide a means of comparing four-phase model results, providing verification that these are indeed accurate.

Chapter 8: Conclusions

8.1. Overall Conclusions

The results presented in this thesis provide a range of new insights into the subsurface characteristics at Lagoon Pingo, with implications and the current understanding of open-system pingo formation, development, and their role as conduits enabling methane release. Electrical resistivity tomography investigations of Lagoon Pingo reveal low resistivities that preclude the presence of a massive ice core, and instead favour the dominance of segregation ice within the internal pingo structure. Notably, this is similar to the findings from studies of the other open-system pingos beneath the Holocene marine limit in Adventdalen (e.g. Ross et al., 2007). The importance of fine-grained frost-susceptible sediment is outlined in the formation of Lagoon Pingo, with a structure that is more representative of a lithalsa than an open-system pingo. Meanwhile, active-source seismic investigations determine that Holocene marine muds and clays are ~68 m thick in this location.

Self-potential measurements recorded around the central pingo spring indicate groundwater flows beneath the pingo complex from the northeast, where an alluvial fan meets fine-grained Holocene marine muds and clays on the valley bottom. Potentials are characterised by high magnitude changes on a low frequency, and correspond with visual observations of recent water flow and hydrofracturing of the pingo icing on the surface. The spatial patten of the potentials recorded theorise that the alluvial fan deposits may provide a hydraulically conductive heterogeneity beneath the pingo spring that enables groundwater flow through poorly permeable Holocene muds and clays. These results also indicate that methane from upland sources, including from dissociation of gas hydrates, require consideration in the context of methane emissions from Lagoon Pingo.

Transient electromagnetic investigations of Lagoon Pingo provide geophysical evidence of this coarser-grained deposits beneath Lagoon Pingo, interfingering with Holocene marine muds and clays. This interpretation is favoured by four-phase modelling, which indicates that a layer with enhanced resistivity can only be explained by a coarser-grained sediment fraction. This

sedimentological interpretation, inferred as related to the alluvial fan on account of its geometry, additionally fits with the perceived regional landscape model, where alluvial fans developed during the early Holocene (Lønne and Nemec, 2004), followed by ongoing marine sedimentation within the valley (Gilbert et al., 2018). Previous theories behind the apparent colocation of alluvial fans and open-system pingos (e.g. Humlum et al., 2003) are inconsistent with the characteristics of Lagoon Pingo; instead it is inferred that the alluvial fan acts as a confined aquifer bound by permafrost and poorly permeable Holocene sediments above, and impermeable sediment and shales beneath. Saturation of the interfingered alluvial fan strata would explain the hydraulic pressurisation of pingo groundwaters, and is consistent with the self-potential observations.

The interpretation of an alluvial fan beneath Lagoon Pingo provides circumstances that are conducive to pockmark formation during the Holocene. As pressurised groundwaters are still required to navigate through ~30 m of poorly permeable sediments between the alluvial fan and the surface, the glacio-isostatic uplift of this pockmark and an associated submarine seep would explain how a surface spring occurs in this location. The depiction of a depression in alluvial fan sediments directly beneath the central pingo spring provides evidence towards this idea, and can be explained in the context of current pockmark formation theory (e.g. Hovland, 1987). Whilst the terrestrial emergence of submarine pockmarks, either by glacio-isostatic uplift or through eustatic sea-level rise is discussed as a potentially significant contributor of methane to past and present climate budgets, future modelling should identify whether formation of a pockmark at Lagoon Pingo is feasible, and whether similar mechanisms may apply to other open-system pingos.

8.2. Recommendations for Future Research

8.2.1. Lagoon Pingo

Whilst the investigations presented in this thesis provide a geophysical characterisation of Lagoon Pingo, further interpretations are limited by the absence of ground truth data. Further investigations of Lagoon Pingo should therefore expand upon this work through the collection of cores or detailed borehole logs, to provide physical evidence that can be used to compare and verify interpretations made through geophysical investigation. Within the permafrost layer, these methods would provide an accurate constraint on the local permafrost thickness, enabling a more precise parametrisation of four-phase modelling (Chapter 6). Cores of this section could be particularly fruitful, and would allow for an assessment of the segregation ice interpretation presented in Chapter 4. Resolving the uncertainty surrounding the interpretation of low resistivities as segregation ice would improve the ability to resolve internal pingo structures using geophysical methods.

Deeper borehole logs and cores should target the interpreted alluvial fan deposits beneath the pingo as a priority. As proximity to an alluvial fan represents the most common geomorphological position for pingos on Svalbard (Demidov et al., 2022), physical evidence of the role of the alluvial fan beneath Lagoon Pingo would form an important step addressing the hydrological problems associated with open-system pingos generally (Ballantyne, 2018). Firstly, radiocarbon dating of alluvial fan sediments beneath Lagoon Pingo would provide constraint on the regional model of landscape evolution (Lønne and Nemec, 2004), enabling further evaluation of the theory that Lagoon Pingo may have evolved from a submarine pingo (Hodson et al., 2019). Secondly, it would provide verification of the presumed interfingering of Holocene muds and clays with the alluvial fan, and the nature of the sedimentology within this section. Lastly, it would provide a greater assessment of the hydrogeological role of the alluvial fan, in providing a confined aquifer and explaining how local groundwaters are hydraulically pressurised in this location. Given the similar geomorphological circumstances of some open-system pingos on Svalbard, these findings could be regionally

important, considering the role of open-system pingos in enabling methane release through the permafrost (Hodson et al., 2019; 2020).

8.2.2. Pingo Sites for Future Work

Theories surrounding the hydrogeological role of alluvial fans and submarine seep uplift have been developed following the interpretation of geophysical data at Lagoon Pingo, but uncertainty remains on whether these represent an isolated case, or whether these mechanisms are feasible for other open-system pingos in the High Arctic. In Chapter 7, a number of active pingos which occur in similar geomorphological positions to Lagoon Pingo are highlighted, and should be considered as priorities for future investigations. Geophysical investigations of these pingos would provide a direct comparison with Lagoon Pingo and other previous studies conducted on the pingos in Adventdalen (Yoshikawa, 1993; Yoshikawa and Harada, 1995; Ross et al., 2007), and would provide further knowledge on the range of pingo structural and hydrological characteristics more generally. Furthermore, investigations of open-system pingos close to the contemporary coastline could be used to evaluate the theory that pingos may arise from submarine springs (e.g. Orvin, 1944).

In tandem with investigations constraining their groundwater chemistry, further investigations in these open-system pingos would elucidate their role in enabling methane emissions from intra- and sub-permafrost reservoirs more broadly. Further constraint in this mechanism would improve the assessment of emissions from open-system pingos in bottom-up methane budgets.

8.2.3. Geophysical Investigation in Permafrost Environments

Saline permafrost environments that have developed from the deposition of fine-grained sediments since the late Holocene are important in the context of Arctic methane budgets (Jones, 2019). In addition to the occurrence of open-system pingos in these environments, they often host accumulations of saturated organic sediments that produce methane (Turetsky et al., 2020).

They are also among some of the most challenging environments for geophysical investigations. For example, ground penetrating radar is ineffective in saline permafrost in fine-grained soils, as these sediments are highly conductive. As evidenced by the electrical resistivity tomography investigation in Chapter 4, the colocation of high resistivity ice with low resistivity saline permafrost is problematic for the sensitivity of geoelectrical methods. As geophysical techniques provide the most efficient non-intrusive method in the determination of permafrost thickness, extent, and in ground ice content, advances in the use of thesel methods in Holocene permafrost environments should be viewed as a research priority. Advances in the application of geophysical methods include improvements in the instrumentation used to collect data, the joint inversion of geophysical datasets, or petrophysical calculations adjusted for clayey contents in these environments. This would enable the more precise determination of these phenomena, their risk to permafrost degradation, and their role in the local and wider methane budget. This would ultimately allow for a more detailed evaluation of the subsurface characteristics of open-system pingos in these environments, and their role as conduits through continuous permafrost enabling methane release.

Appendix 1: Supplementary Material for Chapter 4

Introduction

In this supporting information, we present results and interpretations from initial data evaluations, in addition to results from our appraisal of the crossover between inversions. Section A1.1 and Figure A1.1 present initial analysis of the seismic refraction, from first arrivals of the shot gathers. Section A1.2 and Figures A1.2-A1.3 indicate the pre-inversion results from the Electrical Resistivity Tomography data, with pseudosections depicting the average apparent resistivity, and error between normal and reciprocal measurements. Section A1.3 provides the appraisal of the crossovers between inversions, including Figure A1.4 which shows the extended crossover between long profiles.

A1.1. Common Offset Seismic Refraction Interpretation

The near-surface seismic refraction is clearly present at the top of the common offset gather (Figure 4.4), with an analysis of first seismic arrivals (Figure A1.1) suggesting an overlying apparent layer velocity of 403.2 ms^{-1} with positive offsets, and 384.8 ms^{-1} whereby offsets were negative, and 394 ms^{-1} when both are combined. The thickness of this top layer, as determined by the intercept of the refracted arrivals with the y-axis at a zero offset suggests a layer depth of 2.58 m (± 0.04 m). In comparison, the second layer in this refraction features a greater velocity of 2154 ms^{-1} where offsets are positive, and 2069 ms^{-1} for negative offsets.

A1.2. Electrical Resistivity Tomography Pre-Inversion Results

Pseudosections highlighting the average apparent resistivities received for each quadrupole is shown in Figure A1.2. Apparent resistivities vary in magnitude considerably, with maximum apparent resistivities in the order of ~50 kΩm found at low depths in lines R1, R2 and R3. These apparent resistivities occur at the crossover between these lines, above icings where

active groundwater upwelling is evident on the surface. The smallest apparent resistivities are also found in line R3, with a series of 20 points with negative apparent resistivities found at approximately 170 m along this profile. In contrast, profiles which do not cover icings associated with groundwater springs feature much smaller ranges between maximum and minimum apparent resistivity, with lines R4 and R5 depicting resistivities between ~10 – 450 Ωm, and 20 – 80 Ωm respectively. For each of these lines, a general pattern is evident with increased resistivities in the near surface, compared to lower apparent resistivities at greater depths. Notably, some profiles highlight an absence of measurements for quadrupoles in some sections, with this most evident at depths below 10 m on line R2.

To appraise the quality of the obtained apparent resistivities, pseudosections comparing the difference between normal and reciprocal measurements, normalised against the average for each quadrupole are depicted in Figure A1.3. On the longer profiles, reciprocal errors are lowest at smaller depths, with much greater error and data quality at higher depths. On line R1, much of the reciprocal error appears to stem from individual electrodes, with the pseudosection showing lines of points which all feature highly variable reciprocal error values. Additionally, reciprocal errors in the order of 50% can be found in a region of the profile between 150 m and 180 m, at a depth of 30 m. However, most of the data fit within a suitable range of error, including in points which correspond to high apparent resistivities, negative apparent resistivities, and in sections whereby apparent resistivities depicts a highly heterogeneous subsurface. Besides the missing measurements for line R4, high reciprocal errors are present at great depths (>30 m), whilst measurements above 10 m show reciprocal errors which are largely negligible. This is only disrupted where measurements are missing (at approximately 100 m), or linked to a particular electrode (e.g. at 177.5 m). In contrast, most of the shorter profiles (R4 and R5) depict low reciprocal errors below 10%, with the northern parts of profile R3 depicting much greater variability in resistivities, stemming from the electrode located at 20 m. Points which do not fit within the 10% reciprocal error threshold were removed prior to inversion.

A1.3. Electrical Resistivity Tomography Inversion Crossover Appraisal

The analysis of the crossover between separate tomographic inversions provides an additional means of evaluating the inversions. However, poor sensitivity in lines R1 and R2 whereby the quasi-perpendicular shorter profiles R3 and R4 intersect render a crossover analysis redundant, as these points do not reach the required threshold whereby the inversion is deemed sensitive to the data. Despite this, the crossover between both longer profiles is generally strong, with a comparison of resistivity values from the surface to the edge of sensitivity providing R^2 values that average 0.82. A comparison of the crossover between lines R1 and R2 is shown in Figure A1.4, alongside associated R^2 values for each part of the profile. In general, large sections of the line show strong agreement, with R2 above 0.8 for sections which cover the spring icing where there is sensitivity (245 m and above) and between a distance of 180 – 210 m. The crossover between these profiles is weakest at areas close to the margins of sensitivity, including the end of R^2, and in the area directly to the southeast of the pingo spring, whereby R2 shows a larger low resistivity body (c. 100 Ω m) at the surface compared to R1. For the crossover between R1 and R5, the R^2 obtained equals 0.9432, which suggests strong agreement in the vertical trend of resistivity change. However, the equation of this line equals y = 0.19x + 0.97, and suggests that in spite of a similar resistivity pattern, the change in the magnitude of resistivities of both profiles vary. Whilst an interpretation of increased resistivity at a shallow depth holds true, caution should be taken on any interpretation made upon the magnitude of measurements in this zone.
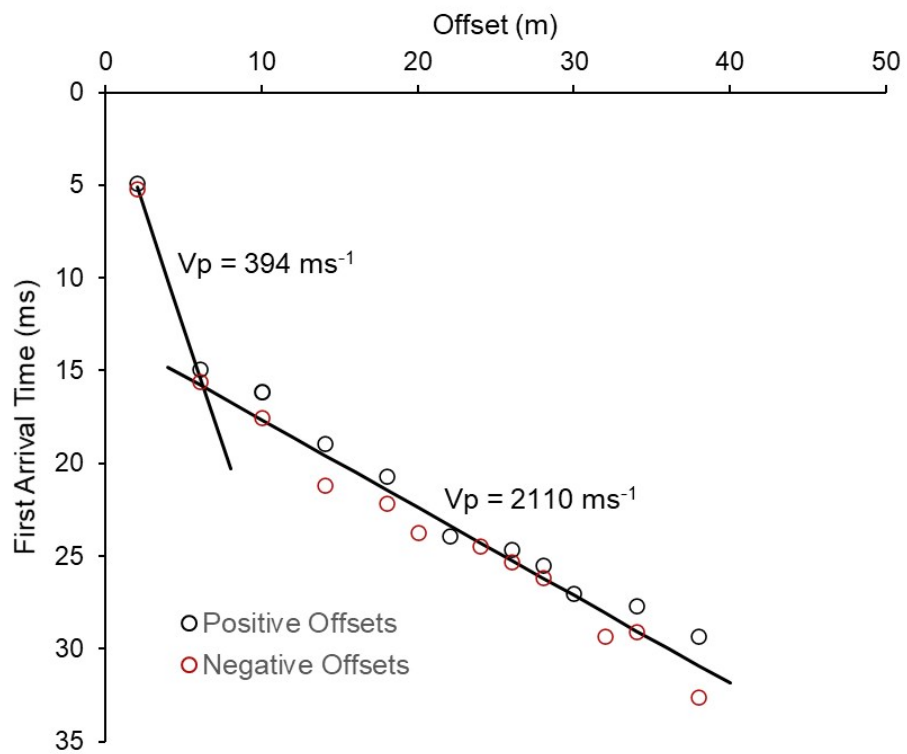
Figure A1.1. Analysis of first arrivals of the common offset gather. A two-layer model (consisting of an active layer and permafrost) is suggested, with average velocities (given positive and negative offsets) shown.
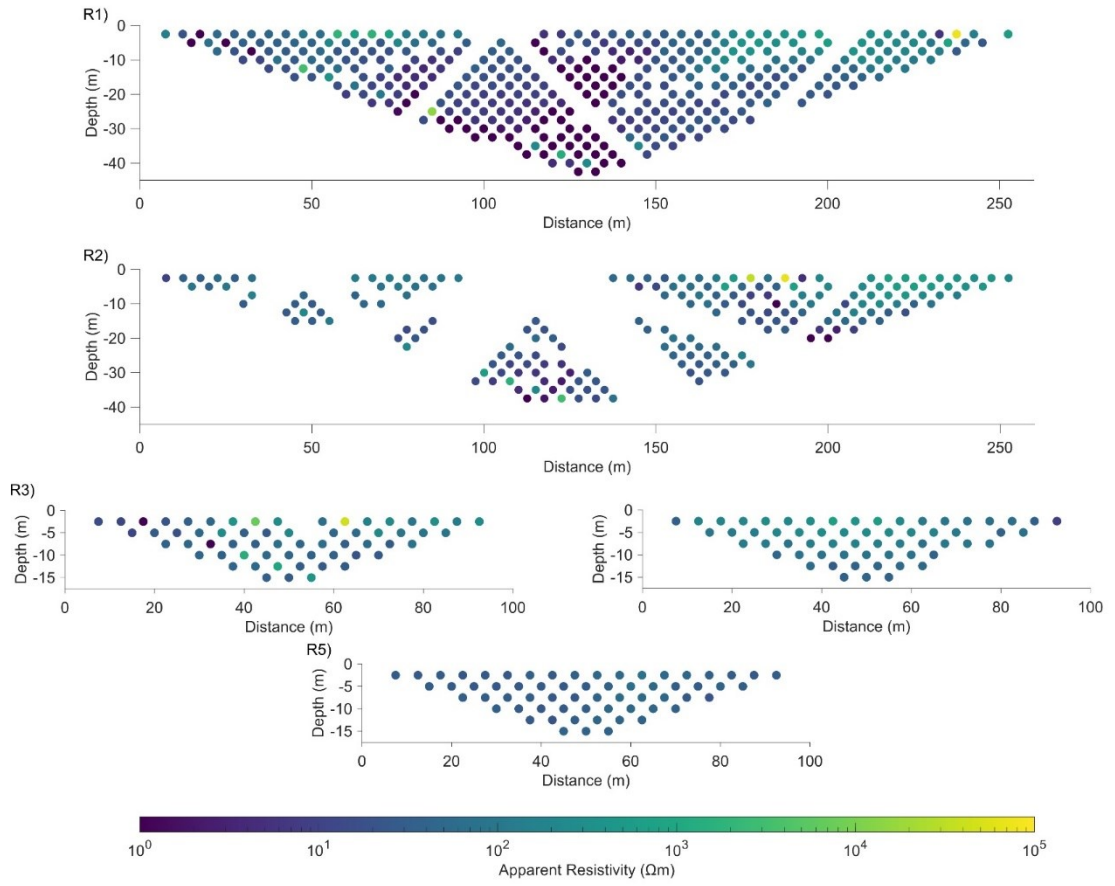
Figure A1.2. Pseudosections depicting the average apparent resistivity obtained for each profile
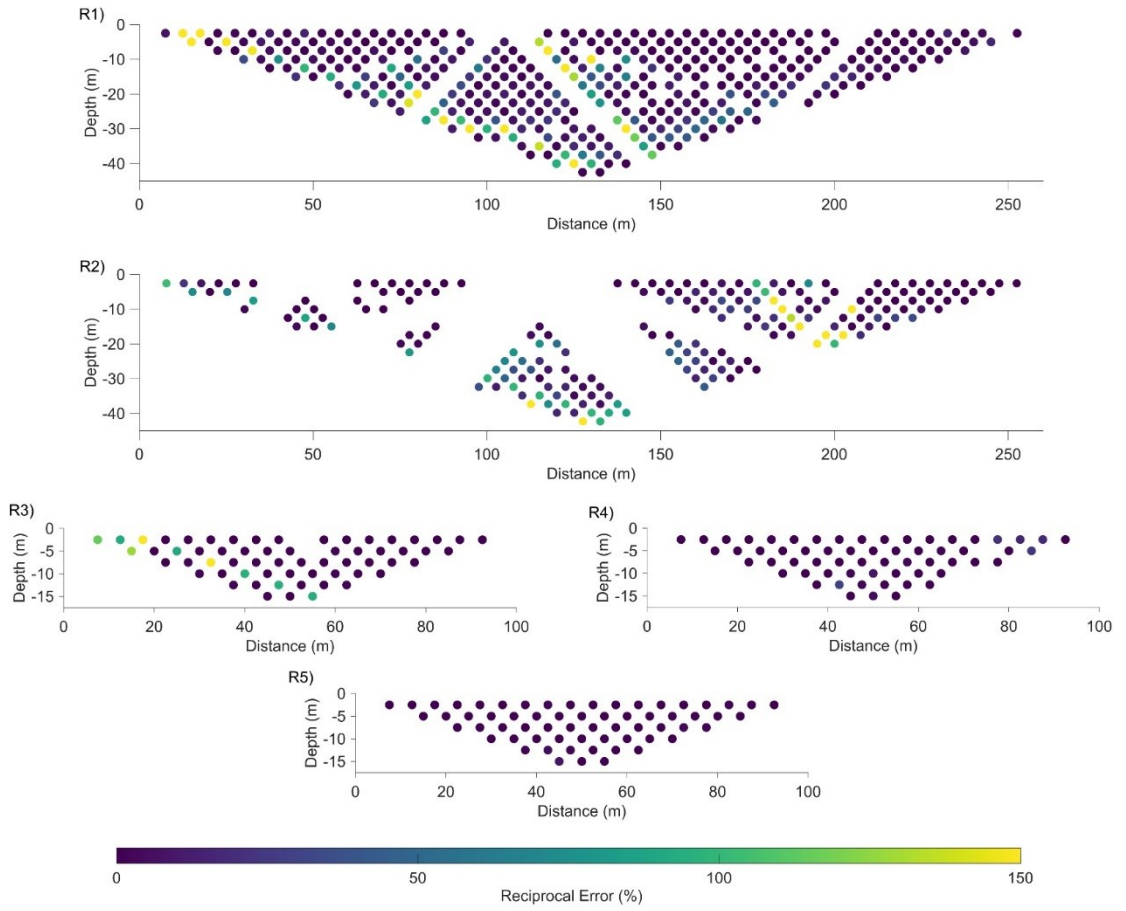
Figure A1.3. Pseudosections showing the difference between normal and reciprocal apparent resistivity measurements for each profile, normalised against the average resistivity.
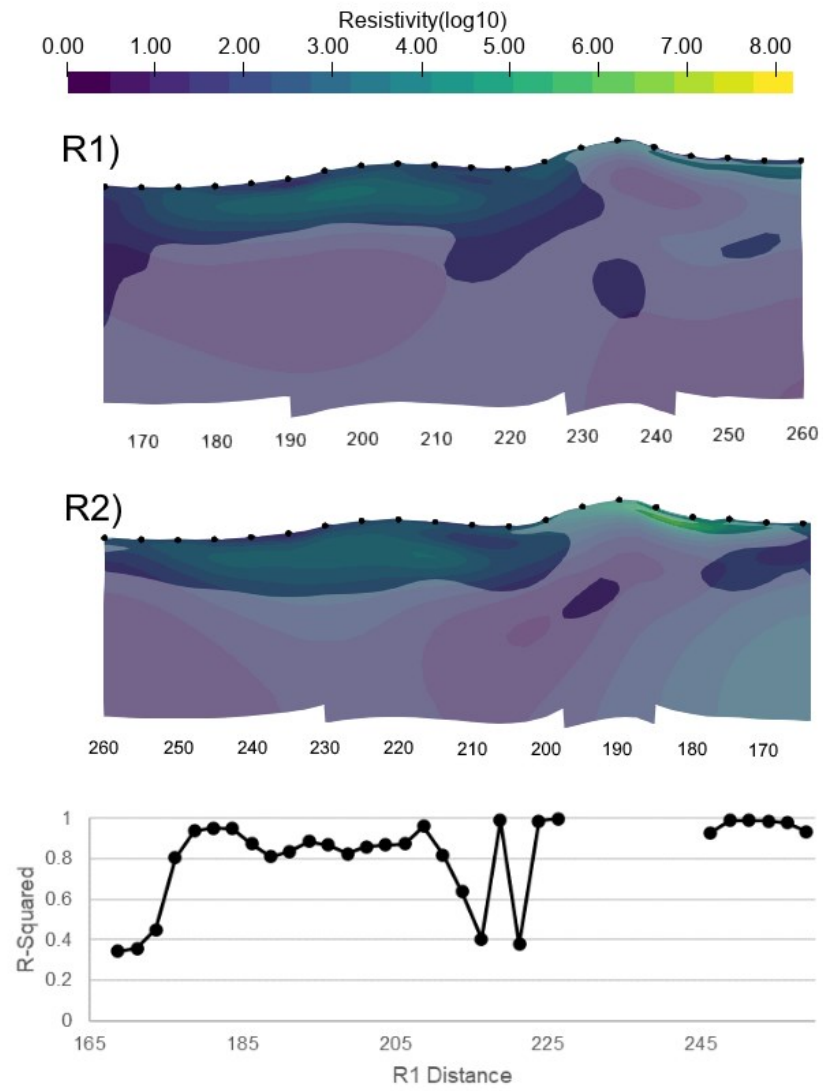
Figure A1.4. Inverted tomogram sections from R1 and R2 which show sections where these overlap, along with R^2 obtained when comparing spatially corroborated interpreted resistivities in sensitive regions from both profiles.

Table A1.1. Parameterisation used for the seismic refraction tomographic model.

Parameter	Value
Space increment	0.5
Maximum number of iterations	20
Maximum time	10800 seconds
Threshold	0.001
Model change A	1
Model change B	0.1
Convergence search	5
Max def. change (%)	200
Def. data-variance	0.01
Maximum beam width	10
Start curved ray	1
Average x smoothing	2
Average z smoothing	0
Minimum velocity	1
Maximum velocity	4000

Reference List

Åkerman, H. J., & Johansson, M. (2008). Thawing permafrost and thicker active layers in sub-arctic Sweden. *Permafrost and Periglacial Processes*, *19*(3), 279–292.

Allard, M., Caron, S., & Bégin, Y. (1996). Climatic and ecological controls on ice segregation and thermokarst: The case history of a permafrost plateau in Northern Quebec. *Permafrost and Periglacial Processes*, 7(3), 207–227.

An, W. & Allard, M. (1995). A mathematical approach to modelling palsa formation: insights on processes and growth conditions. *Cold Regions Science and Technology*, 23, 231-244.

Andersen, D. T., Pollard, W. H., McKay, C. P., & Heldmann, J. (2002). Cold springs in permafrost on Earth and Mars. *Journal of Geophysical Research: Planets*, *107*(E3), 5015.

Andreassen, K., Hubbard, A., Winsborrow, M., Patton, H., Vadakkepuliyambatta, S., Plaza-Faverola, A., et al. (2017). Massive blow-out craters formed by hydrate-controlled methane expulsion from the Arctic seafloor. *Science*, 356(6341), 948–953.

Archie, G. E. (1942). The electrical resistivity log as an aid in determining some reservoir characteristics, *Petroleum Transactions of American Institute of Mining and Metallurgical Engineers (AIME)*, 146, 54–62.

Atchley, A. L., Coon, E. T., Painter, S. L., Harp, D. R., & Wilson, C. J. (2016). Influences and interactions of inundation, peat, and snow on active layer thickness. *Geophysical Research Letters*, *43*(10), 5116–5123.

Auriac, A., Whitehouse, P. L., Bentley, M. J., Patton, H., Lloyd, J. M., & Hubbard, A. (2016). Glacial isostatic adjustment associated with the Barents Sea ice sheet: A modelling inter-comparison. *Quaternary Science Reviews*, 147, 122–135.

Babiñski, Z. (1982). Pingo degradation in the Bayan-Nuurin-Khotnor Basin, Khangai Mountains, Mongolia. *Boreas*, *11*(4), 291–298.

Bælum, K., & Benn, D. I. (2011). Thermal structure and drainage system of a small valley glacier (Tellbreen, Svalbard), investigated by ground penetrating radar. *The Cryosphere*, 5(1), 139–149. https://doi.org/10.5194/tc-5-139-2011

Baelum, K., Johansen, T. A., Johnsen, H., Rod, K., Ruud, B., & Braathen, A. (2012). Subsurface structures of the Longyearbyen CO2 Lab study area in Central Spitsbergen (Arctic Norway), as mapped by reflection seismic data. *Norwegian Journal of Geology*, *92*, 377–389.

Ballantyne, C. K. (2018). Periglacial Geomorphology. Hoboken, NJ: Wiley-Blackwell.

Bayon, G., Loncke, L., Dupré, S., Caprais, J.-C., Ducassou, E., Duperron, S., et al. (2009). Multi-disciplinary investigation of fluid seepage on an unstable margin: The case of the Central Nile deep sea fan. *Marine Geology*, *261*(1), 92–104.

Beck, I., Ludwig, R., Bernier, M., Lévesque, E., & Boike, J. (2015). Assessing Permafrost Degradation and Land Cover Changes (1986–2009) using Remote Sensing Data over Umiujaq, Sub-Arctic Québec. *Permafrost and Periglacial Processes*, *26*(2), 129–141.

Berchet, A., Bousquet, P., Pison, I., Locatelli, R., Chevallier, F., Paris, J.-D., et al. (2016). Atmospheric constraints on the methane emissions from the East Siberian Shelf. *Atmospheric Chemistry and Physics*, *16*(6), 4147–4157.

Betlem, P., Senger, K., & Hodson, A. (2019). 3D thermobaric modelling of the gas hydrate stability zone onshore central Spitsbergen, Arctic Norway. *Marine and Petroleum Geology*, *100*, 246–262.

Binley, A. & Kemna, A. (2005). DC Resistivity and Induced Polarization Methods. In Rubin, Y. & Hubbard, S. S. (Eds.), *Hydrogeophysics* (pp. 129-156). Dordrecht, The Netherlands: Springer.

Binley, A., Ramirez, A. & Daily, W. (1995). Regularised Image Reconstruction of Noisy Electrical Resistance Tomography Data. In: Beck, M. S., Hoyle, B. S., Morris, M. A., Waterfall, R. C. & Williams, R. A. (Eds.) *Process Tomography – 1995, Proceedings of the 4th Workshop of the European Concerted Action on Process Tomography*, Bergen, 6-8 April 1995 (pp. 401-410).

Blanchy, G., Saneiyan, S., Boyd, J., McLachlan, P., & Binley, A. (2020). ResIPy, an intuitive open source software for complex geoelectrical inversion/modeling. *Computers & Geosciences*, 137, 104423.

Bockheim, J. G. (1995). Permafrost distribution in the southern circumpolar region and its relation to the environment: A review and recommendations for further research. *Permafrost and Periglacial Processes*, *6*(1), 27–45.

Bockheim, J. G. (2007). Importance of Cryoturbation in Redistributing Organic Carbon in Permafrost-Affected Soils. *Soil Science Society of America Journal*, *71*(4), 1335–1342.

Bogslovsky, V. A., & Ogilvy, A. A. (1973). Deformations of natural electric fields near drainage structures. *Geophysical Prospecting*, 21, 716-723.

Bohn, T. J., Lettenmaier, D. P., Sathulur, K., Bowling, L. C., Podest, E., McDonald, K. C., & Friborg, T. (2007). Methane emissions from western

Siberian wetlands: Heterogeneity and sensitivity to climate change. *Environmental Research Letters*, *2*(4), 045015.

Bondarev, V. N., Rokos, S. I., D.A., K., Dlugach, A. G., & Polyakova, N. A. (2002). Underpermafrost accumulations of gas in the Upper part of the sedimentary cover of the Pechora Sea. *Geologiya i Geofizika*, *43*, 587–598.

Bostock, H., Jenkins, C., Mackay, K., Carter, L., Nodder, S., Orpin, A., Pallentin, A., & Wysoczanski, R. (2019). Distribution of surficial sediments in the ocean around New Zealand/Aotearoa. Part B: Continental shelf. *New Zealand Journal of Geology and Geophysics*, 62(1), 24–45.

Bowen, G. J., Koch, P. L., Gingerich, P. D., Norris, R. D., Corfield, R. M., & Bains, S. (2001). High-resolution isotope stratigraphy across the Paleocene-Eocene boundary at Polecat Bench, WY (pp 73-88). In: Gingerich, P. D. (Ed.) *Paleocene-Eocene Stratigraphy and Biotic Change in the Bighorn and Clarks Ford Basins, Wyoming*. Ann Arbor, MI: University of Michigan.

Bowen, J. C., Ward, C. P., Kling, G. W., & Cory, R. M. (2020). Arctic Amplification of Global Warming Strengthened by Sunlight Oxidation of Permafrost Carbon to CO2. *Geophysical Research Letters*, *47*(12), e2020GL087085.

Braathen, A., Baelum, K., Christiansen, H., Dahl, T., Eiken, O., Elvebakk, H., et al. (2012). The Longyearbyen CO2 lab of Svalbard, Norway—Initial assessment of the geological conditions for CO2 sequestration. *Norwegian Journal of Geology*, *92*, 353–376.

Bradford, J. H. (2002). Depth characterization of shallow aquifers with seismic reflection, Part I—The failure of NMO velocity analysis and quantitative error prediction. *Geophysics*, 67(1), 89–97.

Bradford, J. H., & Sawyer, D. S. (2002). Depth characterization of shallow aquifers with seismic reflection, Part II—Prestack depth migration and field examples. *Geophysics*, 67(1), 98–109.

Brothers, L. L., Kelley, J. T., Belknap, D. F., Barnhardt, W. A., Andrews, B. D., Legere, C., & Hughes Clarke, J. E. (2012). Shallow stratigraphic control on pockmark distribution in north temperate estuaries. *Marine Geology*, *329–331*, 34–45.

Brown, J., Ferrians, O., Heginbottom, J. A., & Melnikov, E. (2014). *Circum-Arctic Map of Permafrost and Ground-Ice Conditions*. Boulder, CO: National Snow and Ice Data Center.

Brownlow, R., Lowry, D., Fisher, R. E., France, J. L., Lanoisellé, M., White, B., et al. (2017). Isotopic Ratios of Tropical Methane Emissions by Atmospheric Measurement. *Global Biogeochemical Cycles, 31*(9), 1408–1419.

Cable, S., Elberling, B., & Kroon, A. (2018). Holocene permafrost history and cryostratigraphy in the High-Arctic Adventdalen Valley, central Svalbard. *Boreas*, 47(2), 423–442.

Campbell, S. W., Briggs, M., Roy, S. G., Douglas, T. A., & Saari, S. (2021). Ground-penetrating radar, electromagnetic induction, terrain, and vegetation observations coupled with machine learning to map permafrost distribution at Twelvemile Lake, Alaska. *Permafrost and Periglacial Processes*, *32*(3), 407–426.

Cao, B., Gruber, S., Zhang, T., Li, L., Peng, X., Wang, K., et al., (2017). Spatial variability of active layer thickness detected by ground-penetrating radar in the Qilian Mountains, Western China. *Journal of Geophysical Research: Earth Surface*, *122*(3), 574–591.

Chand, S., Rise, L., Ottesen, D., Dolan, M. F. J., Bellec, V., & Bøe, R. (2009). Pockmark-like depressions near the Goliat hydrocarbon field, Barents Sea: Morphology and genesis. *Marine and Petroleum Geology*, *26*(7), 1035–1042.

Chand, S., Thorsnes, T., Rise, L., Brunstad, H., Stoddart, D., Bøe, R., Lågstad, P., & Svolsbru, T. (2012). Multiple episodes of fluid flow in the SW Barents Sea (Loppa High) evidenced by gas flares, pockmarks and gas hydrate accumulation. *Earth and Planetary Science Letters*, *331–332*, 305–314.

Chen, D., Rojas, M., Samset, B. H., Cobb, K., Diongue Niang, P., Edwards, S. et al. (2021). Framing, Context, and Methods. In: Masson-Delmotte, V., Zhai, P., Pirani, A., Connors, S. L., Péan, C., Berger, S. et al. (Eds.) *Climate Change 2021: The Physical Science Basis. Contribution of Working Group I to the Sixth Assessment Report of the Intergovernmental Panel on Climate Change* (pp. 923-1054). Cambridge, UK & New York, NY: Cambridge University Press.

Christensen, T. R., Ekberg, A., Ström, L., Mastepanov, M., Panikov, N., Öquist, M., et al. (2003). Factors controlling large scale variations in methane emissions from wetlands. *Geophysical Research Letters*, *30*(7), 1414.

Christiansen, H. H., Etzelmüller, B., Isaksen, K., Juliussen, H., Farbrot, H., Humlum, O., et al. (2010). The thermal state of permafrost in the Nordic area during the International Polar Year 2007–2009. *Permafrost and Periglacial Processes*, 21(2), 156–181.

Christiansen, H. H., Etzelmüller, B., Isaksen, K., Juliussen, H., Farbrot, H., Humlum, O., et al. (2010). The thermal state of permafrost in the Nordic area during the International Polar Year 2007–2009. *Permafrost and Periglacial Processes*, 21(2), 156–181.

Christiansen, H. H., Gilbert, G. L., Demidov, N., Guglielmin, M., Isaksen, K., Osuch, M. & Boike, J. (2020). Permafrost temperatures and active layer thickness in Svalbard during 2017/2018 (PermaSval) (pp. 236-249). In: Van

den Heuvel F., Hübner C., Błaszczyk M., Heimann M., Lihavainen H. (Eds.) *SESS report 2019. Longyearbyen, Svalbard: Svalbard Integrated Arctic Earth Observing System*.

Christiansen, H. H., Gilbert, G. L., Demidov, N., Guglielmin, M., Isaksen, K., Osuch, M., & Boike, J. (2019) Permafrost thermal snapshot and active-layer thickness in Svalbard 2016-2017 (pp. 26–47). In: Orr et al (eds): *SESS report 2018. Longyearbyen, Svalbard: Svalbard Integrated Arctic Earth Observing System, Longyearbyen*.

Christiansen, H. H., Humlum, O., & Eckerstorfer, M. (2013). Central Svalbard 2000–2011 Meteorological Dynamics and Periglacial Landscape Response. *Arctic, Antarctic, and Alpine Research*, *45*(1), 6–18.

Church, M., & Ryder, J. M. (1972). Paraglacial Sedimentation: A Consideration of Fluvial Processes Condition by Glaciation. *Geological Society of America Bulletin*, 83(10), 3059-3072.

Ciric, E. N. (2019). *Methane Escape from Lowland Terrestrial Seepages: Links to Deglaciation and Permafrost Dynamics* (MSc Thesis). Retrieved from Universidade Do Algarve. Faro, Portugal: Universidade Do Algarve. (https://sapientia.ualg.pt/bitstream/10400.1/13728/1/Dissertac_ao%2BEmma %2BCiric.pdf).

Clayton, L. K., Schaefer, K., Battaglia, M. J., Bourgeau-Chavez, L., Chen, J., Chen, R. H., et al. (2021). Active layer thickness as a function of soil water content. *Environmental Research Letters*, *16*(5), 055028.

Cohen, J., Screen, J. A., Furtado, J. C., Barlow, M., Whittleston, D., Coumou, D., Francis, J., Dethloff, K., Entekhabi, D., Overland, J., & Jones, J. (2014). Recent Arctic amplification and extreme mid-latitude weather. *Nature Geoscience*, *7*(9), 627–637.

Corwin, R. F. (1989). Data quality for engineering self-potential surveys (pp. 51- 72). In: *Proceedings, International Symposium on the detection of subsurface flow phenomena, Lecture Notes in Earth Sciences*. Berlin, Germany: Springler-Verlag.

Dai, A., Luo, D., Song, M., & Liu, J. (2019). Arctic amplification is caused by sea-ice loss under increasing CO2. *Nature Communications*, *10*(1), 121.

Dallmann, W. K. (2019). *Geoscience Atlas of Svalbard* (2nd edition). Tromsø, Norway: Norwegian Polar Institute.

Darnet, M., Marquis, G., & Sailhac, P. (2003). Estimating aquifer hydraulic properties from the inversion of surface Streaming Potential (SP) anomalies. *Geophysical Research Letters*, 30(13), 1679.

Davidson, E. A., & Janssens, I. A. (2006). Temperature sensitivity of soil carbon decomposition and feedbacks to climate change. *Nature*, *440*(7081), 165–173.

Demidov, N., Wetterich, S., Verkulich, S., Ekaykin, A., Meyer, H., Anisimov, M., et al. (2019). Pingo development in Grøndalen, West Spitsbergen. *The Cryosphere*, 13, 3155–3169.

Demidov, V., Demidov, N., Verkulich, S., & Wetterich, S. (2022). Distribution of pingos on Svalbard. *Geomorphology*, *412*, 108326.

Dickens, G. R. (2011). Down the rabbit hole: Toward appropriate discussion of methane release from gas hydrate systems during the Paleocene−Eocene thermal maximum and other past hyperthermal events. *Climate of the Past*, 7, 831−846.

Dlugokencky, E. J., Bruhwiler, L., White, J. W. C., Emmons, L. K., Novelli, P. C., Montzka, S. A., et al. (2009). Observational constraints on recent increases in the atmospheric CH4 burden. *Geophysical Research Letters*, *36*(18).

Dlugokencky, E. J., Nisbet, E. G., Fisher, R., & Lowry, D. (2011). Global atmospheric methane: Budget, changes and dangers. *Philosophical Transactions of the Royal Society A: Mathematical, Physical and Engineering Sciences*, *369*(1943), 2058–2072.

Doherty, R., Kulessa, B., Ferguson, A. S., Larkin, M. J., Kulakov, L. A., & Kalin, R. M. (2010). A microbial fuel cell in contaminated ground delineated by electrical self-potential and normalized induced polarization data. *Journal of Geophysical Research: Biogeosciences*, 115(G3), G00G08.

Doherty, R., McPolin, B., Kulessa, B., Frau, A., Kulakova, A., Allen, C. C. R., & Larkin, M. J. (2015). Microbial Ecology and Geo-electrical Responses across a Groundwater Plume. *Interpretation (Society of Exploration Geophysicists)*, *3*(4), SAB9–SAB21.

Dou, S., Nakagawa, S., Dreger, D., & Ajo-Franklin, J. (2016). A rock-physics investigation of unconsolidated saline permafrost: P-wave properties from laboratory ultrasonic measurements. *Geophysics*, 81(1), WA233–WA245.

Dou, S., Nakagawa, S., Dreger, D., & Ajo-Franklin, J. (2017). An effective-medium model for P-wave velocities of saturated, unconsolidated saline permafrost. *Geophysics*, 82(3), EN33–EN50.

Eckerstorfer, M., & Christiansen, H. H. (2011). Relating meteorological variables to the natural slab avalanche regime in High Arctic Svalbard. *Cold Regions Science and Technology*, *69*(2), 184–193.

Eppelbaum, L. V. (2021). Review of Processing and Interpretation of Self-Potential Anomalies: Transfer of Methodologies Developed in Magnetic Prospecting. *Geosciences*, *11*(5), 194.

Ernstson, K., & Scherer, V. (1986). Self-potential variations with time and their relation to hydrogeologic and meteorological parameters. *Geophysics*, 51, 1967–1977.

Etminan, M., Myhre, G., Highwood, E. J., & Shine, K. P. (2016). Radiative forcing of carbon dioxide, methane, and nitrous oxide: A significant revision of the methane radiative forcing. *Geophysical Research Letters*, *43*(24), 12,614-12,623.

Farbrot, H., Isaksen, K., Etzelmüller, B., & Gisnås, K. (2013). Ground Thermal Regime and Permafrost Distribution under a Changing Climate in Northern Norway. *Permafrost and Periglacial Processes*, *24*(1), 20–38.

Ferré, B., Mienert, J., & Feseker, T. (2012). Ocean temperature variability for the past 60 years on the Norwegian-Svalbard margin influences gas hydrate stability on human time scales. *Journal of Geophysical Research: Oceans*, *117*(C10).

Fisher, R. E., Sriskantharajah, S., Lowry, D., Lanoisellé, M., Fowler, C. M. R., James, R. H., et al. (2011). Arctic methane sources: Isotopic evidence for atmospheric inputs. *Geophysical Research Letters*, *38*(21).

Forster, P., Storelvmo, T., Armour, K., Collins, J.-L., Dufresne, D., Frame, D. J. et al. (2021). The Earth's Energy Budget, Climate Feedbacks, and Climate Sensitivity. In: Masson-Delmotte, V., Zhai, P., Pirani, A., Connors, S. L., Péan, C., Berger, S. et al. (Eds.) *Climate Change 2021: The Physical Science Basis. Contribution of Working Group I to the Sixth Assessment Report of the Intergovernmental Panel on Climate Change* (pp. 923-1054). Cambridge, UK & New York, NY: Cambridge University Press.

Forwick, M., Baeten, N. J., & Vorren, T. O. (2009). Pockmarks in Spitsbergen fjords. *Norwegian Journal of Geology*, 89, 65-77.

Fournier, C. (1989). Spontaneous potentials and resistivity surveys applied to hydrogeology in a volcanic area: Case history of the Chaîne des Puys (Puy-de-Dôme, France). *Geophysical Prospecting*, 37, 647- 668.

French H. M. (2017). *The Periglacial Environment* (4th Edition). Chichester, UK: John Wiley & Sons.

Gautier, D. L., Bird, K. J., Charpentier, R. R., Grantz, A., Houseknecht, D. W., Klett, T. R., et al. (2009). Assessment of Undiscovered Oil and Gas in the Arctic. *Science*, *324*(5931), 1175–1179.

Gilbert, G. L., Instanes, A., Sinitsyn, A. O. & Aalberg, A. (2019). Characterization of two sites for geotechnical testing in permafrost: Longyearbyen, Svalbard. *AIMS Geosciences*, 5(4), 868-885.

Gilbert, G. L., O'Neill, H. B., Nemec, W., Thiel, C., Christiansen, H. H., & Buylaert, J.-P. (2018). Late Quaternary sedimentation and permafrost development in a Svalbard fjord-valley, Norwegian high Arctic. *Sedimentology*, 65(7), 2531–2558.

Gisnås, K., Westermann, S., Schuler, T. V., Melvold, K., & Etzelmüller, B. (2016). Small-scale variation of snow in a regional permafrost model. *The Cryosphere*, *10*(3), 1201–1215.

Graversen, R. G., & Wang, M. (2009). Polar amplification in a coupled climate model with locked albedo. *Climate Dynamics*, *33*(5), 629–643.

Graversen, R. G., Mauritsen, T., Tjernström, M., Källén, E., & Svensson, G. (2008). Vertical structure of recent Arctic warming. *Nature*, *451*(7174), 53–56.

Grosse, G., & Jones, B. M. (2011). Spatial distribution of pingos in northern Asia. *The Cryosphere*, *5*(1), 13–33.

Grosse, G., Romanovsky, V., Jorgenson, T., Anthony, K. W., Brown, J., & Overduin, P. P. (2011). Vulnerability and Feedbacks of Permafrost to Climate Change. *Eos, Transactions American Geophysical Union*, *92*(9), 73–74.

Gruber, S., & Haeberli, W. (2007). Permafrost in steep bedrock slopes and its temperature-related destabilization following climate change. *Journal of Geophysical Research*, 112, F02S18.

Grünberg, I., Wilcox, E. J., Zwieback, S., Marsh, P., & Boike, J. (2020). Linking tundra vegetation, snow, soil temperature, and permafrost. *Biogeosciences*, 17(16), 4261–4279.

Gurney, S. D. (1998). Aspects of the genesis and geomorphology of pingos: perennial permafrost mounds. *Progress in Physical Geography*, 22(3), 307-324.

Gurney, S. D., & Worsley, P. (1996). Genetically complex and morphologically diverse pingos in the Fish Lake area of southwest Banks Island. *Geografiska Annaler A*, 79, 41-56.

Haldorsen, S., Heim, M., Dale, B., Landvik, J. Y., Ploeg, M. van der, Leijnse, A., Salvigsen, O., Hagen, J. O., & Banks, D. (2010). Sensitivity to long-term climate change of subpermafrost groundwater systems in Svalbard. *Quaternary Research*, *73*(2), 393–402.

Hamilton, T. D., & Obi, C. M. (1982). Pingos in the Brooks Range, Northern Alaska, U.S.A. *Arctic and Alpine Research*, 14(1), 13-20.

Hann, R. & Dachauer, A. (2020). *Drone-based mapping of the Lagoon Pingo in Svalbard*. DataverseNO Version 1.

Harada, K., & Yoshikawa, K. (1996). Permafrost age and thickness near Adventfjorden, Spitsbergen. *Polar Geography*, 20(4), 267–281.

Harris, S. A., French, J. A., Heginbottom, J. A., Johnston, G. H., Ladanyi, B., Sego, D. C., & van Everdingen, R. O. (1988). Glossary of Permafrost and Ground-Ice Terms. *National Research Council of Canada Technical Memorandum*, 142, 156 pp.

Harris, S.A., Brouchkov, A., & Guodong, C. (2017). *Geocryology: Characteristics and Use of Frozen Ground and Permafrost Landforms* (1st ed.). London, UK: CRC Press.

Hauck, C., & Vonder Mühll, D. (2003). Inversion and interpretation of two-dimensional geoelectrical measurements for detecting permafrost in mountainous regions. *Permafrost and Periglacial Processes*, 14(4), 305–318.

Hauck, C., Boettcher, M., & Maurer, H. (2011). A new model for estimating subsurface ice content based on combined electrical and seismic data sets. *The Cryosphere*, *5*(2), 453–468.

Hauck, C., Vieira, G., Gruber, S., Blanco, J., & Ramos, M. (2007). Geophysical identification of permafrost in Livingston Island, maritime Antarctica. *Journal of Geophysical Research: Earth Surface*, 112(F2), F02S19.

Haustein, K., Allen, M. R., Forster, P. M., Otto, F. E. L., Mitchell, D. M., Matthews, H. D., & Frame, D. J. (2017). A real-time Global Warming Index. *Scientific Reports*, *7*(1), 15417.

Heijmans, M. M. P. D., Magnússon, R. Í., Lara, M. J., Frost, G. V., Myers-Smith, I. H., van Huissteden, J., et al. (2022). Tundra vegetation change and impacts on permafrost. *Nature Reviews Earth & Environment*, *3*(1), 68–84.

Helmholtz, H. (1879). Studien über electrische Grenzschichten. *Annalen der Physik*, 243, 337-382.

Henriksen, E., Bjørnseth, H. M., Hals, T. K., Heide, T., Kiryukhina, T., Kløvjan, O. S., et al. (2011). Uplift and erosion of the greater Barents Sea: Impact on prospectivity and petroleum systems. *Geological Society, London, Memoirs*, *35*(1), 271–281.

Hill, T. M., Paull, C. K., & Critser, R. B. (2012). Glacial and deglacial seafloor methane emissions from pockmarks on the northern flank of the Storegga Slide complex. *Geo-Marine Letters*, *32*(1), 73–84.

Hinkel, K. M., & Nelson, F. E. (2003). Spatial and temporal patterns of active layer thickness at Circumpolar Active Layer Monitoring (CALM) sites in

northern Alaska, 1995–2000. *Journal of Geophysical Research: Atmospheres*, *108*(D2).

Hinzman, L. D., Deal, C. J., McGuire, A. D., Mernild, S. H., Polyakov, I. V., & Walsh, J. E. (2013). Trajectory of the Arctic as an integrated system. *Ecological Applications*, *23*(8), 1837–1868.

Hipp, T., Etzelmüller, B., & Westermann, S. (2014). Permafrost in alpine rock faces from Jotunheimen and Hurringane, southern Norway. *Permafrost and Periglacial Processes*, 25, 1-13.

Hodson, A. J., Nowak, A., Hornum, M. T., Senger, K., Redeker, K., Christiansen, H. H., et al. (2020). Sub-permafrost methane seepage from open-system pingos in Svalbard. *The Cryosphere*, 14(11), 3829–3842.

Hodson, A. J., Nowak, A., Redeker, K. R., Holmlund, E. S., Christiansen, H. H. & Turchyn, A. V. (2019). Seasonal Dynamics of Methane and Carbon Dioxide From an Open System Pingo: Lagoon Pingo, Svalbard. *Frontiers in Earth Science*, 7, 30.

Holloway, J. E., Lewkowicz, A. G., Douglas, T. A., Li, X., Turetsky, M. R., Baltzer, J. L., & Jin, H. (2020). Impact of wildfire on permafrost landscapes: A review of recent advances and future prospects. *Permafrost and Periglacial Processes*, *31*(3), 371–382.

Holmes, G. W., Hopkins, D. M. , & Foster, H. L. (1968) Pingos in central Alaska. *United States Geological Survey Bulletin*, 1241-H, H1–H40.

Hornum, M. T., Hodson, A. J., Jessen, S., Bense, V., & Senger, K. (2020). Numerical modelling of permafrost spring discharge and open-system pingo formation induced by basal permafrost aggradation. *The Cryosphere*, 14(12), 4627–4651.

Hornum, M.T., Betlem, P. & Hodson, A. (2021). Groundwater flow through continuous permafrost along geological boundary revealed by electrical resistivity tomography. *Geophysical Research Letters*, 48(14), e2021GL092757.

Hovland, M. (1987). The formation of pockmarks and their potential influence on offshore construction. *Quarterly Journal of Engineering Geology and Hydrogeology*, *22*, 131–138.

Hovland, M., & Svensen, H. (2006). Submarine pingoes: Indicators of shallow gas hydrates in a pockmark at Nyegga, Norwegian Sea. *Marine Geology*, *228*, 15–23.

Hovland, M., Gardner, J. V., & Judd, A. G. (2002). The significance of pockmarks to understanding fluid flow processes and geohazards. *Geofluids*, *2*(2), 127–136.

Hrbáček, F., Láska, K., & Engel, Z. (2016). Effect of Snow Cover on the Active-Layer Thermal Regime – A Case Study from James Ross Island, Antarctic Peninsula. *Permafrost and Periglacial Processes*, *27*(3), 307–315.

Hu, F. S., Higuera, P. E., Duffy, P., Chipman, M. L., Rocha, A. V., Young, A. M., Kelly, R., & Dietze, M. C. (2015). Arctic tundra fires: Natural variability and responses to climate change. *Frontiers in Ecology and the Environment*, *13*(7), 369–377.

Hugelius, G., Strauss, J., Zubrzycki, S., Harden, J. W., Schuur, E. A. G., Ping, C.-L., et al. (2014). Estimated stocks of circumpolar permafrost carbon with quantified uncertainty ranges and identified data gaps. *Biogeosciences*, *11*(23), 6573–6593.

Huggel, C., Fischer, L., Schneider, D., & Haeberli, W. (2010). Research advances on climate-induced slope instability in glacier and permafrost high-mountain environments. *Geographica Helvetica*, *65*(2), 146–156.

Humlum O., Instanes A. & Sollid J. L. (2003). Permafrost in Svalbard: a review of research history, climatic background and engineering challenges. *Polar Research*, 22(2), 191-215.

Humlum, O. (2005). Holocene permafrost aggradation in Svalbard. *Geological Society London Special Publications*, 242(1), 119–129.

Hunter, J. A. M. (1973), The application of shallow seismic methods to mapping of frozen surficial materials. In: *Proceedings of the Second International Conference on Permafrost* (pp. 527–535). Washington, DC: National Academy of Sciences.

Huq, F., Smalley, P. C., Mørkved, P. T., Johansen, I., Yarushina, V., & Johansen, H. (2017). The Longyearbyen CO2 Lab: Fluid communication in reservoir and caprock. *International Journal of Greenhouse Gas Control*, *63*, 59–76.

in't Zandt, M. H., Liebner, S., & Welte, C. U. (2020). Roles of thermokarst lakes in a warming world. *Trends in Microbiology*, 28 (9), 769-779.

Isaksen, K., Holmlund, P., Sollid, J. L., & Harris, C. (2001). Three deep Alpine-permafrost boreholes in Svalbard and Scandinavia. *Permafrost and Periglacial Processes*, 12(1), 13–25.

Jakobsson, M., Ingólfsson, Ó., Long, A. J., & Spielhagen, R. F. (2014). The dynamic Arctic. *Quaternary Science Reviews*, *92*, 1–8.

Jansson, J. K., & Taş, N. (2014). The microbial ecology of permafrost. *Nature Reviews Microbiology*, *12*(6), 414–425.

Jiang, G., Kennedy, M. J., & Christie-Blick, N. (2003). Stable isotopic evidence for methane seeps in Neoproterozoic postglacial cap carbonates. *Nature*, 426(6968), 822–826.

Johansen, T. A., Digranes, P., van Schaack, M., & Lonne, I. (2003). Seismic mapping and modeling of near-surface sediments in polar areas. *Geophysics*, *68*(2), 566–573.

Johnsen, M. G. (2021). *Geomagnetic Data*. Tromsø Geophysical Observatory, Faculty of Science and Technology, UiT The Arctic University of Norway. Available online: https://flux.phys.uit.no/geomag.html   Date accessed: 2nd June 2021.

Johnson, A. H. (2011). Global resource potential of gas hydrate – a new calculation. *Fire Ice*, 11(2), 1-4.

Jones, E. L. (2019). *The Biogeochemistry of the Active Layer and Shallow Permafrost in a High Arctic Fjord Valley, Svalbard* (PhD Thesis). Sheffield, UK: University of Sheffield

Jones, M. (2012). *Diagram of zeta potential and slipping plane*. Available online. https://commons.wikimedia.org/wiki/File:Diagram_of_zeta_potential_and_slipping_planeV2.svg (Date accessed: 19 September 2022).

Jorgenson, M. T., Romanovsky, V., Harden, J., Shur, Y., O'Donnell, J., Schuur, E. A. G., et al. (2010). Resilience and vulnerability of permafrost to climate change. *Canadian Journal of Forest Research*, *40*(7), 1219–1236.

Jorgenson, M. T., Shur, Y., & Pullman, E. R. (2006). Abrupt increase in permafrost degradation in Arctic Alaska. *Geophysical Research Letters*, 33, L02503.

Jorgenson, M. T., Yoshikawa, K., Kanevskiy, M., Shur, Y., Romanovsky, V., Marchenko, S., et al. (2008). Permafrost characteristics of Alaska. *Proceedings of the Ninth International Conference on Permafrost*, *3*, 121–122.

Juliussen, H., Oswald, A., Watanabe, T., Christiansen, H. H., & Matsuoka, N. (2012). Monitoring active layer thaw and freeze-back in four different periglacial landforms in Svalbard using Electrical Resistivity Tomography (ERT). *Geophysical Research Abstracts*, 14, 8963.

Jung, H.-K., Min, D.-J., Lee, H. S., Oh, S., & Chung, H. (2009). Negative apparent resistivity in dipole–dipole electrical surveys. *Exploration Geophysics*, 40(1), 33–40.

Kaiser, C., Meyer, H., Biasi, C., Rusalimova, O., Barsukov, P., & Richter, A. (2007). Conservation of soil organic matter through cryoturbation in arctic soils in Siberia. *Journal of Geophysical Research: Biogeosciences*, *112*(G2).

Kasprzak, M. (2015). High-resolution electrical resistivity tomography applied to patterned ground, Wedel Jarlsberg Land, south-west Spitsbergen. *Polar Research*, 34, 25678.

Kasprzak, M., Strzelecki, M. C., Traczyk, A., Kondracka, M., Lim, M., & Migała, K. (2017). On the potential for a bottom active layer below coastal permafrost: The impact of seawater on permafrost degradation imaged by electrical resistivity tomography (Hornsund, SW Spitsbergen). *Geomorphology*, *293*, 347–359.

Keating, K., Binley, A., Bense, V., Dam, R. L. V., & Christiansen, H. H. (2018). Combined Geophysical Measurements Provide Evidence for Unfrozen Water in Permafrost in the Adventdalen Valley in Svalbard. *Geophysical Research Letters*, 45(15), 7606–7614.

Kemna, A. (2000). *Tomographic Inversion of Complex Resistivity: Theory and Application* (PhD Thesis). Retrieved from University of Bonn. (https://www.geo.uni-bonn.de/mitarbeiter/Andreas-Kemna/dissertation). Bochum, Germany: University of Bochum.

Kemp, D. B., Coe, A. L., Cohen, A. S., & Schwark, L. (2005). Astronomical pacing of methane release in the Early Jurassic period, *Nature*, 437(7057), 396–399.

Kennedy, M. J., Christie-Blick, N., & Sohl, L. E. (2001). Are Proterozoic cap carbonates and isotopic excursions a record of gas hydrate destabilization following Earth's coldest intervals? *Geology*, 29(5), 443–446.

Kennett, J. P., Cannariato, K. G., Hendy, I. L., & Behl, R. J. (2000). Carbon isotopic evidence for methane hydrate instability during Quaternary interstadials. *Science*, 288(5463), 128–133.

Kennett, J. P., Cannariato, K. G., Hendy, I. L., & Behl, R. J. (2003). *Methane Hydrates in Quaternary Climate Change: The Clathrate Gun Hypothesis*. Washington, DC: American Geophysical Union.

Khvorostyanov, D. V., Ciais, P., Krinner, G., Zimov, S. A., Corradi, Ch., & Guggenberger, G. (2008). Vulnerability of permafrost carbon to global warming. Part II: Sensitivity of permafrost carbon stock to global warming. *Tellus B*, *60*(2), 265–275.

Killingbeck, S. F., Booth, A. D., Livermore, P. W., Bates, C. R., & West, L. J. (2020). Characterisation of subglacial water using a constrained transdimensional Bayesian transient electromagnetic inversion. *Solid Earth*, *11*(1), 75–94.

Killingbeck, S. F., Booth, A. D., Livermore, P. W., West, L. J., Reinardy, B. T., & Nesje, A. (2019). Subglacial sediment distribution from constrained seismic

inversion, using MuLTI software: Examples from Midtdalsbreen, Norway. *Annals of Glaciology*, *60*(79), 206–219.

King, M. S., Zimmerman, R. W., & Corwin, R. F. (1988). Seismic and Electrical Properties of Unconsolidated Permafrost1. *Geophysical Prospecting*, 36(4), 349–364.

Kirschke, S., Bousquet, P., Ciais, P., Saunois, M., Canadell, J. G., Dlugokencky, E. J., et al. (2013). Three decades of global methane sources and sinks. *Nature Geoscience*, *6*(10), 813–823.

Klein, K. A., & Santamarina, J. C. (2003). Electrical Conductivity in Soils: Underlying Phenomena. *Journal of Environmental and Engineering Geophysics*, 8(4), 263–273.

Kneisel, C. & Hauck, C. (2008). Electrical methods. In Hauck, C., & Kniesel, C. (Eds.). *Applied Geophysics in Periglacial Environments* (pp. 3-27). Cambridge, UK: Cambridge University Press.

Kneisel, C., Hauck, C., Fortier, R., & Moorman, B. (2008). Advances in geophysical methods for permafrost investigations. *Permafrost and Periglacial Processes*, *19*(2), 157–178.

Knittel, K., & Boetius, A. (2009). Anaerobic oxidation of methane: Progress with an unknown process. *Annual Review of Microbiology*, *63*, 311–334.

Koestel, J., Kemna, A., Javaux, M., Binley, A., & Vereecken, H. (2008). Quantitative imaging of solute transport in an unsaturated and undisturbed soil monolith with 3-D ERT and TDR. *Water Resources Research*, 44(12).

Koevoets, M. J., Abay, T. B., Hammer, Ø., & Olaussen, S. (2016). High-resolution organic carbon–isotope stratigraphy of the Middle Jurassic–Lower Cretaceous Agardhfjellet Formation of central Spitsbergen, Svalbard. *Palaeogeography, Palaeoclimatology, Palaeoecology*, *449*, 266–274.

Koevoets, M. J., Hammer, Ø., Olaussen, S., Senger, K., & Smelror, M. (2018). Integrating subsurface and outcrop data of the Middle Jurassic to Lower Cretaceous Agardhfjellet Formation in central Spitsbergen. *Norwegian Journal of Geology 98*(4), 1-34.

Kottek, M., Grieser, J., Beck, C., Rudolf, B., & Rubel, F. (2006). World Map of the Köppen-Geiger climate classification updated. *Meteorologische Zeitschrift*, 15(3), 259-263.

Koven, C. D., Ringeval, B., Friedlingstein, P., Ciais, P., Cadule, P., Khvorostyanov, D., Krinner, G., & Tarnocai, C. (2011). Permafrost carbon-climate feedbacks accelerate global warming. *Proceedings of the National Academy of Sciences*, 108(36), 14769–14774.

Krajewski, K. (1990). Phosphoritization in a starved shallow shelf environment: the Brentskardhaugen Bed (Toarcian-Bajocian) in Spitsbergen. *Polish Polar Research*, 11(3-4), 331-344.

Kukemilks, K., & Wagner, J.-F. (2021). Detection of Preferential Water Flow by Electrical Resistivity Tomography and Self-Potential Method. *Applied Sciences*, *11*(9), 4224.

Kulessa, B. (2007). A critical review of the low-frequency electrical properties of ice sheets and glaciers. Journal of Environmental and Engineering *Geophysics*, 12(1), 23-36.

Kulessa, B., Hubbard, B., & Brown, G. H. (2003a). Cross-coupled flow modelling of coincident streaming and electrochemical potentials and application to self-potential data. *Journal of Geophysical Research*, 108(B8), 2381.

Kulessa, B., Hubbard, B., & Brown, G. H. (2006). Time-lapse imaging of subglacial drainage conditions using three-dimensional inversion of borehole electrical resistivity data. *Journal of Glaciology*, *52*(176), 49–57.

Kulessa, B., Hubbard, B., Brown, G. H., & Becker, J. (2003b). Earth tide forcing of glacier drainage. *Geophysical Research Letters*, 30(1), 1011.

Kunz, J., & Kneisel, C. (2021). Three-dimensional investigation of an open- and a closed-system Pingo in northwestern Canada. *Permafrost and Periglacial Processes*, 1-17.

Kvenvolden, K. A. (1993). Gas hydrates—Geological perspective and global change. *Reviews of Geophysics*, *31*(2), 173–187.

Lamontagne-Hallé, P., McKenzie, J. M., Kurylyk, B. L., & Zipper, S. C. (2018). Changing groundwater discharge dynamics in permafrost regions. *Environmental Research Letters*, *13*(8), 084017.

Landvik, J.Y., Bondevik, S., Elverhøi, A., Fjeldskaar, W., Mangerud, J., Siegert, M.J., et al (1998) The last glacial maximum of Svalbard and the Barents Sea area: ice sheet extent and configuration. *Quaternary Science Reviews*, 17, 43–75.

Lara, M. J., Lin, D. H., Andresen, C., Lougheed, V. L., & Tweedie, C. E. (2019). Nutrient Release From Permafrost Thaw Enhances CH4 Emissions From Arctic Tundra Wetlands. *Journal of Geophysical Research: Biogeosciences*, *124*(6), 1560–1573.

Lawrence, D. M., & Slater, A. G. (2005). A projection of severe near-surface permafrost degradation during the 21st century. *Geophysical Research Letters*, *32*(24).

Lawrence, D. M., & Slater, A. G. (2010). The contribution of snow condition trends to future ground climate. *Climate Dynamics*, *34*(7), 969–981.

Lawrence, D. M., Koven, C. D., Swenson, S. C., Riley, W. J., & Slater, A. G. (2015). Permafrost thaw and resulting soil moisture changes regulate projected high-latitude CO2 and CH4 emissions. *Environmental Research Letters*, 10(9), 094011.

Lawrence, D. M., Slater, A. G., Romanovsky, V. E., & Nicolsky, D. J. (2008). Sensitivity of a model projection of near-surface permafrost degradation to soil column depth and representation of soil organic matter. *Journal of Geophysical Research: Earth Surface*, 113(F2), F02011.

Lee, K. S., & Cho, I. K. (2020). Negative apparent resistivities in surface resistivity measurements. *Journal of Applied Geophysics*, 176, 104010.

Léger, E., Dafflon, B., Soom, F., Peterson, J., Ulrich, C., & Hubbard, S. (2017). Quantification of Arctic Soil and Permafrost Properties Using Ground-Penetrating Radar and Electrical Resistivity Tomography Datasets. *IEEE Journal of Selected Topics in Applied Earth Observations and Remote Sensing*, 10(10), 4348–4359.

Lewkowicz, A. G., & Way, R. G. (2019). Extremes of summer climate trigger thousands of thermokarst landslides in a High Arctic environment. *Nature Communications*, *10*(1), 1329.

Li, X.-Y., Jin, H.-J., Wang, H.-W., Marchenko, S. S., Shan, W., Luo, D.-L., et al. (2021). Influences of forest fires on the permafrost environment: A review. *Advances in Climate Change Research*, *12*(1), 48–65.

Liestøl, O. (1977). Pingos, springs and permafrost in Spitsbergen. In: Norwegian Polar Institute (Ed.), *Norsk Polarinstitutt Årbok*, 1975 (pp. 7–29). Oslo, Norway: Norwegian Polar Institute.

Liestøl, O. (1996). Open-system pingos in Spitsbergen. *Norwegian Journal of Geography*, *50*(1), 81–84.

Lønne, I., & Nemec, W. (2004). High-arctic fan delta recording deglaciation and environment disequilibrium. *Sedimentology*, 51(3), 553–589.

Loranty, M. M., Abbott, B. W., Blok, D., Douglas, T. A., Epstein, H. E., Forbes, B. C. et al. (2018). Reviews and syntheses: Changing ecosystem influences on soil thermal regimes in northern high-latitude permafrost regions. *Biogeosciences*, 15(17), 5287–5313.

Mackay, J. R. (1962). Pingos of the Pleistocene Mackenzie Delta area. *Geographical Bulletin*, 18, 21-63.

Mackay, J. R. (1973). The Growth of Pingos, Western Arctic Coast, Canada. *Canadian Journal of Earth Sciences*, 10(6), 979-1004.

Mackay, J. R. (1978). Sub-pingo water lenses, Tuktoyaktuk Peninsula, Northwest Territories. *Canadian Journal of Earth Sciences*, 15, 1219-1277.

Mackay, J. R. (1979). Pingos of the Tuktoyaktuk Peninsula Area, Northwest Territories. *Géographie Physique et Quaternaire*, *33*(1), 3–61.

Mackay, J. R. (1985). Pingo ice of the western Arctic coast, Canada. *Canadian Journal of Earth Sciences*, 22(10), 1452-1464.

Mackay, J. R. (1987). Some mechanical aspects of pingo growth and failure, western Arctic coast, Canada. *Canadian Journal of Earth Sciences*, 24, 1108-1119.

Mackay, J. R. (1988). Pingo collapse and palaeoclimatic reconstruction. *Canadian Journal of Earth Sciences*, 25, 495-511.

Mackay, J. R. (1994). Pingos and pingo ice of the western Arctic coast, Canada. *Terra*, 106, 1-11.

Mackay, J. R. (1998). Pingo Growth and collapse, Tuktoyaktuk Peninsula Area, Western Arctic Coast, Canada: a long-term field study. *Géographie physique et Quaternaire*, 52(3), 1-53.

Mackay, J. R., & Burn, C. R. (2011). A century of change in a collapsing pingo, Parry Peninsula, western Arctic coast, Canada. *Permafrost and Periglacial Processes*, 22, 266-272.

Major, H., Haremo, P., Dallmann, W.K. & Andresen, A. (2000) *Geological Map of Svalbard 1:100 000*, Sheet C9G: Adventdalen. Tromsø: Norwegian Polar Institute.

Makogon, Y. F., Holditch, S. A., & Makogon, T. Y. (2007). Natural gas-hydrates—A potential energy source for the 21st Century. *Journal of Petroleum Science and Engineering*, *56*(1), 14–31.

Martens, C. S., Albert, D. B., & Alperin, M. J. (1998). Biogeochemical processes controlling methane in gassy coastal sediments—Part 1. A model coupling organic matter flux to gas production, oxidation and transport. *Continental Shelf Research*, *18*(14), 1741–1770.

Matsuoka, N., Christiansen, H. H., & Watanabe, T. (2018). Ice-wedge polygon dynamics in Svalbard: Lessons from a decade of automated multi-sensor monitoring. *Permafrost and Periglacial Processes*, *29*(3), 210–227.

McGuire, A. D., Anderson, L. G., Christensen, T. R., Dallimore, S., Guo, L., Hayes, D. J., et al. (2009). Sensitivity of the carbon cycle in the Arctic to climate change. *Ecological Monographs*, *79*(4), 523–555.

McGuire, A. D., Lawrence, D. M., Koven, C., Clein, J. S., Burke, E., Chen, G., et al. (2018). Dependence of the evolution of carbon dynamics in the northern

permafrost region on the trajectory of climate change. *Proceedings of the National Academy of Sciences*, *115*(15), 3882–3887.

Micallef, A., Averes, T., Hoffmann, J., Crutchley, G., Mountjoy, J. J., Person, M., et al. (2022). Multiple drivers and controls of pockmark formation across the Canterbury Margin, New Zealand. *Basin Research*, *34*(4), 1374–1399.

Milkov, A. V., & Sassen, R. (2003). Two-dimensional modeling of gas hydrate decomposition in the northwestern Gulf of Mexico: Significance to global change assessment. *Global and Planetary Change*, *36*(1), 31–46.

Miner, K. R., Turetsky, M. R., Malina, E., Bartsch, A., Tamminen, J., McGuire, A. D., et al. (2022). Permafrost carbon emissions in a changing Arctic. *Nature Reviews Earth & Environment*, *3*(1), 55–67.

Minshull, T. A., Marín-Moreno, H., Armstrong McKay, D. I., & Wilson, P. A. (2016). Mechanistic insights into a hydrate contribution to the Paleocene-Eocene carbon cycle perturbation from coupled thermohydraulic simulations. *Geophysical Research Letters*, *43*(16), 8637–8644.

Minsley, B. (2007). *Modeling and Inversion of Self-Potential Data* (PhD Thesis). Retrieved from Massachusetts Institute of Technology. Cambridge, MA: Massachusetts Institute of Technology. Retrieved from: https://core.ac.uk/download/pdf/4432319.pdf

Mishra, U., Hugelius, G., Shelef, E., Yang, Y., Strauss, J., Lupachev, A. et al. (2021). Spatial heterogeneity and environmental predictors of permafrost region soil organic carbon stocks. *Science Advances*, *7*(9), eaaz5236.

Mollaret, C., Hilbich, C., Pellet, C., Flores-Orozco, A., Delaloye, R., & Hauck, C. (2019). Mountain permafrost degradation documented through a network of permanent electrical resistivity tomography sites. *The Cryosphere*, 13(10), 2557–2578.

Mollaret, C., Wagner, F. M., Hilbich, C., Scapozza, C., & Hauck, C. (2020). Petrophysical Joint Inversion Applied to Alpine Permafrost Field Sites to Image Subsurface Ice, Water, Air, and Rock Contents. *Frontiers in Earth Science*, *8*.

Morelli, G. & LaBrecque, D.J., (1996). Advances in ERT inverse modeling. *European Journal of Environmental and Engineering Geoph*ysics, 1, 171-186.

Müller F. (1959). Beobachtungen über Pingos: Detailuntersuchungen in Ostgrönland und in der kanadischen Arktis. Copenhagen: CA Reitzelsforlag.

Myhre, C. L., Ferré, B., Platt, S. M., Silyakova, A., Hermansen, O., Allen, G., et al. (2016). Extensive release of methane from Arctic seabed west of Svalbard during summer 2014 does not influence the atmosphere. *Geophysical Research Letters*, *43*(9), 4624–4631.

Natali, S. M., Holdren, J. P., Rogers, B. M., Treharne, R., Duffy, P. B., Pomerance, R., & MacDonald, E. (2021). Permafrost carbon feedbacks threaten global climate goals. *Proceedings of the National Academy of Sciences*, *118*(21), e2100163118.

Naudet, V., Revil, A., Bottero, J.-Y., & Bégassat, P. (2003). Relationship between self-potential (SP) signals and redox conditions in contaminated groundwater, *Geophysical Research Letters*, 30(21), 2091.

Naudet, V., Revil, A., Rizzo, E., Bottero, J.-Y., & Bégassat, P. (2004). Groundwater redox conditions and conductivity in a contaminant plume from geoelectrical investigations. *Hydrology Earth System Science*, 8(1), 8-22.

Neuzil, C. E. (2012). Hydromechanical effects of continental glaciation on groundwater systems. *Geofluids*, *12*(1), 22–37.

Nielsen, D. M., Pieper, P., Barkhordarian, A., Overduin, P., Ilyina, T., Brovkin, V., et al. (2022). Increase in Arctic coastal erosion and its sensitivity to warming in the twenty-first century. *Nature Climate Change*, 12, 263-270.

Nilsen, T. (2020). Svalbard experienced hottest summer on record. The Barents Observer. Available online: https://thebarentsobserver.com/en/climate-crisis/2020/09/svalbard-experienced-hottest-summer-record Date accessed: 23rd October 2020

Nisbet, E. G., Dlugokencky, E. J., & Bousquet, P. (2014). Methane on the Rise—Again. *Science*, *343*(6170), 493–495.

Nisbet, E. G., Dlugokencky, E. J., Manning, M. R., Lowry, D., Fisher, R. E., France, J. L., et al. (2016). Rising atmospheric methane: 2007–2014 growth and isotopic shift. *Global Biogeochemical Cycles*, 30, 1356–1370.

Nisbet, E. G., Fisher, R. E., Lowry, D., France, J. L., Allen, G., Bakkaloglu, S., et al. (2020). Methane Mitigation: Methods to Reduce Emissions, on the Path to the Paris Agreement. *Reviews of Geophysics*, 58(1), e2019RG000675.

Norwegian Meterological Institute (2021). *Norwegian Centre for Climate Services*. Available online: https://seklima.met.no/ Date accessed: 4th April 2022

Norwegian Polar Institute (2014). *Terrengmodell Svalbard (S0 Terrengmodell)* [Data set]. Norwegian Polar Institute.

Norwegian Polar Institute (2021). *Svalbard Orthophoto*. Available Online: https://geodata.npolar.no/arcgis/rest/services/Basisdata/NP_Ortofoto_Svalbard_WMTS_25833/MapServer?f=jsapi (date accessed: 12th February 2022).

O'Neill, H. B., Roy-Leveillee, P., Lebedeva, L., & Ling, F. (2020). Recent advances (2010–2019) in the study of taliks. *Permafrost and Periglacial Processes*, *31*(3), 346–357.

O'Neill, H. B., Wolfe, S. A., & Duchesne, C. (2019). New ground ice maps for Canada using a paleogeographic modelling approach. *The Cryosphere*, *13*(3), 753–773.

Oh, Y., Zhuang, Q., Liu, L., Welp, L. R., Lau, M. C. Y., Onstott, T. C., et al. (2020). Reduced net methane emissions due to microbial methane oxidation in a warmer Arctic. *Nature Climate Change*, 1–5.

Ohm, S.E., Larsen., L., Olaussen, S., Senger, K., Birchall, T., Demchuk, T, et al. (2019). Discovery of shale gas in organic rich Jurassic successions, Adventdalen, central Spitsbergen; Norway. *Norwegian Journal of Geology*, 99, 343–370.

Olaussen, S., Senger, K., Braathen, A., Grundvåg, S.-A., & Mørk, A. (2020). You learn as long as you drill; research synthesis from the Longyearbyen CO2 Laboratory, Svalbard, Norway. *Norwegian Journal of Geology*, 99(2), 157-182.

Olefeldt, D., Goswami, S., Grosse, G., Hayes, D., Hugelius, G., Kuhry, P., et al. (2016). Circumpolar distribution and carbon storage of thermokarst landscapes. *Nature Communications*, *7*(1), 1–11.

Orvin, A. K. (1944). Litt om kilder på Svalbard. *Norwegian Journal of Geology*, 10, 1.

Osterkamp, T. E. (2005). The recent warming of permafrost in Alaska. *Global and Planetary Change*, *49*(3), 187–202.

Osterkamp, T. E., & Burn, C. R. (2002). Permafrost. In J. R. Holton (Ed.), *Encyclopedia of Atmospheric Sciences* (pp. 1717–1729). Cambridge, MA: Academic Press.

Osterkamp, T. E., Jorgenson, M. T., Schuur, E. A. G., Shur, Y. L., Kanevskiy, M. Z., Vogel, J. G., & Tumskoy, V. E. (2009). Physical and ecological changes associated with warming permafrost and thermokarst in Interior Alaska. *Permafrost and Periglacial Processes*, *20*(3), 235–256.

Overduin, P. P., Westermann, S., Yoshikawa, K., Haberlau, T., Romanovsky, V., & Wetterich, S. (2012). Geoelectric observations of the degradation of nearshore submarine permafrost at Barrow (Alaskan Beaufort Sea). *Journal of Geophysical Research: Earth Surface*, *117*(F2).

Park, H., Fedorov, A. N., Zheleznyak, M. N., Konstantinov, P. Y., & Walsh, J. E. (2015). Effect of snow cover on pan-Arctic permafrost thermal regimes. *Climate Dynamics*, *44*(9), 2873–2895.

Park, S. K., & Van, G. P. (1991). Inversion of pole-pole data for 3-D resistivity structure beneath arrays of electrodes. *Geophysics*, 56(7), 951–960.

Paull, C. K., Ussler, W., Dallimore, S. R., Blasco, S. M., Lorenson, T. D., Melling, H., Medioli, B. E., Nixon, F. M., & McLaughlin, F. A. (2007). Origin of

pingo-like features on the Beaufort Sea shelf and their possible relationship to decomposing methane gas hydrates. *Geophysical Research Letters*, *34*(1), L01603.

Pavlov, A. V. (1994). Current changes of climate and permafrost in the arctic and sub-arctic of Russia. *Permafrost and Periglacial Processes*, *5*(2), 101–110.

Pellet, C., Hilbich, C., Marmy, A., & Hauck, C. (2016). Soil Moisture Data for the Validation of Permafrost Models Using Direct and Indirect Measurement Approaches at Three Alpine Sites. *Frontiers in Earth Science*, *3*, 91.

Perrier, F., & Morat, P. (2000). Characterization of electrical daily variations induced by capillary flow in the non-saturated zone. *Pure Applied Geophysics*, 157, 785–810.

Peterson, B. J., Holmes, R. M., McClelland, J. W., Vörösmarty, C. J., Lammers, R. B., Shiklomanov, A. I., et al. (2002). Increasing river discharge to the Arctic Ocean. *Science*, 298(5601), 2171-2173.

Petiau, G. (2000). Second Generation of Lead-lead Chloride Electrodes for Geophysical Applications. *Pure and Applied Geophysics*, *157*(3), 357–382.

Péwé, T.L. (1975). Quaternary geology of Alaska. *USGS Numbered Series*, 835, 145 pp.

Pissart, A. (1985). Pingos and palsas: A review of the present state of knowledge. *Polar Geography*, 9(3), 171-195.

Pissart, A. (2002). Palsas, lithalsas and remnants of these periglacial mounds. A progress report. *Progress in Physical Geography*, 26(4), 605–621.

Pithan, F., & Mauritsen, T. (2014). Arctic amplification dominated by temperature feedbacks in contemporary climate models. *Nature Geoscience*, 7(3), 181–184.

Pohl, S., Marsh, P., & Bonsal, B. (2007). Modeling the Impact of Climate Change on Runoff and Annual Water Balance of an Arctic Headwater Basin. *Arctic*, *60*, 173-186.

Porsild, A. E. (1938). Earth mounds in unglaciated Arctic northwestern America. *Geographical Review*, 28, 46-58.

Portnov, A., Smith, A. J., Mienert, J., Cherkashov, G., Rekant, P., Semenov, P., et al. (2013). Offshore permafrost decay and massive seabed methane escape in water depths > 20m at the South Kara Sea shelf. *Geophysical Research Letters*, 40(15), 3962–3967.

Portnov, A., Vadakkepuliyambatta, S., Mienert, J., & Hubbard, A. (2016). Ice-sheet-driven methane storage and release in the Arctic. *Nature Communications*, *7*, 10314.

Post, E., Alley, R. B., Christensen, T. R., Macias-Fauria, M., Forbes, B. C., Gooseff, M. N., Iler, A., Kerby, J. T., Laidre, K. L., Mann, M. E., Olofsson, J., Stroeve, J. C., Ulmer, F., Virginia, R. A., & Wang, M. (2019). The polar regions in a 2°C warmer world. *Science Advances*, *5*(12), eaaw9883.

Previdi, M., Smith, K. L., & Polvani, L. M. (2021). Arctic amplification of climate change: A review of underlying mechanisms. *Environmental Research Letters*, *16*(9), 093003.

Rangel, R. C., Parsekian, A. D., Farquharson, L. M., Jones, B. M., Ohara, N., Creighton, A. L et al. (2021). Geophysical Observations of Taliks Below Drained Lake Basins on the Arctic Coastal Plain of Alaska. *Journal of Geophysical Research: Solid Earth*, 126(3), e2020JB020889.

Reagan, M. T., & Moridis, G. J. (2008). Dynamic response of oceanic hydrate deposits to ocean temperature change. *Journal of Geophysical Research: Oceans*, *113*(C12), C12023.

Reeburgh, W. S. (2007). Oceanic Methane Biogeochemistry. *Chemical Reviews*, *107*(2), 486–513.

Repelewska-Pękalowa, J., & Pękala, K. (2004). Active-Layer Dynamics at the Calypsostranda CALM Site, Recherche Fiord Region, Spitsbergen. *Polar Geography*, *28*(4), 326–343.

Revil, A., & Glover, P. W. J. (1998). Nature of surface electrical conductivity in natural sands, sandstones, and clays. *Geophysical Research Letters*, 25(5), 691–694.

Revil, A., & Jardani, A. (2013). *The Self-Potential Method: Theory and Applications in Environmental Geosciences*. Cambridge, UK: Cambridge University Press.

Revil, A., Cary, L., Fan, Q., Finizola, A. & Trolard, F. (2005) Self-potential signals associated with preferential ground water flow pathways in a buried paleo-channel. *Geophysical Research Letters*, 32, L07401.

Revil, A., Coperey, A., Shao, Z., Florsch, N., Fabricus, I. L., Deng, Y., et al. (2017) Complex conductivity of soils. Water Resources Research, 53(8), 7121-7147.

Revil, A., Hermitte, D., Voltz, M., Moussa, R., Lacas, J.-G., Bourrié, G., & Trolard, F. (2002). Self-potential signals associated with variations of the hydraulic head during an infiltration experiment. *Geophysical Research Letters*, *29*(7), 1106.

Revil, A., Karaoulis, M., Johnson, T., & Kemna, A. (2012). Review: Some low-frequency electrical methods for subsurface characterization and monitoring in hydrogeology. *Hydrogeology Journal*, *20*(4), 617–658.

Revil, A., Karaoulis, M., Srivastava, S., & Byrdina, S. (2013). Thermoelectric self-potential and resistivity data localize the burning front of underground coal fires. *Geophysics*, 78(5), B259–B273.

Revil, A., Mendonça, C. A., Atekwana, E., Kulessa, B., Hubbard, S. S., Bolhen, K. (2010) Understanding biogeobatteries: where geophysics meets microbiology. *Journal of Geophysical Research: Biogeosciences*, 115(G1), G00G02.

Revil, A., Naudet, V., Nouzaret, J., and Pessel, M. (2003), Principles of electrography applied to self-potential electrokinetic sources and hydrogeological applications, *Water Resources Research*, 39(5), 1114.

Reynolds, J. M. (2011). *An Introduction to Applied and Environmental Geophysics (2nd Edition)*. Chichester, UK: Wiley-Blackwell.

Riboulot, V., Cattaneo, A., Sultan, N., Garziglia, S., Ker, S., Imbert, P., & Voisset, M. (2013). Sea-level change and free gas occurrence influencing a submarine landslide and pockmark formation and distribution in deepwater Nigeria. *Earth and Planetary Science Letters*, 375, 78–91.

Riboulot, V., Imbert, P., Cattaneo, A., & Voisset, M. (2019). Fluid escape features as relevant players in the enhancement of seafloor stability? *Terra Nova*, *31*(6), 540–548.

Riera, R., Paumard, V., de Gail, M., Saqab, M. M., Lebrec, U., Lang, S. C., & Lane, A. (2022). Origin of seafloor pockmarks overlying submarine landslides: Insights from semi-automated mapping of 3D seismic horizons (North West Shelf, Australia). *Marine and Petroleum Geology*, 136, 105453.

Rizzo, E., Suski, B., Revil, A., Straface, S., & Troisi, S. (2004). Self-potential signals associated with pumping tests experiments. *Journal of Geophysical Research: Solid Earth*, 109(B10), B10203.

Robson, B. A., MacDonell, S., Ayala, Á., Bolch, T., Nielsen, P. R., & Vivero, S. (2022). Glacier and rock glacier changes since the 1950s in the La Laguna catchment, Chile. *The Cryosphere*, *16*(2), 647–665.

Romanovsky, V. E., Sazonova, T. S., Balobaev, V. T., Shender, N. I., & Sergueev, D. O. (2007). Past and recent changes in air and permafrost temperatures in eastern Siberia. *Global and Planetary Change*, *56*(3), 399–413.

Ross, N. (2013). Frost Mounds: Active and Relict Forms (pp. 472-480). In: Elias, S. A., & Mock, C. J. (Eds.) *Encyclopedia of Quaternary Science* (2nd Edition), 472–480. Amsterdam, Netherlands: Elsevier.

Ross, N., Brabham, P. J., Harris, C., & Christiansen, H. H. (2007). Internal Structure of Open System Pingos, Adventdalen, Svalbard: The Use of Resistivity Tomography to Assess Ground-ice Conditions. *Journal of Environmental and Engineering Geophysics*, 12(1), 113–126.

Ross, N., Harris, C., Christiansen, H. H., & Brabham, P. J. (2005). Ground penetrating radar investigations of open system pingos, Adventdalen, Svalbard. *Norwegian Journal of Geography*, *59*(2), 129–138.

Rossi, G., Accaino, F., Boaga, J., Petronio, L., Romeo, R., & Wheeler, W. (2018). Seismic survey on an open pingo system in Adventdalen Valley, Spitsbergen, Svalbard. *Near Surface Geophysics*, 16(1), 1–15.

Roy, S., Senger, K., Braathen, A., Hovland, M., Olaussen, S., & Noormets, R. (2014). Fluid migration pathways to seafloor seepage in inner Isfjorden and Adventfjorden, Svalbard. *Norwegian Journal of Geology*, *94*, 99–119.

Ruppel, C. (2015). Permafrost-Associated Gas Hydrate: Is It Really Approximately 1 % of the Global System? *Journal of Chemical & Engineering Data*, *60*(2), 429–436.

Ruppel, C. D., & Kessler, J. D. (2017). The interaction of climate change and methane hydrates. *Reviews of Geophysics*, *55*(1), 126–168.

Sandmeier, K. J. (2020). *REFLEXW Version 9.5*. Retrieved online: https://www.sandmeier-geo.de/Download/reflexw_manual_a4.pdf. Date accessed: 25th October 2020.

Saunois, M., Bousquet, P., Poulter, B., Peregon, A., Ciais, P., Canadell, J. G., et al. (2016b). The global methane budget 2000–2012. *Earth System Science Data*, *8*(2), 697–751.

Saunois, M., Jackson, R. B., Bousquet, P., Poulter, B., & Canadell, J. G. (2016a). The growing role of methane in anthropogenic climate change. *Environmental Research Letters*, *11*(12), 120207.

Saunois, M., Stavert, A. R., Poulter, B., Bousquet, P., Canadell, J. G., Jackson, R. B., et al. (2019). The Global Methane Budget 2000-2017. *Earth System Science Data Discussions*, 1–138.

Scapozza, C., Gex, P., Lambiel, C., & Reynard, E. (2008). *Contribution of self-potential (SP) measurements in the study of alpine periglacial hydrology: Examples from the southern Swiss Alps*. 1583–1588. Ninth International Conference on Permafrost, Fairbanks, USA.

Schaefer, K., Lantuit, H., Romanovsky, V. E., Schuur, E. A. G., & Witt, R. (2014). The impact of the permafrost carbon feedback on global climate. *Environmental Research Letters*, *9*(8), 085003.

Scheidegger, J. M., V. F. Bense, and S. E. Grasby (2012), Transient nature of Arctic spring systems driven by subglacial meltwater, *Geophysical Research Letters*, 39, L12405.

Scholz, H., & Baumann, M. (1997). An 'open system pingo' near Kangerlussuaq (Søndre Strømfjord), West Greenland. *Geology of Greenland Survey Bulletin*, *176*, 104–108.

Schrott, L. & Hoffmann, T. (2008). Refraction seismics. In Hauck, C., & Kniesel, C. (Eds.). *Applied Geophysics in Periglacial Environments* (pp. 57-80). Cambridge, UK: Cambridge University Press.

Schrott, L., & Sass, O. (2008). Application of field geophysics in geomorphology: Advances and limitations exemplified by case studies. *Geomorphology*, 93(1), 55–73.

Schuur, E. A. G., Bockheim, J., Canadell, J. G., Euskirchen, E., Field, C. B., Goryachkin, S. V., et al. (2008). Vulnerability of Permafrost Carbon to Climate Change: Implications for the Global Carbon Cycle. *BioScience*, *58*(8), 701–714.

Schuur, E. A. G., McGuire, A. D., Schädel, C., Grosse, G., Harden, J. W., Hayes, D. J., et al. (2015). Climate change and the permafrost carbon feedback. *Nature*, *520*(7546), 171–179.

Schuur, E. A. G., Vogel, J. G., Crummer, K. G., Lee, H., Sickman, J. O., & Osterkamp, T. E. (2009). The effect of permafrost thaw on old carbon release and net carbon exchange from tundra. *Nature*, *459*(7246), 556–559.

Schwamborn, G. J., Dix, J. K., Bull, J. M., & Rachold, V. (2002). High-resolution seismic and ground penetrating radar–geophysical profiling of a thermokarst lake in the western Lena Delta, Northern Siberia. *Permafrost and Periglacial Processes*, 13(4), 259–269.

Scott, W., Sellmann, P., & Hunter, J. (1990). Geophysics in the study of permafrost. *Geotechnical and Environmental Geophysics*, 1, 355–384.

Semenov, A. S. (1980). Elektrorazvedka metodom Estectvennogo Elektricheskogo Polya. Leningrad (St. Petersburg), Russia: Nedra.

Senger, K., Betlem, P., Liira, M., Roy, S., Midttømme, K., Beka, T., Olaussen, S., & Ohm, S. (2017). *Integrated thermo-baric modelling of the gas hydrate stability zone onshore Svalbard, Arctic Norway*. 9th International Conference on Gas Hydrates, Denver, CO, U.S.A.

Seppälä, M. (1988). Rock pingos in northern Ungava Peninsula, Quebec, Canada. *Canadian Journal of Earth Sciences*, *25*(4), 629–634.

Serov, P., Portnov, A., Mienert, J., Semenov, P., & Ilatovskaya, P. (2015). Methane release from pingo-like features across the South Kara Sea shelf, an area of thawing offshore permafrost. *Journal of Geophysical Research: Earth Surface*, *120*(8), 1515–1529.

Serov, P., Vadakkepuliyambatta, S., Mienert, J., Patton, H., Portnov, A., Silyakova, A., et al. (2017). Postglacial response of Arctic Ocean gas hydrates to climatic amelioration. *Proceedings of the National Academy of Sciences*, 114(24), 6215–6220.

Serrano-Silva, N., Sarria-Guzmán, Y., Dendooven, L., & Luna-Guido, M. (2014). Methanogenesis and Methanotrophy in Soil: A Review. *Pedosphere*, *24*(3), 291–307.

Serreze, M. C., Barrett, A. P., Stroeve, J. C., Kindig, D. N., & Holland, M. M. (2009). The emergence of surface-based Arctic amplification. *The Cryosphere*, *3*(1), 11–19.

Shakhova, N., Semiletov, I., Leifer, I., Salyuk, A., Rekant, P., & Kosmach, D. (2010a). Geochemical and geophysical evidence of methane release over the East Siberian Arctic Shelf. *Journal of Geophysical Research: Oceans*, *115*(C8), C08007.

Shakhova, N., Semiletov, I., Leifer, I., Sergienko, V., Salyuk, A., Kosmach, D., et al. (2014). Ebullition and storm-induced methane release from the East Siberian Arctic Shelf. *Nature Geoscience*, *7*(1), 64–70.

Shakhova, N., Semiletov, I., Salyuk, A., Yusupov, V., Kosmach, D., & Gustafsson, Ö. (2010b). Extensive Methane Venting to the Atmosphere from Sediments of the East Siberian Arctic Shelf. *Science*, *327*(5970), 1246–1250.

Shearer, J. M., Macnab, R. F., Pelletier, B. R., & Smith, T. B. (1971). Submarine Pingos in the Beaufort Sea. *Science*, *174*(4011), 816–818.

Shur, Y. (1988). *The upper horizon of permafrost soils. In: Proceedings, 1st International Conference on Permafrost, Vol. 1* (pp. 867-871). Trondheim, Norway: Tapir Publishers.

Shur, Y., French, H. M., Bray, M. T., & Anderson, D. A. (2004). Syngenetic permafrost growth: Cryostratigraphic observations from the CRREL tunnel near Fairbanks, Alaska. *Permafrost and Periglacial Processes*, *15*(4), 339–347.

Shur, Y., Hinkel, K. M., & Nelson, F. E. (2005). The transient layer: Implications for geocryology and climate-change science. *Permafrost and Periglacial Processes*, *16*(1), 5–17.

Sjöberg, Y., Marklund, P., Pettersson, R., & Lyon, S. W. (2015). Geophysical mapping of palsa peatland permafrost. *The Cryosphere*, 9(2), 465–478.

Smith, M. W. (1985). Models of soil freezing. In: Church, M., Slaymaker, O (Eds.) *Field and Theory: Lectures in Geocryology* (pp. 96– 120). Vancouver, BC: University of British Columbia Press.

Soloviev, P. A. (1973). Thermokarst phenomena and landforms due to frost heaving in central Yakutia. *Builetyn Peryglacjalny*, 23, 135–155.

Sørensen, K. I., Christiansen, A. V., & Auken, E. (2006). 4.4 The Transient Electromagnetic Method (TEM). In: Kirsch, R. (Ed.) *Groundwater Resources in Buried Valleys, a Challenge for Geosciences*. Hannover, Germany: BurVal Working Group.

Stranne, C., O'Regan, M., Dickens, G. R., Crill, P., Miller, C., Preto, P., & Jakobsson, M. (2016). Dynamic simulations of potential methane release from East Siberian continental slope sediments. *Geochemistry, Geophysics, Geosystems*, *17*(3), 872–886.

Stranne, C., O'Regan, M., Hong, W.-L., Brüchert, V., Ketzer, M., Thornton, B. F., & Jakobsson, M. (2022). Anaerobic oxidation has a minor effect on mitigating seafloor methane emissions from gas hydrate dissociation. *Communications Earth & Environment*, *3*(1), 1–10.

Svensson, H. (1971). Pingos i ytre dele nav Adventdalen. In: *Norsk Polarinstitutt Årbok 1969*. Tromsø, Norway: Norwegian Polar Institute.

Tarnocai, C. (1999). The effect of climate warming on the carbon balance of cryosols in Canada. *Permafrost and Periglacial Processes*, *10*(3), 251–263.

Tavakoli, S., Gilbert, G., Lysdahl, A. O. K., Frauenfelder, R., & Forsberg, C. S. (2021). Geoelectrical properties of saline permafrost soil in the Adventdalen valley of Svalbard (Norway), constrained with in-situ well data. *Journal of Applied Geophysics*, *195*, 104497.

Thompson, R. L., Sasakawa, M., Machida, T., Aalto, T., Worthy, D., Lavric, J. V., Lund Myhre, C., & Stohl, A. (2017). Methane fluxes in the high northern latitudes for 2005–2013 estimated using a Bayesian atmospheric inversion. *Atmospheric Chemistry and Physics*, *17*(5), 3553–3572.

Thompson, S., Kulessa, B., & Luckman, A. (2012). Integrated electrical resistivity tomography (ERT) and self-potential (SP) techniques for assessing hydrological processes within glacial lake moraine dams. *Journal of Glaciology*, *58*(211), 849–858.

Timur, A. (1968). Velocity of compressional waves in porous media at permafrost temperatures, *Geophysics*, 33(4), 584–595.

Turetsky, M. R., Abbott, B. W., Jones, M. C., Anthony, K. W., Olefeldt, D., Schuur, E. A. G et al. (2019). Permafrost collapse is accelerating carbon release. *Nature*, 569(7754), 32–34.

Turetsky, M. R., Abbott, B. W., Jones, M. C., Anthony, K. W., Olefeldt, D., Schuur, E. A. G et al. (2020). Carbon release through abrupt permafrost thaw. *Nature Geoscience*, 13(2), 138–143.

University Centre in Svalbard (2022). *Weather Stations*. Available online: https://www.unis.no/resources/weather-stations/ Date accessed: 22nd May 2022.

Vallée, S., & Payette, S. (2007). Collapse of permafrost mounds along a subarctic river over the last 100 years (northern Québec). *Geomorphology*, *90*(1), 162–170.

van Asperen, H., Alves-Oliveira, J. R., Warneke, T., Forsberg, B., de Araújo, A. C., & Notholt, J. (2021). The role of termite CH_4 emissions on the ecosystem scale: A case study in the Amazon rainforest. *Biogeosciences*, *18*(8), 2609–2625.

van der Sluis A. & van der Vorst H.A. (1987). Numerical solution of large sparse linear algebraic systems arising from tomographic problems. In: Nolet, G. (Ed.), *Seismic Tomography* (pp. 49–83). Dordrecht, The Netherlands: Reidel Publishing Co.

van Everdingen, R. O., *Multi-language Glossary of Permafrost and Related Ground Ice Terms* (Revised Edition). Boulder, CO: National Snow and Ice Data Center and World Center for Glaciology.

Van Vliet-Lanoë, B. (1998). Frost and soils: Implications for paleosols, paleoclimates and stratigraphy. *Catena*, *34*(1), 157–183.

Vasconcelos, S. S., Mendonça, C. A., & Silva, N. (2014). Self-potential signals from pumping tests in laboratory experiments. *Geophysics*, *79*(6), EN125–EN133.

Vaughn, T. L., Bell, C. S., Pickering, C. K., Schwietzke, S., Heath, G. A., Pétron, G., et al. (2018). Temporal variability largely explains top-down/bottom-up difference in methane emission estimates from a natural gas production region. *Proceedings of the National Academy of Sciences*, *115*(46), 11712–11717.

Vidale, J. (1988). Finite-difference calculation of travel times. *Bulletin of the Seismological Society of America*, 78, 2062– 2076.

Vidale, J. E. (1990). Finite-difference calculation of traveltimes in three dimensions. *Geophysics*, 55, 521– 526.

Vieira, G., Bockheim, J., Guglielmin, M., Balks, M., Abramov, A. A., Boelhouwers, J., et al. (2010). Thermal state of permafrost and active-layer monitoring in the antarctic: Advances during the international polar year 2007–2009. *Permafrost and Periglacial Processes*, *21*(2), 182–197.

Vieira, G., Hauck, C., Gruber, S., Blanco, J., & Ramos, M. (2008). *Massive Ice Detection using Electrical Tomography Resistivity. Examples from Livingston and Deception Islands, Maritime Antarctic*. 6ª Assembleia Luso Espanhola de Geodesia e Geofísica, Tomar.

Vogt, C., Laihem, K., & Wiebusch, C. (2008). Speed of sound in bubble-free ice. *The Journal of the Acoustical Society of America*, *124*(6), 3613–3618.

Voigt, C., Marushchak, M. E., Abbott, B. W., Biasi, C., Elberling, B., Siciliano, S. D., Sonnentag, O., Stewart, K. J., Yang, Y., & Martikainen, P. J. (2020). Nitrous oxide emissions from permafrost-affected soils. *Nature Reviews Earth & Environment*, *1*(8), 420–434.

von Smoluchowski, M. (1903). Contribution to the theory of electro-osmosis and related phenomena. *Bulletin international de l'Académie des sciences de Cracovie*, 3, 184–199.

Walter Anthony, K. M., Anthony, P., Grosse, G., & Chanton, J. (2012). Geologic methane seeps along boundaries of Arctic permafrost thaw and melting glaciers. *Nature Geoscience*, 5(6), 419–426.

Walter Anthony, K., Schneider von Deimling, T., Nitze, I., Frolking, S., Emond, A., Daanen, R., Anthony, P., Lindgren, P., Jones, B., & Grosse, G. (2018). 21st-century modeled permafrost carbon emissions accelerated by abrupt thaw beneath lakes. *Nature Communications*, *9*(1), 3262.

Walter, K. M., Edwards, M. E., Grosse, G., Zimov, S. A., & Chapin, F. S. (2007). Thermokarst Lakes as a Source of Atmospheric CH_4 During the Last Deglaciation. *Science*, *318*(5850), 633–636.

Walvoord, M. A., & Kurylyk, B. L. (2016). Hydrologic impacts of thawing permafrost—A review. *Vadose Zone Journal*, *15*(6).

Waxman, M. H., & Smits, L. J. M. (1968). Electrical Conductivities in Oil-Bearing Shaly Sands. *Society of Petroleum Engineers Journal*, 8, 107-122.

Weigand, M., Wagner, F. M., Limbrock, J. K., Hilbich, C., Hauck, C., & Kemna, A. (2020). A monitoring system for spatiotemporal electrical self-potential measurements in cryospheric environments. *Geoscientific Instrumentation, Methods and Data Systems*, *9*(2), 317–336.

Westbrook, G. K., Thatcher, K. E., Rohling, E. J., Piotrowski, A. M., Pälike, H., Osborne, A. H., et al. (2009). Escape of methane gas from the seabed along

the West Spitsbergen continental margin. *Geophysical Research Letters*, *36*(15), L15608.

Westoby, M. J., Brasington, J., Glasser, N. F., Hambrey, M. J., & Reynolds, J. M. (2012). 'Structure-from-Motion' photogrammetry: A low-cost, effective tool for geoscience applications. *Geomorphology*, 179, 300–314.

Wetterich, S., Schirrmeister, L., Nazarova, L., Palagushkina, O., Bobrov, A., Pogosyan, L., et al (2018). Holocene thermokarst and pingo development in the Kolyma Lowland (NE Siberia). *Permafrost and Periglacial Processes*, *29*(3), 182–198.

Winton, M. (2006). Amplified Arctic climate change: What does surface albedo feedback have to do with it? *Geophysical Research Letters*, *33*(3).

Wolfe, S. A., Stevens, C. W., Gaanderse, A. J., & Oldenborger, G. A. (2014). Lithalsa distribution, morphology and landscape associations in the Great Slave Lowland, Northwest Territories, Canada. *Geomorphology*, 204, 302–313.

Woo M.-K. (2012). *Permafrost Hydrology*. Heidelberg, Germany: Springer.

Worden, J. R., Bloom, A. A., Pandey, S., Jiang, Z., Worden, H. M., Walker, T. W., Houweling, S., & Röckmann, T. (2017). Reduced biomass burning emissions reconcile conflicting estimates of the post-2006 atmospheric methane budget. *Nature Communications*, *8*(1), 2227.

Worsley, P., & Gurney, S. D. (1996). Geomorphology and hydrogeological significance of the Holocene pingos in the Karup Valley area, Traill Island, northern east Greenland. *Journal of Quaternary Science*, *11*(3), 249–262.

Xiao, K., Zou, C., Shang, J., Yang, Y., & Zhang, H. (2019). Numerical simulation of AVO response characteristics from pore-filling gas hydrate in Qilian mountain permafrost, China. *Arabian Journal of Geosciences*, *12*(12), 379.

Yoshikawa, K. & Harada, K. (1995). Observations on nearshore pingo growth, Adventdalen, Spitsbergen. *Permafrost and Periglacial Processes*, 6, 361-372.

Yoshikawa, K. & Hinzman, L. D. (2003). Shrinking thermokarst ponds and groundwater dynamics in discontinuous permafrost near Council, Alaska. *Permafrost and Periglacial Processes*, 14, 151-160.

Yoshikawa, K. (1993). Notes on open-system pingo ice, Adventdalen, Spitsbergen. Permafrost and Periglacial Processes, 4, 327-334.

Yoshikawa, K., & Nakamura, T. (1996). Pingo growth ages in the delta area, Adventdalen, Spitsbergen. *Polar Record*, 32(183), 347–352.

Yoshikawa, K., Leuschen, C., Ikeda, A., Harada, K., Gogineni, P., Hoekstra, P., et al. (2006). Comparison of geophysical investigations for detection of massive ground ice (pingo ice). *Journal of Geophysical Research: Planets*, 111(E6).

You, Y., Yu, Q., Pan, X., Wang, X., & Guo, L. (2013). Application of electrical resistivity tomography in investigating depth of permafrost base and permafrost structure in Tibetan Plateau. *Cold Regions Science and Technology*, 87, 19–26.

Zhang, T., Barry, R. G., Knowles, K., Heginbottom, J. A., & Brown, J. (1999). Statistics and characteristics of permafrost and ground-ice distribution in the Northern Hemisphere. *Polar Geography*, *23*(2), 132–154.

Zhang, X., Zhao, M., & Wang, K. (2022). Understanding the influence of rock content on streaming potential phenomenon of soil-rock mixture: an experimental study. *Sensors*, 22, 585.

Zimmerman, R. W., & King, M. S. (1986). The effect of the extent of freezing on seismic velocities in unconsolidated permafrost. *Geophysics*, 51(6), 1285–1290.